

# **Tuning of Organic Ligands in Metal Complexes for Anticancer Activity and Selective Delivery**

**Ph.D. Thesis**

By

**PRACTI**



**DEPARTMENT OF CHEMISTRY  
INDIAN INSTITUTE OF TECHNOLOGY INDORE  
AUGUST 2023**



# Tuning of Organic Ligands in Metal Complexes for Anticancer Activity and Selective Delivery

A THESIS

*Submitted in partial fulfillment of the  
requirements for the award of the degree  
of*  
**DOCTOR OF PHILOSOPHY**

*by*  
**PRAGTI**



**DEPARTMENT OF CHEMISTRY  
INDIAN INSTITUTE OF TECHNOLOGY INDORE  
AUGUST 2023**





# INDIAN INSTITUTE OF TECHNOLOGY INDORE

## CANDIDATE'S DECLARATION

I hereby certify that the work which is being presented in the thesis entitled **Tuning of Organic Ligands in Metal Complexes for Anticancer Activity and Selective Delivery** in the partial fulfillment of the requirements for the award of the degree of **DOCTOR OF PHILOSOPHY** and submitted in the **Department of Chemistry, Indian Institute of Technology Indore**, is an authentic record of my own work carried out during the time period from **July 2018** to **August 2023** under the supervision of **Prof. Suman Mukhopadhyay**, Professor, Department of Chemistry, Indian Institute of Technology Indore.

The matter presented in this thesis has not been submitted by me for the award of any other degree of this or any other institute.

 20.08.2023

Signature of the student with date  
(**PRAGTI**)

---

This is to certify that the above statement made by the candidate is correct to the best of my/our knowledge.

 20.08.2023

Signature of Thesis Supervisor with date  
(**Prof. SUMAN MUKHOPADHYAY**)

---

**MS. PRAGTI** has successfully given her Ph.D. Oral Examination held on...~~16.01.2024~~....

 16.01.2024

Signature of Thesis Supervisor with date  
(**Prof. SUMAN MUKHOPADHYAY**)

---



## **ACKNOWLEDGEMENTS**

After a long journey of five years, today is the day: writing this note of thanks is the finishing touch on my thesis. It has been a period of intense learning for me, not only in the scientific arena, but also on a personal level. Writing this thesis has had a big impact on me. I would like to reflect on the people who have supported and helped me so much throughout this period.

It is my great pleasure to express my deep sense of gratitude to my PhD thesis supervisor, Prof. Suman Mukhopadhyay for his constant guidance, encouragement and help throughout the whole course of the thesis work. I am greatly indebted to him for his support, motivation and guidance. His vision and dedication in developing the thesis injected a remarkable impact on my academic career. I have been very privileged to have the most hard working and supportive advisor anyone could ask for. At a personal level, I will always cherish the valuable lessons and suggestions I received from him. I am also thankful to my PSPC committee members, Dr. Satya S. Bulusu and Dr. Abhinav Raghuvanshi for their valuable suggestions and guidance. I wish to express my gratitude to Prof. Suhas S. Joshi, Director, IIT Indore for his continuous support in every aspect. I would like to thank IIT Indore and SIC, IIT Indore for providing financial support and instrumentation facility, respectively. I am also thankful to Dr. Sheikh. M. Mobin, Dr. Rakesh Ganguly, Dr. Avinash Sonawane, Dr. Ivo Grabchev, Dr. Bidyut Kumar Kundu, and Mr. Satyam Singh, for their active support in various research projects. I would also like to thank all the faculty members of Department of Chemistry, IIT Indore for their guidance and help during the course of the thesis work. I personally extend my heartiest gratitude to Dr. Bidyut Kumar Kundu and Dr. Rinky Singh for their constant guidance, help and support at all the ups and downs in those initial days of the PhD programme. I convey my deep thanks to my dear group members, Dr. Chanchal Sonkar, Dr. Rishi Ranjan, Ms. Reena, Mr. Arghya Chakraborty, Mr. Sayantan Sarkar for their selfless co-operation and help to make my work successful. I would also like to thank Mr. Kinny Pandey, Mr. Ravinder Kumar, Mr. Ghanshyam Bhavsar, Mr. Manish

Kushwaha Mr. Rameshwar Dohare, and Ms. Vinita Kothari for their technical support without which it would not be possible to continue my work. I would like to thank all my co-researchers at IIT Indore. I would like to acknowledge all the technical and non-technical staffs of IIT Indore for their assistance and service. It has been a wonderful experience to work with many friends during my Ph.D. who really helped me in many aspects. I would like to record my thanks to Dr. Sushmita Dwivedi , Dr. Tulika Dixit, Mr. Pradyuman Kumar Arya , Mr. Manish Badole, Ms. Srijita Pal, Mr. Ritik, and many more in my friend circle.

I thank my beloved parents (Mr. Shyam Babu, and Mrs. Manju Gupta) for their wise counsel and sympathetic ear. They are always there for me. I don't have enough word to describe all the sacrifices they continue to make to see me through this milestone. Without your constant support and unconditional love, it would not have been possible. I want to say thanks to my brothers and my sister. It would take up too much space to list even the biggest things but know that I couldn't have done it without you too!

Last but not the least, there are many more who have directly or indirectly contributed in making this journey successful. I wish I could thank them all but time and space compel me to stop here!!!

August 2023

*Pragti*

*Dedicated to my  
beloved family*



# ABSTRACT

## 1. Introduction

Metal ions, combined with organic and inorganic ligands provide an excellent opportunity to deal with various aspects of diagnosis and treatment of different diseases with a multitude of tasks. [1] With the luxury of choosing from tens of metal ions and thousands of ligand systems, coordination and organometallic chemists can explore the possibilities to hit the right combination to come up with new molecules for extensive medical applications. Among various medical challenges, cancer remains the leading cause of death worldwide, with over ten million cases in a calendar year. [2] The utilization of metallodrugs against cancer has started to be investigated in a modern scientific way with the discovery of cisplatin, which has been found to be cytotoxic in nature. [3] With the success of cisplatin in cancer treatment in the seventies, various other platinum-based compounds have been tested as prospective anticancer agents, and among them, carboplatin, oxaliplatin, nedaplatin, lobaplatin, and heptaplatin have been approved by different drug controlling agencies for cancer treatment. [4] This group of metallodrugs can work efficiently against testicular, cervical, ovarian, head and neck and non-small cell lung cancer. [5] Nevertheless, certain limitations restrict their extensive use in the treatment. Among them, poor selectivity of the drugs towards cancer -specific cells complicates the treatment with unavoidable side effects, and increasing chemoresistance remains another major concern. [6] Therefore, there is an urgency to look beyond platinum for alternative improved metallodrugs with better efficiency, reduced side effects and lesser chemoresistance. As an alternative option new metal ion(s) with the ability of different mechanistic pathways and toxicity profiles started to get investigated with time. Among various metal ions, ruthenium has been found to be very much effective with several advantages that can be exploited to prepare better anticancer metallodrugs. [7] Ruthenium, with its preference for hexa-coordinated geometry, provides ample opportunity to load the coordination sphere with various bioactive ligands. It is also observed that ruthenium (III) compounds

tend to act as prodrugs and get activated inside the tumor cells where a hypoxic condition exists and induces the reduction of ruthenium(III) to ruthenium(II). Until now, four ruthenium complexes have entered clinical trials viz NAMI-A, KP1019, KP1339, and TLD1433. [8] NAMI-A entered the phase II trials but due to limited efficacy could not proceed further for clinical development. Another ruthenium complex KP1019 entered the phase I trials, but its low solubility halted its further development. However, the sodium salt of KP1019, KP1339 are still under clinical trials. Altogether ruthenium has shown many attractive characteristics to be exploited for providing alternative metallodrugs for cancer treatment. Apart from ruthenium, zinc, a naturally occurring metal, also plays a significant role in treating many diseases. [9] Zinc-containing compounds have been found to exhibit antiviral, antibacterial, and anticancer activities. Moreover, zinc-based drugs have shown promise in treating Alzheimer's disease and diabetes. [10] The flexibility of zinc's coordination geometry allows it to interact with different ligands, making it a versatile element in biological systems. Zinc complexes are getting much attention in developing anticancer drugs with the conception that they will show less toxicity toward healthy cells. [11]

Apart from developing metal-based drugs, one of the biggest obstacles in the success story of such therapeutic agents is their proper delivery in targeted cells. Controlling drug delivery can help to overcome these drawbacks. Using nanotechnology-based drug delivery systems is one promising approach to reducing the side effects of bare drugs. [12] These intelligent drug delivery systems can lower side effects and enhance therapeutic results by optimizing drug concentrations at the target site. Certain nanocarriers are designed to encapsulate the complexes, enhancing their activity while minimizing the adverse side effects. [13]

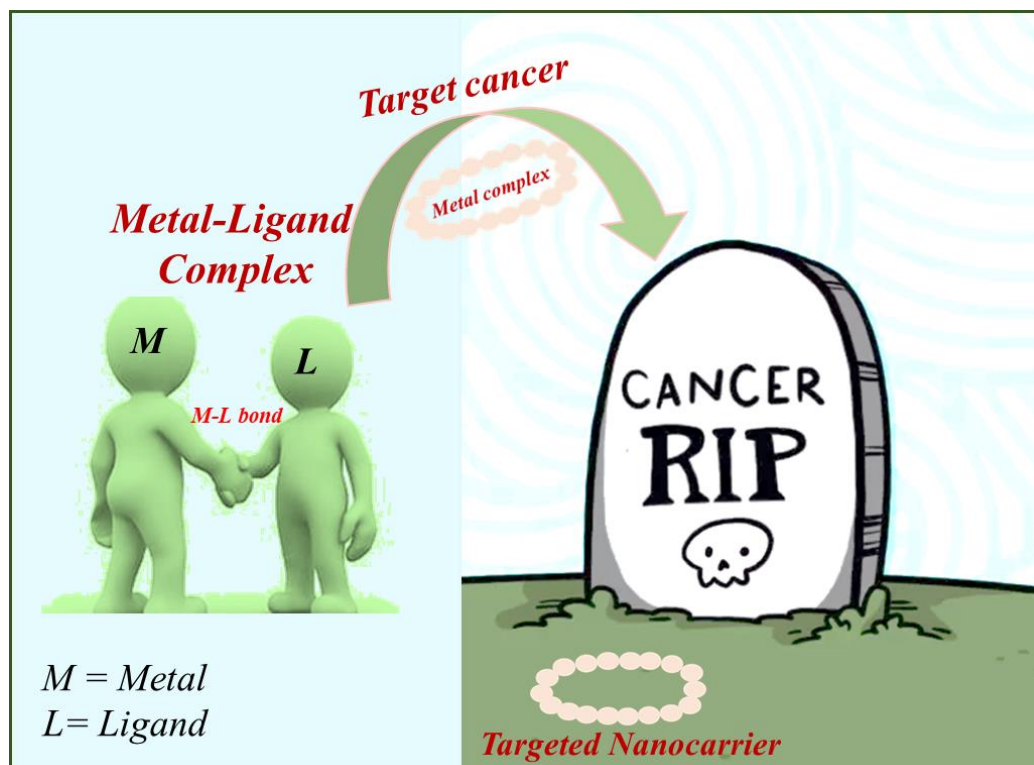


**Figure 1.** General representation of metal ligand complex formation and their targeted drug delivery

## 2. Objectives

The primary objectives which have been set for this thesis are the following:

- To develop new metal complexes by employing suitable organic ligands (fluorescent and nonfluorescent) for prospective cancer treatment and their characterization through various analytical and spectroscopic techniques.
- To synthesize cancer targeted drug delivery nanocarriers like mesoporous silica nanoparticles, and nanogels, exclusively targeting cancer cells and minimizing potential damage to healthy cells.
- To explore the interactions of metal complexes with biomolecules: DNA/ Protein binding and cleavage is a key research field for metal complexes as it can help to develop new therapeutic metallodrugs.
- To investigate the potential anticancer properties of synthesized compounds in cancerous and noncancerous cells.
- To explore cell imaging study to understand the effect of compounds on cellular morphology and function.

- To investigate possible mechanistic pathways to determine the mode of action of synthesized compounds and *in vivo* study (in Zebra fish)

### **3. Summary of research work**

The contents of each chapter included in the thesis are discussed briefly as follows:

#### **3.1. Chapter 1: General Introduction and Background**

A brief overview of the basic concepts and recent scientific developments towards generating metal-based anticancer drugs have been reported. Moreover, the importance of introducing ruthenium metal as a potential candidate in cancer therapy has also been discussed. Finally, a summary of the research reported in this thesis and the relevance in the prospects of recent developments have been put forward.

#### **3.2. Chapter 2: Modulation of catalytic and biomolecular binding properties of ruthenium (II)-arene complexes with the variation of coligands for selective toxicity against cancerous cells**

Four ruthenium(II)-arene complexes, viz.  $[\text{Ru}(\text{p-cym})(2\text{-ampy})\text{Cl}]\text{PF}_6$  **1**,  $[\text{Ru}(\text{benzene})(2\text{-ampy})\text{Cl}]\text{SO}_3\text{CF}_3$  **2**,  $[\text{Ru}(\text{p-cym})(2\text{-ampy})\text{PPh}_3](\text{PF}_6)_2$  **3** and  $[\text{Ru}(\text{benzene})(2\text{-ampy})\text{PPh}_3](\text{SO}_3\text{CF}_3)_2$  **4** [2-ampy = 2-aminomethyl pyridine] have been synthesized and characterized. Different analytical techniques have been utilized to characterize **1–4**, and a DFT study was used to optimize the geometries and calculate the energies of the frontier molecular orbitals. An MTT assay revealed the potency of complexes **1–4** against MCF-7 (breast cancer) and Hela (cervical cancer) cell lines. The presence of the triphenyl phosphine ligand in complexes **3** and **4** makes the complexes more cytotoxic with respect to their chloro-analogues. The complexes are found to be specifically cytotoxic against cancerous cell lines, as they were inactive against the normal HEK 293 cell line. An absorption and fluorescence titration study of complexes **1–4** showed significant interactions with DNA and proteins. Interestingly, all the complexes show potent catalytic activity for the hydrogen transfer of NADH and converted NADH to  $\text{NAD}^+$ , which helps to induce the accumulation of intracellular reactive oxygen species (ROS) in MCF-7 cells.

To analyze the morphological changes in the cells, the Hoechst staining method was applied to capture images of apoptotic cells through confocal microscopy.

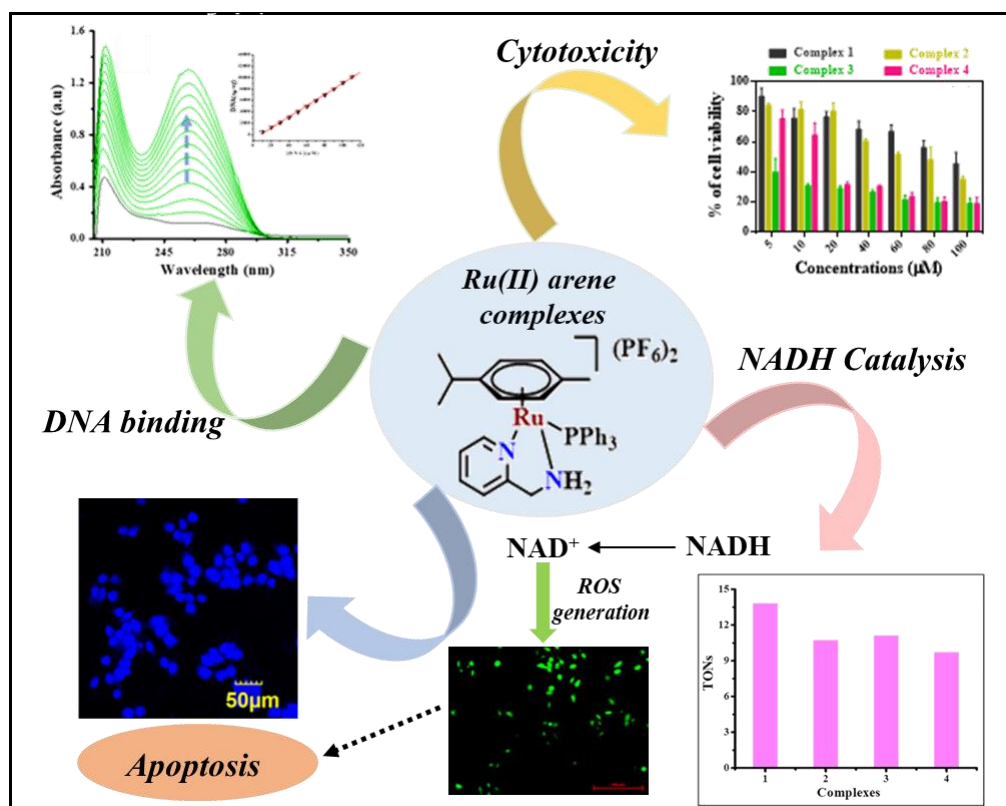


**Figure 2.** Schematic diagram depicting the role of Ru(II)-arene complexes with 2-aminomethyl pyridine coligand that modulate the cell redox balance (NADH catalysis) and enhance anticancer activity leads to cell apoptosis.

### 3.3. Chapter 3: Pyrene-based fluorescent Ru(II)-arene complexes for significant biological applications: catalytic potential, DNA/protein binding, two photon cell imaging and in vitro cytotoxicity

Four new organometallic Ru(II)-arene complexes [Ru( $\eta^6$ -p-cymene)(L)Cl] **5**, [Ru( $\eta^6$ -benzene)(L)Cl] **6**, [Ru( $\eta^6$ -p-cymene)(L)N<sub>3</sub>] **7** and [Ru( $\eta^6$ -benzene)(L)N<sub>3</sub>] **8** [HL = (E)-N'-(pyren-1-ylmethylene)thiopene-2-carbohydrazide] have been synthesized and characterized that have anticancer, antimetastatic and two-photon cell imaging abilities. Moreover, these compounds also display good catalytic activity in the transfer hydrogenation of NADH to NAD<sup>+</sup>. All the complexes, **5–8**, are well characterized by

spectroscopic techniques (NMR, mass, FTIR, UV-Vis and fluorescence). The single crystal X-ray diffraction technique proved that the ligand **HL** coordinates through an N,O-bidentate chelating fashion in the solid-state structures of complexes **5** and **6**. The stability study of the complexes was performed through UV-visible spectroscopy. The cytotoxicities of all the complexes were screened through an MTT assay, and the results revealed that the complexes have potential anticancer activity against various cancerous cells (HeLa, MCF7 and A431). Studies with spectroscopic techniques revealed that complexes **5–8** exhibit strong interactions with biological molecules i.e. proteins (HSA and BSA) and CT-DNA. The density functional theory (DFT-D) method has been employed in the present study to know the interaction between DNA and complexes by calculating the HOMO and LUMO energy. A plausible mechanism for NADH oxidation has also been explored and the DFT calculations are in accord with the experimental observation. Furthermore, the capabilities of intracellular reactive oxygen species (ROS) generation in the MCF7 breast cancer cell line were studied. The Hoechst/PI dual staining method confirmed the apoptosis mode of cell death. Meanwhile, complexes **5–8** show capabilities to prevent the metastasis phase of cancer cells by inhibiting cell migration.

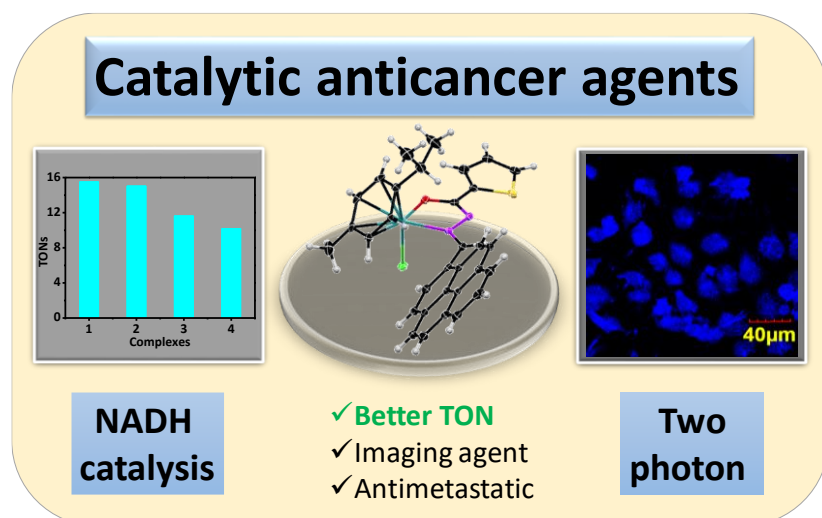


**Figure 3.** Schematic diagram depicting the role of Ru(II)-arene complexes with pyrene based moiety as coligand that have better TON values in NADH catalysis, having antimetastatic property and act as cell imaging agent

### **3.4. Chapter 4: Chitosan-Biotin Conjugated pH Responsive Ru(II) Glucose Nanogel: A Dual Pathway of Targeting Cancer Cells and Self-Drug Delivery**

The current study paves the way for improved chemotherapy by creating pH-responsive nanogels (**GC9** and **GC10**) that are loaded with new synthetic ruthenium(II) arene complexes (**9** and **10**) to increase biological potency. Nanogels are fabricated by the conjugation of chitosan-biotin biopolymers that selectively target the cancer cells, as chitosan has the pH-responsive property, which helps in releasing the drug in cancer cells (pH 5.5), and biotin provides the way to target the cancer cells selectively due to the overexpression of integrin in them. With the use of spectroscopic and analytical techniques like NMR, ESI-MS, FTIR, UV-visible, SEM, TEM, XPS, rheology, BET, and others, the compounds and synthesized nanogels were thoroughly characterized. Nanogels (NGs) displayed exceptional increased efficacy toward cancerous cells with  $IC_{50}$  values ranging from 7.50 to 18.86  $\mu$ M via induced apoptosis in a group of three human cancer cell lines. Apart from its potency, NGs found to be highly selective towards cancer cells. Moreover, based on the results of immunoblot analysis, it was observed that the synthesized compounds exhibit a significant increase in the expression of cleaved caspase-3 and a decrease in the expression of the anti-apoptotic protein BCL-XL. Additionally, it was discovered that NG-induced apoptosis is dependent on ROS production and DNA targeting. Furthermore, a narrower range of  $LD_{50}$  values (1185.93 and 823.03  $\mu$ M) was seen after administering NGs to zebrafish embryos *in vivo*. The results support using drug-loaded nanogels as potential chemotherapeutic and chemopreventive agents for human cancer cells.

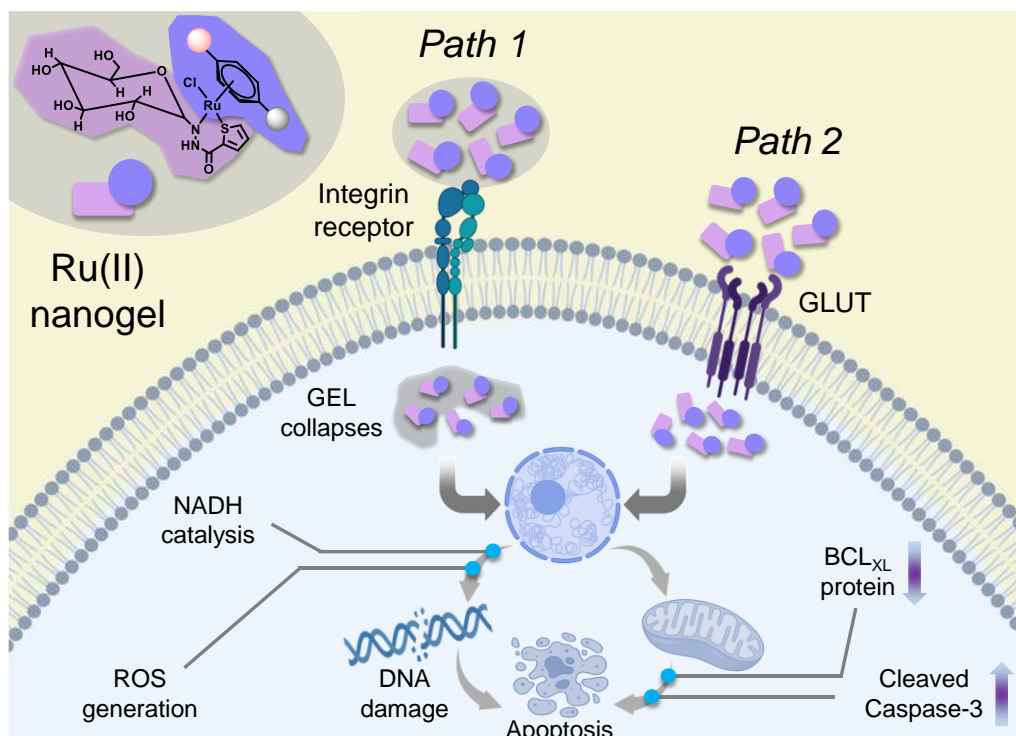


**Figure 4.** Schematic diagram depicting the probable mechanism of nanogels loaded with glucose ring conjugated Ru(II) arene complexes that shows targeted drug delivery

### 3.5. Chapter 5: Cancer-Targeted Chitosan–Biotin-Conjugated Mesoporous Silica Nanoparticles as Carriers of Zinc Complexes to Achieve Enhanced Chemotherapy *In Vitro* and *In Vivo*

Despite being the most common component of numerous metalloenzymes in the human body, zinc complexes are still under-rated as chemotherapeutic agents. Herein, the present study opens up a key route toward enhanced chemotherapy with the help of two Zn (II) Mannich base complexes: ZnMBC (complex **11** and complex **12**) synthesized alongside Mannich base ligands to investigate their biological potency. Further, well-established mesoporous silica nanoparticles (MSNs) have been chosen as carriers of the titled metallodrugs in order to achieve anticancer drug delivery. A pH sensitive additive, namely, chitosan (CTS) conjugated with biotin is tagged to MSNs for the targeted release of core agents inside tumors selectively. In general, CTS blocks ZnMBC inside the mesopores of MSNs, and biotin acts as a targeting ligand to improve tumor-specific cellular uptake. CTS–biotin surface

decoration significantly enhanced the cellular uptake of ZnMBC through endocytosis. A panel of four human cancer cell lines has revealed that ZnMBC (11/12)@ MSNs-CTS-biotin nanoparticles (NPs) exhibits unprecedented enhanced cytotoxicity toward cancer cells with IC<sub>50</sub> values ranging from 6.5 to 28.8 μM through induction of apoptosis. NPs also possess excellent selectivity between normal and cancer cells along with their enhanced efficacy. Two-photon-excited *in vitro* imaging of normal (HEK) and cancer (HeLa) cells has been performed to confirm the drug delivery. Also, NP-induced apoptosis was found to be dependent on targeting DNA and ROS generation. Moreover, a lower range of LD<sub>50</sub> values (153.6–335.5 μM) were observed upon treatment of zebrafish embryos with NPs *in vivo*. Because of the anatomical similarity to the human heart, the heart rate of NP-treated zebrafish has been analyzed in assessing the cardiac functions, which is in favor of the early clinical trials of ZnMBC (11/12)@MSNs-CTS-biotin candidates for their further evaluation as a chemotherapeutic and chemopreventive agent toward human cancers, especially adenocarcinoma.

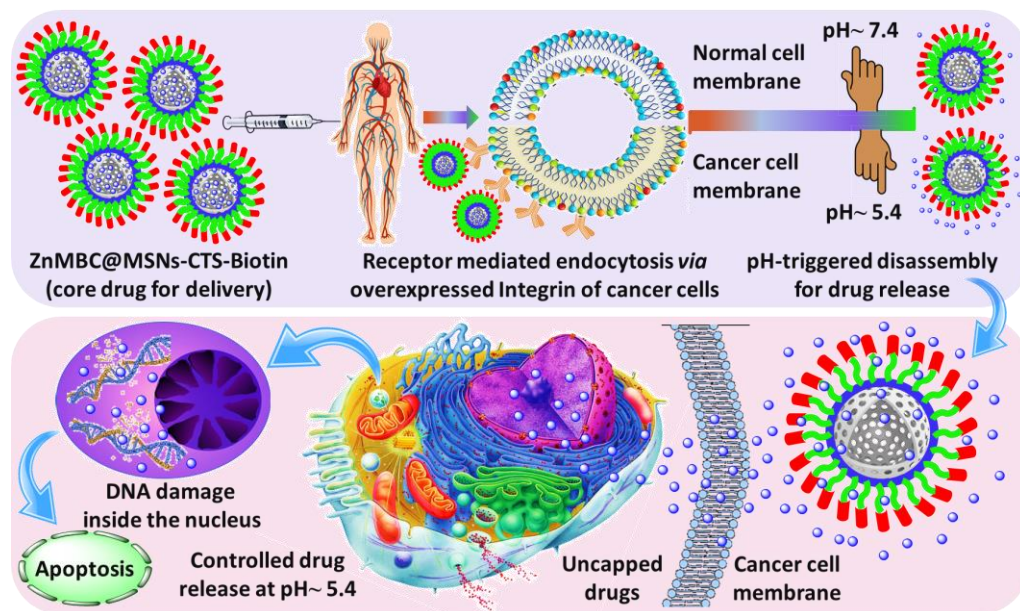


**Figure 5.** Schematic diagram depicting pH-responsive targeted drug delivery of zinc(II) complexes from targeted mesoporous silica nanoparticles and their probable cell death mechanism (cellular apoptosis)

### 3.6. Chapter 6: General conclusions and future scope

- In this thesis work, it has been observed that ruthenium and zinc metal complexes and with different organic and inorganic show promising cytotoxic activity, whereas the free ligands are mostly non-cytotoxic in the same condition.
- Coordinated with biologically active ligands, ruthenium (II) complexes have shown promising antiproliferative and antimetastatic activity. Thus, attaching this type of ligands to Ru(II) center can be explored further to develop potential metallodrugs for cancer therapy.
- It has been found that drug-loaded nanogels and loaded nanoparticles support the increased selectivity of ruthenium and zinc complexes between cancer and normal cells, subsequently establishing an improved anticancer property. The successful fabrication of nanogels and nanoparticles loaded with drugs offers a promising avenue for the advancement of targeted anticancer treatments, thereby contributing to significant progress in the field of cancer therapeutics.
- In the future, *in-vivo* research on mice can be conducted to evaluate the effect of these complexes on the living organism, as this would provide much more in-depth insight into the activities of complexes. Such investigations offer an invaluable opportunity to gain comprehensive insights into the activities and potential therapeutic benefits of these complexes. Additionally, *in-vivo* studies on mice can provide valuable preclinical data that can guide the design and optimization of future clinical trials, enabling a more informed and targeted approach towards the development of anticancer therapies.

## 4. REFERENCES

- [1] Mukherjee, A., Sadler, P.J., Metals in medicine: therapeutic agents, Wiley Encyclopedia of Chemical Biology, **2007**, 1-47. (DOI: 10.1002/9780470048672.wecb333)
- [2] Ferlay, J., Colombet, M., Soerjomataram, I., Mathers, C., Parkin, D.M., Piñeros, M., Znaor, A., Bray, F., Estimating the global cancer incidence and

- mortality in 2018: GLOBOCAN sources and methods, *International journal of cancer*, **2019**, 144(8), 1941-1953. (DOI: 10.1002/ijc.31937)
- [3] Jin, S., Guo, Y., Guo, Z. and Wang, X., Monofunctional platinum (II) anticancer agents, *Pharmaceuticals*, **2021**, 14(2), 133. (DOI: 10.3390/ph14020133)
- [4] Dilruba, S., Kalayda, G.V., Platinum-based drugs: past, present and future. *Cancer chemotherapy and pharmacology*, **2016**, 77, 1103-1124. (DOI: 10.1007/s00280-016-2976-z)
- [5] Khot, V.M., Salunkhe, A.B., Pricl, S., Bauer, J., Thorat, N.D., Townley, H., Nanomedicine-driven molecular targeting, drug delivery, and therapeutic approaches to cancer chemoresistance, *Drug Discovery Today*, **2021**, 26(3), 724-739. (DOI: 10.1016/j.drudis.2020.12.016)
- [6] Dianat-Moghadam, H., Heidarifard, M., Jahanban-Esfahlan, R., Panahi, Y., Hamishehkar, H., Pouremamali, F., Rahbarghazi, R., Nouri, M., Cancer stem cells-emanated therapy resistance: implications for liposomal drug delivery systems, *Journal of controlled release*, **2018**, 288, 62-83. (DOI: 10.1016/j.jconrel.2018.08.043)
- [7] Pragti., Kundu, B.K., Mukhopadhyay, S., Target based chemotherapeutic advancement of ruthenium complexes. *Coordination Chemistry Reviews*, **2021**, 448, 214169. (DOI: 10.1016/j.ccr.2021.214169)
- [8] Sonkar, C., Sarkar, S., Mukhopadhyay, S., Ruthenium (II)–arene complexes as anti-metastatic agents, and related techniques, *RSC Medicinal Chemistry*, **2022**, 13(1), 22-38. (DOI: 10.1039/D1MD00220A)
- [9] Kaur, K., Gupta, R., Saraf, S.A. Saraf, S.K., Zinc: the metal of life. *Comprehensive Reviews in Food Science and Food Safety*, **2014**, 13(4), 358-376. (DOI: 10.1111/1541-4337.12067)
- [10] Li, Z., Liu, Y., Wei, R., Yong, V.W., Xue, M., The Important Role of Zinc in Neurological Diseases. *Biomolecules*, **2022**, 13(1), 28. (DOI: 10.3390/biom13010028)

[11] Pellei, M., Del Bello, F., Porchia, M. and Santini, C., Zinc coordination complexes as anticancer agents, *Coordination Chemistry Reviews*, **2021**, 445, 214088. (10.1016/j.ccr.2021.214088)

[12] Kanwar, R., Rathee, J., Salunke, D.B., Mehta, S.K., Green nanotechnology-driven drug delivery assemblies. *ACS omega*, **2019**, 4(5), 8804-8815. (DOI: 10.1021/acsomega.9b00304)

[13] Kumar, R., Dalvi, S.V., Siril, P.F., Nanoparticle-based drugs and formulations: current status and emerging applications, *ACS Applied Nano Materials*, **2020**, 3(6), 4944-4961. (DOI: 10.1021/acsanm.0c00606)

## 5. List of publications

1. **Pragti.**, Kundu, B. K., Sonkar, C., Ganguly, R., Mukhopadhyay, S. (2021). Modulation of catalytic and biomolecular binding properties of ruthenium (II)-arene complexes with the variation of coligands for selective toxicity against cancerous cells. *Polyhedron*, 207, 115379.(DOI: 10.1016/j.poly.2021.115379)
2. **Pragti.**, Kundu, B. K., Upadhyay, S.N., Sinha, N., Ganguly, R., Grabchev, I., Pakhira, S., Mukhopadhyay, S. (2022). Pyrene-based fluorescent Ru (II)-arene complexes for significant biological applications: catalytic potential, DNA/protein binding, two photon cell imaging and in vitro cytotoxicity. *Dalton Transactions*, 51(10),3937-3953. (DOI: 10.1039/d1dt04093f)
3. **Pragti.**, Kundu, B.K., Carlton Ranjith, W.A., Shankar, U., Kannan, R.R., Mobin, S.M., Bandyopadhyay, A. and Mukhopadhyay, S., (2021). Cancer-Targeted Chitosan–Biotin-Conjugated Mesoporous Silica Nanoparticles as Carriers of Zinc Complexes to Achieve Enhanced Chemotherapy *In Vitro* and *In Vivo*. *ACS Applied Bio Materials*, 5, 190-204. (DOI: 10.1021/acsabm.1c01041)
4. **Pragti**, Kundu, B. K., Singh, S., Carlton Ranjith, W. A., Shankar, Sarkar, S., Sonawane, A., Mukhopadhyay, S. (2023), Chitosan-Biotin Conjugated pH Responsive Ru(II) Glucose Nanogel: A Dual Pathway of Targeting Cancer Cells and Self-Drug Delivery, *ACS Appl. Mater. Interfaces*, 15, 37, 43345–43358 (DOI: 10.1021/acсами.3c07157)

5. **Pragti.**, Kundu, B.K. and Mukhopadhyay, S., (2021). Target based chemotherapeutic advancement of ruthenium complexes. **Coordination Chemistry Reviews**, 448, 214169. ( DOI: 10.1016/j.ccr.2021.214169)
6. **Pragti**, Nayek, S., Singh, S., Sonawane, A., Grabchev, I., Ganguly, R., Mukhopadhyay, S. (2023). Studies on anticancer properties with varying co-ligands in Ru(II) arene benzimidazole system. **Dalton Transactions**, 52, 7104-7118. (DOI: 10.1039/D3DT00528C)
7. Kundu, B. K., **Pragti.**, Biswas, S., Mondal, A., Mazumdar, S., Mobin, S. M., & Mukhopadhyay, S. (2021). Unveiling the urease like intrinsic catalytic activities of two dinuclear nickel complexes towards the in situ syntheses of aminocyanopyridines. **Dalton Transactions**, 50(14), 4848-4858. (DOI: 10.1039/D1DT00108F)
8. Kundu, B. K., **Pragti.**, Mobin, S. M., & Mukhopadhyay, S. (2020). Studies on the influence of the nuclearity of zinc (ii) hemi-salen complexes on some pivotal biological applications. **Dalton Transactions**, 49(43), 15481-15503. (DOI: 10.1039/D0DT02941F)
9. Chhabra, V., Kundu, B. K., Ranjan, R., **Pragti.**, Mobin, S. M., & Mukhopadhyay, S. (2020). Coligand driven efficiency of catecholase activity and proteins binding study of redox active copper complexes. **Inorganica Chimica Acta**, 502, 119389-119409. (DOI: 10.1016/j.ica.2019.119389)
10. Kundu, B. K., **Pragti.**, Mobin, S. M., & Mukhopadhyay, S. (2019). Mechanistic and thermodynamic aspects of a pyrene-based fluorescent probe to detect picric acid. **New Journal of Chemistry**, 43(29), 11483-11492. (DOI: 10.1039/C9NJ02342A)

**Note: Publications 1-5 are included in the thesis work.**

## **LIST OF CONFERENCES**

1. In-house Chemistry symposium (CHEM-2019) on National Science Day, IIT Indore, 28th Feb, 2019
2. International Conference on “EMERGING TRENDS IN CHEMISTRY”, IIT Indore, 12th-15th July, 2019
3. 1-week Hands-on workshop on Human/Cancer Cell Culture Techniques and MTT Assay, International Center for Stem Cells, Cancer and Biotechnology (ICSCCB), Pune, India 4th-10th Nov, 2019
4. International Workshop on “Supporting Chemistry Research with modern DFT (Density Functional Theory): Software, Techniques, and Applications”, Gujarat -384315, India 5th-16th Feb, 2021
5. International Conference on Modern Trends in Inorganic Chemistry (MTIC-XIX), BHU, Varanasi 15th-17th Dec, 2022.
6. In-House Chemistry Symposium (CHEM 2022), IIT Indore, 11th March, 2022
7. 31st CRSI-NSC Symposium, NIT Rourkela, July 6-8, 2023
8. ACS Fall 2023, San Francisco, California, USA, August 13<sup>th</sup>-17<sup>th</sup>, 2023

# TABLE OF CONTENTS

List of Nomenclature .....	xxvii
List of Acronyms .....	xxix
List of Figures.....	xxxii
List of Schemes .....	xxlvii
List of Tables .....	xxlix
<b>Chapter 1 .....</b>	<b>1</b>
<b>General Introduction and Background .....</b>	<b>1</b>
1.1 Introduction.....	1
1.2 Cancer: A Growing Humanitarian Threat.....	4
1.3 Cancer: Types and Treatment .....	5
1.3.1 Carcinomas .....	5
1.3.2 Sarcomas .....	5
1.3.3 Leukaemia and Lymphomas .....	5
1.3.4 Brain or spinal cord cancers.....	5
1.3.5 Blastomas .....	5
1.4 Current Approaches in Cancer Therapy: An Overview.....	5
1.4.1 Radiotherapy .....	6
1.4.2 Hormonal therapy .....	6
1.4.3 Immunotherapy .....	6
1.4.4 Stem cell transplantation therapy.....	6
1.4.5 Targeted therapy .....	6
1.4.6 Chemotherapy .....	7
1.4.6.1 Goals of Chemotherapy .....	7
1.4.6.2 Classification of chemotherapy agents .....	8
1.5 Metal based chemotherapy agents .....	10
1.5.1 Specific properties of metal complexes .....	10
1.5.2 Multiple targets of metallodrugs in cancer treatment.....	11
1.6 Platinum complexes as anticancer drug: Cisplatin & other derivatives .....	12
<b>1.6.1 How does cisplatin work and its mechanism.....</b>	<b>13</b>

1.7 Other metal complexes as anticancer agents: Non platinum complexes.....	14
1.7.1 Ruthenium complexes as anticancer agents.....	15
1.7.2 Overview of NAMI-A and its limitations .....	16
1.7.3 Overview of KP1019 and its limitations.....	16
1.7.4 Organoruthenium arene complexes as anticancer agents.....	17
1.7.4.1 Piano Stool complexes .....	17
1.7.4.2 RAPTA-C and RAED complexes.....	18
1.8 Motivation behind the selection of current work.....	19
1.9 Structure–activity relationship of Ru(II) arene complexes.....	21
2.0 Mode of action of ruthenium complex: A brief overview.....	22
2.1 Advantage of naturally occurring metal ions and their complexes as anticancer agents.....	23
2.1.1 Zinc complexes as anticancer agents .....	23
2.2 Cancer targeted drug delivery carriers .....	26
2.2.1 Liposomes .....	27
2.2.2 Micelles.....	27
2.2.3 Carbon nanotubes.....	28
2.2.4 Dendrimers.....	28
2.2.5 Polymeric nanoparticles .....	28
2.2.6 Quantum dots .....	29
2.2.7 Nanogels.....	29
2.2.8 Mesoporous silica nanoparticles .....	29
2.3 Purpose of present investigation .....	30
<b>Chapter 2 .....</b>	<b>45</b>
<b>Modulation of catalytic and biomolecular binding properties of ruthenium (II)-arene complexes with the variation of coligands for selective toxicity against cancerous cells .....</b>	<b>45</b>
2.1 Introduction .....	47
2.2 Experimental section.....	48
2.2.1 Materials and methods .....	48

2.2.2 Synthesis and Characterization .....	49
2.2.2.1 Synthesis of 1 $[\text{Ru}(\eta^6\text{-p-cym})(2\text{-ampy})\text{Cl}]\text{PF}_6$ .....	49
2.2.2.2 Synthesis of 2 $[\text{Ru}(\eta^6\text{-benzene})(2\text{-ampy})\text{Cl}]\text{SO}_3\text{CF}_3$ .....	50
2.2.2.3 Synthesis of 3 $[\text{Ru}(\eta^6\text{-p-cym})(2\text{-ampy})\text{PPh}_3](\text{PF}_6)_2$ .....	50
2.2.2.4 Synthesis of 4 $[\text{Ru}(\eta^6\text{-benzene})(2\text{-ampy})\text{PPh}_3]\text{SO}_3\text{CF}_3$ .....	51
2.2.3 Crystallographic Elucidation of Compound 1 and 2.....	52
2.2.4 Protein Binding Study.....	53
2.2.4.1 Competitive binding experiments .....	53
2.2.4.2 Circular dichroism (CD) spectral studies.....	54
2.2.5 DNA binding study .....	54
2.2.5.1 Absorption spectral studies .....	54
2.2.5.2 Competitive binding experiments .....	55
2.2.6 Cytotoxic assay .....	55
2.2.6.1 Evaluation of cytotoxicity.....	56
<b>2.2.7 Reactive Oxygen Species (ROS) generation .....</b>	<b>56</b>
<b>2.2.8 Hoechst Staining.....</b>	<b>57</b>
2.2.9 DFT calculations .....	57
2.3 Results and discussion .....	57
2.3.1 Synthesis and characterization.....	57
2.3.2 Stability study of the complexes .....	66
2.3.3 Protein binding study .....	67
2.3.3.1 Emission Spectra.....	67
2.3.3.2 Circular dichroism (CD) spectral studies.....	70
2.3.4 DNA binding study .....	71
2.3.4.1 Electronic absorption spectroscopy .....	71
2.3.4.2 Competitive fluorometric DAPI displacement assay.....	73
2.3.5 In vitro cytotoxicity assay .....	74
2.3.6 Catalytic Oxidation of NADH .....	76
2.3.7 Reactive Oxygen Species (ROS) generation .....	79
2.3.8 Apoptosis study with Hoechst staining method.....	80
2.3.9 Density functional theory (DFT) Study .....	81

2.4 Conclusions .....	83
2.5 Declaration .....	83
2.6 References .....	84
<b>Chapter 3 .....</b>	<b>91</b>
<b>Pyrene based fluorescent Ru(II)-arene complexes towards significant biological applications: catalytic potential, DNA/protein binding, two photon cell imaging and in vitro cytotoxicity.....</b>	<b>91</b>
3.1 Introduction .....	92
3.2 Experimental section.....	94
3.2.1 Materials and methods .....	94
3.2.2 Syntheses of compounds.....	94
3.2.2.1 Synthesis of ligand, <b>HL</b> .....	94
3.2.2.2 Synthesis of complex <b>5</b> [Ru( $\eta^6$ -p-cymene)(L)Cl] .....	94
3.2.2.3 Synthesis of complex <b>6</b> [Ru( $\eta^6$ -benzene)(L)Cl] .....	95
3.2.2.4 Synthesis of complex <b>7</b> [Ru( $\eta^6$ -p-cymene)(L)N <sub>3</sub> ] .....	95
3.2.2.5 Synthesis of complex <b>8</b> [Ru( $\eta^6$ - benzene)(L)N <sub>3</sub> ].....	96
3.2.3 X-ray crystallography.....	96
3.2.4 Protein Binding Study.....	96
3.2.5 DNA binding study .....	97
3.2.6 Evaluation of cytotoxicity .....	97
3.2.7 Wound healing assay.....	97
3.2.8 Two-photon cell imaging analysis .....	97
3.2.9 Dual staining assay with Hoechst and PI.....	98
3.2.10 Reactive Oxygen Species (ROS) generation.....	98
3.2.11 Methodology and Computational Details .....	98
3.3 Results and discussions .....	100
3.3.1 Synthesis and characterization .....	100
3.3.2 X-ray crystallography study of complex 5 and 6.....	108
3.3.3 Stability studies .....	113
3.3.4 Protein binding study .....	114

3.3.5 DNA binding study .....	118
3.3.6 In vitro cytotoxicity assay (MTT assay) .....	122
3.3.7 Inhibition of cell migration .....	124
3.3.8 NADH Catalytic Oxidation and generation of Reactive Oxygen Species (ROS) .....	125
3.3.8.1 Theoretical Study of NADH Oxidation .....	128
3.3.9 Two-photon cell imaging study .....	131
3.3.10 Dual Staining (Hoechst/PI and AO/EtBr).....	132
3.3.11 Molecular docking study.....	132
3.3.12 Density functional theory (DFT) study.....	133
3.4 Conclusions.....	136
3.5 Declaration.....	136
3.6 References.....	137
<b>Chapter 4 .....</b>	<b>143</b>
<b>Chitosan-Biotin Conjugated pH Responsive Ru(II) Glucose Nanogel: A Dual Pathway of Targeting Cancer Cells and Self-Drug Delivery</b>	
4.1 Introduction.....	145
4.2 Experimental Section .....	148
4.2.1 Materials and methods .....	148
4.2.2 Syntheses of compounds.....	149
4.2.2.1 Synthesis of ligand, HGluL.....	149
4.2.2.2 Synthesis of complex C9 [Ru( $\eta^6$ -p-cymene)(GluL)Cl] .....	149
4.2.2.3 Synthesis of complex C10 [Ru( $\eta^6$ - benzene)(GluL)Cl].....	150
4.2.2.4 Preparation of Nanoparticles.....	150
4.2.3 Experimental Methods .....	152
4.2.3.1 Theoretical Study .....	152
4.2.3.2 In vitro drug release .....	152
4.2.3.3 Cytotoxic assay .....	152
4.2.3.4 Western blotting.....	152
4.2.3.5 In vitro cellular uptake by ICP-OES analysis .....	153
4.2.3.6 Reactive Oxygen Species (ROS) generation .....	153

4.2.3.7 Hoechst staining assay .....	153
4.2.3.8 Dual staining assay with Acridine orange and EtBr .....	154
4.2.3.9 Wound healing assay .....	154
4.2.3.10 In vivo assessment using zebrafish embryos .....	154
4.3 Results and discussion .....	155
4.3.1 Preparation and characterization of glucose-based Ru anticancer drug and delivery systems .....	155
4.3.2 Rheology Study for confirmation of gels formation .....	169
4.3.3 Solvent dependency of nanogels formation .....	170
4.3.4 Effect on NADH catalytic activity .....	171
4.3.5 Anticancer activity of core complexes and drug loaded nanogel .....	172
4.3.6 Drug loading capacity and pH-mediated drug release study .....	174
4.3.7 In vitro cellular uptake study.....	175
4.3.8 Protein immunoblotting assay.....	177
4.3.9 Metastasis Inhibition Assay .....	178
4.3.10 ROS production in cancer cells.....	179
4.3.11 Cell Morphology study via Hoechst Staining .....	181
4.3.12 Acridine Orange/EtBr dual staining assay .....	182
4.3.13 Quantification of toxicity in zebrafish embryos: in vivo study ....	184
4.3.14 Self-healing nature of gel .....	187
4.4 Conclusions .....	189
4.5 References .....	189
<b>Chapter 5 .....</b>	<b>197</b>
<b>Cancer-Targeted Chitosan–Biotin Conjugated Mesoporous Silica Nanoparticles as Carriers of Zinc Complexes to Achieve Enhanced Chemotherapy In Vitro and In Vivo .....</b>	<b>198</b>
5.1 Introduction .....	198
5.2 Experimental section.....	201
5.2.1 Materials and methods .....	201
5.2.2 Syntheses of compounds .....	202

5.2.2.1 Synthesis of Mannich base ligands (HL1 and HL2).....	202
5.2.2.2 Synthesis of 2,4-Dimethyl-6- {[ (2'-dimethyl aminoethyl)- methylamino]methyl}-phenol (HL <sup>1</sup> ).....	202
5.2.2.3 Synthesis of 2-Methyl-4-t-butyl-6- {[ (2'-dimethyl aminoethyl)- methylamino]methyl}-phenol (HL <sup>2</sup> ).....	202
5.2.2.4 Synthesis of complex Zn <sub>2</sub> L <sup>1</sup> <sub>2</sub> N <sub>3</sub> (OH) (ZnMBC 11).....	203
5.2.2.5 Synthesis of complex Zn <sub>2</sub> L <sup>2</sup> <sub>2</sub> (N <sub>3</sub> ) <sub>2</sub> (ZnMBC 12).....	203
5.2.2.6 Preparation of Nanoparticles.....	204
5.3 Results and discussion .....	210
5.3.1 Preparation and characterization of drug delivery systems .....	225
5.3.2 Drug loading and pH-based delivery .....	225
5.3.3 Stability studies of nanodrugs in biological media .....	228
5.3.4 In Vitro cellular uptake of ZnMBC 11/12, (11/12)@MSNs-CTS and (11/12)@MSNs-CTS-Biotin.....	229
5.3.5 Anticancer activity of ZnMBC 11/12 and (11/12)@MSNs-CTS-Biotin .....	230
5.3.6 Metastasis inhibition assay .....	232
5.3.7 In Vivo toxicity measurements in zebrafish embryos.....	234
5.3.8 Elucidating binding parameters for compound-biomolecules interaction .....	236
5.3.9 Nucleus tracking via two photons confocal microscopy .....	240
5.3.10 Dual staining assay exploiting various dyes .....	242
5.3.11 Monitoring the production of reactive oxygen species (ROS) .....	244
5.4 Conclusions.....	246
5.5 Declaration.....	246
5.6 References.....	246
<b>Chapter 6 .....</b>	<b>253</b>
<b>General conclusions and future scope.....</b>	<b>255</b>



## List of Nomenclature

$\alpha$	Alpha
$\beta$	Beta
$\gamma$	Gama
$\tau$	Fluorescence Lifetime
$\text{\AA}$	Angstrom
$\chi$	Chi
$\lambda$	Wavelength
$\mu$	Micro
$\pi$	Pi
nm	Nanometer
ns	Nanosecond
mM	Milli Molar
$\mu\text{M}$	Micro Molar
$K_{sv}$	Stern Volmer Quenching Constant
$\epsilon$	Molar Extinction coefficient
cm	Centimeter
$^{\circ}$	Degree
K	Kelvin
mL	Milliliter
$\mu\text{L}$	Microliter
a. u.	Arbitrary Unit
$\lambda_{ex}$	Excitation Wavelength
$\lambda_{em}$	Emission Wavelength
pH	The negative logarithm of hydronium-ion concentration
$\eta$	Eta (Efficiency)
$K_a$	Binding Constant



## List of Acronyms

BSA	Bovine Serum Albumin
CAPS	N-cyclohexyl-3-aminopropanesulfonic acid
CCDC	Cambridge Crystallographic Data Centre
CD	Circular Dichroism
$\text{CDCl}_3$	Chloroform - <i>d</i>
CLSI	Clinical & Laboratory Standards Institute
CPE	Constant Phase Element
DAPI	4',6-Diamidine-2'-phenylindole dihydrochloride
DFT	Density Functional Theory
DMEM	Dulbecco's Modified Eagle's Medium
DMF	Dimethylformamide
DMPC	1,2-dimyristoyl-sn-glycero-3-phosphocholine
$\text{DMSO-}d_6$	Dimethyl sulfoxide – <i>d</i> <sub>6</sub>
DNA	Deoxyribonucleic acid
EB	Ethidium Bromide
EDX	Energy-dispersive X-ray
EPR	Electron Paramagnetic Resonance
ESI-MS	Electron Spin Ionization Mass Spectroscopy
FE-SEM	Field-emission Scanning Electron Microscope
GOF	Goodness of Factor
HOMO	Highest Occupied Molecular Orbital
HSA	Human Serum Albumin
IR	Infrared
J	Joule
LUMO	Lowest Unoccupied Molecular Orbital
Val	Valine
MeOH	Methanol
MTT	3-(4,5-dimethylthiazol-2-yl)-2,5-diphenyltetrazolium bromide

NMR	Nuclear Magnetic Resonance
OD	Open density
PBS	Phosphate-buffered saline
PDB	Protein Data Bank
PI	Propidium Iodide
SCXRD	Single Crystal X-Ray Diffraction
SDD	Spin Density Difference
SOMO	Singly Occupied Molecular Orbital
TOF	Turn Over Frequency
TON	Turn Over Number
TRIS	Tris(Hydroxymethyl)aminomethane
UV	Ultra Violet
XPS	X-ray Photoelectron Spectroscopy
NAMI-A	Imidazolium trans-imidazoledimethylsulfoxide tetrachlororuthenate (III)
p-cymene	<i>Para-cymene</i>
PDB	Protein Data Bank

# List of Figures

## Chapter 1

<b>Figure 1.1.</b> Timeline view of FDA approved organic and inorganic compounds as anticancer drugs .....	4
<b>Figure 1.2.</b> Chemical structure of an alkylating agents.....	8
<b>Figure 1.3.</b> Chemical structure of an antimetabolites .....	9
<b>Figure 1.4.</b> Chemical structure of topoisomerase inhibitors .....	9
<b>Figure 1.5.</b> Chemical composition of mitotic inhibitors .....	10
<b>Figure 1.6.</b> Diagrammatic view of discovery of Cisplatin.....	12
<b>Figure 1.7.</b> Chemical Structure of carboplatin and oxaliplatin.....	13
<b>Figure 1.8.</b> Schematic presentation of cytotoxic pathway for cisplatin in the tumor cells.....	14
<b>Figure 1.9.</b> Molecular Structure of NAMI-A and KP1019.....	17
<b>Figure 1.10.</b> S The typical "piano stool" structures of organoruthenium(II) half-sandwich complexes (a) and (b), and the molecular structure of the first cytotoxic transition metal-arene complex $\text{Ru}(\eta^6\text{-C}_6\text{H}_6)(\text{metronidazole})\text{Cl}_2(\text{c})$ .. ..	18
<b>Figure 1.11.</b> Molecular structure of three classic organoruthenium arene complexes .....	19
<b>Figure 1.12.</b> (a) Possible targets of ruthenium complexes and (b)mechanism of actions of ruthenium complexes. ....	23
<b>Figure 1.13.</b> (a) Molecular structure of Zn(II) tryptanthrin complex with curcumin chelating ligands a promising anticancer agent (b) Zn(II) bis(thiosemicarbazonato) complexes as a fluorophore and anticancer agents.....	25
<b>Figure 1.14.</b> Various smart delivery carriers for targeted drug delivery.....	27
<b>Figure 1.15.</b> Diagrammatic presentation of targeting drug delivery mechanism of nanocarriers .....	30

## **Chapter 2**

<b>Figure 2.1.</b> $^1\text{H}$ NMR spectra of complex 1.....	59
<b>Figure 2.2.</b> $^1\text{H}$ NMR spectra of complex 2.....	60
<b>Figure 2.3.</b> $^1\text{H}$ NMR spectra of complex 3.....	60
<b>Figure 2.4.</b> $^1\text{H}$ NMR spectra of complex 4.....	61
<b>Figure 2.5.</b> $^{13}\text{C}$ NMR spectra of complex 1.....	61
<b>Figure 2.6.</b> $^{13}\text{C}$ NMR spectra of complex 2.....	62
<b>Figure 2.7.</b> $^{13}\text{C}$ NMR spectra of complex 3.....	62
<b>Figure 2.8.</b> $^{13}\text{C}$ NMR spectra of complex 4.....	63
<b>Figure 2.9.</b> ESI-MS of complex 1.....	63
<b>Figure 2.10.</b> ESI-MS of complex 2.....	64
<b>Figure 2.11.</b> ESI-MS of complex 3.....	64
<b>Figure 2.12.</b> ESI-MS of complex 4.....	64
<b>Figure 2.13.</b> FTIR stretching frequencies (in KBr pallet) of (a) complex 1, (b) complex 2, (c) complex 3, and (d) complex 4, respectively.....	65
<b>Figure 2.14.</b> ORTEP diagram (50% thermal probability of ellipsoids) of (a) complex 1, and (b) complex 2, respectively.....	65
<b>Figure 2.15.</b> UV-visible spectra of complexes 1-4 in 1% DMSO-PBS mixture at a different time period 0, 24, and 48 hrs. (a) complex 1, (b) complex 2, (c) complex 3, and (d) complex 4.....	66
<b>Figure 2.16.</b> Time dependent $^1\text{H}$ NMR spectra of (a) complex 3 and (b) complex 4 at different time interval 0, 24, 72, and 96 hrs.....	67
<b>Figure 2.17.</b> Fluorescence quenching spectra of HSA (10 $\mu\text{M}$ ) at different concentrations (0-100 $\mu\text{M}$ ) of complexes 1-4 at 298 K. Inset: Plots of $F_0/F$ vs. $[\text{Q}](\text{mol/L})$ .....	68
<b>Figure 2.18.</b> Fluorescence quenching spectra of BSA (10 $\mu\text{M}$ ) at different concentrations (0-100 $\mu\text{M}$ ) of complexes 1-4 at 298 K. Inset: Plots of $F_0/F$ vs. $[\text{Q}](\text{mol/L})$ .....	69
<b>Figure 2.19.</b> CD spectra of HSA (10 $\mu\text{M}$ ) in absence or presence of complex in different concentration (0-100 $\mu\text{M}$ ) at pH $\sim 7.4$ .....	70

<b>Figure 2.20.</b> CD spectra of BSA protein (10 $\mu\text{M}$ ) in absence or presence of complex in different concentration (0-100 $\mu\text{M}$ ) at pH $\sim$ 7.4 .....	71
<b>Figure 2.21.</b> Electronic absorption spectra of only complexes 1-4 and with addition of CT-DNA. (a) complex 1, (b) complex 2, (c) complex 3, and (d) complex 4. Inset: Plots of $[\text{DNA}]$ vs. $[\text{DNA}]/\epsilon_a - \epsilon_f$ for the titration of CT-DNA with the complexes.....	72
<b>Figure 2.22.</b> Fluorescence quenching spectra of DNA (0-100 $\mu\text{M}$ ) at gradually addition of complexes 1-4 at 298 K. Inset: Plots of $F_0/F$ vs. $[\text{Q}](\text{mol/L})$ for the titration of DNA with the complexes.....	74
<b>Figure 2.23.</b> (a) Percentage of cell viability of all compounds against MCF-7 cell line (b) HeLa cell line (c) HEK 293 (normal cell line). Normalized log of concentrations of the compound doses and corresponding cell viabilities for respectively cancer cell lines (d) MCF-7 (e) Hela cells (f) HEK 293 (normal cell line). .....	75
<b>Figure 2.24.</b> UV-visible spectra of complexes 1-4 (1 $\mu\text{M}$ ) react with NADH (100 $\mu\text{M}$ ). (a) complex 1, (b) complex 2, (c) complex 3, and (d) complex 4.	123
<b>Figure 2.25.</b> The turnover numbers (TONs) of complexes 1-4 .....	78
<b>Figure 2.26.</b> (a) Inverted microscopic image of ROS generation, treated and untreated MCF-7 cells through DCFH-DA fluorescence staining procedure. (b) Fluorescence intensity graph of ROS. ....	80
<b>Figure 2.27.</b> Confocal image of treated MCF-7 cells with complexes 3 and 4 stained by Hoechst dye. ....	81
<b>Figure 2.28.</b> Frontier molecular orbitals of complexes and their HOMO-LUMO energy gaps (a) complex 1 (b) complex 2 (c) complex 3, and (d) complex 4.....	83
<b>Figure 2.29.</b> Frontier MOs contour plots of (a) complex 1 (b) complex 2 (c) complex 3 and (d) complex 4.....	83
<b><u>Chapter 3</u></b>	
<b>Figure 3.1.</b> $^1\text{H}$ NMR Spectra of Complex 5 in DMSO- $d_6$ (400.13 MHz, 298K). .....	101

<b>Figure 3.2.</b> $^1\text{H}$ NMR Spectra of Complex 6 in DMSO- $\text{d}_6$ (400.13 MHz, 298K).	102
<b>Figure 3.3.</b> $^1\text{H}$ NMR Spectra of Complex 7 in DMSO- $\text{d}_6$ (400.13 MHz, 298K).	102
<b>Figure 3.4.</b> $^1\text{H}$ NMR Spectra of Complex 8 in DMSO- $\text{d}_6$ (400.13 MHz, 298K).	103
<b>Figure 3.5.</b> $^{13}\text{C}$ NMR Spectra of Complex 5 in DMSO- $\text{d}_6$ (400.13 MHz, 298K).	103
<b>Figure 3.6.</b> $^{13}\text{C}$ NMR Spectra of Complex 6 in DMSO- $\text{d}_6$ (400.13 MHz, 298K).	104
<b>Figure 3.7.</b> $^{13}\text{C}$ NMR Spectra of Complex 7 in DMSO- $\text{d}_6$ (400.13 MHz, 298K).	104
<b>Figure 3.8.</b> $^{13}\text{C}$ NMR Spectra of Complex 8 in DMSO- $\text{d}_6$ (400.13 MHz, 298K).	105
<b>Figure 3.9.</b> ESI-MS spectra of synthesized complex 5.	105
<b>Figure 3.10.</b> ESI-MS spectra of synthesized complex 6.	105
<b>Figure 3.11.</b> ESI-MS spectra of synthesized complex 7.	106
<b>Figure 3.12.</b> ESI-MS spectra of synthesized complex 8.	106
<b>Figure 3.13.</b> FTIR stretching frequencies (in KBr pallet) of (a) HL, (b) complex 5, (c) complex 6, (d) complex 7 and (e) complex 8, respectively.	107
<b>Figure 3.14.</b> (a) UV-Visible spectra (b) emission spectra of complexes 5-8 in DMSO.	107
<b>Figure 3.15.</b> ORTEP presentation of (a) complex 5 and (c) complex 6, at 50% thermal probability level. Supramolecular framework via intermolecular hydrogen bonding for (b) complex 5 and (d) complex 6.	109
<b>Figure 3.16.</b> Crystal polymeric framework. (a) and (b) 2D framework of complex 5 and complex 6. (c) and (d) Supramolecular interaction in complex 5 and 6 via intermolecular hydrogen bonding and $\text{CH}\dots\pi$ stacking interaction.	110
<b>Figure 3.17.</b> The equilibrium 3D bulk crystal structure of the Complex 5 and Complex 6 is depicted here, and the unit cell is highlighted by a cube.	113

<b>Figure 3.18.</b> Stability studies of the complexes 5-8 (1% DMSO in PBS Solution).....	114
<b>Figure 3.19.</b> Emission titration spectra of HSA (10 $\mu$ M) in Tris-HCl buffer with complexes 5-8 (5-50 $\mu$ M) at 298 K. Inset: Plots of F <sub>0</sub> /F vs. [Q](mol/L) for HSA.....	115
<b>Figure 3.20.</b> Emission titration spectra of BSA (10 $\mu$ M) in Tris-HCl buffer with complexes 5-8 (5-50 $\mu$ M) at 298 K. Inset: Plots of F <sub>0</sub> /F vs. [Q](mol/L) for BSA.....	116
<b>Figure 3.21.</b> BSA proteins (10 $\mu$ M) Circular dichroism spectra with or without complex at different concentration (0-40 $\mu$ M).....	118
<b>Figure 3.22.</b> HSA proteins (10 $\mu$ M) Circular dichroism spectra with or without complex at different concentration (0-40 $\mu$ M).....	118
<b>Figure 3.23.</b> Absorption titration spectra of complexes 5-8 with CT-DNA (a) complex 5 (b) complex 6 (c) complex 7 and (d) complex 8. Inset: Plots of [DNA] vs. [DNA]/ $\epsilon_a - \epsilon_f$ for the titration of CT-DNA with the complexes..	120
<b>Figure 3.24.</b> The molecular orbitals analysis of the optimized complexes and their corresponding HOMO-LUMO energy gaps (a) complex 5 (b) complex 6 (c) complex 7, and (d) complex 8. ....	121
<b>Figure 3.25.</b> Fluorescence quenching spectra of DAPI-DNA with complexes 5-8 (0-50 $\mu$ M)..	121
<b>Figure 3.26.</b> Cell viabilities curve of complexes 5-8 for respectively cancer cell lines (a) HeLa (b) A431 (c) MCF7 and (d) for HEK 293 (normal cell line). ....	123
<b>Figure 3.27.</b> Cell viabilities curve of complexes 5-8 for respectively cancer cell lines (a) HeLa (b) A431 (c) MCF7 and (d) for HEK 293 (normal cell line) ....	123
<b>Figure 3.28.</b> (a) Wound healing motility assay of HeLa untreated and treated cell with complexes 5-8, Image were taken at 0 and 24 h (b) Histogram of wound closure ratio of heal wound at 24 h (c) Measuring scale .....	125
<b>Figure 3.29.</b> UV-visible spectra of complexes 5-8 (3 $\mu$ M) react with NADH (100 $\mu$ M) (a) only NADH (b) complex 5 (c) complex 6 (d) complex 7 (e)	

complex 8 and (f) Histogram graph of complexes 5-8 turnover numbers(TONs)	127
<b>Figure 3.30.</b> (a) Inverted microscopic image of ROS generation, treated and untreated HeLa cells through DCFH-DA fluorescence staining procedure (b) Fluorescence intensity graph of ROS.....	128
<b>Figure 3.31.</b> Reaction free energy profile diagram of the proposed mechanism for complex 5 .....	131
<b>Figure 3.32.</b> Two-photon confocal laser scanning microscopy images in HeLa cells (excitation at 790 nm) .....	131
<b>Figure 3.33.</b> (a) Hoechst and PI, (b) Acridine orange and EtBr double staining confocal microscopy images of HeLa cells after complexes 5-8 treatment and cells without treatment as a control.....	132
<b>Figure 3.34.</b> Docking images of complex 5 with (a) DNA (b) HSA and (c) BSA and complex 6 with (d) DNA (e) HSA and (f) BSA.....	133
<b>Figure 3.35.</b> a) Reaction path of the $[(\eta^6\text{-p-cymene})\text{RuCl}_2]_2$ and ligand, HL with adduct A-1, TS-1, and complex 5; b) reaction path of the $[(\eta^6\text{-benzene})\text{RuCl}_2]_2$ and ligand, HL with adduct A-2, TS-2, and complex 6; c) reaction path of the $[(\eta^6\text{-p-cymene})\text{Ru}(\text{N}_3)_2]_2$ , and ligand, HL with adduct A-3, TS-3, and complex 7; d) reaction path of the $[(\eta^6\text{-benzene})\text{Ru}(\text{N}_3)_2]_2$ and ligand, HL with adduct A-4, TS-4, and complex 8 are shown here.....	135
<b>Figure 3.36.</b> Equilibrium geometries computed by the DFT method are presented here; a) Ligand, HL, b) $[(\eta^6\text{-benzene})\text{RuCl}_2]_2$ , c) $[(\eta^6\text{-p-cymene})\text{RuCl}_2]_2$ , d) $[(\eta^6\text{-benzene})\text{Ru}(\text{N}_3)_2]_2$ , e) $[(\eta^6\text{-p-cymene})\text{Ru}(\text{N}_3)_2]_2$ , f) Complex 5, g) Complex 6, h) Complex 7, i) Complex 8, j) TS-1 is the transition state between A1 adduct and Complex 5 product. k) TS-2 is the transition state between A2 adduct and Complex 6 product. l) TS-3 is the transition state between A3 adduct and Complex 7 product. m) TS-4 is the transition state between A4 adduct and Complex 8 product.....	136

## **Chapter 4**

<b>Figure 4.1.</b> <sup>1</sup> H NMR Spectra of ligand GluL in DMSO-d <sub>6</sub> (400.13 MHz, 298K). .....	157
<b>Figure 4.2.</b> <sup>1</sup> H NMR Spectra of complex 9 in DMSO-d <sub>6</sub> (400.13 MHz, 298K). .....	158
<b>Figure 4.3.</b> <sup>1</sup> H NMR Spectra of complex 10 in DMSO-d <sub>6</sub> (400.13 MHz, 298K). .....	158
<b>Figure 4.4.</b> <sup>13</sup> C NMR Spectra of ligand GluL in DMSO-d <sub>6</sub> (400.13 MHz, 298K). .....	159
<b>Figure 4.5.</b> <sup>13</sup> C NMR Spectra of complex 9 in DMSO-d <sub>6</sub> (400.13 MHz, 298K). .....	159
<b>Figure 4.6.</b> <sup>13</sup> C NMR Spectra of complex 10 in DMSO-d <sub>6</sub> (400.13 MHz, 298K). .....	160
<b>Figure 4.7.</b> ESI-MS data for ligand (HGluL) at room temperature. ....	160
<b>Figure 4.8.</b> ESI-MS data for complex C9 at room temperature.....	160
<b>Figure 4.9.</b> ESI-MS data for complex C10 at room temperature. ....	161
<b>Figure 4.10.</b> (a) FTIR Spectra and (b) UV-vis spectra of ligand (HGluL), C9 and C10. ....	161
<b>Figure 4.11.</b> Geometry optimized structure of (a) HGluL, (b) C9, and (c) C10. The Stuttgart/Dresden (SDD) basis set and effective core potential were used for the Ru atom, and 6-311 G* basis set was applied for H, C, O, N, S, and Cl. (d) Calculated frontier molecular orbitals viz HOMO and LUMO of HGluL, C9, and C10 (Isovalue = 0.04). ....	162
<b>Figure 4.12.</b> Time dependent stability study of (a) complex 9 (b) complex 10 at different time interval 0 h, 24 h and 48 h.....	163
<b>Figure 4.13.</b> Digital images of Gel formation of a. reported Ru complex (not forming gel) b. ligand HGluL (runny gel formed) c. Ru-dimer (not forming gel).. ..	164
<b>Figure 4.14.</b> FE-SEM images of NGs: (a) GC9 at 10 μm, and (b) magnified range of GC9 at 100 nm. (c) HR-TEM image of GC9. (d) EDS analysis (e) mapping data of C9@MSNs, showcasing the elemental composition. ....	165

<b>Figure 4.15.</b> FE-SEM images of NGs: (a) GC10 at 10 $\mu\text{m}$ , and (b) magnified range of GC10 at 100 nm. (c) HR-TEM image of GC10. (d) EDS analysis (e) mapping data of C10@MSNs, showcasing the elemental composition.. .....	165
<b>Figure 4.16.</b> N <sub>2</sub> adsorption isotherms of (a) MSNs, (b) C9@MSNs, (c) C10@MSNs, (d) GC9 and, (e) GC10. ....	166
<b>Figure 4.17.</b> Pore size distribution curve analyzed by BET method for (a) MSNs, (b) C9@MSNs, (c) C10@MSNs, (d) GC9, and (e) GC10. ....	167
<b>Figure 4.18.</b> (a) FTIR spectra of MSNs, CTS-Biotin, GC9, and GC10. (b) TGA graph in the temperature range of 0-800 oC of synthesized compounds. (c) UV-vis spectra of MSNs, CTS, C9, C10, GC9, and GC10 in PBS at pH~7.4.....	168
<b>Figure 4.19.</b> X-ray photoelectron spectroscopic (XPS) analysis of drug delivery systems (NGs). Representation of XPS survey spectra of (a) GC9, and (b) GC10, respectively. High resolution deconvoluted XPS spectra of (c) C1s (d) O1s, (e) N1s, and (f) Ru 3d <sub>3/2</sub> , and Ru 3d <sub>5/2</sub> in case of GC9.....	168
<b>Figure 4.20.</b> High resolution deconvoluted XPS spectra of (a) C1s, (b) O1s, (c) N1s, and (d) Ru 3d <sub>3/2</sub> , and Ru 3d <sub>5/2</sub> in case of GC10.....	169
<b>Figure 4.21.</b> (a) Linear viscoelastic graph, (b) time-oscillation strain-sweep experiment, and (c) dynamic frequency sweep of GC9. (d) Linear viscoelastic graph, (e) time-oscillation strain-sweep experiment, and (f) dynamic frequency sweep of GC10. ‘■’ and ‘●’ denote the storage modulus (G'), and loss modulus (G''), respectively. ....	170
<b>Figure 4.22.</b> Digital images of nanogel formation captured by a handheld camera under different solvent conditions. ....	171
<b>Figure 4.23.</b> UV-vis spectra of the mixture of Ru(II) complex (3 $\mu\text{M}$ ), and NADH (100 $\mu\text{M}$ ) in PBS buffer at pH~7.4. (a) Self-catalysis of NADH in absence of C9 and C10. (b) Time-dependent absorption spectra of NADH catalysis in presence of C9. (c) Linear curve fitting of NADH absorption maxima at 339 nm in presence of C9. (d) Time-dependent absorption spectra of NADH catalysis in presence of C10. (e) Linear curve fitting of NADH absorption maxima at 339 nm in presence of C10. (f) The histogram	

representing the turnover numbers (TONs) of NADH catalysis by C9 and C10..  
.....172

**Figure 4.24.** IC<sub>50</sub> values of various cancer cells after the treatment of C9, C10, GC9, GC10, and positive control viz cisplatin. A temperature of 37 °C and 5% CO<sub>2</sub> were thoroughly maintained during 24 h of incubation period. The histograms represent the IC<sub>50</sub> values of the treated: (a) HeLa cervical cancer, (b) MCF7 breast cancer, (c) A431 epidermoid cancer cell, and (d) human embryonic HEK-293 kidney normal cell lines. ....173

**Figure 4.25.** (a) Drug release profile of nanogels measured via UV-vis analysis under different pH environments. (b) Cellular uptake profile of C9, C10, GC9, and GC10 in MCF7 cancer, and HEK-293 normal cells. (b) Illustrating drug release mechanism from NGs to cancer, and normal cells. ....177

**Figure 4.26.** Representation of Western blotting experiments to examine the expression levels of proteins associated to apoptosis (e.g., BCLXL and Cleaved caspase-3) in HeLa cancer cells. The IC<sub>50</sub> concentrations were used to perform the blotting experiments, such as C9 (15.01 μM), C10 (24.05 μM), GC9 (7.50 μM), and GC10 (10.17 μM) exposing through a period of 24 h...178

**Figure 4.27.** (a) Depiction of wound healing assay in MCF7 cancer cells having incubation period of 24 h. Control experiment represents the wound closure without treating any compound. (b) Histogram summarizing the percentage wound closure ratio of treated and untreated MCF7 cancer cells.179

**Figure 4.28.** (a) Fluorescence microscopic images showing ROS generation in HeLa cancer cells after treating with C9, C10, GC9, and GC10 (10 μM). Untreated control does not emit green fluorescence. The acronym ‘DIC’ stands for differential interference contrast. (b) Concentration dependent fluorescence microscopic images of GC9 treated HeLa cancer cells (b1: 20 μM, and b2: 30 μM). (c) The normalized ROS intensity calculated using ImageJ programme. Standard deviations are provided for three independent events. ....180

**Figure 4.29.** (a) Confocal images of treated and untreated HeLa cancer cells stained with Hoechst. Arrows indicate morphological changes of nucleus. (b) Treated HeLa cancer cells along with Hoechst staining at different

concentration of GC9 (b1: 1  $\mu$ M, b2: 5  $\mu$ M, b3: 10  $\mu$ M, b4: 15  $\mu$ M, b5: 20  $\mu$ M, and b6: 25  $\mu$ M). (c) Concentration dependent fluorescence intensity plot of treated cells, using ImageJ programme..... 182

**Figure 4.30.** Confocal Images analysis of HeLa treated cells with synthesized compounds and untreated cells as a control, stained with AO/EtBr ..... 184

**Figure 4.31.** (a) In vivo zebrafish dual staining (AO/PI) assay after treatment with drug loaded nanogels at 72 hpf. (A) control larvae of Zebrafish; (B) AO-stained zebrafish control larvae emitting green fluorescence; (C) no red fluorescence in control larvae when stained with PI; (D) dual stained merged image of zebrafish showing only green emission at 72 hpf. (E) 800  $\mu$ M of GC9 treated zebrafish showing deformities; (F), and (G) are zebrafish images stained with AO, and PI, respectively treated with 800  $\mu$ M of GC9. (H) is the merged image of (F), and (G) indicating live, and dead cells. (I) Zebrafish deformities upon treating 800  $\mu$ M of GC10. (J), and (K) are zebrafish images stained with AO, and PI, respectively treated with 800  $\mu$ M of GC10. (H) is the merged image of (F), and (G) indicating live, and dead cells. No such deformations were observed at LD50 concentrations. (b) Determining toxicity (LD50) of nanogels in zebrafish embryos at different concentrations of GC9, and GC10 (10, 25, 50, 100, 200, 400, 800, 1200, and 1600  $\mu$ M). (c) Heartbeat rate (in bpm) percentage bar chart of control, GC9 and GC10. Arrows indicates increase or decrease heartbeat rate percentage when compared to control. Control represents by first bar, next three represents the GC9 treated zebrafish embryos with increase heartbeat rate of 13.42 %, and 19.04 % at 200, and 400  $\mu$ M and decrease heartrate 30.18 % at 800  $\mu$ M. The last three bar represents the GC10 treated zebrafish embryos with increase heartbeat rate of 8.33 %, 4.17 %, and 25.0 % at 200, 400, and 800  $\mu$ M, respectively. (d) Malformations observed in zebrafish embryos at 48 hpf after treatment with GC9, and GC10. Where (d1) control zebrafish, (d2, d3 and d5, d6) embryos treated with 200  $\mu$ M and 400  $\mu$ M of GC9 and GC10 showing no observable deformities, (d4 and d7) embryos treated with 800  $\mu$ M of GC9 and GC10 displaying stunned

growth, blood congestion, edema, stunted growth, tail, and head malformation after 48 hpf.....186

**Figure 4.32.** Self-healing nature of NGs recorded with a handheld camera. Images depict: (a) gel GC9, (b) gel separated into two pieces, (c) one side of the gel doped with a red dye, (d) doped and undoped sides start healing on contact, (e) 30 min, and (f) 60 min after the contact showing entirely self-healed nature of the gel. (g) Histogram representing increment of self-healing with time. ....188

## **Chapter 5**

**Figure 5.1.**  $^1\text{H}$  NMR Spectra of  $\text{HL}^1$  in  $\text{CDCl}_3$  (400.13 MHz, 298K). .....212

**Figure 5.2.**  $^1\text{H}$  NMR Spectra of  $\text{HL}^2$  in  $\text{CDCl}_3$  (400.13 MHz, 298K). .....212

**Figure 5.3.**  $^{13}\text{C}$  NMR Spectra of  $\text{HL}^1$  in  $\text{CDCl}_3$  (400.13 MHz, 298K). .....213

**Figure 5.4.**  $^{13}\text{C}$  NMR Spectra of  $\text{HL}^2$  in  $\text{CDCl}_3$  (400.13 MHz, 298K). .....213

**Figure 5.5.** ESI-MS data of  $\text{HL}^1$  at room temperature. ....214

**Figure 5.6.** ESI-MS data of  $\text{HL}^2$  at room temperature. ....214

**Figure 5.7.** ESI-MS data of complex 11 at room temperature. ....214

**Figure 5.8.** ESI-MS data of complex 12 at room temperature. ....214

**Figure 5.9.** (a) FTIR stretching frequencies of  $\text{HL}^1$ ,  $\text{HL}^2$ ,  $\text{Zn}_2\text{L}^1_2(\text{N}_3)(\text{OH})$  (11) and  $\text{Zn}_2\text{L}^2_2(\text{N}_3)_2$  (12) (b) UV-Visible transitions of ligands and complexes (10  $\mu\text{M}$  in HPLC DMSO- $\text{H}_2\text{O}$  (1:9) solvent at 25  $^\circ\text{C}$ ).....215

**Figure 5.10.** The Oak Ridge Thermal Ellipsoid Plot (ORTEP) (ellipsoids with 50% thermal probability level) of ZnMBC (a) 11, and (b) 12. Omitting hydrogens and wireframe as the style occasionally used for simplicity. Formation of three-dimensional supramolecular framework via hydrogen bond interactions in (c) 11, and (d) 12. ....216

**Figure 5.11.** FE-SEM diagrams of (a) free MSNs, (b) ZnMBC loaded MSNs, i.e., (11)@MSNs, and (c) functionalization of ZnMBC loaded MSNs with CTS-Biotin, i.e., (11)@MSNs-CTS-Biotin. (d-g) HRTEM profiles of MSNs, (11)@MSNs, (11)@MSNs-CTS-biotin, and (12)@MSNs-CTS-biotin. (h-j) Corresponding diffraction patterns of MSNs-based drug candidates using HR-TEM. ....219

<b>Figure 5.12.</b> N <sub>2</sub> adsorption isotherms of (a) MSNs, (b) (11)@MSNs, (c) (12)@MSNs, (d) (11)@MSNs-CTS-Biotin, (e) (12)@MSNs-CTS-Biotin, and (f) Combine data of BET isotherms.....	220
<b>Figure 5.13.</b> Pore size distribution curve analyzed by BET/DFT method for (a) MSNs, (b) (11)@MSNs, (c) (12)@MSNs, (d) (11)@MSNs-CTS-Biotin, and (e) (12)@MSNs-CTS-Biotin.....	221
<b>Figure 5.14.</b> TGA curves in the temperature range of 0–800 °C.....	222
<b>Figure 5.15.</b> (a) UV-Visible spectra of ZnMBC and drug delivery systems in PBS buffer medium (b) Relative Raman spectra of nanocarrier and drug candidates (c) FTIR spectra of core drug candidates (inset) and drug delivery systems.....	223
<b>Figure 5.16.</b> (a-b) Survey spectrum of drug delivery systems by X-ray photoelectron spectroscopic (XPS) analysis. High resolution deconvoluted XPS spectra of (c) C1s, (d) N1s, (e) O1s, and (f) Zn 2p <sub>1/2</sub> , and Zn 2p <sub>3/2</sub> in case of (11)@MSNs-CTS-Biotin. Representation implies the subtracted data in dots and cumulative peak fitting in lines.....	224
<b>Figure 5.17.</b> High resolution deconvoluted XPS spectra of C1s, N1s, O1s, and Zn 2p <sub>1/2</sub> , and Zn 2p <sub>3/2</sub> in case of (12)@MSNs-CTS-Biotin. Representation indicates the subtracted data in dots and cumulative peak fitting in lines....	224
<b>Figure 5.18.</b> (a) pH-mediated drug release profile of nanodrugs. In vitro release profiles of ZnMBC 11 from (11)@MSNs-CTS-Biotin at pH 7.4 (●) and pH 5.5 (●), and ZnMBC 12 from (12)@MSNs-CTS-Biotin at pH 7.4 (■) and pH 5.5 (■). (b) Representing pH-responsive targeted drug delivery and cellular apoptosis.....	228
<b>Figure 5.19.</b> Mass spectrometry (ESI-MS, +Ve) of ZnMBC 11 (a), and ZnMBC 12 (b) in different time intervals (0 h, 24 h, and 96 h). Condition: 1% DMSO/PBS solution mixture at 25 °C... ..	229
<b>Figure 5.20.</b> Cellular uptake/ accumulation study of core anticancer agents ZnMBC 11/12, (11/12)@MSNs-CTS, and (11/12)@MSNs-CTS-Biotin in MCF7 cancer and HEK-293 normal cells.....	230

**Figure 5.21.** Induction of apoptosis by measuring IC<sub>50</sub> values (after 24 h incubation at 37 °C, 5% CO<sub>2</sub>) in various cancer cells and normal cell lines after the treatment of ZnMBC 11/12 (complexes), (11/12)@MSNs-CTS-Biotin (nanoparticles), doxorubicin (DOX), 5-fluorouracil (5-FU), and cis-Platin (+ve controls). .....232

**Figure 5.22.** (a) Wound healing motility assay of HeLa treated with complexes ZnMBC (11/12) and nanodrugs (11)@MSNs-CTS-Biotin, and (12)@MSNs-CTS-Biotin, and untreated as control (Scale bar: 200 μm). Bright field images were captured at 0 h and 24 h. (b) Histogram describing wound closure ratio of heal wound within time lag of 0 h and 24 h.....233

**Figure 5.23.** (a) Toxicity comparison by determining LD<sub>50</sub> of (11)@MSNs-CTS-Biotin (NP 1), and (12)@MSNs-CTS-Biotin (NP 2) in zebrafish embryos at different doses (10, 25, 50, 100, 200, 400, 800, 1200, and 1600 μM). (b) Bar chart for percentage heartbeat rate (in bpm) of control, NP 1, and NP 2. Arrows denote percentage increase or decrease in heartbeat when compared to control. The first bar represents the control. The next three bars represent the NP 1 (200 μM, 400 μM, and 800 μM) treated zebrafish embryos with the decrease in heartbeat rate (0%, 13.04%, and 44.06%, respectively). The last three bars attribute the decrease of heartbeat of 10.34 %, 23.52 %, and 23.52 %, respectively, when treated with increasing concentration (200 μM, 400 μM, and 800 μM) of NP 2. (c) Representing the number of frames for a single systole and diastole for control, NP 1, and NP 2. Higher heartbeat rate has less frames to complete a single systole and diastole whereas lower heart beat rate has higher frames. Each bar signifies the number of frames for single systole and diastole cycle of larvae incubated with or without nanodrugs. (d) Malformations observed in zebrafish embryos at 48 hpf after treatment with NP 1, and NP 2. Where (A) control zebrafish, (B,C) embryos treated with 200 μM and 400 μM of NP 1 showing no observable deformities, (D) embryos treated with 800 μM of NP 1 displaying stunned growth, (E) embryos treated with 200 μM of NP 2 presents blood congestion, edema, stunted growth, tail and head malformation, (F) embryos treated with 400 μM of NP 2 producing

delayed hatching after 48 hpf, and (G) embryos treated with 800  $\mu\text{M}$  of NP 2 screening the dead larvae after 48 hpf..... 235

**Figure 5.24.** UV-Visible titration diagram of BSA (10  $\mu\text{M}$ ) and HSA (10  $\mu\text{M}$ ) by successive addition of ZnMBC 11 [Graph-(a) and (c)], and ZnMBC 12 [Graph-(b) and (d)] (0-50  $\mu\text{M}$  in 0.01 M Tris-HCl buffer). (e-f) Electronic titration of fixed concentration (10  $\mu\text{M}$ ) of complex 11 with raising conc. (0-50  $\mu\text{M}$ ) of CT-DNA in 0.01 M Tris-HCl buffer of pH~ 7.4. Spectral change happening at 260 nm, and 262 nm for ZnMBC 11, and ZnMBC 12, respectively. Arrows indicates the change in absorbance upon increasing DNA concentration. Inset: Plots of [ct-DNA] vs. [ct-DNA]/  $\epsilon_a - \epsilon_f$  for the titration of ct-DNA with complexes..... 237

**Figure 5.25.** (a-b) Fluorescence quenching spectra of BSA (10  $\mu\text{M}$ ) at different concentrations (0-50  $\mu\text{M}$ ) of ZnMBC 11, and ZnMBC 12 at 298 K. (c-d) Fluorescence quenching spectra of HSA (10  $\mu\text{M}$ ) at different concentrations (0-50  $\mu\text{M}$ ) of ZnMBC 11, and ZnMBC 12 at 298 K. (e-f) Representing EtBr displacement assay of ZnMBC 11, and ZnMBC 12. [CT-DNA] = 10  $\mu\text{M}$  with ethidium bromide (EB 15  $\mu\text{M}$ ) and [complex] = 0-80  $\mu\text{M}$  in Tris-HCl/ NaCl buffer (5 mM/ 50 mM, pH~ 7.4). The arrow shows the fluorescence changes upon increasing the CT-DNA concentration... .. 238

**Figure 5.26.** Fluorescence quenching profile and statistical analysis of ZnMBC 11, and ZnMBC 12: (a, c, and e) Scatchard plots, and (b, d, and f) Stern-Volmer (SV) plots for BSA, HSA, and CT-DNA, respectively.... .. 239

**Figure 5.27.** Measurement of lifetime decay parameters of BSA (left), and HSA (right) before and after the compound treatment (where, 11 = ZnMBC 11, and 12 = ZnMBC 12) ..... 240

**Figure 5.28.** Two photon confocal laser scanning microscopy (CLSM) profiles after the treatment of (a) (12)@MSNs-CTS-Biotin in HEK-293 normal cells, (b) (12)@MSNs-CTS-Biotin in HeLa cancer cells while arrows denote the significant damage in nucleus, and (c) untreated HeLa cancer cells under physiological condition at 24 h. IC50 concentration of the nanoparticle (12)@MSNs-CTS-Biotin has been used in this experiment. .... 241

**Figure 5.29.** Two photon confocal laser scanning microscopy (CLSM) profiles after the treatment of (a) (11)@MSNs-CTS-Biotin in HEK-293 normal cells, and (b) (11)@MSNs-CTS-Biotin in HeLa cancer cells while arrows denote the significant damage in nucleus under physiological condition at 24 h. ....242

**Figure 5.30.** Hoechst and propidium iodide (PI) dual staining assay profile of HeLa cells after treating with and without core anticancer agents and nanoparticles after 24 h (a) control (b) ZnMBC 11 (c) ZnMBC 12 (d) (11)@MSNs-CTS-Biotin and, (e) (12)@MSNs-CTS-Biotin.. .....243

**Figure 5.31.** Nanoparticles (11)@MSNs-CTS-Biotin, and (12)@MSNs-CTS-Biotin induced apoptotic and/or necrotic fluorescence signal. Image of AO/PI double staining in zebrafish after treatment with nanoparticles (72 hpf). (A) Zebrafish control larvae (B) zebrafish control larvae stained with AO emitting green fluorescence. (C) Absence of red fluorescence in control fishes when stained with PI. (D) Merged Image of dual stained zebrafish showing live cells at 72 hpf. (E) 400  $\mu$ M of (11)@MSNs-CTS-Biotin treated zebrafish showing deformities. (F, G) zebrafish treated with 400  $\mu$ M of (11)@MSNs-CTS-Biotin and stained with AO ,and PI, respectively. (H) merged image of (F) and (G) showing live and dead cells. (I) 200  $\mu$ M of (12)@MSNs-CTS-Biotin treated zebrafish screening deformities. (J, K) zebrafish treated with 200  $\mu$ M of (12)@MSNs-CTS-Biotin and stained with AO, and PI, respectively. (L) AO and PI fluorescent-stained merged image displaying live and dead cells. No such deformations were observed at LD<sub>50</sub> concentrations... .....244

**Figure 5.32.** (a) ROS generation induced by core anticancer agents ZnMBC 1/2, and the corresponding nanodrugs (11/12)@MSNs-CTS-Biotin (at 10  $\mu$ M concentration) after 24 h confirming the influence of ROS to the cellular apoptosis (in HeLa cell lines). Untreated cells give no green fluorescence. (b) Time dependent ROS production in presence of (12)@MSNs-CTS-Biotin at IC<sub>50</sub> concentration. (c) Normalize intensity percentage (including standard deviation) of ROS overproduction calculated using ImageJ programme. DIC denotes differential interference contrast confocal technique... .....245



# List of Schemes

## Chapter 2

**Scheme 2.1.** Synthesis of complexes 1  $[\text{Ru}(\eta^6\text{-p-cym})(2\text{-ampy})\text{Cl}]\text{PF}_6$ , 2  $[\text{Ru}(\eta^6\text{-benzene})(2\text{-ampy})\text{Cl}]\text{SO}_3\text{CF}_3$ , 3  $[\text{Ru}(\eta^6\text{-p-cym})(2\text{-ampy})\text{PPh}_3](\text{PF}_6)_2$ , 4  $[\text{Ru}(\eta^6\text{-benzene})(2\text{-ampy})\text{PPh}_3]\text{SO}_3\text{CF}_3$ .....58

**Scheme 2.2.** The probable mechanism of the catalytic oxidation of NADH to  $\text{NAD}^+$  in presence of complex 1 .....79

## Chapter 3

**Scheme 3.1.** Synthesis of complexes 1  $[\text{Ru}(\eta^6\text{-p-cym})(2\text{-ampy})\text{Cl}]\text{PF}_6$ , 2  $[\text{Ru}(\eta^6\text{-benzene})(2\text{-ampy})\text{Cl}]\text{SO}_3\text{CF}_3$ , 3  $[\text{Ru}(\eta^6\text{-p-cym})(2\text{-ampy})\text{PPh}_3](\text{PF}_6)_2$ , 4  $[\text{Ru}(\eta^6\text{-benzene})(2\text{-ampy})\text{PPh}_3]\text{SO}_3\text{CF}_3$ . .....100

**Scheme 3.2.** The Probable mechanism of catalytic oxidation of NADH to  $\text{NAD}^+$  for complex 5.....130

## Chapter 4

**Scheme 4.1.** Diagrammatic illustration of (a) the synthesis of Ru(II) arene complex-loaded NGs, and (b) the gel formation strategy through the loading of Ru(II) arene complexes in MSNs followed by wrapping of CTS-biotin, where C9:  $[\text{Ru}(\text{GluL})(\text{p-cymene})\text{Cl}]$  and C10:  $[\text{Ru}(\text{GluL})(\text{benzene})\text{Cl}]$ .....148

**Scheme 4.2.** Synthesis of Glucose ring conjugated ligand (HGluL).....156

**Scheme 4.3.** Synthesis of Glucose ring conjugated Ru(II) arene complexes. 156

## Chapter 5

**Scheme 5.1.** Schematic demonstration of the synthesis of zinc(II) nanodrug candidates.....199

**Scheme 5.2.** Synthesis of Mannich base ligands and core drug candidates...211



# List of Tables

## Chapter 2

<b>Table 2.1.</b> Crystallographic information and structure refinement parameters for complexes 1 and 2. ....	52
<b>Table 2.2.</b> Parameters of SV constant, bimolecular quenching constant ( $K_q$ ), binding constant ( $K_a$ ) and number of binding site ( $n$ ) for HSA and BSA protein .....	69
<b>Table 2.3.</b> The values of intrinsic binding constant ( $K_b$ ) for the interaction between complexes and DNA.....	73
<b>Table 2.4.</b> Absorption and emission spectral parameters of SV constant, bimolecular quenching constant, apparent binding constant for CT-DNA .....	76

## Chapter 3

<b>Table 3.1.</b> Experimental crystal and structure refinement data of complex 5 and 6. ....	110
<b>Table 3.2.</b> Selected bond lengths ( $\text{\AA}$ ) and bond angles ( $^\circ$ ) of complexes 5 and 6 .....	111
<b>Table 3.3.</b> Equilibrium structural parameters of the optimized crystal structure of the Complex 5 and complex 6. ....	113
<b>Table 3.4.</b> Determination of various spectral parameters to check the interaction of compounds with HSA and BSA protein.....	116
<b>Table 3.5.</b> Emission <sup>a</sup> and absorption <sup>b</sup> spectral data of DNA interaction with titled compound. ....	122
<b>Table 3.6.</b> <i>In vitro</i> anticancer efficacy of titled compounds against cancerous cell (HeLa, A431, MCF7) and compare with normal cell line (HEK 293) after 24 hours incubation at 37 °C, 5% CO <sub>2</sub> .....	124

## Chapter 4

<b>Table 4.1.</b> Selected bond lengths ( $\text{\AA}$ ) and bond angles ( $^\circ$ ) for Ligand (HGluL), C9 and C10 (calculated data). ....	163
--	-----

**Table 4.2.** IC<sub>50</sub> values of complexes and NGs (GC9 and GC10) against cancer cell line as well as normal cell line.. ..... 174

## **Chapter 5**

**Table 5.1.** Crystallographic information and structure refinement parameters for ZnMBC 11, and ZnMBC 12..... 216

**Table 5.2.** Selected bond lengths (Å) and bond angles (deg) of ZnMBC 11, and ZnMBC 12..... 218

**Table 5.3.** BET adsorption results of nanocarrier and drug delivery systems. .... 221

**Table 5.4.** Binding energies (in eV) of (11)@MSNs-CTS-Biotin, and (12)@MSNs-CTS-Biotin through XPS interpretation. .... 225

**Table 5.5.** Comparing IC<sub>50</sub> values (in μM, 24 h, 37 °C) of the complexes, nanoparticles, and commercially available chemotherapeutic drugs (FDA approved)..... 253

**Table 5.6.** Determination of various spectral parameters to check the interaction between the titled compounds with CT-DNA, BSA, and HSA, respectively. .... 231

*Chapter 1*

*General Introduction and Background*



## **Chapter 1**

### **General introduction and background**

#### **1.1 Introduction**

Over the years, significant progress has been made in discovering and developing anticancer drugs, moving from organic compounds to more diverse classes of molecules, including inorganic compounds. Natural products, organic compounds derived from plants and microorganisms, were the main focus at the early stages of developing anticancer drugs. Two notable examples from that era are the discovery of the anti-estrogen drug tamoxifen and the vinca alkaloids (vincristine and vinblastine) derived from the Madagascar periwinkle. Paclitaxel (Taxol), an organic compound was one of the first drugs to successfully target and kill cancer cells without causing excessive harm to healthy cells, which represented a significant advancement in the field of cancer treatment [1]. The field of discovering anticancer drugs has been dominated by organic compounds, but from the late 20th century to the present, inorganic compounds have also attracted attention (Figure 1.1).

For thousands of years, metals and metal complexes have been used as antibacterial and antiviral compounds for health and healing [2]. Examples from history include the use of gold-based medicines in China and the Middle East 3500 years ago, silver pots were used to cleanse drinking water in the Persian empire, and mercurous chloride was used as a diuretic during the Renaissance period. In the last century, the application of inorganic drugs expanded, leading to the development of therapeutic treatments for many widespread diseases.

In 1969, the discovery of the pharmacological activity of cisplatin by Rosenberg introduced the first purely inorganic antitumor drug into clinical practice [3]. This breakthrough treatment effectively addressed testicular cancer, which until the late 1970s had been almost incurable. Despite cisplatin's widespread success in treating various types of malignancies, the benefits are limited due to the intrinsic and acquired resistance mechanisms of

tumor cells [4]. However, the success of cisplatin indicates that metal compounds have significant potential for new chemotherapeutic approaches.

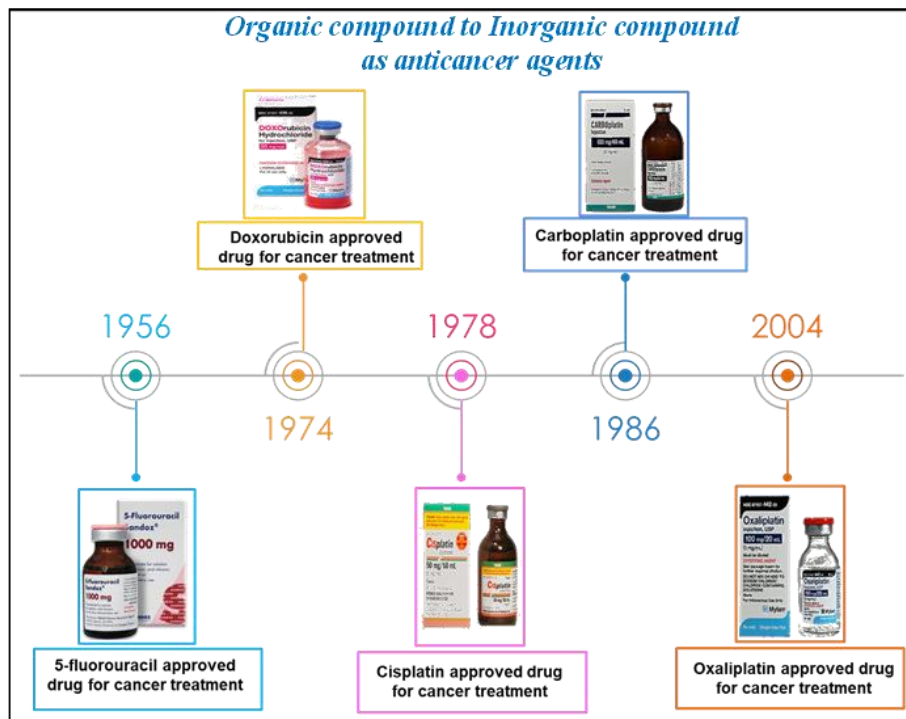


**Figure 1.1.** Timeline view of FDA approved organic and inorganic compounds as anticancer drugs

## 1.2 Cancer: A Growing Humanitarian Threat

Cancer is a leading cause of morbidity and mortality worldwide, with millions of new cases and cancer-related deaths reported annually [5]. This disease has become a major focus of research due to its significant impact on global health. The number of cancer-related deaths reported globally is alarmingly high, second only to cardiovascular disease.

Cancer arises due to uncontrolled cell proliferation, leading to the formation of a solid mass that is typically confined to one or more organs of the body. Some malignant cancers can metastasize, spreading to other sites beyond the primary tumor through direct invasion in the bloodstream or lymphatic systems.

The transformation of normal cells into cancer cells results from genetic mutations that arise through endogenous mechanisms, inherited from ancestors, or acquired through environmental factors such as chemical

carcinogens, radiation, and viruses. Oncogenes, which direct cells towards disproportionate multiplication leading to cancer, and tumor suppressor genes, which regulate cell division, are two families of genes that malfunction in cancer.

### **1.3 Cancer: Types and Treatment**

Based on their location, cause, and behaviour, cancer can be divided into various types. Here are some common classifications for cancer.

**1.3.1 Carcinomas:** Cancers that arise from epithelial cells, which cover the body's surface or line internal organs. Carcinomas account for about 80% of all cancer cases.

**1.3.2 Sarcomas:** Sarcoma is a rare type of cancerous growth that originates in bone and connective tissue like fat, muscle, blood vessels, nerves, and the tissue enveloping bones and joints.

**1.3.3 Leukaemia and Lymphomas:** Cancers that develop in the bone marrow or lymphatic system (leukaemia and lymphoma, respectively). White blood cells in the bloodstream grow abnormally, which leads to the development of lymphoma or leukaemia.

**1.3.4 Brain or spinal cord cancers:** Cancers that arise in the brain or spinal cord.

**1.3.5 Blastomas:** Blastomas are cancers that develop from immature, undifferentiated cells.

### **1.4 Current Approaches in Cancer Therapy: An Overview**

The treatment of cancer is a complex process that varies based on several factors including the types of cancer, stages of cancer, locations of the tumour, and the overall health of the patient. Cancer surgery involves a surgical procedure aimed at removing a tumor along with potentially adjacent tissue. This form of cancer treatment has ancient origins and remains effective in addressing a wide range of cancer types in contemporary medicine. Following are some common therapies for cancer treatment:

#### **1.4.1 Radiotherapy**

Radiation therapy is an approach to treating cancer, often known as radiotherapy. High-energy electrons, gamma rays, X-rays, or heavy particles are used to destroy DNA inside cancer cells. With almost half of all patients requiring it at some time during the disease, radiation therapy is one of the most frequently utilised cancer therapies. It can also be used in combination with other cancer therapies, such as chemotherapy and surgery. Malignancies in the head and neck area, lung, breast, prostate, and brain are the types of cancers for which radiation therapy is commonly used.

#### ***1.4.2 Hormonal therapy***

Cancer cells that depend on hormones to grow are the target of hormonal therapy, a type of cancer treatment. This type of treatment works by preventing the hormones that promote the growth of cancer cells from being produced or acting. Breast cancer and prostate cancer are the most frequent cancers that can be treated with hormonal therapy because they frequently rely on oestrogen and androgen hormones, respectively, for their growth.

#### ***1.4.3 Immunotherapy***

Immunotherapy is a type of cancer treatment that uses the patient's immune system to eliminate tumours. This method employs a variety of techniques, including monoclonal antibodies, specifically designed to bind to specific targets in the body, triggering an immune response against cancer cells. Numerous cancers, including melanoma, lung, kidney, bladder, head and neck cancers, Hodgkin's lymphoma, and some forms of leukaemia, can be successfully treated with immunotherapy.

#### ***1.4.4 Stem cell transplantation therapy***

Replacement of damaged bone marrow with healthy stem cells from the patient or a donor with genetic match is the goal of stem cell transplant therapy, also known as bone marrow transplantation. This therapy is primarily used for treating patients with leukemia.

#### ***1.4.5 Targeted therapy***

Targeted therapy is a type of cancer treatment that employs drugs specifically designed to attack cancer cells only while harming normal cells as little as

possible. These drugs are designed to reduce cancer cells' ability to multiply and prevent the formation of new cancer cells. Because it operates in an alternative way than traditional chemotherapy, targeted therapy is less likely to harm normal cells. Drugs for targeted therapy can be taken orally, intravenously, or by injection. These medications can be used alone or in combination. Targeted therapy in the treatment of breast cancer, lung cancer, melanoma, leukaemia, and lymphoma has shown promising results.

#### ***1.4.6 Chemotherapy***

Chemotherapy treats cancer by using pharmaceutical substances to eradicate cancer cells. These compounds can target DNA or enzymes involved in cell replication or block the mitosis pathway to achieve their desired effects. Chemotherapy medications can be given by oral, intravenous, or injection route, and they can be used alone or in combination with other cancer treatments like surgery or radiation therapy.

Chemotherapy affects healthy cells, going through normal cell division, because it is a systemic therapy that circulates throughout the entire body. Chemotherapy may harm healthy cells as a result, which can result in a variety of side effects, including hair loss and nausea.

##### ***1.4.6.1 Goals of Chemotherapy***

Chemotherapy goals are determined by the patient's unique cancer diagnosis and treatment strategy. Here the primary goals are,

- (i) Curative:*** To completely eradicate all cancer cells from the body in order to cure cancer.
- (ii) Adjuvant:*** To remove any cancer cells that are still present after surgery or radiation treatment, lowering the risk of cancer recurrence.
- (iii) Neoadjuvant:*** Reducing a tumor's size before surgery or radiation therapy to make it easier to eliminate or treat.
- (iv) Palliative care:*** Treating patients with advanced or metastatic cancer who may not recover long by alleviating their symptoms and enhancing their quality of life.

##### ***1.4.6.2 Classification of chemotherapy agents***

Chemotherapy agents can be divided into different categories based on their chemical compositions, mode of actions, and the stages of the cell cycle at which they are most effective. Following are some standard categories for chemotherapy agents:

**(i) Alkylating agents:**

Chemotherapy drugs in the alkylating agent family cause DNA damage in cancer cells. They achieve this by adding an alkyl group to the DNA molecule, which prevents the cell from properly replicating and dividing. Alkylating agents can slow or stop the growth of cancer cells by interfering with DNA synthesis, which ultimately results in their death.

Cyclophosphamide, ifosfamide, chlorambucil, and melphalan are a few examples of alkylating substances (Figure 1.2). Leukaemia, lymphoma, and solid tumours like ovarian and lung cancer are cancers that are treated with these drugs.

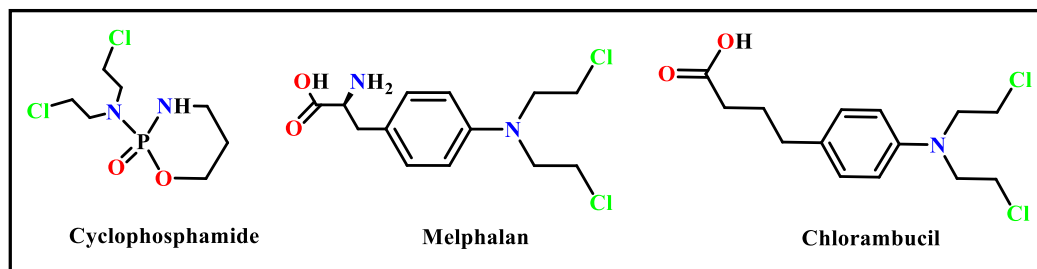


**Figure 1.2.** Chemical structure of an alkylating agents

**(ii) Antimetabolites:**

A subclass of chemotherapy drugs known as antimetabolites prevents cancer cells from producing DNA and RNA. These drugs share structural similarities with purines and pyrimidines, which are organic compounds necessary for the synthesis of DNA. Antimetabolites can interfere with the normal functioning of cancer cells and ultimately kill them by mimicking these substances.

Methotrexate, 5-fluorouracil, cytarabine, and gemcitabine are a few examples of antimetabolites (Figure 1.3). Leukaemia, lymphoma, breast cancer, pancreatic cancer, and other cancers are all treated with these drugs.

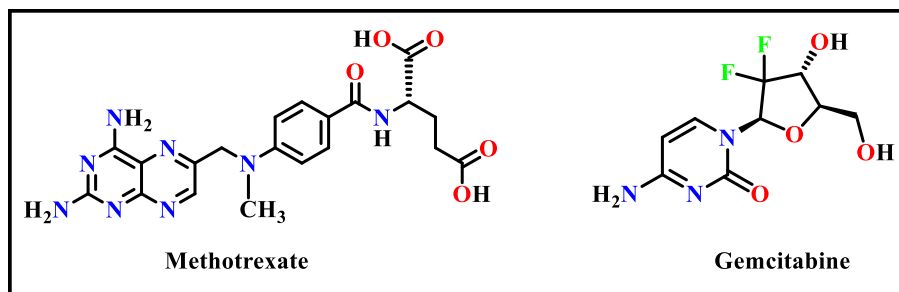


**Figure 1.3.** Chemical structure of an antimetabolites

**(iii) Topoisomerase inhibitors:**

Topoisomerase inhibitors are a class of chemotherapy drugs that prevent the activity of topoisomerase, an enzyme that is essential for DNA replication and repair in cells. Topoisomerase inhibitors are classified into two categories: topoisomerase I inhibitors, which include drugs like irinotecan and topotecan, and topoisomerase II inhibitors, which include drugs like etoposide and doxorubicin (Figure 1.4). Leukaemia, lymphoma, lung, breast, and ovarian cancers are treated by these drugs.

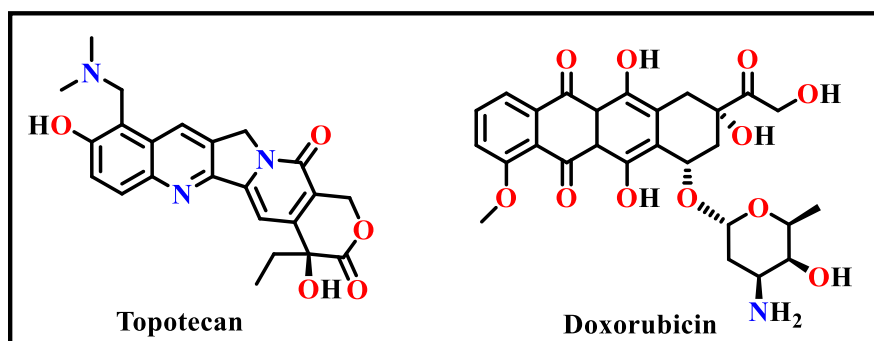


**Figure 1.4.** Chemical structure of topoisomerase inhibitors

**(iii) Mitotic inhibitors:**

Mitotic inhibitors are natural compounds such as plant alkaloids that are largely used in the treatment of cancer. Mitotic inhibitors, in general, prohibit cells from going through mitosis by interrupting microtubule polymerization, hence inhibiting malignant development. Mitotic inhibitors function by interfering with and stopping mitosis (often during the M phase of the cell cycle), causing the cell to stop dividing. Paclitaxel, docetaxel, vinblastine, vincristine, and vinorelbine are mitotic inhibitors commonly used in cancer

therapy (Figure 1.5). These drugs are used to treat various cancers, including breast cancer, lung cancer, ovarian cancer, and lymphoma.

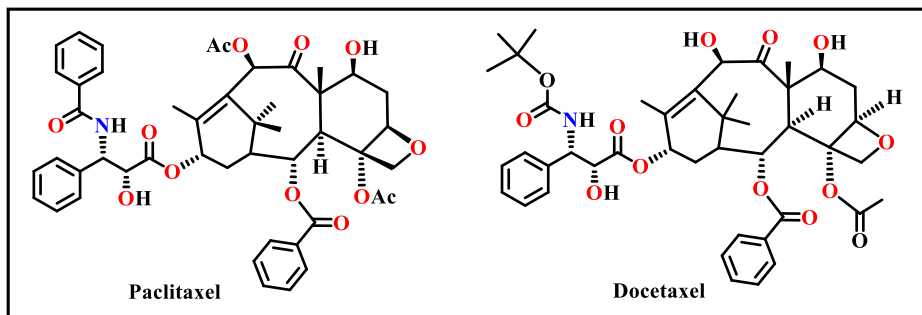


**Figure 1.5.** Chemical composition of mitotic inhibitors

### 1.5 Metal based chemotherapy agents

Metal ions have special features, including redox activity, various coordination modes, and reactivity with organic substrates making them useful as drugs and diagnostic agents in biology. In medicinal chemistry, coordination complexes serve as attractive probes because of their reactivity and potential as drugs or pro-drugs, but their usage needs to be carefully controlled to prevent negative consequences.

#### 1.5.1 Specific properties of metal complexes

Metal complexes can coordinate with ligands in a 3D structure, allowing groups to be customized for specific functions.

*(i) Variation in Charge:* Metal ions are positively charged entities that exist in aqueous solutions. The charge may be changed to produce species that can be cationic, anionic, or neutral, depending on its existing coordination environment. The most significant aspect is that the positively charged ions in an aqueous solution can interact with negatively charged biological molecules.

*(ii) Geometry and chemical Bonding:* Metal complexes display a broad spectrum of coordination geometries that give them specific shapes. Different bonds have different lengths, angles, and coordination sites depending on the metal and its oxidation state. In addition, it is possible to structurally alter metal-based complexes to produce a variety of unique molecular species with a wide range of coordination numbers and geometries.

(iii) **Interaction Between Metal and Ligand:** There are several ways that metals and ligands might interact, but most of the time, these interactions result in the formation of complexes that are unique from those of the individual metals or ligands. Ligand exchange reactions are influenced by the thermodynamic and kinetic properties of metal-ligand interactions. The ability of metals to go through these reactions gives them various benefits to interact with biological molecules.

(iv) **Lewis Acid Properties:** Because of their strong electron affinity, most metal ions may readily polarize groups that are coordinated to them, facilitating their hydrolysis.

(v) **Redox Activity:** Oxidation and reduction processes frequently occur with transition metals. The key factor in the design of the coordination complex is the oxidation state of these metals. Metal ions are often used in biological redox catalysis to activate coordinated substrates and to participate in redox-active sites for charge accumulation.

### 1.5.2 Multiple targets of metallodrugs in cancer treatment

Traditional chemotherapeutic strategies aim to increase cell death by targeting and inhibiting a variety of biomolecules involved in cancer cell survival and proliferation. These comprise:

(i) **Targeting Genetic Materials:** Targeting mitochondria and nuclear DNA can cause DNA damage and stop replication. Cell death (apoptosis) can be induced by altering proteins like bcl-2 and BH-3 proteins (BaX and Bak) [6].

(ii) **Key enzymes:** Cyclooxygenases, glutathione S-Transferases, thioredoxin reductases, PARP, cytochrome P450, topoisomerases, peptidases, carbonic anhydrases, aldo-keto reductases, aromatases, cathepsins B, and ureases, which are upregulated in cancer cells, can be selectively inhibited to disrupt cancer cell biological processes [7].

(iii) **Cell signaling pathways as target:** It may be advantageous to focus on the signalling pathways that regulate cancer cell survival and growth. A method of inhibiting hormone synthesis by targeting oestrogen or progesterone receptors is used in tumours that are hormone-dependent [8].

(iv) **Targeting cell cycle progression:** By inhibiting cyclin-dependent kinases (CDKs) and cyclins, cell cycle progression can be stopped that induced cell death [9].

(v) **Redox balance and metabolic process as targets:** According to the Warburg effect, it is possible to kill cancer cells by blocking certain metabolic processes, such as aerobic glycolysis, or by disrupting redox equilibrium by generating reactive oxygen species (ROS) [10].

### 1.6 Platinum complexes as anticancer drug: Cisplatin & other derivatives

Around 50% of all cancer patients are treated with cisplatin, the first platinum metal-based chemotherapeutic drug [11]. It is a widely used and effective drug for cancer treatment, with annual global sales of around \$2 billion. Michele Peyrone synthesised cisplatin in 1845, but its biological function wasn't revealed until 1965, when Barnett Rosenberg, a biophysicist, found that it inhibited cell division [12]. Barnett Rosenberg had decided to examine whether electrical currents played a role in cellular division. Using *Escherichia coli* cells in ammonium chloride buffer, Barnett Rosenberg investigated the influence of electrical currents on cellular division and discovered elongated and filamentous cells. Later, it was determined that the phenomena were not caused by the electrical current but by the products of platinum hydrolysis from the platinum electrodes utilized in the experiment (Figure 1.6).

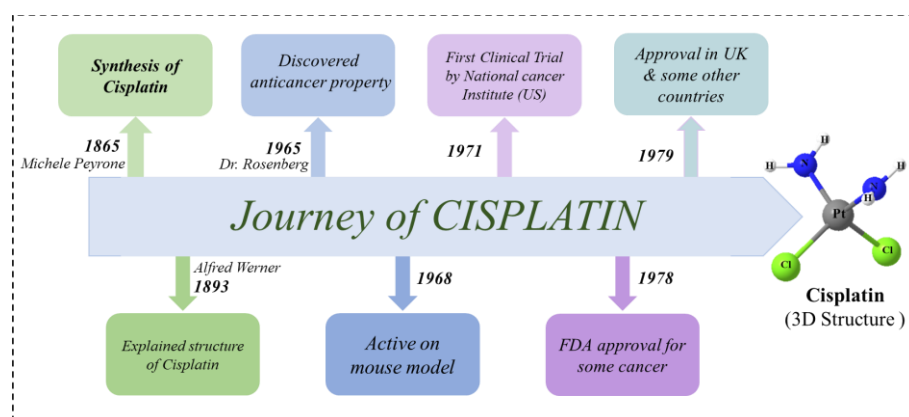


**Figure 1.6.** Diagrammatic view of discovery of Cisplatin

Many cisplatin analogue drugs have been developed, however, only carboplatin and oxaliplatin have received FDA approval due to their increased

efficacy and a wider range of activity. Compared to cisplatin, carboplatin has a reduced toxic profile and fewer side effects, allowing for greater dosages with better results (Figure 1.7). Oxaliplatin, which can overcome cisplatin resistance, is used to treat colon cancer. As a result, oxaliplatin has been approved for the treatment of colon cancer in France, the United Kingdom, and other European countries.

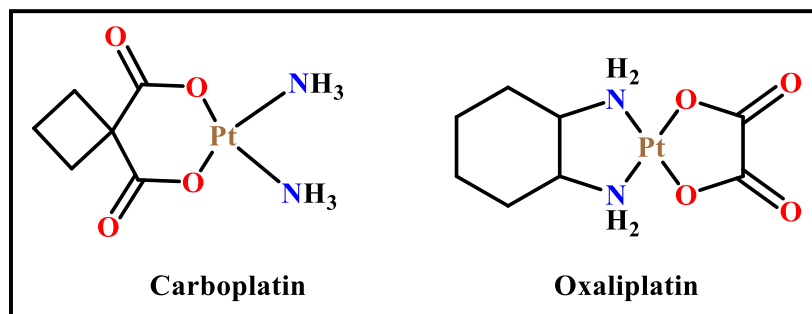


**Figure 1.7.** Chemical Structure of carboplatin and oxaliplatin

### 1.6.1 How does cisplatin work and its mechanism:

A well-known chemotherapeutic drug called cisplatin functions by interacting with DNA and inducing programmed cell death. However, when it is administered to patients through their bloodstreams, it comes into contact with blood plasma that contains a higher concentration (approx. 100 mM) of chloride. This makes it challenging for the drug to efficiently exchange its chloride molecules for water molecules, which is essential for its efficacy. Comparatively, a lower concentration (approx. 4 mM) of chloride is present inside the cell than outside. Therefore, one of the chloride molecules in the cell is replaced by a water molecule. When cisplatin enters the cell, and a positively charged species is generated; as a result, it stays inside the cell. According to *in vitro* studies, the majority (98%) of the platinum that attaches to the DNA in the cell nucleus is accounted for by this positively charged species. A monofunctional DNA adduct is formed when it combines with one of the DNA bases, generally guanine, and later bifunctional intrastrand cross-links of the types 1,2-d(GpG) and 1,2-d(ApG) are formed. These adducts cause a conformational change in the DNA, which inhibits DNA replication and

transcription and results in programmed cell death in malignant tissue (Figure 1.8).

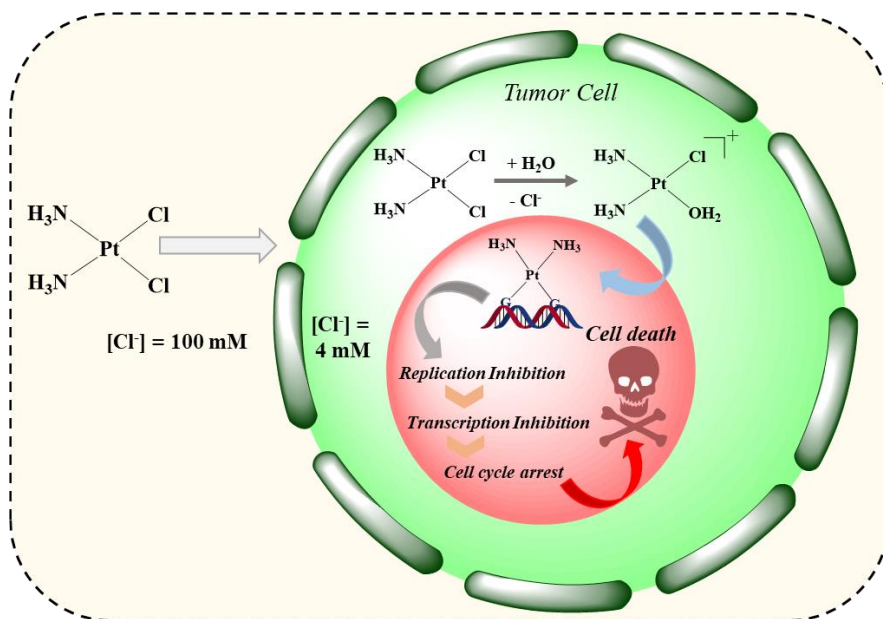


**Figure 1.8.** Schematic presentation of cytotoxic pathway for cisplatin in the tumor cells

### 1.7 Other metal complexes as anticancer agents: Non platinum complexes

Despite the clinical effectiveness of platinum-based anticancer drugs like cisplatin, its drawbacks have prompted researchers to look for alternate chemotherapeutic strategies based on other metal complexes. Therefore, scientists worldwide are looking for novel anticancer drugs that have greater selectivity for tumor cells and a broader range of activity than cis-platin. Numerous non-platinum compounds composed by ruthenium / iridium / osmium / gadolinium have also been investigated for their ability to induce apoptosis [13]. They have demonstrated the capacity to instigate programmed cell death and destroy cancer cells. It has been discovered that these compounds cause the apoptosis of chondrocytes, which are cartilage-forming cells. It has been shown that natural aldehyde thiosemicarbazones and their complexes with nickel and copper are toxic to U937 leukaemia cells, triggered by apoptosis. Similar to this, compounds containing zinc and cadmium metals with p-isopropyl benzaldehyde and methyl 2-pyridyl ketone thiosemicarbazone have been reported to be active against Pamras cells and can mediate through

apoptosis cell death. It is very obvious from the preceding instances that the induction of apoptosis by organometallic complexes are highly promising to show anticancer character.

### 1.7.1 Ruthenium complexes as anticancer agents

Although the use of metal-based complexes, notably platinum complexes, in treating cancer has been successful, there are still certain drawbacks, including drug resistance, a narrow activity range, and more adverse effects. In order to address those issues, researchers have investigated other metal-based complexes, and ruthenium has emerged as the most promising alternative [7, 14]. Its ability to form octahedral complexes enables a broader range of ligands to be studied than platinum(II) complexes, which only form square planar complexes. Ruthenium compounds are also known to have fewer side effects [15]. Ruthenium can build multinuclear and supramolecular structures, developing ruthenium cluster complexes, DNA intercalators, and ruthenium-platinum-mixed metal compounds as potential therapeutic candidates. In directed treatment, an organic compound with a recognized biological target is combined with ruthenium to assist the drugs in finding their target cells and becoming more effective. Ruthenium complexes can also imitate the binding of iron-binding serum proteins. Some ruthenium metal complexes have extraordinary cytotoxic properties and DNA binding ability. In this context, complexes with ligands attached that are biologically active are discovered to have remarkable anticancer properties. Ru(III) and Ru(II) complexes are widely used as anticancer complexes. NAMI-A and KP1019 are examples of such complexes, which have shown considerable cytotoxic activity and entered clinical studies. KP1019 is cytotoxic to cancer cells, and NAMI-A is relatively non-toxic but has antimetastatic activity (Figure 1.9).

### 1.7.2 Overview of NAMI-A and its limitations

The ruthenium(III) coordination complex NAMI-A ((ImH)[trans-RuCl<sub>4</sub>(dmsos)(Im)], Im = imidazole) has received a lot of interest in the scientific community of medical inorganic chemistry, as one of the most promising anticancer therapeutic candidates. The Ru(III) core of NAMI-A exhibits

pseudo-octahedral geometry with DMSO and imidazole occupying the two axial positions, and four chloride ligands occupy the four equatorial axes. Although NAMI-A is stable in its solid state, but its Ru(III) center undergoes conversion to Ru(II) in the presence of biological reducing agents such as cysteine, ascorbic acid, or glutathione. As a result, the equatorial chloride ligands begin to hydrolyse sequentially. Next, the DMSO ligand is substituted, which leads to the formation of uncharacterized dark-green polyoxo species. The explanation for NAMI-A's antimetastatic effects may be its capacity to bind to diverse protein molecules. According to studies, NAMI-A can inhibit the growth in the metastatic phase of various cancer cells, including lung, breast, and colon cancer. Furthermore, NAMI-A has been shown to have minimal toxicity and to have no severe adverse effects. Studies by Sava et al. revealed that NAMI-A preferentially targets cancer cells with metastatic potential inside the primary tumor, such as in lung carcinoma, while having minimal impact on the primary tumor itself [16]. Sava and Lay's research shows that at low, non-toxic doses of ruthenium, NAMI-A can target and interfere with the metastatic ability of cancer cells.[17] This shows that NAMI-A may be able to prevent critical processes in the metastasis phase in cancer cells.

### **1.7.3 Overview of KP1019 and its limitations**

KP1019 HInd[trans-RuCl<sub>4</sub>(Ind)<sub>2</sub>] (Ind = indazole)] is a ruthenium metal-based anticancer drug that has shown promising results in preliminary clinical trials. KP1019 has an octahedral structure with two trans N-donor indazole and four chloride ligands in the equatorial plane. It has poor water solubility, making it difficult to transfer in the bloodstream. To increase the aqueous solubility of the complex, its Na-salt has been prepared Na[trans-[RuCl<sub>4</sub>(Ind)<sub>2</sub>] has shown remarkable antiproliferative activity both *in vitro* and *in vivo* against human colon carcinoma cell lines and a variety of primary tumour models Comparing the DNA binding study of KP1019 with cisplatin has revealed that KP1019 can attach irreversibly to DNA by changing its conformation via a different mechanism than cisplatin. While cisplatin makes covalent interaction with the

DNA molecule, KP1019 interacts with the DNA in a non-covalent manner by attaching to specific binding site on the DNA double helix, such as the minor groove. The specific mode of action of KP1019 signifies that it may have an advantage over cisplatin and other typical chemotherapy drugs, perhaps leading to better treatment results for cancer patients. However, further study is needed to fully understand KP1019's mode of action and its potential as a cancer therapeutic.

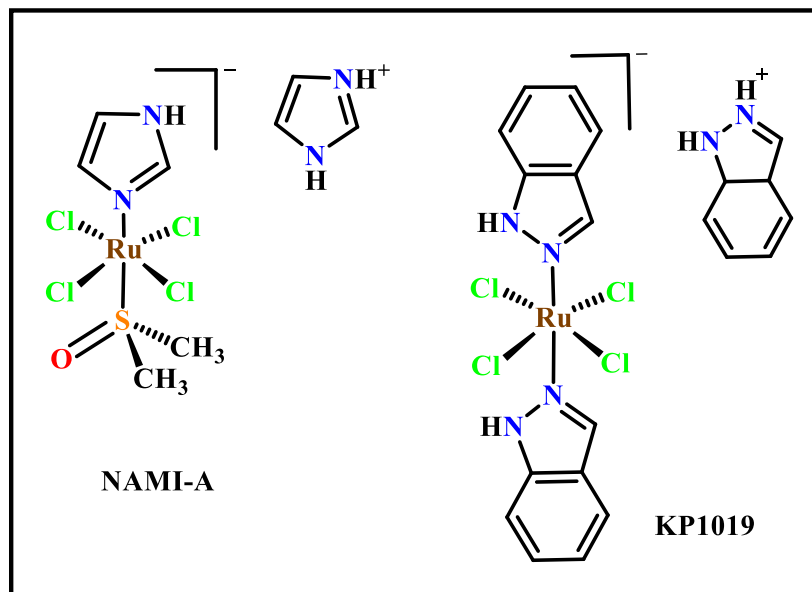


**Figure 1.9.** Molecular Structure of NAMI-A and KP1019

#### 1.7.4 Organoruthenium arene complexes as anticancer agents

Apart from above mentioned complexes, another class of organoruthenium(II) arene complexes have also shown potential anticancer activities [18-21]. A lot of research has been done on mainly three kinds of organometallic ruthenium complexes because of their biological activity.

##### 1.7.4.1 Piano Stool complexes

In recent years, organoruthenium(II) compounds have emerged as a promising class of metallodrugs for cancer treatment [14, 22]. Among these compounds, half-sandwich ruthenium(II)-arene complexes have shown particular potential due to their unique chemical properties and high selectivity for cancer cells. These complexes resemble the typical 'piano-stool' structure of general formulation  $[(\eta^6\text{-arene})\text{Ru}(\text{X})(\text{Y}/\text{Z})]$  [23]. The arene ligand can be varied to

tune the electronic properties of the complex, while X, Y, and Z can be selected to control the coordination geometry and reactivity.  $\text{Ru}(\eta^6\text{-C}_6\text{H}_6)(\text{metronidazole})\text{Cl}_2$  is the first organometallic compound that was evaluated for antiproliferative activity among the transition metal–arene complexes (Figure 1.10) [24]. By interfering with DNA replication and repair process and preventing angiogenesis and metastasis, it has been discovered that these complexes cause apoptosis in cancer cells [25]. Moreover, they display less toxicity to healthy cells, which make them an attractive alternative to traditional chemotherapy drugs. The goal of ongoing research is to improve the efficacy and selectivity of these complexes through design optimisation and the investigation of novel mechanisms of action [26]. In general, the formation of organoruthenium(II) compounds is a promising path toward the development of novel chemotherapy drugs with enhanced safety and efficacy profiles [27].

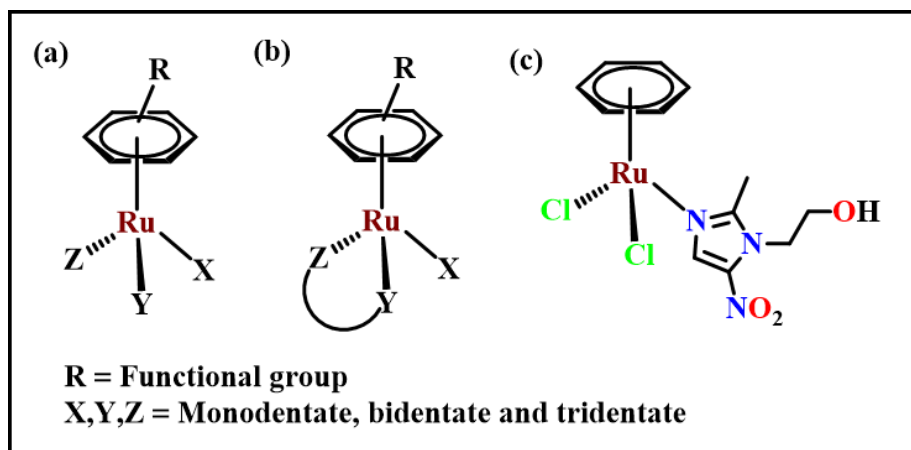


**Figure 1.10.** The typical "piano stool" structures of organoruthenium(II) half-sandwich complexes (a) and (b), and the molecular structure of the first cytotoxic transition metal-arene complex  $\text{Ru}(\eta^6\text{-C}_6\text{H}_6)(\text{metronidazole})\text{Cl}_2$ (c).

#### 1.7.4.2 RAPTA-C and RAED complexes

Ruthenium-arene complexes with the 1,3,5-triaza-7-phosphatricyclo-[3.3.1.1]decane ligand and 1,2-ethylenediamine ligand are known as RAPTA and RAED compounds, respectively [28]. The successful formation of two well-known Ru(II)-arene anticancer drug candidates RAPTA-C and RAED, by Sadler and Dyson, have shown promising results in cancer treatment [29-36].

This inspired a surge of interest in the investigation of organoruthenium complexes as possible anticancer agents. RAPTA-C has the intriguing property to target cancer cells through multiple pathways [27, 37-47]. It has been demonstrated that it specifically targets, damages DNA in a pH-dependent way, and inhibits the activity of many enzymes, including cathepsin-B and thioredoxin reductase. Because of these characteristics and its unique method of action, RAPTA-C is a prospective candidate for cancer therapy. Another noteworthy Ru(II)-arene drug combination is RM175 ( $[\text{RuCl}(\text{ethylenediamine})(\eta^6\text{-biphenyl})]^+$ ), which has shown promise in both *in vitro* and *in vivo* cytotoxicity tests [48]. RM175 has demonstrated notable *in vitro* cytotoxic activity, with  $\text{IC}_{50}$  values similar to those of the chemotherapeutic drug cisplatin (Figure 1.11).

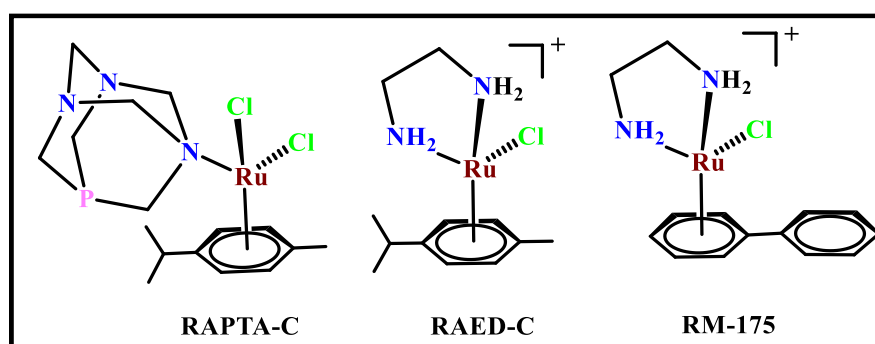


**Figure 1.11.** Molecular structure of three classic organoruthenium arene complexes

### 1.8 Motivation behind the selection of current work

Drug development is a complex process that requires careful planning and execution at every stage. Designing metal complexes with different molecular targets to initiate apoptotic mechanisms has drawn much interest. To develop more effective chemotherapeutic molecules, researchers are looking to add various functionalities to naturally occurring zinc and ruthenium metal centres to better target cancer cells. The selective targeting of cancer cells and induction of apoptosis by the Ru(II)-arene complexes have led to extensive research into their potential as anti-cancer agents. Future drug development will be significantly impacted by the identification of novel drug resistance mechanisms and modes of action due to the development of Ru(II)-arene

complexes with organic ligands. Ru(II)-arene complexes have numerous and exciting potential medical uses, leading to much research and development in this field. However, the roughly 2400 publications that have appeared in the last ten years show that a wide variety of ruthenium compounds with anti-cancer properties have recently been identified. Paira et al. used a one-pot synthesis process to form a series of half-sandwich Ru(II)-*p*-cymene-N<sup>^</sup>N compounds and isolated the regioisomers using preliminary TLC [49]. The main coligands used are 2-(6-bromopyridyl), 2-(6-arylpyridyl), and 2-quinolinyl substituted benzoxazole, benzothiazole, and benzimidazole. All the complexes exhibited significant anticancer effect towards Caco-2, HeLa (cancerous) and HEK-293 (normal) cell lines. Jian Zhao and Shaohua Gao developed two ruthenium complexes [Ru(bipy)<sub>2</sub>(cur)]Cl and [Ru(bipy)(cur)(dppn)]Cl utilising curcumin, a turmeric molecule renowned for its potential in cancer treatment [50]. The complexes were tested on A549, MCF7, and SGC7901 cell lines and had excellent anti-cancer activity [51]. Lanmei Chen et al. developed two ruthenium complexes comprising O,O-chelated ligands, Ru(dip)<sub>2</sub>(SA) and Ru(dmp)<sub>2</sub>(SA) [dip = 4,7-diphenyl-1,10-phenanthroline; dmp = 2,9-dimethyl-1,10-phenanthroline; SA = salicylate] [52]. The salicylate ligand was chosen to investigate the anti-cancer efficacy of O, O-chelating ligands coupled to ruthenium ion. Gasser et al. synthesized four new Ru(II) polypyridyl compounds: [Ru(DIP)<sub>2</sub>flv]X, where flv stands for various flavonoid ligands (5-hydroxyflavone, genistein, chrysin, and morin) and DIP stands for 4,7-diphenyl-1,10-phenanthroline [53]. X is the counterion (PF<sub>6</sub> or OTf<sup>-</sup>). On numerous cancer cell lines, the anti-cancer efficacy of complexes was evaluated. Among them, Ru(DIP)<sub>2</sub>(gen) showed the most promising results, comparable to cisplatin and doxorubicin [53].

Trinuclear complexes have also been studied as potential anticancer substances. According to studies, the outstanding biological activity of cationic triruthenium clusters like [(<sup>i</sup>PrC<sub>6</sub>H<sub>4</sub>Me)(C<sub>6</sub>Me<sub>6</sub>)<sub>2</sub>Ru<sub>3</sub>(μ<sub>2</sub>H)μ<sub>3</sub>O)]<sup>+</sup> may be due to a supramolecular mechanism occurring inside of cancer cells. A μ<sub>3</sub>-oxo ligand, which is present in the system, can interact with hydroxyl groups in

these clusters, allowing supramolecular interactions to occur with proteins or other biological targets. Despite numerous reports on Ru-arene compounds having potent anticancer action, no molecule has been used successfully as an anticancer drug. Ru(II)-arene complex-related concerns, such as solubility problems, stability problems, target specificity, and active species of drug complexes, have been the focus of more research in this area

### 1.9 Structure–activity relationship of Ru(II) arene complexes

The most crucial step in increasing pharmaceutical and biological activities is the core design and synthesis of Ru (II) arene complexes. Compared to platinum complexes, Ru (II) arene complexes have several advantages due to their variable coordinating sites. These complexes have a unique scaffold that helps in increasing their cytotoxicity against various cancer cell lines. As mentioned below, these complexes are typically endowed with the crucial structural features surrounding the Ru-center and are sometimes directly related to biological activity.[7]

**(i) Arene ring:** Arene moieties play a key role in improving the effectiveness of metal drugs. In addition, arene moieties bind to receptor surfaces on cell membranes and aid in drug transport across biological barriers. As a result, there is an improvement in pharmacokinetic properties and increased therapeutic potential.

**(ii) Ancillary bidentate ligand:** Through various noncovalent interactions, an ancillary bidentate ligand with nitrogen/oxygen/mixed donor sets (NN-, NO-, OO-) or with two monodentate ligands can control the reactivity towards various biomolecules (e.g., DNA, enzymes).

**(iii) The X leaving group:** Activity can be increased by a leaving group (X) that is easily dissociable from the ruthenium centre after being attacked by water or biomolecules through covalent interactions to form another analogous group.

**(iv) Nature of counterion:** The solubility, hydrolysis, toxicity, and ion pairing of ruthenium(II) cationic complexes can all be influenced by the counter-ion identity.

## **2.0 Mode of action of ruthenium complex: A brief overview**

Research is ongoing to understand the mechanism of action of ruthenium complexes thoroughly. Ruthenium metal complexes can potentially induce apoptosis in cancerous cells by targeting several cellular pathways. Cell apoptosis (programmed cell death) is a natural process of cell suicide in which the body eliminates unnecessary or damaged cells [54-58]. Apoptosis is typically produced in cells by two pathways, the intrinsic and extrinsic pathways. The mitochondrial pathway is known as an intrinsic pathway [59, 60]. Activation of this pathway happens from the signals like damage of cellular DNA, generation of oxidative stress, or other types of stress which comes from the cells [61-63]. The most effective ways to kill cancer cells are the induction of mitochondrial apoptosis and mitochondrial dysfunction. During this induction, Bcl-2, and BAX, two proapoptotic proteins, are activated and aid in releasing cytochrome c (Cyto c) [64, 65]. Cyto c triggers the caspase protein cascade reaction, and the results cause apoptosis in cancer cells. Ruthenium complexes can activate or induce mitochondrial apoptosis, which kills cancer cells by causing dysfunction in the mitochondria [66].

Chen, Chao, and colleagues studied the impact of Ru(II) complexes on the intrinsic apoptosis pathway [14]. The death receptor pathway significantly regulates cellular death, also called the extrinsic pathway. When cytokines or other extracellular signaling molecules bind to the death receptors (Fas or TRAIL receptors) on the cell surface, they activate, starting a series of events that ultimately lead to programmed cell death. This process results in activating caspases, enzymes that cleave specific proteins inside the cell. When caspases are activated, a series of events take place that ultimately cause DNA fragmentation and cell death [67-70]. Ruthenium complexes may induce apoptosis in cancer cells by activating the extrinsic pathway and inducing death receptors, which will cause the cells to self-destruct. This method can be less harmful than conventional chemotherapy, which frequently targets healthy and cancerous cells simultaneously (Figure 1.12).

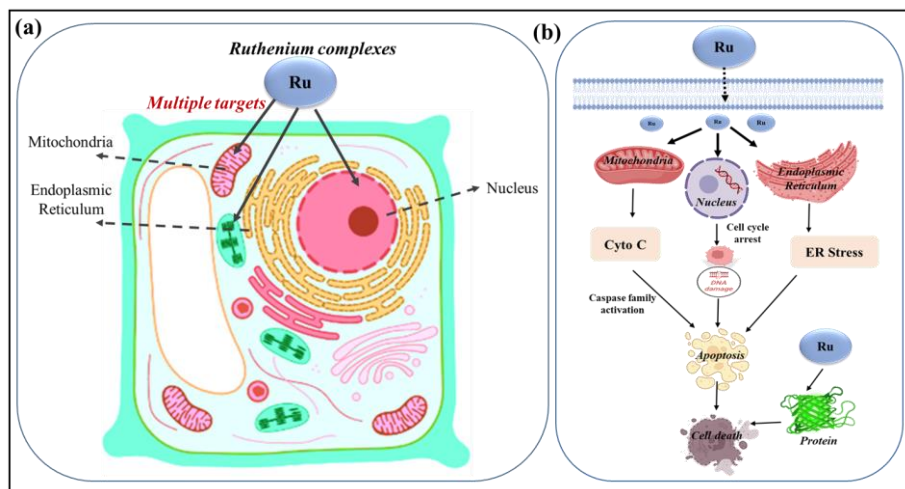


**Figure 1.12.** (a) Possible targets of ruthenium complexes and (b) mechanism of actions of ruthenium complexes

## 2.1 Advantage of naturally occurring metal ions and their complexes as anticancer agents

As anticancer agents, naturally occurring metal ions (like Zn) have several advantages, such as biocompatibility, selectivity towards cancer cells, a variety of mechanisms of action, the potential for therapeutic synergy, targeted delivery options, versatility, abundance, and the potential for imaging and diagnostics. The human body frequently has well-tolerated metal ions that occur naturally, lowering the risk of severe adverse effects. They are already present in biological systems and participate in various essential cellular processes, making them naturally biocompatible. In addition, some naturally occurring metal ions have demonstrated synergistic effects when combined with other anticancer therapies like chemotherapy or radiation therapy. This synergy can potentially improve overall treatment efficacy and overcome resistance mechanisms that cancer cells may develop. Because of these benefits, they are promising candidates for developing effective and safer anticancer treatments.

### 2.1.1 Zinc complexes as anticancer agents

Zn is the second-most abundant trace element in the human body, and it is essential for development and growth as well as for many biological processes because it is indispensable for numerous cell functions and a key regulatory

ion in cell metabolism [71-73]. It plays a vital role in various physiological processes, such as gene expression, enzyme activity, and immune function. Zinc's unique properties, like significant Lewis acidity, nucleophilic generation, leaving group stabilization, low toxicity, flexible coordination geometry, lack of redox property, and 'borderline' hard-soft behavior make it an ideal candidate for drug design and development. Zinc-containing compounds have been found to exhibit antiviral, antibacterial, and anticancer activities [74-76]. Moreover, zinc-based drugs have shown promise in treating Alzheimer's disease and diabetes [77]. The flexibility of zinc's coordination geometry allows it to interact with different ligands, making it a versatile element in biological systems. It does not participate in unwanted oxidation-reduction reactions that can cause cell damage because it lacks redox properties. Overall, zinc's unique properties make it an essential component in biological systems with potential applications in treating disease and developing new drugs.

Furthermore, the function of proteins and enzymes involved in several cellular processes depends on zinc, a critical component of biological systems. Apoptosis is one such process; it is a tightly controlled mechanism of programmed cell death necessary for maintaining tissue homeostasis and eliminating damaged or undesirable cells [78]. In numerous cell types, including ovarian epithelial cells, glial cells, and prostate epithelial cells, the role of zinc in triggering programmed cell death has been thoroughly investigated [79, 80]. It has been demonstrated that zinc stimulates the p53 pathway, causing apoptosis in ovarian epithelial cells. Similarly, zinc triggers apoptosis in glial cells by activating caspases and inhibiting Bcl-2. Zinc upregulates the expression of pro-apoptotic genes in prostate epithelial cells, which leads to the activation of a mitochondrial-dependent apoptotic pathway. Interestingly, recent research has also suggested that zinc may influence immune cell differentiation and function [81, 82]. T-cell dysfunction and increased susceptibility to infections have been associated with zinc deficiency. The precise molecular mechanisms underlying zinc-induced

programmed cell death are not fully understood but involve a complex interplay between zinc ions, specific proteins, signaling cascades, and gene expression regulation.

Zinc(II) complexes have grown in popularity due to their diverse biological functions and versatile applications in various fields. They have seen widespread application in fluorescence imaging, photodynamic therapy, photon fluorescent probing, and potential anti-tumor activity [83-88]. Several types of Zinc(II) complexes have received significant attention. For example, Zn(II) bis(thiosemicarbazonato) probes are well-known for their excellent imaging capabilities and high selectivity towards specific biomolecules [89]. The ability of Zn(II) phthalocyanine photodynamic drugs to produce reactive oxygen species upon exposure to light makes them helpful in treating cancer [90]. Zinc (II) 2,2'-dipicolylamine derivatives have demonstrated potential as antimicrobials and cell-penetrating peptides. Benzo[d]imidazole Zn(II) complexes and Zn(II) terpyridine-phenanthroline exhibit potent anti-tumor activity by inducing apoptosis in cancer cells [91, 92]. More study is required to fully comprehend zinc's function in cellular processes and its potential therapeutic uses (Figure 1.13).

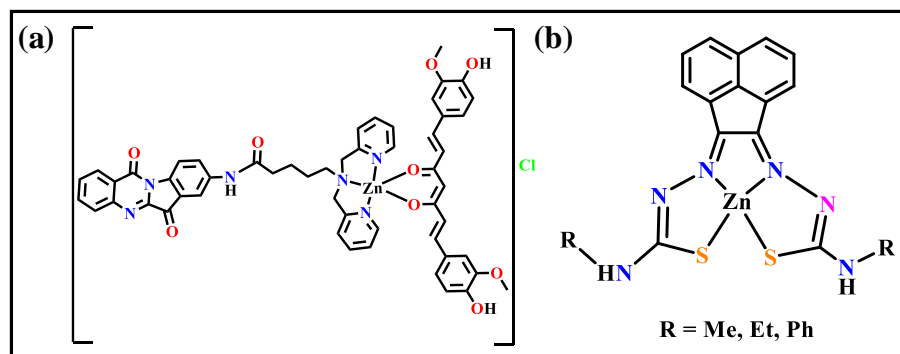


**Figure 1.13.** (a) Molecular structure of Zn(II) tryptanthrin complex with curcumin chelating ligands a promising anticancer agent (b) Zn(II) bis(thiosemicarbazonato) complexes as a fluorophore and anticancer agents

## 2.2 Cancer targeted drug delivery carriers

Effectively delivering therapeutic compounds to the desired site is one of the main challenges in treating many cancers. Limited efficacy, insufficient body

distribution, and a lack of specificity are all characteristic drawbacks of the conventional drug application method. Controlling drug delivery can help to overcome these restrictions and drawbacks. Researchers have been investigating various drug delivery systems that can enhance the pharmacokinetics and pharmacodynamics of therapeutic compounds to address these issues. Using nanotechnology-based drug delivery systems such as liposomes, micelles, carbon nanotubes, polymeric nanoparticles, dendrimers, quantum dots, nanogels, and mesoporous silica nanoparticles is one promising approach to reduce the side effects of bare drugs. These systems can encapsulate drugs, protect them from degradation, increase their solubility and stability, and target them to specific tissues or cells. Another method for precise delivery is to modify the surface of drug carriers with ligands that can recognize and bind to particular receptors or biomolecules on the target cells. This can enhance drug absorption and retention at the target site while reducing exposure to healthy tissues. Additionally, some drug delivery systems can be activated by outside factors like light, temperature, or magnetic fields to release drugs on demand or in a controlled way. These intelligent drug delivery systems can lower side effects and enhance therapeutic results by optimizing drug concentrations at the target site (Figure 1.14- Figure 1.15).[93]

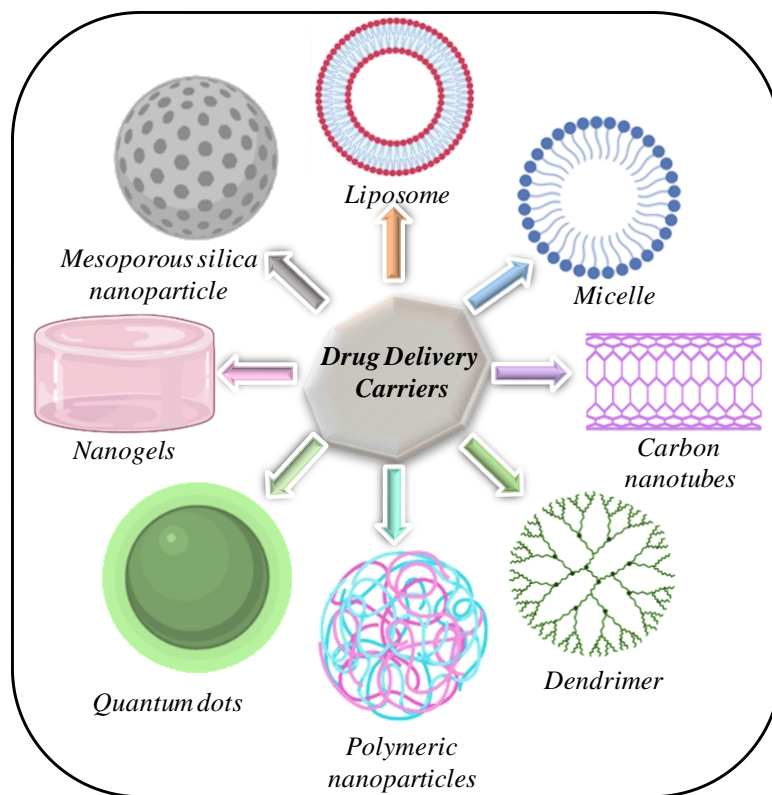


**Figure 1.14.** Various smart delivery carriers for targeted drug delivery

### 2.2.1 Liposomes

Amphipathic phospholipid-based nanocarriers called liposomes are found in nature. In 1973, Gregory Gregordians demonstrated that phospholipids self-assemble into a bilayer vesicle when introduced to an aqueous medium, with the polar ends facing the water and the non-polar ends forming a bilayer [94]. Liposomes have a bilayer core that can effectively trap water- or water-soluble drugs. Liposomes are promising in the co-delivery of chemotherapeutic drugs [95], gene agents with chemotherapeutics, and chemotherapeutics with anticancer metals. With ongoing research and development, liposomes hold great promise for improving cancer treatment and patient outcomes.

### 2.2.2 Micelles

Amphiphilic molecules in aqueous solutions formed self-assembling structures called micelles. They are made up of a hydrophobic core and a hydrophilic outer shell. Hydrophobic drugs are transported by micelles in drug delivery [96], which increases the solubility and bioavailability of the drug. They can

gather in target tissues because they are small and can be altered for active targeting. Proteins and nucleic acids can both be delivered and protected by micelles. In general, micelles present a promising effective, focused drug delivery method.

### **2.2.3 Carbon nanotubes**

CNTs are an example of fullerene, a group of carbon allotropes that can take the form of hollow spheres, ellipsoids, tubes, and many other shapes. CNTs that range in size from 50 to 100 nm can be readily absorbed by cells, making them suitable for a number of uses. In order to enhance their capabilities, carbon nanotubes (CNTs) can be "smart" through chemical or physical modification. These modifications allow CNTs to transport genetic materials such as plasmid DNA, small interfering RNA (siRNA), and aptamers [97]. CNTs have demonstrated significant promise for gene and targeted drug delivery in cancerous cells.

### **2.2.4 Dendrimers**

Dendrimers are synthetic macromolecules with well-defined structures that are highly branched [98]. They have a tree-like architecture because they have a central core surrounded by layers of branching units. Dendrimers are desirable candidates for drug delivery applications due to their distinctive properties. Dendrimers' capacity for drug delivery can be precisely controlled by tailoring their physical characteristics, such as size, shape, and surface functionality [99]. Drug molecules can be encapsulated by dendrimer interiors, improving their solubility and preventing deterioration.

### **2.2.5 Polymeric nanoparticles**

Polymeric nanoparticles (NPs) are excellent for drug delivery due to their many beneficial characteristics [100]. Biodegradability, water solubility, biocompatibility, biomimetic properties, and stability are the characteristics of polymeric NPs. They are helpful in cancer treatment, gene therapy, and diagnostics because their surfaces are changeable for additional targeting, enabling them to deliver drugs, proteins, and genetic material to particular tissues.

### **2.2.6 Quantum dots**

The semiconductor nanocrystals, known as quantum dots (QDs), have unique optical and electrical characteristics. Proteins, peptides, small molecules, and nucleic acids can all be transported by quantum dots during the administration of drugs [101]. These nanoscale structures have generated much interest in drug delivery applications because of their ability to encapsulate and distribute therapeutic agents to particular areas.

### **2.2.7 Nanogels**

Hydrogel systems with a highly cross-linked nanoscale structure are known as nanogels. Nanogels are highly compact and suitable for a variety of applications because their typical size ranges from 20 to 200 nm. The use of nanogels in next-generation drug delivery systems appears promising and has many advantages [102]. Nanogels are hydrophilic and biocompatible due to their customizable size characteristics, which also facilitate their facile preparation. Additionally, nanogels can be programmed to react to stimuli like temperature, pH, light, or biological agents, enabling on-site controlled delivery. Because of their great biocompatibility, they shield drugs from severe environments and are suitable for continuous drug release with minimum toxicity. Nanogels offer a successful and adaptable drug delivery system that may be tailored to meet particular needs.

### **2.2.8 Mesoporous silica nanoparticles**

Due to their unique structural properties and versatile surface chemistry, mesoporous silica nanoparticles (MSNs) have emerged as promising drug delivery carriers [103]. These nanoparticles have a mesoporous silica core with a large surface area and a porous structure, which enables effective loading and controlled release of different therapeutic agents. The term "mesoporous structure" of MSNs describes the presence of regularly spaced pores within the silica matrix, usually between 2 and 50 nm. There are several benefits to using this highly ordered pore structure for drug delivery applications. Due to their porous nature, drugs can be trapped or adsorbed within the pores of MSNs, preventing premature release and deterioration. To enhance their

biocompatibility, stability, and targeting capabilities, the surface of MSNs can be modified. For instance, polyethylene glycol (PEG) chains can be added to MSNs to increase their stability in a physiological environment [104]. Due to their small size, MSNs can be quickly excreted from the body through renal excretion, lowering the chance of long-term accumulation and potential toxicity.

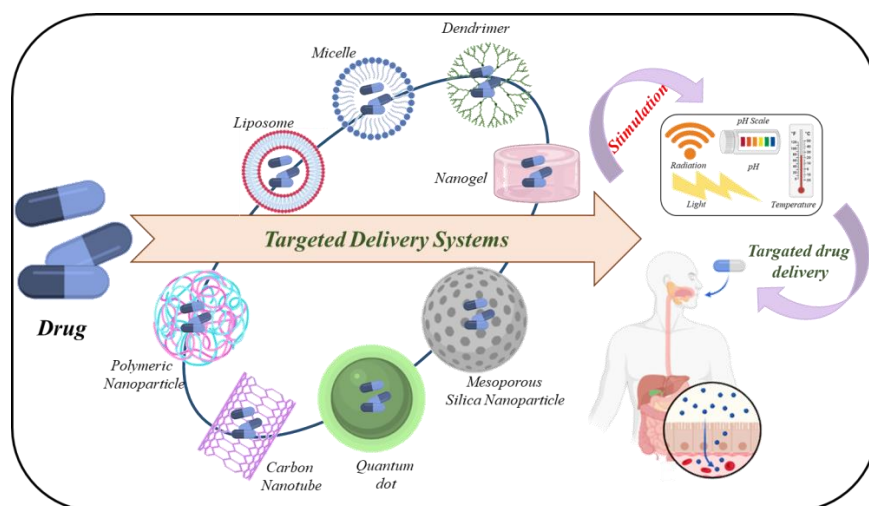


**Figure 1.15.** Diagrammatic presentation of targeting drug delivery mechanism of nanocarriers

### 2.3 Purpose of present investigation

The above discussion emphasizes the significance of metal complexes such as Ru(II)-arene and Zn complexes with related ligands in various biological activities, including anti-proliferative, anti-metastatic, and bio-imaging purposes. Additionally, ligands are essential for the formation of anticancer metal complexes because they offer targeting abilities, stability, biocompatibility, synergistic effects, pharmacokinetic optimization, and overcoming strategies. These advantages contribute to the effectiveness and selectivity of the complexes in combating cancer while minimizing side effects.

This thesis contains two chapters covering a variety of ruthenium (II) complexes synthesized by using ligands and coligands that enhance complex stability and efficacy as anticancer drugs. Another chapter covers the synthesis of the targeted ruthenium (II) complexes and their selective delivery in cancer

cells. The last chapter presents a couple of zinc(II) complexes as anticancer agents and their selective delivery to cancerous cells.

The chapter summaries are listed below:

**Chapter 2** includes the synthesis and characterization of four ruthenium(II) arene complexes **1–4**, with 2-aminomethyl pyridine as a coligand providing stability and biocompatibility of complexes. All the complexes show significant cytotoxicity against HeLa and MCF-7 cancer cell lines, whereas compounds **3** and **4**, with a triphenylphosphine ligand, show better activity because of their enhanced hydrophobicity. The complexes are catalytically active in oxidizing NADH to NAD<sup>+</sup>, leading to ROS production and apoptosis.

**Chapter 3** reports the synthesis of four fluorescent Ru(II) arene complexes **5–8**. These complexes are designed with pyrene-based ligands, endowing them with inherent fluorescence properties. Furthermore, these complexes interact with DNA and proteins and catalyze NADH oxidation, resulting in enhanced ROS generation and cell death. These complexes provide a significant option for high-resolution biological system visualization with their two-photon cell imaging capabilities. The complexes also displayed higher anticancer activity and cell migration inhibition.

Chapter **4** demonstrates pH-responsive nanogels (GC1 and GC2) loaded with synthetic ruthenium(II) arene complexes **9–10** to increase biological potency. For the synthesis of complexes, glucose-based ligands are designed to mimic the structure of glucose, allowing them to bind to the GLUT transporter with high affinity and specificity for targeted drug delivery.

Chapter **5** explores the significance of zinc (Zn), a naturally occurring and highly abundant metal, and its metal complexes as potential anticancer agents. In this study, a mannish-based ligand is used to synthesise core zinc complexes **11–12**. Additionally, using mesoporous silica nanoparticles as effective nanocarriers, the research examines the targeted delivery of these complexes. This innovative strategy has the potential to significantly improve the therapeutic effectiveness of zinc complexes in the treatment of cancer.

Chapter 6 gives an overview of the results obtained and the future scope of such research.

## 2.4 References

- [1] M.A. Jordan, L. Wilson, (2004), Microtubules as a target for anticancer drugs, *Nature reviews cancer*, 4 253-265. (DOI: 10.1038/nrc1317).
- [2] S. Medici, M. Peana, V.M. Nurchi, J.I. Lachowicz, G. Crisponi, M.A. Zoroddu, (2015), Noble metals in medicine: Latest advances, *Coord. Chem. Rev.*, 284 329-350. (DOI: 10.1016/j.ccr.2014.08.002).
- [3] T.C. Johnstone, G.Y. Park, S. Lippard, (2014), Understanding and improving platinum anticancer drugs—phenanthriplatin, *Anticancer Res.*, 34 471-476.
- [4] A. Brown, S. Kumar, P.B. Tchounwou, (2019), Cisplatin-based chemotherapy of human cancers, *Journal of cancer science therapy*, 11.
- [5] T. Ferkol, D. Schraufnagel, (2014), The global burden of respiratory disease, *Annals of the American Thoracic Society*, 11 404-406. (DOI: 10.1513/AnnalsATS.201311-405PS).
- [6] S. Gupta, G.E. Kass, E. Szegezdi, B. Joseph, (2009), The mitochondrial death pathway: a promising therapeutic target in diseases, *Journal of cellular molecular medicine*, 13 1004-1033. (DOI: 10.1111/j.1582-4934.2009.00697.x).
- [7] Pragti, B.K. Kundu, S. Mukhopadhyay, (2021), Target based chemotherapeutic advancement of ruthenium complexes, *Coord. Chem. Rev.*, 448 214169. (DOI: 10.1016/j.ccr.2021.214169).
- [8] H. Ishibashi, T. Suzuki, S. Suzuki, H. Niikawa, L. Lu, Y. Miki, T. Moriya, S.-i. Hayashi, M. Handa, T. Kondo, (2005), Progesterone receptor in non-small cell lung cancer—a potent prognostic factor and possible target for endocrine therapy, *Cancer Research*, 65 6450-6458. (DOI: 10.1158/0008-5472.CAN-04-3087).
- [9] J.A. Stanley, J. Lee, T.K. Nithy, J.A. Arosh, R.C. Burghardt, S.K. Banu, (2011), Chromium-VI arrests cell cycle and decreases granulosa cell proliferation by down-regulating cyclin-dependent kinases (CDK) and cyclins

and up-regulating CDK-inhibitors, *Reproductive Toxicology*, 32 112-123. (DOI: 10.1016/j.reprotox.2011.05.007).

[10] M. Ishaq, M. Evans, K. Ostrikov, (2014), Effect of atmospheric gas plasmas on cancer cell signaling, *International journal of cancer*, 134 1517-1528. (DOI: 10.1002/ijc.28323).

[11] S. Ghosh, (2019), Cisplatin: The first metal based anticancer drug, *Bioorg. Chem.*, 88 102925. (DOI: 10.1016/j.bioorg.2019.102925).

[12] V. Petinou, (2015), Anti-cancer effects and mechanism of actions of aspirin-like drugs in the treatment of gliomas, University of Central Lancashire.

[13] H. Li, Y. Zeng, H. Zhang, Z. Gu, Q. Gong, K. Luo, (2021), Functional gadolinium-based nanoscale systems for cancer theranostics, *J. Controlled Release*, 329 482-512. (DOI: 10.1016/j.jconrel.2020.08.064).

[14] L. Zeng, P. Gupta, Y. Chen, E. Wang, L. Ji, H. Chao, Z.-S. Chen, (2017), The development of anticancer ruthenium (II) complexes: from single molecule compounds to nanomaterials, *Chem. Soc. Rev.*, 46 5771-5804. (DOI: 10.1039/C7CS00195A).

[15] M. Abid, F. Shamsi, A. Azam, (2016), Ruthenium complexes: An emerging ground to the development of metallopharmaceuticals for cancer therapy, *Mini reviews in medicinal chemistry*, 16 772-786. (DOI: 10.2174/1389557515666151001142012).

[16] G. Sava, E. Alessio, A. Bergamo, G. Mestroni, (1999), Sulfoxide ruthenium complexes: non-toxic tools for the selective treatment of solid tumour metastases, *Metallopharmaceuticals I: DNA Interactions*, 143-169. (DOI: 10.1007/978-3-662-03815-4\_6).

[17] A. Levina, A. Mitra, P.A. Lay, (2009), Recent developments in ruthenium anticancer drugs, *Metallomics*, 1 458-470. (DOI: 10.1039/b904071d).

[18] M. Bashir, I.A. Mantoo, F. Arjmand, S. Tabassum, I. Yousuf, (2023), An overview of advancement of organoruthenium (II) complexes as prospective anticancer agents, *Coord. Chem. Rev.*, 487 215169. (DOI: 10.1016/j.ccr.2023.215169).

- [19] C. Sumithaa, M. Ganeshpandian, (2023), Half-Sandwich Ruthenium Arene Complexes Bearing Clinically Approved Drugs as Ligands: The Importance of Metal–Drug Synergism in Metallodrug Design, *Molecular Pharmaceutics*, 20 1453-1479. (DOI: 10.1016/j.ccr.2023.215169).
- [20] Pragti, B.K. Kundu, S.N. Upadhyay, N. Sinha, R. Ganguly, I. Grabchev, S. Pakhira, S. Mukhopadhyay, (2022), Pyrene-based fluorescent Ru(II)-arene complexes for significant biological applications: catalytic potential, DNA/protein binding, two photon cell imaging and in vitro cytotoxicity, *Dalton Transactions*, 51 3937-3953. (DOI: 10.1039/D1DT04093F).
- [21] Pragti, B.K. Kundu, C. Sonkar, R. Ganguly, S. Mukhopadhyay, (2021), Modulation of catalytic and biomolecular binding properties of ruthenium(II)-arene complexes with the variation of coligands for selective toxicity against cancerous cells, *Polyhedron*, 207 115379. (DOI: 10.1016/j.poly.2021.115379).
- [22] I. Yousuf, M. Bashir, F. Arjmand, S. Tabassum, (2021), Advancement of metal compounds as therapeutic and diagnostic metallodrugs: Current frontiers and future perspectives, *Coord. Chem. Rev.*, 445 214104. (DOI: 10.1016/j.ccr.2021.214104).
- [23] B.E. Bursten, R.H. Cayton, Electronic structure of piano stool dimers. 4. (1987), Electronically induced changes in the electrophilic and nucleophilic reactions and the conformations of a series of isovalent hydrocarbyl-bridged complexes, *J. Am. Chem. Soc.*, 109 6053-6059. (DOI: 10.1021/ja00254a025).
- [24] C.S. Allardyce, A. Dorcier, C. Scolaro, P.J. Dyson, (2005), Development of organometallic (organo-transition metal) pharmaceuticals, *Appl. Organomet. Chem.*, 19 1-10. (DOI: 10.1002/aoc.725).
- [25] T. Ozben, (2007), Oxidative stress and apoptosis: impact on cancer therapy, *J. Pharm. Sci.*, 96 2181-2196. (DOI: 10.1002/jps.20874).
- [26] P. Khongorzul, C.J. Ling, F.U. Khan, A.U. Ihsan, J. Zhang, (2020), Antibody–drug conjugates: a comprehensive review, *Molecular Cancer Research*, 18 3-19. (DOI: 10.1158/1541-7786.MCR-19-0582).

- [27] R.G. Kenny, C.J. Marmion, (2019), Toward multi-targeted platinum and ruthenium drugs—a new paradigm in cancer drug treatment regimens?, *Chem. Rev.*, 119 1058-1137. (DOI: 10.1021/acs.chemrev.8b00271).
- [28] S.Y. Lee, C.Y. Kim, T.-G. Nam, (2020), Ruthenium complexes as anticancer agents: A brief history and perspectives, *Drug design, development therapy*, 5375-5392. (DOI: 10.2147/DDDT.S275007).
- [29] I. Romero-Canelón, P.J. Sadler, (2013), Next-Generation Metal Anticancer Complexes: Multitargeting via Redox Modulation, *Inorg. Chem.*, 52 12276-12291. (DOI: 10.1021/ic400835n).
- [30] I. Romero-Canelón, M. Mos, P.J. Sadler, (2015), Enhancement of Selectivity of an Organometallic Anticancer Agent by Redox Modulation, *J. Med. Chem.*, 58 7874-7880. (DOI: 10.1021/acs.jmedchem.5b00655).
- [31] F. Wang, J. Xu, A. Habtemariam, J. Bella, P.J. Sadler, (2005), Competition between Glutathione and Guanine for a Ruthenium(II) Arene Anticancer Complex: Detection of a Sulfenato Intermediate, *J. Am. Chem. Soc.*, 127 17734-17743. (DOI: 10.1021/ja053387k).
- [32] T. Sriskandakumar, S. Behyan, A. Habtemariam, P.J. Sadler, P. Kennepohl, (2015), Electrophilic Activation of Oxidized Sulfur Ligands and Implications for the Biological Activity of Ruthenium(II) Arene Anticancer Complexes, *Inorg. Chem.*, 54 11574-11580. (DOI: 10.1021/acs.inorgchem.5b02493).
- [33] S.J. Dougan, M. Melchart, A. Habtemariam, S. Parsons, P.J. Sadler, (2006), Phenylazo-pyridine and Phenylazo-pyrazole Chlorido Ruthenium(II) Arene Complexes: Arene Loss, Aquation, and Cancer Cell Cytotoxicity, *Inorg. Chem.*, 45 10882-10894. (DOI: 10.1021/ic061460h).
- [34] F. Wang, H. Chen, J.A. Parkinson, P.d.S. Murdoch, P.J. Sadler, (2002), Reactions of a Ruthenium(II) Arene Antitumor Complex with Cysteine and Methionine, *Inorg. Chem.*, 41 4509-4523. (DOI: 10.1021/ic025538f).
- [35] O. Novakova, H. Chen, O. Vrana, A. Rodger, P.J. Sadler, V. Brabec, (2003), DNA Interactions of Monofunctional Organometallic Ruthenium(II)

Antitumor Complexes in Cell-free Media, *Biochemistry*, 42 11544-11554. (DOI: 10.1021/bi034933u).

[36] J.J. Soldevila-Barreda, I. Romero-Canelón, A. Habtemariam, P.J. Sadler, (2015), Transfer hydrogenation catalysis in cells as a new approach to anticancer drug design, *Nature Communications*, 6 6582. (DOI: 10.1038/ncomms7582).

[37] M. Rausch, P.J. Dyson, P. (2019), Nowak-Sliwinska, Recent Considerations in the Application of RAPTA-C for Cancer Treatment and Perspectives for Its Combination with Immunotherapies, *Advanced Therapeutics*, 2 1900042. (DOI: 10.1002/adtp.201900042).

[38] K.J. Kilpin, S.M. Cammack, C.M. Clavel, P.J. Dyson, (2013), Ruthenium(ii) arene PTA (RAPTA) complexes: impact of enantiomerically pure chiral ligands, *Dalton Transactions*, 42 2008-2014. (DOI: 10.1039/C2DT32333H).

[39] L. Biancalana, H. Kostrhunova, L.K. Batchelor, M. Hadiji, I. Degano, G. Pampaloni, S. Zacchini, P.J. Dyson, V. Brabec, F. Marchetti, (2021), Hetero-Bis-Conjugation of Bioactive Molecules to Half-Sandwich Ruthenium(II) and Iridium(III) Complexes Provides Synergic Effects in Cancer Cell Cytotoxicity, *Inorg. Chem.*, 60 9529-9541. (DOI: 10.1021/acs.inorgchem.1c00641).

[40] R.H. Berndsen, A. Weiss, U.K. Abdul, T.J. Wong, P. Meraldi, A.W. Griffioen, P.J. Dyson, P. Nowak-Sliwinska, (2017), Combination of ruthenium(II)-arene complex [Ru( $\eta^6$ -p-cymene)Cl<sub>2</sub>(pta)] (RAPTA-C) and the epidermal growth factor receptor inhibitor erlotinib results in efficient angiostatic and antitumor activity, *Scientific Reports*, 7 43005. (DOI: 10.1038/srep43005).

[41] J. Palmucci, F. Marchetti, R. Pettinari, C. Pettinari, R. Scopelliti, T. Riedel, B. Therrien, A. Galindo, P.J. Dyson, (2016), Synthesis, Structure, and Anticancer Activity of Arene–Ruthenium(II) Complexes with Acylpyrazolones Bearing Aliphatic Groups in the Acyl Moiety, *Inorg. Chem.*, 55 11770-11781. (DOI: 10.1021/acs.inorgchem.6b01861).

- [42] A. Guerriero, W. Oberhauser, T. Riedel, M. Peruzzini, P.J. Dyson, L. Gonsalvi, (2017), New Class of Half-Sandwich Ruthenium(II) Arene Complexes Bearing the Water-Soluble CAP Ligand as an in Vitro Anticancer Agent, *Inorg. Chem.*, 56 5514-5518. (DOI: 10.1021/acs.inorgchem.7b00915).
- [43] L.K. Batchelor, D. Ortiz, P.J. Dyson, (2019), Histidine Targeting Heterobimetallic Ruthenium(II)–Gold(I) Complexes, *Inorg. Chem.*, 58 2501-2513. (DOI: 10.1021/acs.inorgchem.8b03069).
- [44] P. Nowak-Sliwinska, C.M. Clavel, E. Păunescu, M.T. te Winkel, A.W. Griffioen, P.J. Dyson, (2015), Antiangiogenic and Anticancer Properties of Bifunctional Ruthenium(II)–p-Cymene Complexes: Influence of Pendant Perfluorous Chains, *Molecular Pharmaceutics*, 12 3089-3096. (DOI: 10.1021/acs.molpharmaceut.5b00417).
- [45] L. Pietracci, R. Pettinari, A. Tombesi, F. Marchetti, C. Pettinari, A. Galindo, F. Fadaei-Tirani, M. Hadiji, P.J. Dyson, (2023), Steric and Electronic Effects Responsible for N,O- or N,N-Chelating Coordination of Pyrazolones Containing a Pyridine Ring in Ruthenium Arene Systems, *Organometallics*, 42 1495-1504. (DOI: 10.1021/acs.organomet.3c00121).
- [46] A. Annunziata, M.E. Cucciolito, M. Di Ronza, G. Ferraro, M. Hadiji, A. Merlino, D. Ortiz, R. Scopelliti, F. Fadaei Tirani, P.J. Dyson, F. Ruffo, (2023), Ruthenium(II)–Arene Complexes with Glycosylated NHC-Carbene Co-Ligands: Synthesis, Hydrolytic Behavior, and Binding to Biological Molecules, *Organometallics*, 42 952-964. (DOI: 10.1021/acs.organomet.3c00128).
- [47] R. Pettinari, F. Marchetti, A. Petrini, C. Pettinari, G. Lupidi, P. Smoleński, R. Scopelliti, T. Riedel, P.J. Dyson, (2016), From Sunscreen to Anticancer Agent: Ruthenium(II) Arene Avobenzene Complexes Display Potent Anticancer Activity, *Organometallics*, 35 3734-3742. (DOI: 10.1021/acs.organomet.6b00694).
- [48] A. Bergamo, A. Masi, A.F. Peacock, A. Habtemariam, P.J. Sadler, G. Sava, (2010), In vivo tumour and metastasis reduction and in vitro effects on invasion assays of the ruthenium RM175 and osmium AFAP51

organometallics in the mammary cancer model, *J. Inorg. Biochem.*, 104 79-86. (DOI: 10.1016/j.jinorgbio.2009.10.005).

[49] A. Mondal, U. Sen, N. Roy, V. Muthukumar, S.K. Sahoo, B. Bose, P. Paira, (2021), DNA targeting half sandwich Ru (II)-p-cymene-N<sup>^</sup> N complexes as cancer cell imaging and terminating agents: Influence of regioisomers in cytotoxicity, *Dalton Transactions*, 50 979-997. (DOI: 10.1039/D0DT03107K).

[50] S. Li, G. Xu, Y. Zhu, J. Zhao, S. Gou, (2020), Bifunctional ruthenium (II) polypyridyl complexes of curcumin as potential anticancer agents, *Dalton Transactions*, 49 9454-9463. (DOI: 10.1039/D0DT01040E).

[51] S. Emami, S. Dadashpour, (2015), Current developments of coumarin-based anti-cancer agents in medicinal chemistry, *European Journal of Medicinal Chemistry*, 102 611-630. (DOI: 10.1016/j.ejmech.2015.08.033).

[52] J. Chen, J. Wang, Y. Deng, T. Wang, T. Miao, C. Li, X. Cai, Y. Liu, J. Henri, L. Chen, (2020), Ru (II) complexes bearing O, O-chelated ligands induced apoptosis in A549 cells through the mitochondrial apoptotic pathway, *Bioinorganic Chemistry Applications*, 2020. (DOI: 10.1155/2020/8890950).

[53] A.-C. Munteanu, A. Notaro, M. Jakubaszek, J. Cowell, M. Tharaud, B. Goud, V. Uivarosi, G. Gasser, (2020), Synthesis, characterization, cytotoxic activity, and metabolic studies of ruthenium (II) polypyridyl complexes containing flavonoid ligands, *Inorg. Chem.*, 59 4424-4434.

[54] J. John Bright, A. Khar, Apoptosis: programmed cell death in health and disease, *Biosci. Rep.*, 14 (1994) 67-81. (DOI: 10.1146/annurev.phyto.36.1.393).

[55] D. Gilchrist, (1998), Programmed cell death in plant disease: the purpose and promise of cellular suicide, *Annual review of phytopathology*, 36 393-414. (DOI: 10.1021/acs.inorgchem.9b03562).

[56] J.C. Ameisen, (2002), On the origin, evolution, and nature of programmed cell death: a timeline of four billion years, *Cell Death Differentiation*, 9 367-393. (DOI: 10.1021/acs.inorgchem.9b03562).

- [57] Y. Fuchs, H. Steller, (2011), Programmed cell death in animal development and disease, *Cell*, 147 742-758. (DOI: 10.1016/j.cell.2011.10.033).
- [58] Y. Fuchs, H. Steller, (2015), Live to die another way: modes of programmed cell death and the signals emanating from dying cells, *Nature reviews Molecular cell biology*, 16 329-344. (DOI: 10.1038/nrm3999).
- [59] C.J. Gibson, M.S. Davids, (2015), BCL-2 antagonism to target the intrinsic mitochondrial pathway of apoptosis, *Clinical cancer research*, 21 5021-5029. (DOI: 10.1158/1078-0432.CCR-15-0364).
- [60] D. Brenner, T.W. Mak, (2009), Mitochondrial cell death effectors, *Current opinion in cell biology*, 21 871-877. (DOI: 10.1016/j.ceb.2009.09.004).
- [61] J.L. Evans, I.D. Goldfine, B.A. Maddux, G.M. Grodsky, (2003), Are oxidative stress-activated signaling pathways mediators of insulin resistance and  $\beta$ -cell dysfunction?, *Diabetes*, 52 1-8. (DOI: 10.2337/diabetes.52.1.1).
- [62] J.L. Martindale, N.J. Holbrook, (2002), Cellular response to oxidative stress: signaling for suicide and survival, *J. Cell. Physiol.*, 192 1-15. (DOI: 10.1002/jcp.10119).
- [63] M. Schieber, N.S. Chandel, (2014), ROS function in redox signaling and oxidative stress, *Current biology*, 24 R453-R462. (DOI: 10.1016/j.cub.2014.03.034).
- [64] X. Lei, Y. Chen, G. Du, W. Yu, X. Wang, H. Qu, B. Xia, H. He, J. Mao, W. Zong, (2006), Gossypol induces Bax/Bak-independent activation of apoptosis and cytochrome c release via a conformational change in Bcl-2, *The FASEB journal*, 20 2147-2149. (DOI: 10.1096/fj.05-5665fje).
- [65] A. Letai, M.C. Bassik, L.D. Walensky, M.D. Sorcinelli, S. Weiler, S.J. Korsmeyer, (2002), Distinct BH3 domains either sensitize or activate mitochondrial apoptosis, serving as prototype cancer therapeutics, *Cancer cell*, 2 183-192. (DOI: 10.1016/S1535-6108(02)00127-7).
- [66] L. Chen, G. Li, F. Peng, X. Jie, G. Dongye, K. Cai, R. Feng, B. Li, Q. Zeng, K. Lun, (2016), The induction of autophagy against mitochondria-

mediated apoptosis in lung cancer cells by a ruthenium (II) imidazole complex, *Oncotarget*, 7 80716. (DOI: 10.18632/oncotarget.13032).

[67] I. Kitazumi, M. Tsukahara, (2011), Regulation of DNA fragmentation: the role of caspases and phosphorylation, *The FEBS journal*, 278 427-441. (DOI: 10.1111/j.1742-4658.2010.07975.x).

[68] L. Galluzzi, M.C. Maiuri, I. Vitale, H. Zischka, M. Castedo, L. Zitvogel, G. Kroemer, (2007), Cell death modalities: classification and pathophysiological implications, *Cell death differentiation*, 14 1237. (DOI: 10.1038/sj.cdd.4402148).

[69] O. Surova, B. Zhivotovsky, Various modes of cell death induced by DNA damage, *Oncogene*, 32 (2013) 3789-3797. (DOI: 10.1038/onc.2012.556).

[70] W.P. Roos, B. Kaina, (2013), DNA damage-induced cell death: from specific DNA lesions to the DNA damage response and apoptosis, *Cancer letters*, 332 237-248. (DOI: 10.1016/j.canlet.2012.01.007).

[71] B.K. Kundu, Pragti, W.A. Carlton Ranjith, U. Shankar, R.R. Kannan, S.M. Mobin, A. Bandyopadhyay, S. Mukhopadhyay, (2022), Cancer-Targeted Chitosan–Biotin-Conjugated Mesoporous Silica Nanoparticles as Carriers of Zinc Complexes to Achieve Enhanced Chemotherapy In Vitro and In Vivo, *ACS Applied Bio Materials*, 5 190-204. (DOI: 10.1021/acsabm.1c01041).

[72] W. Maret, (2013), Zinc biochemistry: from a single zinc enzyme to a key element of life, *Advances in nutrition*, 4 82-91. (DOI: 10.3945/an.112.003038).

[73] P. Georgiev, H. Okkenhaug, A. Drews, D. Wright, S. Lambert, M. Flick, V. Carta, C. Martel, J. Oberwinkler, P. Raghu, (2010), TRPM channels mediate zinc homeostasis and cellular growth during *Drosophila* larval development, *Cell metabolism*, 12 386-397. (DOI: 10.1016/j.cmet.2010.08.012).

[74] M.M. Melk, S.S. El-Hawary, F.R. Melek, D.O. Saleh, O.M. Ali, M.A. El Raey, N.M. Selim, (2021), Antiviral activity of zinc oxide nanoparticles mediated by *Plumbago indica* L. extract against Herpes Simplex Virus Type 1

- (HSV-1), *International Journal of Nanomedicine*, 8221-8233. (DOI: 10.2147/IJN.S339404).
- [75] A. Scozzafava, T. Owa, A. Mastrolorenzo, C.T. Supuran, (2003), Anticancer and antiviral sulfonamides, *Current medicinal chemistry*, 10 925-953. (DOI: 10.2174/0929867033457647).
- [76] A. Hameed, M. Al-Rashida, M. Uroos, S. Abid Ali, K.M. Khan, (2017), Schiff bases in medicinal chemistry: a patent review (2010-2015), *Expert opinion on therapeutic patents*, 27 63-79. (DOI: 10.1080/13543776.2017.1252752).
- [77] P.H. Nguyen, A. Ramamoorthy, B.R. Sahoo, J. Zheng, P. Faller, J.E. Straub, L. Dominguez, J.-E. Shea, N.V. Dokholyan, A. De Simone, (2021), Amyloid oligomers: A joint experimental/computational perspective on Alzheimer's disease, Parkinson's disease, type II diabetes, and amyotrophic lateral sclerosis, *Chem. Rev.*, 121 2545-2647. (DOI: 10.1021/acs.chemrev.0c01122).
- [78] C. Mondello, A.I. Scovassi, (2010), Apoptosis: a way to maintain healthy individuals, *Genome Stability Human Diseases*, 307-323. (DOI: 10.1007/978-90-481-3471-7\_16).
- [79] M. Frezza, S. Hindo, D. Chen, A. Davenport, S. Schmitt, D. Tomco, Q. Ping Dou, Novel metals and metal complexes as platforms for cancer therapy, *Current pharmaceutical design*, 16 (2010) 1813-1825. (DOI: 10.2174/138161210791209009).
- [80] S.V.S. Rana, (2008), Metals and apoptosis: recent developments, *Journal of trace elements in medicine biology*, 22 262-284. (DOI: 10.1016/j.jtemb.2008.08.002).
- [81] H. Haase, L. Rink, (2014), Zinc signals and immune function, *Biofactors*, 40 27-40. (DOI: 10.1002/biof.1114).
- [82] F. Franco, A. Jaccard, P. Romero, Y.-R. Yu, P.-C. Ho, (2020), Metabolic and epigenetic regulation of T-cell exhaustion, *Nature metabolism*, 2 1001-1012. (DOI: 10.1038/s42255-020-00280-9).

- [83] L.P. Roguin, N. Chiarante, M.C.G. Vior, J. Marino, (2019), Zinc (II) phthalocyanines as photosensitizers for antitumor photodynamic therapy, *The international journal of biochemistry cell biology*, 114 105575. (DOI: 10.1016/j.biocel.2019.105575)
- [84] J. Karges, U. Basu, O. Blacque, H. Chao, G. Gasser, (2019), Polymeric encapsulation of novel homoleptic bis (dipyrrinato) zinc (II) complexes with long lifetimes for applications as photodynamic therapy photosensitisers, *Angew. Chem. Int. Ed.*, 131 14472-14478. (DOI: 10.1002/ange.201907856)
- [85] W. Sun, L. Luo, Y. Feng, Y. Qiu, C. Shi, S. Meng, X. Chen, H. Chen, (2020), Gadolinium–Rose Bengal Coordination Polymer Nanodots for MR-/Fluorescence-Image-Guided Radiation and Photodynamic Therapy, *Adv. Mater.*, 32 2000377. (DOI: 10.1002/adma.202000377)
- [86] X. Li, S. Lee, J. Yoon, (2018), Supramolecular photosensitizers rejuvenate photodynamic therapy, *Chem. Soc. Rev.*, 47 1174-1188. (DOI: 10.1039/C7CS00594F)
- [87] X. Wei, X.-H. Guo, J.-F. Guo, T.-F. He, G.-Y. Qin, L.-Y. Zou, A.-M. Ren, (2022), Photophysical Exploration of Zn(II) Polypyridine Photosensitizers in Two-Photon Photodynamic Therapy: Insights from Theory, *Inorg. Chem.*, 61 18729-18742. (DOI: 10.1021/acs.inorgchem.2c03232)
- [88] Y. Yao, N. Li, X. Zhang, J. Ong’achwa Machuki, D. Yang, Y. Yu, J. Li, D. Tang, J. Tian, F. Gao, (2019), DNA-Templated Silver Nanocluster/Porphyrin/MnO<sub>2</sub> Platform for Label-Free Intracellular Zn<sup>2+</sup> Imaging and Fluorescence-/Magnetic Resonance Imaging-Guided Photodynamic Therapy, *ACS Applied Materials & Interfaces*, 11 13991-14003. (DOI: 10.1021/acsami.9b01530)
- [89] F. Cortezon-Tamarit, S. Sarpaki, D.G. Calatayud, V. Mirabello, S.I. Pascu, (2016), Applications of “Hot” and “Cold” Bis (thiosemicarbazonato) metal complexes in multimodal imaging, *The Chemical Record*, 16 1380-1397. (DOI: 10.1002/tcr.201500292)
- [90] Ł. Lamch, J. Kulbacka, M. Dubińska-Magiera, J. Saczko, K.A. Wilk, (2019), Folate-directed zinc (II) phthalocyanine loaded polymeric micelles

engineered to generate reactive oxygen species for efficacious photodynamic therapy of cancer, *Photodiagnosis Photodynamic Therapy*, 25 480-491. (DOI: 10.1016/j.pdpdt.2019.02.014)

[91] M. Schmittel, V. Kalsani, P. Mal, J.W. Bats, (2006), The HETTAP approach: self-assembly and metal ion sensing of dumbbell-shaped molecules and clip molecules, *Inorg. Chem.*, 45 6370-6377.

[92] Z.-F. Wang, Q.-X. Nong, H.-L. Yu, Q.-P. Qin, F.-H. Pan, M.-X. Tan, H. Liang, S.-H. Zhang, (2022), Complexes of Zn (II) with a mixed tryptanthrin derivative and curcumin chelating ligands as new promising anticancer agents, *Dalton Transactions*, 51 5024-5033. (DOI: 10.1021/ic0604031)

[93] S.P. Dunuweera, R.M.S.I. Rajapakse, R.B.S.D. Rajapakshe, S.H.D.P. Wijekoon, M.G.G.S. Nirodha Thilakarathna, R.M. Rajapakse, (2019), Review on targeted drug delivery carriers used in nanobiomedical applications, *Current Nanoscience*, 15 382-397. (DOI: 10.2174/1573413714666181106114247)

[94] S. Hossen, M.K. Hossain, M. Basher, M. Mia, M. Rahman, M.J. Uddin, (2019), Smart nanocarrier-based drug delivery systems for cancer therapy and toxicity studies: A review, *Journal of advanced research*, 15 1-18. (DOI: 10.1016/j.jare.2018.06.005)

[95] S.Z. Vahed, R. Salehi, S. Davaran, S. Sharifi, (2017), Liposome-based drug co-delivery systems in cancer cells, *Materials Science Engineering: C*, 71 1327-1341. (DOI: 10.1016/j.msec.2016.11.073)

[96] H. Liu, S. Farrell, K. Uhrich, (2000), Drug release characteristics of unimolecular polymeric micelles, *J. Controlled Release*, 68 167-174. (DOI: 10.1016/S0168-3659(00)00247-9)

[97] Y.-K. Oh, T.G. Park, siRNA delivery systems for cancer treatment, *Advanced drug delivery reviews*, 61 (2009) 850-862. (DOI: 10.1016/j.addr.2009.04.018)

[98] E. Abbasi, S.F. Aval, A. Akbarzadeh, M. Milani, H.T. Nasrabadi, S.W. Joo, Y. Hanifehpour, K. Nejati-Koshki, R. Pashaei-Asl, (2014), Dendrimers: synthesis, applications, and properties, *Nanoscale research letters*, 9 1-10. (DOI: 10.1186/1556-276X-9-247)

- [99] S. Svenson, D.A. Tomalia, (2012), Dendrimers in biomedical applications—reflections on the field, *Advanced drug delivery reviews*, 64 102-115. (DOI: 10.1016/j.addr.2012.09.030)
- [100] M. Zu, Y. Ma, B. Cannup, D. Xie, Y. Jung, J. Zhang, C. Yang, F. Gao, D. Merlin, B. Xiao, (2021), Oral delivery of natural active small molecules by polymeric nanoparticles for the treatment of inflammatory bowel diseases, *Advanced Drug Delivery Reviews*, 176 113887.
- [101] A.M. Smith, H. Duan, A.M. Mohs, S. Nie, (2008), Bioconjugated quantum dots for in vivo molecular and cellular imaging, *Advanced drug delivery reviews*, 60 1226-1240. (DOI: 10.1016/j.addr.2021.113887)
- [102] I. Neamtu, A.G. Rusu, A. Diaconu, L.E. Nita, A.P. Chiriac, (2017), Basic concepts and recent advances in nanogels as carriers for medical applications, *Drug Delivery*, 24 539-557. (DOI: 10.1080/10717544.2016.1276232)
- [103] C. Bharti, U. Nagaich, A.K. Pal, N. Gulati, (2015), Mesoporous silica nanoparticles in target drug delivery system: A review, *International journal of pharmaceutical investigation*, 5 124. (DOI: 10.4103/2230-973X.160844)
- [104] Y. Guan, L.-y. Wang, B. Wang, M.-h. Ding, Y.-l. Bao, S.-w. Tan, (2020), Recent advances of D- $\alpha$ -tocopherol polyethylene glycol 1000 succinate based stimuli-responsive nanomedicine for cancer treatment, *Current medical science*, 40 218-231. (DOI: 10.1007/s11596-020-2185-1)

## *Chapter 2*

*Modulation of catalytic and biomolecular binding properties of ruthenium (II)-arene complexes with the variation of coligands for selective toxicity against cancerous cells*



## **Chapter 2**

### **Modulation of catalytic and biomolecular binding properties of ruthenium (II)-arene complexes with the variation of coligands for selective toxicity against cancerous cells**

#### **2.1 Introduction**

"Cancer is the second leading cause of death globally" (WHO) [1,2]. It arises from faulty DNA, which means changes in the genes [3,4]. Mutations can occur in genes for various reasons, causing normal cells to become cancerous [5,6]. These mutations cause the cells to divide uncontrollably, which becomes lethal if not treated. At present, the development of new drugs against cancer belongs among the priority areas in medicinal research. In recent years, metal-based antitumor drugs have emerged as a significant contributor to antitumor chemotherapy [7]; where cisplatin is regarded as one of the most effective anticancer drugs used in the clinic. Thus, the research, development, and production of metal-based drugs are a highly evolving field that has been getting considerable attention recently. In spite of the remarkable efficacy of platinum-based drugs against ovarian, bladder and testicular cancers, a variety of adverse effects and acquired resistance are observed in patients receiving such chemotherapy [8,9,10]. To overcome these problems, researchers focus on alternative transition metals with the same efficacy but reduced side effects [11, 12]. Among various other metals, ruthenium complexes have raised significant interest due to their potential anticancer nature and flexible scaffold for optimizing efficiency by tuning different ligands [13]. Hereby, it is important to note that arene-ruthenium(II) based complexes have the advantage of their amphiphilic nature due to the presence of an arene ring in combination with a hydrophilic metal center. It is also worth mentioning that ruthenium complexes show similar ligand exchange kinetics to platinum(II) complexes in aqueous medium, which is also an essential factor for antiproliferative activity [14,15]. After considering all the above factors, this chapter involves the

development of four organoruthenium arene complexes where the metal center is coordinated with pyridine based 2-amino methyl pyridine as coligand. It is well known in the literature that many ligands derived from pyridyl moiety (pyridine based), when coupled with metals, resulted in complexes that exhibit high cytotoxicity and have proved to be antitumor agents [16]. Furthermore, a series of half-sandwich ruthenium(II) complexes with imino-pyridyl and imino-quinoline ligands with cytotoxic effect is reported which operates through catalytic oxidation of NADH and generation of ROS [17]. Herein, four ruthenium(II)-arene compounds viz.  $[\text{Ru}(\text{p-cym})(2\text{-ampy})\text{Cl}]\text{PF}_6$  1,  $[\text{Ru}(\text{benzene})(2\text{-ampy})\text{Cl}]\text{SO}_3\text{CF}_3$  2,  $[\text{Ru}(\text{p-cym})(2\text{-ampy})\text{PPh}_3](\text{PF}_6)_2$  3,  $[\text{Ru}(\text{benzene})(2\text{-ampy})\text{PPh}_3](\text{SO}_3\text{CF}_3)_2$  4, are synthesized and their anticancer properties are studied in terms of evaluation of cytotoxicity towards different cell lines. Among them, one of the utilized compounds  $[\text{Ru}(\text{p-cym})(2\text{-ampy})\text{Cl}]\text{PF}_6$  [2-ampy = 2-picolyl amine] 1 has been reported earlier and the other complex  $[\text{Ru}(\text{benzene})(2\text{-ampy})\text{Cl}]^+$  in its cationic form have also been reported and tested towards various catalytic activities of organic transformation reactions [18]. DNA binding and serum albumin (HSA/BSA) binding studies of compounds 1-4 have been performed using UV-Visible and fluorescence spectroscopy. The ability of ruthenium(II) complexes to transfer hydrogen from NADH and change it into  $\text{NAD}^+$  has been investigated. The result indicates the complexes' ability to destabilize the redox balance of the cells to generate ROS, which has been investigated herewith, and the morphological changes of the cells upon treatment with 1-4 have been explored. Furthermore, DFT studies were performed to calculate the energy of FMOs and optimize the geometry of all the complexes, which reveals the expected structure of the compounds. This theoretical data also helped to compare the probable interactions of the various complexes with DNA.

## 2.2 Experimental section

### 2.2.1 Materials and methods

All the chemicals required are purchased from Sigma and used without further purification. Chemical for biological experiments (3-(4,5-dimethylthiazol-2-

yl)-2,5-diphenyltetrazolium bromide (MTT), PBS buffer were purchased from Himedia Chemical, India. An AVANCE III 400 Ascend Bruker BioSpin spectrometer was used to record  $^1\text{H}$  and  $^{13}\text{C}$  NMR spectroscopy at room temperature. Infrared (FTIR) spectra (range: 4000 to 500  $\text{cm}^{-1}$ ) were conducted on BRUKER TENSOR 27 instrument. Elemental analyses (C, H, N and S content) were performed with a MicroTOF-Q II mass spectrometer and ThermoFlash 2000 elemental analyzer. ESI-MS data were taken on Bruker-Daltonics. Spectrophotometric measurements for the absorption study were done using a quartz cuvette with a path length of 1 cm on a Varian UV-Vis spectrophotometer (Model: Cary 100). A Perkin-Elmer lambda-650 DRS UV-Vis spectrophotometer, equipped with an integration sphere diffuse reflectance attachment in the range of 200-1200 nm against  $\text{BaSO}_4$  as a reference, was utilized for UV-Vis diffuse reflectance spectral (UV-Vis/ DRS) analyses. The far-ultraviolet (UV) (190 to 260 nm) spectra were recorded in a 0.1 cm path length cell (Hellma, Muellheim/Baden, Germany) using a step size of 0.5 nm, the bandwidth of 1 nm, and a scan rate of 20  $\text{nm min}^{-1}$ . Fluorescence emission spectra were recorded at  $25.0 \pm 0.2$   $^\circ\text{C}$  on a Fluoromax-4p spectrofluorometer from Horiba JobinYvon (Model: FM-100) using a quartz cuvette with a path length of 2 cm. Hoechst stain experiments were done with the help of a confocal microscope Fluoview FV100 (OLYMPUS, 449 Tokyo, Japan).

## 2.2.2 Synthesis and Characterization

### 2.2.2.1 Synthesis of **1** $[\text{Ru}(\eta^6\text{-p-cym})(2\text{-ampy})\text{Cl}]\text{PF}_6$

Ruthenium compound **1** was synthesized by the dropwise addition of methanolic solution (10 mL) of 2-aminomethyl pyridine (2-ampy) (0.034 g, 0.33 mmol) into the methanolic/ $\text{CH}_2\text{Cl}_2$  solution mixture of dimeric ruthenium compound  $[(\eta^6\text{-p-cymene})\text{RuCl}_2]_2$  (0.1 g, 0.16 mmol) with continuous stirring for 4 hrs at room temperature. After that a methanolic solution of  $\text{NH}_4\text{PF}_6$  (0.052 g, 0.33 mmol) was added and stirred for 2 hrs. Then the reaction was stopped and the solvent mixture was evaporated under high vacuum to obtain a brown coloured solid product. Diffraction quality crystals of complex **1** were obtained by vapour diffusion of diethyl ether into a saturated methanolic

solution of complex **1**. Yield: 75%.  $^1\text{H}$  NMR (400.13 MHz, 298K, DMSO- $d_6$ )  $\delta$ : 9.16[d, 1H, CH of  $\text{C}_6\text{H}_8\text{N}_2$ ], 8.00[t, 1H, CH of  $\text{C}_6\text{H}_8\text{N}_2$ ], 7.57[t, 1H, CH of  $\text{C}_6\text{H}_8\text{N}_2$ ], 5.89[d, 2H, 2X CH of  $\text{C}_6\text{H}_4$ ], 5.69[d, 2H, 2X CH of  $\text{C}_6\text{H}_4$ ], 4.45[s, 2H, CH of  $\text{C}_6\text{H}_8\text{N}_2$ ], 4.21[m, 1H,  $\text{CH}(\text{CH}_3)_2$ ], 2.74[s, 3H,  $\text{C}_6\text{H}_4\text{CH}_3$ ], 1.16[d, 6H,  $\text{CH}(\text{CH}_3)_2$ ], 1.98[s, 2H,  $\text{NH}_2$  of  $\text{C}_6\text{H}_8\text{N}_2$ ].  $^{13}\text{C}$  NMR (100.61 MHz, DMSO- $d_6$ )  $\delta$ : 161.4, 155.13, 139.45, 125.5[C of Py ring], 103.4, 98.3, 85.2-82.2 [ $\text{C}_6\text{H}_4$ ], 52.3[C of  $\text{C}_6\text{H}_8\text{N}_2$ ], 30.8[CH], 22.21[CMe $_2$ ], 18.1[Me]. ESI-MS (+ve mode):  $[\text{Ru}(\eta^6\text{-p-cymene})(\text{amp})\text{Cl}]^+$  : 379.3( $m/z$ ). Elemental analysis (%): calc. For  $\text{C}_{16}\text{H}_{22}\text{ClN}_2\text{Ru}$  C, 50.72; H, 5.85; N, 7.39. Found: C, 51.50; H, 5.87; N, 7.38. IR (KBr,  $\text{cm}^{-1}$ ): 3227  $\nu(\text{N-H})$ , 1561  $\nu(\text{C=N})$ , 1412  $\nu(\text{C=C})$ , 841  $\nu(\text{Ru-Cl})$ . Analytical results are similar to the reported complex as per reference [18].

### 2.2.2.2 Synthesis of **2** $[\text{Ru}(\eta^6\text{-benzene})(2\text{-ampy})\text{Cl}]\text{SO}_3\text{CF}_3$

Compound **2** was synthesized by a similar method described for compound **1**. Only instead of  $\text{NH}_4\text{PF}_6$ , a methanolic solution of  $\text{AgSO}_3\text{CF}_3$  (0.1 g, 0.4 mmol) was added for counter anion. After evaporation of the solvent mixture under a high vacuum, a dark brown-coloured solid product was obtained. Diffraction quality crystals of **2** were obtained by vapour diffusion of diethyl ether into a saturated solution of **2** in methanol. Yield 70%.  $^1\text{H}$  NMR (400.13 MHz, 298K, DMSO- $d_6$ )  $\delta$ : 9.21[d, 1H, CH of  $\text{C}_6\text{H}_8\text{N}_2$ ], 7.96[t, 1H, CH of  $\text{C}_6\text{H}_8\text{N}_2$ ], 7.52[t, 1H, CH of  $\text{C}_6\text{H}_8\text{N}_2$ ], 7.20[d, 1H, CH of  $\text{C}_6\text{H}_8\text{N}_2$ ], 5.92[s, 6H, CH of  $\text{C}_6\text{H}_6$ ], 4.58[s, 2H CH of  $\text{C}_6\text{H}_8\text{N}_2$ ].  $^{13}\text{C}$  NMR (100.61 MHz, DMSO- $d_6$ )  $\delta$ : 162.0, 155.1, 139.7, 125.1, 121.7 [C of Py ring], 88.0, 85.0 [C of  $\text{C}_6\text{H}_6$ ], 52.3 [C of  $\text{C}_6\text{H}_8\text{N}_2$ ].  $[\text{Ru}(\eta^6\text{-benzene})(2\text{-ampy})\text{Cl}]^+$  : 322.9 ( $m/z$ ) (Figure S7). Elemental analysis (%): calc. For  $\text{C}_{13}\text{H}_{14}\text{ClF}_3\text{N}_2\text{O}_3\text{RuS}$  C, 33.09; H, 2.99; N, 5.94. Found: C, 33.49; H, 3.03; N, 5.80. FTIR (KBr,  $\text{cm}^{-1}$ ): 3435  $\nu(\text{N-H})$ , 1567  $\nu(\text{C=N})$ , 1433  $\nu(\text{C=C})$ , 843  $\nu(\text{Ru-Cl})$ .

### 2.2.2.3 Synthesis of **3** $[\text{Ru}(\eta^6\text{-p-cym})(2\text{-ampy})\text{PPh}_3](\text{PF}_6)_2$

Ruthenium compound **3** was synthesized by the dropwise addition of triphenylphosphine (0.068 g, 0.26 mmol) into the methanolic solution of complex **1** (0.1 g, 0.26 mmol) and stirring it overnight at room temperature.

The resulting solution was then evaporated and dried to obtain a brown-colored solid product. After that, a methanolic solution of  $\text{NH}_4\text{PF}_6$  (0.04 g, 0.26 mmol) was added to the methanolic solution of dark brown solid and stirred the mixture for 2 hrs at room temperature. Then the solvent was evaporated under vacuum, and a brown solid was obtained. The compound was further recrystallized from the slow evaporation of the methanolic solution. Yield 65%.  $^1\text{H}$  NMR (400.13 MHz, 298K,  $\text{DMSO-d}_6$ )  $\delta$ : 9.13 [d, 1H, CH of  $\text{C}_6\text{H}_8\text{N}_2$ ], 7.95 [t, 1H, CH of  $\text{C}_6\text{H}_8\text{N}_2$ ], 7.52 [t, 1H, CH of  $\text{C}_6\text{H}_8\text{N}_2$ ], 7.39-7.24 [aromatic proton of  $\text{PPh}_3$ ], 5.96-5.71 [aromatic proton of p-cymene ring], 4.19 [s, 2H, CH of  $\text{C}_6\text{H}_8\text{N}_2$ ], 2.70 [m, 1H,  $\text{CH}(\text{CH}_3)_2$ ], 1.96 [s, 3H,  $\text{C}_6\text{H}_4\text{CH}_3$ ], 1.16 [d, 6H,  $\text{CH}(\text{CH}_3)_2$ ].  $^{13}\text{C}$  NMR (100.61 MHz,  $\text{DMSO-d}_6$ )  $\delta$ : 161.7, 155.0, 139.6, 125.3, 121.6 [C of Py ring], 137.0-125.3 [C of  $\text{PPh}_3$  ring] 85.2, 83.5, 82.7, 82.2 [C of p-cymene ring], 52.5 [C of  $\text{C}_6\text{H}_8\text{N}_2$ ], 30.7 [CH of p-cymene ring], 22.7 [CMe<sub>2</sub> of p-cymene ring], 18.1 [Me of p-cymene ring]. ESI-MS (+ve mode): [ $\text{Ru}(\eta^6\text{-p-cymene})(2\text{-ampy})(\text{PPh}_3)^{2+}$ ] : 302.1 (*m/z*). Elemental analysis (%): calc. For  $\text{C}_{34}\text{H}_{37}\text{F}_6\text{N}_2\text{P}_2\text{Ru}$  C, 54.40; H, 4.97; N, 3.73. Found: C, 54.59; H, 5.01; N, 3.65. FTIR (KBr,  $\text{cm}^{-1}$ ): 3426  $\nu_{(\text{N-H})}$ , 1570  $\nu_{(\text{C=N})}$ , 1423  $\nu_{(\text{C=C})}$ .

#### 2.2.2.4 Synthesis of **4** [ $\text{Ru}(\eta^6\text{-benzene})(2\text{-ampy})\text{PPh}_3$ ] $\text{SO}_3\text{CF}_3$

Compound **4** was synthesized by dropwise adding triphenylphosphine (0.068 g, 0.26 mmol) into the methanolic solution of complex **2** (0.1 g, 0.26 mmol) and stirring it overnight at room temperature. The resulting solution was then evaporated and dried. A brown-coloured compound was obtained, which was further dissolved in methanol, and a methanolic solution of silver triflate (0.07 g, 0.30 mmol) was added and stirred for two hrs more. After that, the solvent was evaporated to obtain the final product. Recrystallization was carried out by the slow evaporation method of the methanolic solution of the compound. Yield 68%  $^1\text{H}$  NMR (400.13 MHz, 298K,  $\text{DMSO-d}_6$ )  $\delta$ : 9.21 [d, 1H, CH of  $\text{C}_6\text{H}_8\text{N}_2$ ], 7.64 [t, 1H, CH of  $\text{C}_6\text{H}_8\text{N}_2$ ], 7.56 [t, 1H, CH of  $\text{C}_6\text{H}_8\text{N}_2$ ], 7.45- 7.08 [aromatic proton of  $\text{PPh}_3$ ], 5.91 [aromatic proton of ruthenium coordinated benzene ring], 4.15 [s, 2H, CH of  $\text{C}_6\text{H}_8\text{N}_2$ ].  $^{13}\text{C}$  NMR (100.61 MHz,  $\text{DMSO-d}_6$ )  $\delta$ : 162.0, 155.2, 139.6, 125.1, 121.6 [C of Py ring], 137.1-128.9 [C of  $\text{PPh}_3$

ring], 85.0, 83.7 [C of benzene ring], 52.5 [C of C<sub>6</sub>H<sub>8</sub>N<sub>2</sub>]. ESI-MS (+ve mode): [Ru( $\eta^6$ -benzene)(2-ampy)PPh<sub>3</sub>]<sup>2+</sup>: 275.0 (*m/z*). Elemental analysis (%): calc. For C<sub>31</sub>H<sub>29</sub>F<sub>3</sub>N<sub>2</sub>O<sub>3</sub>PRuS C, 53.29; H, 4.18; N, 4.01. Found: C, 53.80; H, 4.72; N, 3.99. FTIR (KBr, cm<sup>-1</sup>): 3431  $\nu$ (N-H), 1571  $\nu$ (C=N), 1425  $\nu$ (C=C).

### 2.2.3 Crystallographic Elucidation of Compound 1 and 2

Single crystal X-ray structural studies of complexes **1**, and **2** were mounted onto quartz fibers, and the X-ray diffraction intensity data were measured at 293 K with a Bruker APEX II diffractometer equipped with a CCD detector, employing Mo K $\alpha$  radiation ( $\lambda = 0.71073 \text{ \AA}$ ), with the SMART suite of programs. All data were processed and corrected for Lorentz and polarization effects with SAINT and for absorption effects with SADABS [19]. Structure solution and refinement were carried out with the SHELXTL suite of programs [20]. Data were corrected for absorption effects using the multi-scan method (SADABS). The structures were solved by Patterson maps to locate the heavy atoms, followed by difference maps for the light, non-hydrogen atoms. All non-hydrogen atoms were refined with anisotropic thermal parameters. Crystal data and structural parameters are provided in Table 2.1.

**Table 2.1.** Crystallographic information and structure refinement parameters for complexes **1** and **2**.

Parameter	Complex 1	Complex 2
<b>Empirical Formula</b>	C <sub>16</sub> H <sub>22</sub> ClF <sub>6</sub> N <sub>2</sub> PRu	C <sub>13</sub> H <sub>14</sub> ClF <sub>3</sub> N <sub>2</sub> O <sub>3</sub> RuS
<b>Formula weight</b>	523.84	471.84
<b>Crystal system</b>	Monoclinic	Triclinic
<b>Space group</b>	P 1 21/n 1	P -1
<b><i>a</i> (Å)</b>	8.9823(2)	7.5303(2)
<b><i>b</i> (Å)</b>	21.1120(6)	9.0425(2)
<b><i>c</i> (Å)</b>	11.1235(3)	11.8427(4)
<b><math>\alpha</math> (°)</b>	90	84.3921(11)
<b><math>\beta</math> (°)</b>	112.1637(9)	80.5826(9)
<b><math>\gamma</math> (°)</b>	90	84.3429(9)
<b>V (Å<sup>3</sup>)</b>	1953.53(9)	788.92(4)
<b><math>\lambda</math> (Å)</b>	0.71073	0.71073
<b><math>\rho_{\text{calcd}}</math> (mg m<sup>-3</sup>)</b>	1.781	1.986
<b>Z</b>	4	2

<b>T (K)</b>	100(2)	100(2)
<b><math>\mu</math> (mm<sup>-1</sup>)</b>	1.080	1.343
<b>F(0 0 0)</b>	1048	468
<b>Crystal size (mm<sup>3</sup>)</b>	0.160 x 0.180 x 0.220	0.160 x 0.180 x 0.220
<b><math>\theta</math> ranges (°)</b>	2.50 to 27.50	2.75 to 27.48
<b>h/k/l</b>	-10,11/-27,23/-14,14	-9,9/-11,11/-15,15
<b>Reflections collected</b>	17840	13187
<b>Independent reflections</b>	4463	3548
<b>T<sub>max</sub> and T<sub>min</sub></b>	0.8460 and 0.7970	0.8140 and 0.7560
<b>Data/restraints/parameters</b>	4463 / 0 / 247	3548 / 591 / 272
<b>GOF</b>	1.093	1.043
<b>Final R indices [I &gt; 2<math>\sigma</math>(I)]</b>	R1 = 0.0275, wR2 = 0.0542	R1 = 0.0265, wR2 = 0.0639
<b>R indices (all data)</b>	R1 = 0.0334, wR2 = 0.0567	R1 = 0.0279, wR2 = 0.0651
<b>Largest peak and hole (e Å<sup>-3</sup>)</b>	0.494 and -0.429	0.975 and -0.849

## 2.2.4 Protein Binding Study

### 2.2.4.1 Competitive binding experiments

Protein binding studies of the synthesized compounds were carried out by tryptophan fluorescence quenching experiments using human serum albumin (HSA). The excitation wavelength for HSA was 280 nm, and the quenching of the emission intensity of the tryptophan residues of HSA at 345 nm was monitored using the complexes as a quencher with increased concentration. The excitation and emission slit widths and scan rates were kept constant throughout the experiment. A 10  $\mu$ M stock solution of HSA was prepared using 50 mM tris buffer solution and stored at 4°C for further use. Stock solutions of 5 mM strength were made using synthesized compounds. Fluorometric titration was carried out taking 2 mL of the protein solution, and the fluorescence intensity was measured as blank. For titration, each time, 10  $\mu$ L of the stock solution was added to the protein solution and the fluorescence

intensity was measured. For all four complexes, up to 100  $\mu\text{L}$  of the solution was added to measure fluorescence quenching. The fluorescence quenching data were further analyzed by using the Stern–Volmer equation, which again can be expressed in terms of the bimolecular quenching rate constant and the average life time of the fluorophore as shown in the following equation: [21]

$$F_0/F = 1 + K_{sv} [Q] = 1 + K_q \tau_0 [Q] \dots (1)$$

where  $F_0$  and  $F$  are the fluorescence intensities in the absence and presence of a quencher,  $K_q$  is the bimolecular quenching rate constant,  $\tau_0$  is the average lifetime of a fluorophore in the absence of a quencher and  $[Q]$  is the concentration of a quencher (metal complexes).  $K_{sv}$  is the Stern–Volmer quenching constant in  $\text{M}^{-1}$ . The binding constant  $K_a$  and number of complex bound to BSA ( $n$ ) are calculated using the following formula. [22]

$$\log [(F_0 - F)/F] = \log K_a + n \log [Q] \dots (2)$$

The magnitudes of  $K_a$  and  $K_q$  of complexes are  $10^5 \text{ M}^{-1}$  and  $10^{13} \text{ M}^{-1}\text{s}^{-1}$ , respectively, indicating a good binding ability to serum protein.

#### 2.2.4.2 Circular dichroism (CD) spectral studies

Monitoring the far UV-CD spectra (190-250 nm) provides important information to get an insight into the change in the secondary structure of serum albumin proteins. At first, the spectra of free BSA (10 $\mu\text{M}$ ) and HSA (10 $\mu\text{M}$ ) was recorded, and then changes in CD spectra were obtained by monitoring the binding of metal complexes upon the addition of 0-100  $\mu\text{M}$  of metal complexes successively. For titration, 10  $\mu\text{L}$  of the stock solution was added to the protein solution each time, and the ellipticity ( $q$ ) in CD spectra was measured [21].

#### 2.2.5 DNA binding study

##### 2.2.5.1 Absorption spectral studies

The interactions between metal complexes and DNA were studied using the electronic absorption method. Disodium salt of calf thymus CT-DNA was stored at 4°C. Solution of CT-DNA in the buffer 50 mM NaCl/ 5 mM Tris (pH 7.2) in water gave a ratio of 1.9 of UV absorbance at 260 and 280 nm ( $A_{260}/A_{280}$ ,  $A$  = absorbance), indicating that the DNA was sufficiently free

from protein. The concentration of DNA was measured using its extinction coefficient ( $\epsilon$ ) at 260 nm after 1:100 dilutions. Stock solutions were stored at 4°C and used for not more than four days. Concentrated stock solutions of the complexes were prepared by dissolving the complexes in DMSO and diluting them suitably with the corresponding buffer to the required concentration for measurements. Absorption spectra titrations were performed at room temperature in Tris HCl/ NaCl buffer (5 mM/ 50 mM buffer, pH 7.4) to investigate the binding affinity between CT-DNA and complex. A fixed concentration of the complex (10  $\mu$ M) was titrated with increasing amounts of CT-DNA concentration. The intrinsic binding constants for the interaction of complexes with CT-DNA were obtained from spectral absorption data [21].

#### **2.2.5.2 Competitive binding experiments**

The relative bindings of complexes to CT-DNA were determined with an EB-bound CT-DNA solution in Tris-HCl/ NaCl buffer (5 mM/ 50 mM, pH=7.4). DNA was pre-treated with ethidium bromide for 30 min by maintaining the fixed ratio of [DNA]/ [DAPI] = 2.0. The fluorescence quenching effect on the addition of complex to the DAPI-DNA complex has been analyzed by recording the fluorescence emission spectra with excitation at 350 nm and emission at 458 nm. The titration quenching experiment was carried out by keeping the concentration of DNA constant in the buffer ([CT-DNA] = 10  $\mu$ M and [dye] = 15  $\mu$ M) and adding the sample solution within the concentrations range of 0-100  $\mu$ M. After the addition of the sample solution, the solution was kept for 1 min and then fluorescence intensity was measured. The quenching efficiency was calculated from Stern-Volmer (SV) equation.

#### **2.2.5 Cytotoxic assay**

The cell line was obtained from the National Centre for Cell Sciences (NCCS) Pune, India. It was cultured in the Dulbecco's Modified Eagles medium (DMEM) supplemented with 10% fetal bovine serum (FBS), 200 mM L-glutamine, 100  $\mu$ g/mL penicillin, and 10 mg/mL streptomycin in a humidified atmosphere consisting of 5 % CO<sub>2</sub> at 37 °C. Cells were cultured and

maintained in the logarithmic growth phase until the number of cells reached  $1.0 \times 10^6$  cells/mL.

### 2.2.5.1 Evaluation of cytotoxicity

The cytotoxic effect of complex against HeLa and MCF-7 cells was evaluated by MTT [3-(4, 5-dimethylthiazol-2-yl)-2, 5-diphenyltetrazoliumbromide] assay. All cells were seeded ( $5 \times 10^4$  cells/well) in a 96-well plate and kept in CO<sub>2</sub> for attachment and growth for 24 h. Then, the cells were treated with various concentrations of complex dissolved in DMSO or water (0.25-100  $\mu$ M) and incubated for 24 h. After incubation, the culture medium was removed, and 10  $\mu$ L of MTT solution (5 mg/mL in PBS) was added to each well. Following 4 h incubation in the dark, MTT was discarded, and DMSO or water (100  $\mu$ L/well) was added to solubilize the purple formazan product. The experiment was carried out in triplicates, and the medium without complex served as a control. The absorbance was measured colorimetrically at 570 nm using an ELISA microplate reader. The percentage of cell viability was calculated using the following formula and expressed as: % cell viability = (OD value of treated cells)/(OD value of untreated cells (control))  $\times$  100 [ 23]. The cytotoxic concentration/ dose that killed 50 % of the cells (IC<sub>50</sub>) was determined from the absorbance (OD) versus concentration linear regression curve using the Prism GraphPad software package. Each well was triplicated, and each experiment was repeated at least three times. IC<sub>50</sub> values quoted are mean  $\pm$  SEM.

### 2.2.6 Reactive Oxygen Species (ROS) generation

To know the probable reason of the apoptotic induction, redox status was assessed by DCFH-DA dye according to the standard procedure because generation of the intracellular ROS can be an important factor in apoptosis induction. MCF-7 cells were seeded in 6 well tissue culture plate and incubated for 24 hrs in the CO<sub>2</sub> incubator. Cells were then treated with complexes **3** and **4** at their IC<sub>50</sub> values and again incubated for 24 hrs and untreated cells were taken as control. After incubation the cells were washed twice with PBS, and stained with 10  $\mu$ M of DCFH-DA dye at 37°C for 30 min. Then after cells

were again washed twice with PBS and 100  $\mu$ L DMEM were added to each well. The cells from different wells of the culture plate were subjected to inverted fluorescence microscopy, and green fluorescence was detected and photographed.

### **2.2.7 Hoechst Staining**

The morphology of the cells was evaluated using Hoechst stain 33258. The  $5 \times 10^4$  MCF-7 cells were placed in six-well plates with a coverslip in each well and incubated overnight in the CO<sub>2</sub> incubator for attachment. The cells were then treated with corresponding IC<sub>50</sub> concentrations of complexes 3 and 4 for 24 h and untreated cells were taken as control. These cells were then fixed with 4% paraformaldehyde followed by permeabilization with 0.1% Triton x 100. These cells were now stained with 5  $\mu$ g/mL Hoechst 33258 for 30 min at room temperature followed by washing with PBS buffer. Then the coverslips were mounted on glass slides, and the fluorescence was viewed under OLYMPUS confocal microscope [24].

### **2.2.8 DFT calculations**

In order to explore the electronic structure and optimize the structure of complexes 1-4, DFT calculations were performed using the Gaussian 09 software. All calculations were done at the B3LYP level of theory employing the Lan12DZ basis set for Ru and 6-31G\* basis set for the remaining atoms. The geometries were optimized without imposing symmetry or any other restraints [25,26].

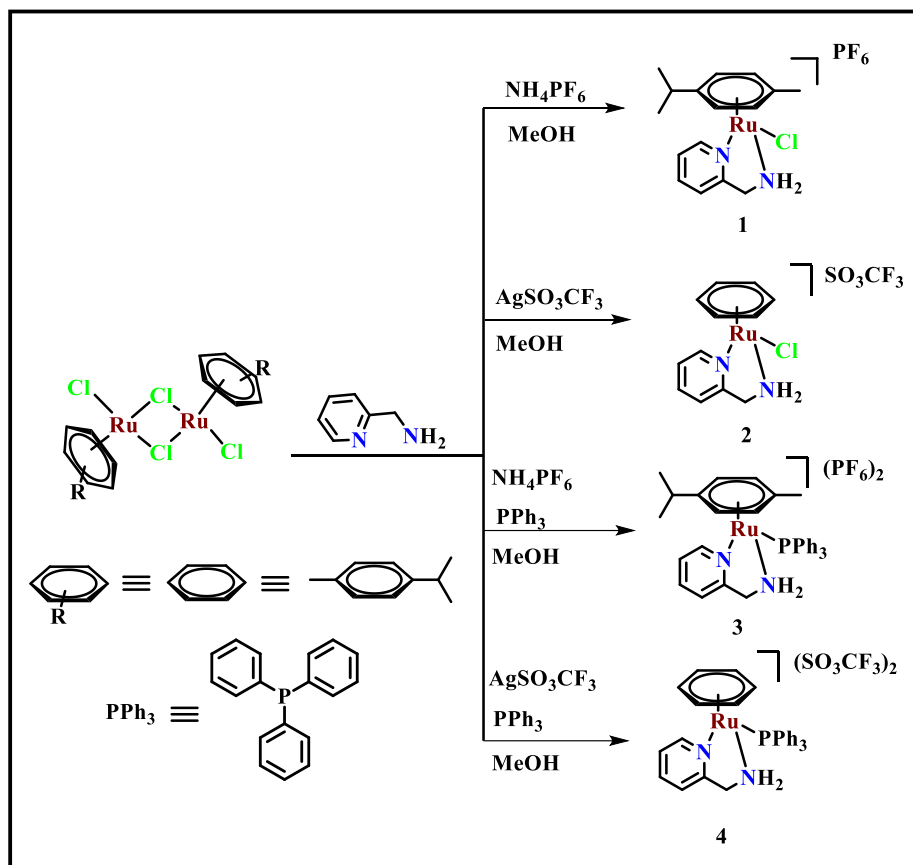
## **2.3 Results and discussion**

### **2.3.1 Synthesis and characterization**

Piano-stool ruthenium(II) arene complexes can show interesting apoptotic properties for various cancerous cells, making them interesting candidates for detailed anticancer studies. Coligands utilized in forming such complexes can play an important role in making the complex more effective in cytotoxicity and targeting only the cancerous cells. As per literature reports amino pyridines and derivatives are an important class of molecules that can act as

suitable coligands to attribute enhanced cytotoxicity of the synthesized complexes [27].

Herein, this report contains the synthesis of four Ru(II)-arene complexes where 2-aminomethyl pyridine has been utilized as coligand. It binds the metal center in a N, N-donor chelating fashion. The chloro-complexes (**1** and **2**) have been obtained by treating the dimeric ruthenium precursor with the 2-ampy ligand and the compounds were obtained as monomeric cationic form as per previous literature (Scheme 2.1) [18].



**Scheme 2.1:** Synthesis of complexes **1**  $[Ru(\eta^6\text{-}p\text{-cym})(2\text{-ampy})Cl]PF_6$ , **2**  $[Ru(\eta^6\text{-benzene})(2\text{-ampy})Cl]SO_3CF_3$ , **3**  $[Ru(\eta^6\text{-}p\text{-cym})(2\text{-ampy})PPh_3](PF_6)_2$ , **4**  $[Ru(\eta^6\text{-benzene})(2\text{-ampy})PPh_3]SO_3CF_3$

Treatment of the chloro-complexes with triphenylphosphine furnished the phosphorus coordinated complexes upon the addition of excess counter anion (**3** and **4**). The counterions *viz.* hexafluorophosphate and triflate have been chosen for this study as these anions provide a high solubility in most of the

polar organic solvents, higher thermal stability, relatively low reactivity with atmospheric moisture and its non-coordinative tendency [28]. All the complexes are found to be soluble in methanol, DMSO, DMF and sparingly soluble in water, acetone, dichloromethane, chloroform, acetonitrile, and benzene. All the complexes are yellow to brown in color, air-stable, and non-hygroscopic. They were characterized by different spectroscopic methods.  $^1\text{H}$  NMR spectra of complexes **1-4** show significant peaks for aromatic protons in the 5.31-9.84 ppm region. Complexes **1** and **3** display peaks in the region 5.31-5.86 ppm for the p-cymene ring protons and 2.16-2.13, 2.36 and 1.11-1.02 ppm for the side chain of p-cymene moiety. Complexes **2** and **4** show a singlet peak at 5.92 ppm for benzene ring protons (Figure 2.1- Figure 2.4) [29].

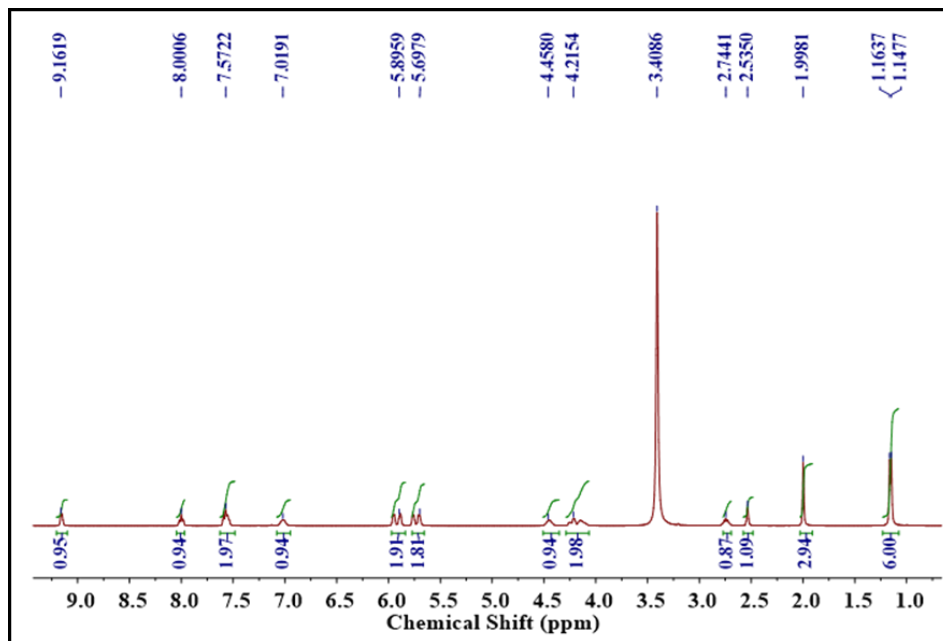


**Figure.2.1:**  $^1\text{H}$  NMR spectra of complex **1**

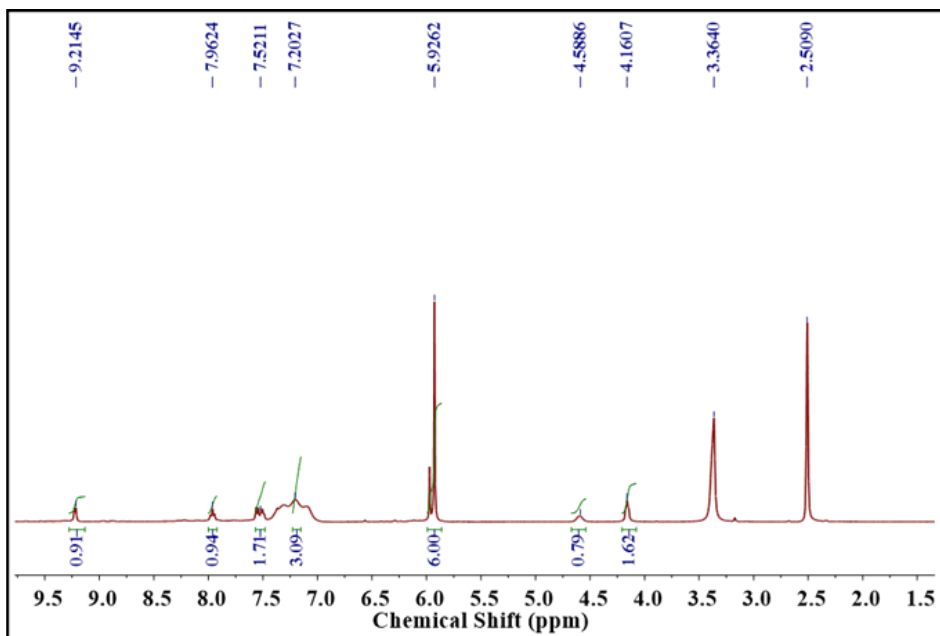


Figure.2.2:  $^1\text{H}$  NMR spectra of complex 2

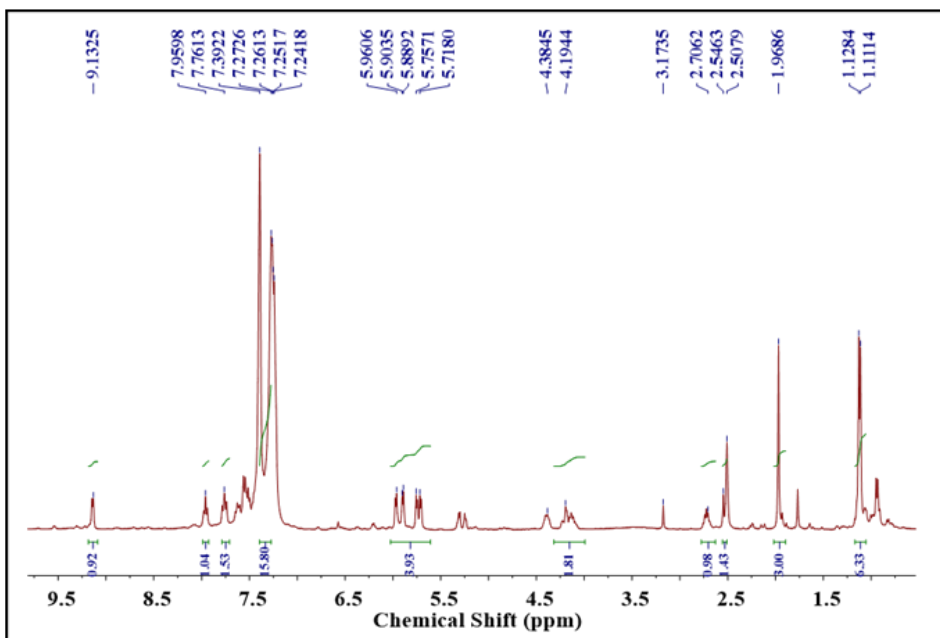
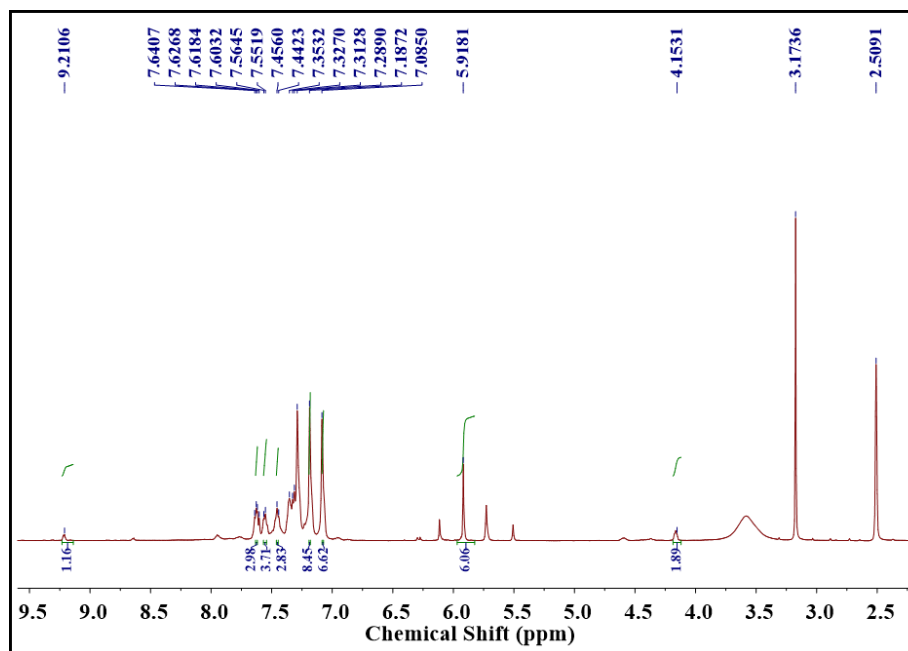
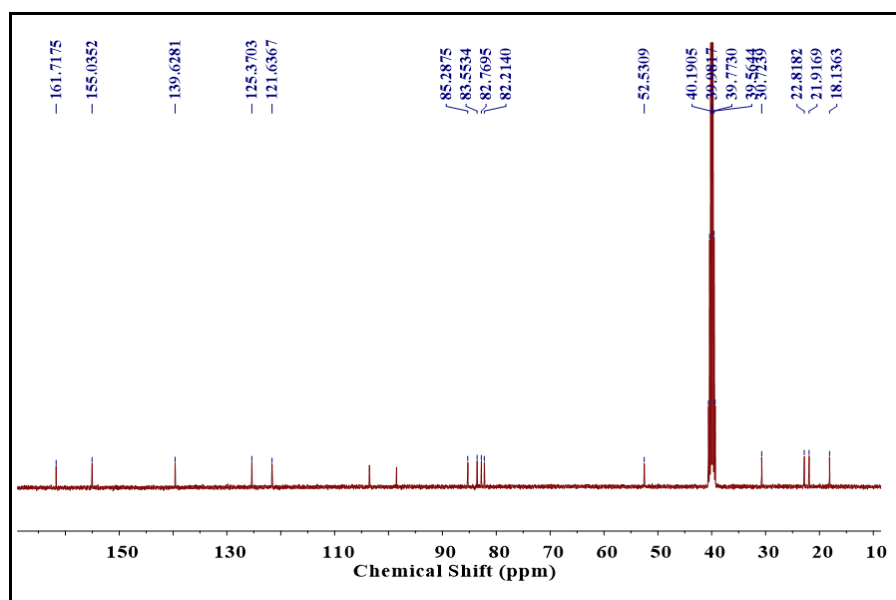


Figure.2.3:  $^1\text{H}$  NMR spectra of complex 3



**Figure.2.4:**  $^1\text{H}$  NMR spectra of complex **4**

The  $^{13}\text{C}$  spectra for complexes **1-4** also corroborate the proposed structure (Figure 2.5-Figure 2.8).



**Figure.2.5:**  $^{13}\text{C}$  NMR spectra of complex **1**

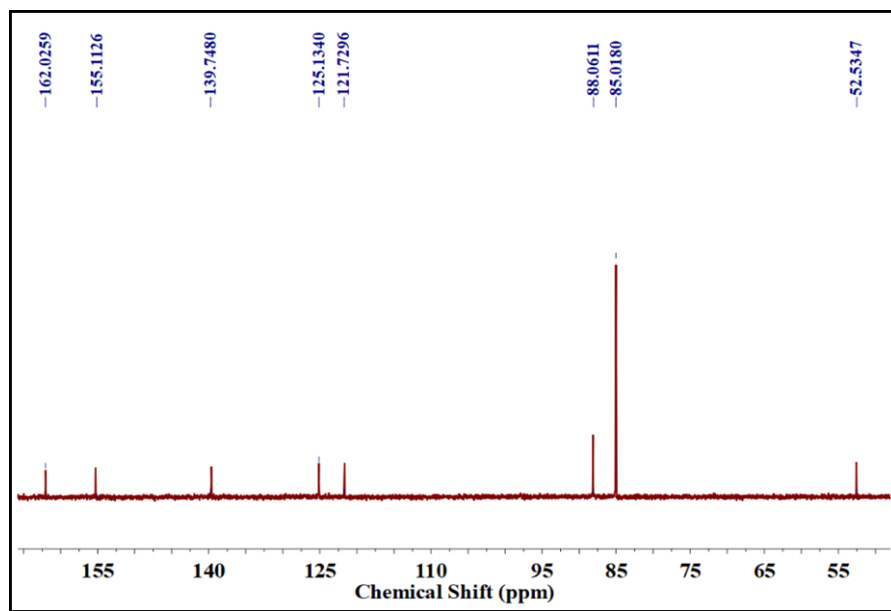


Figure.2.6:  $^{13}\text{C}$  NMR spectra of complex 2

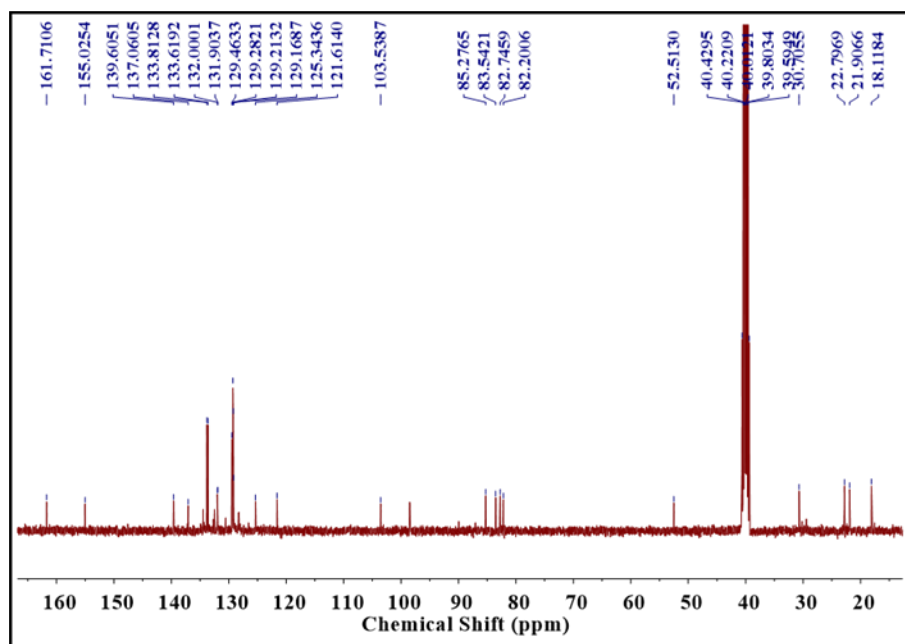
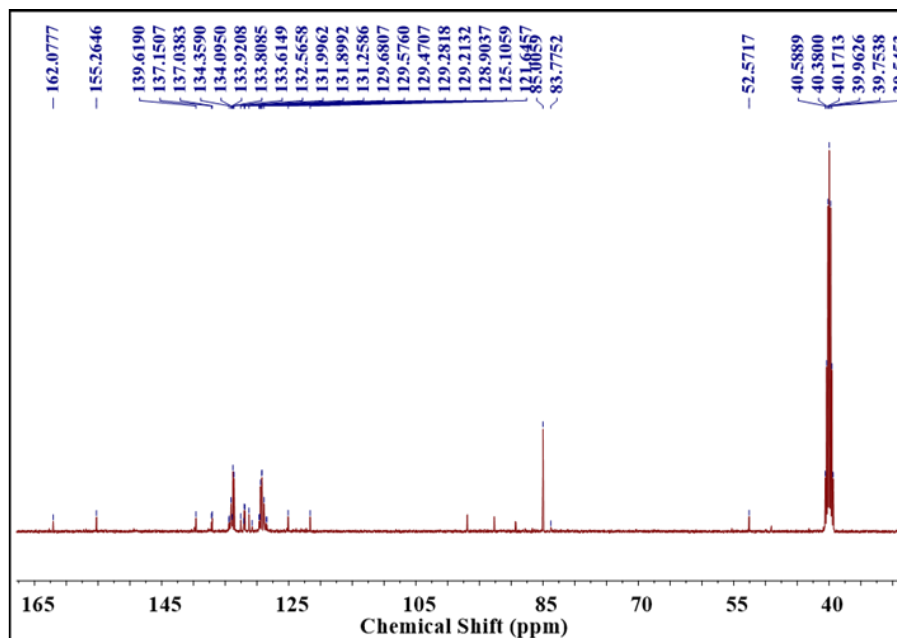
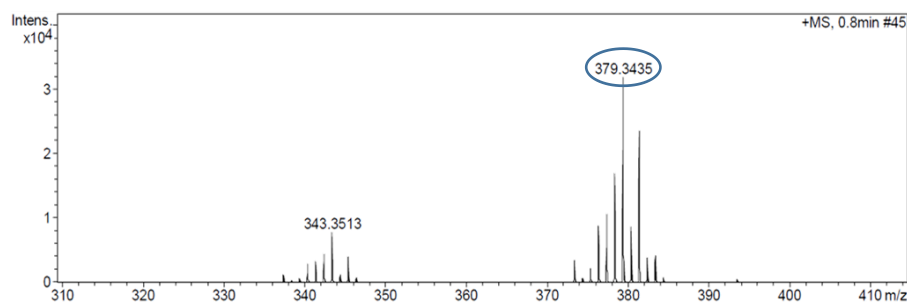


Figure.2.7:  $^{13}\text{C}$  NMR spectra of complex 3



**Figure.2.8:**  $^{13}\text{C}$  NMR spectra of complex **4**

The ESI-MS data reveal one major peak at 379.34 and 322.99 envelop indicating  $[\text{Ru}(\eta^6\text{-p-cymene})(2\text{-ampy})\text{Cl}]^+$ ,  $[\text{Ru}(\eta^6\text{-benzene})(2\text{-ampy})\text{Cl}]^+$  respectively, moiety after the release of the labile chlorido ligand in **1** and **2** confirming the proposed structures. For complexes **3** and **4**, major peaks come around at 302.10 and 275.06, confirming the presence of the proposed structures  $[\text{Ru}(\eta^6\text{-p-cymene})(2\text{-ampy})(\text{PPh}_3)]^{2+}$ ,  $[\text{Ru}(\eta^6\text{-benzene})(2\text{-ampy})(\text{PPh}_3)]^{2+}$ , respectively (Figure 2.9-Figure 2.12).



**Figure.2.9:** ESI-MS of complex **1**

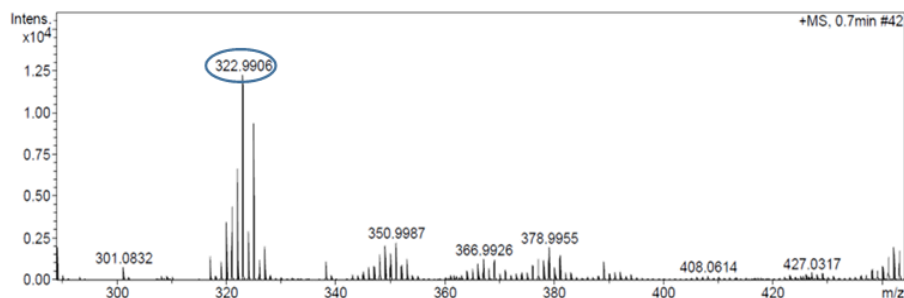


**Figure.2.10:** ESI-MS of complex 2

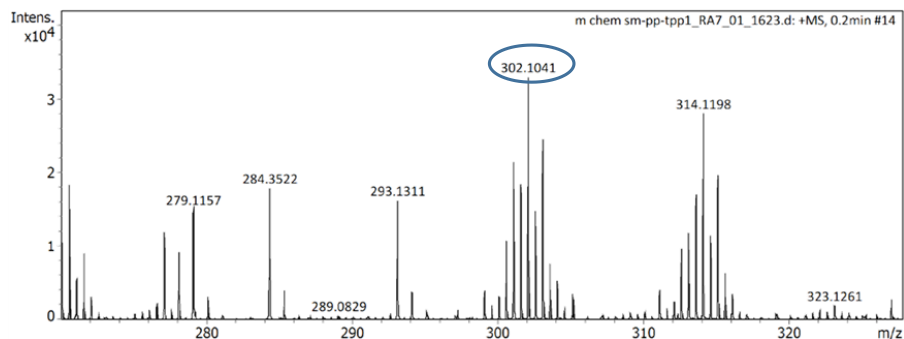


**Figure.2.11:** ESI-MS of complex 3

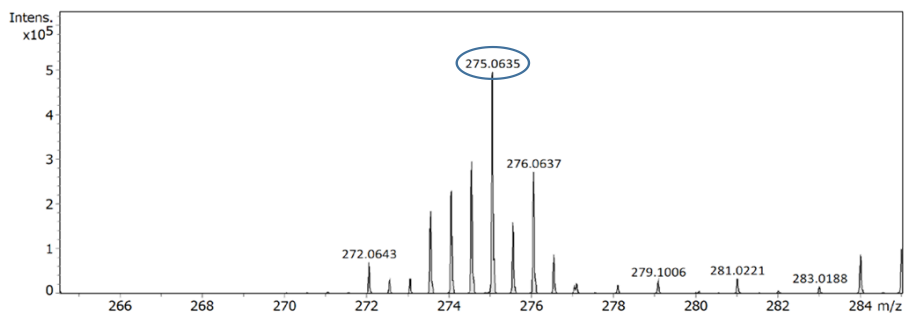


**Figure.2.12:** ESI-MS of complex 4

FTIR spectra of compounds **1-4** display characteristic bands for C=N (ring) stretching in the region of  $1560\text{-}1571\text{ cm}^{-1}$ . Complexes **1** and **2** give a characteristic band responsible for the metal halide (Ru-Cl) formation in the region of  $800\text{-}850\text{ cm}^{-1}$  (Figure 2.13) [30].

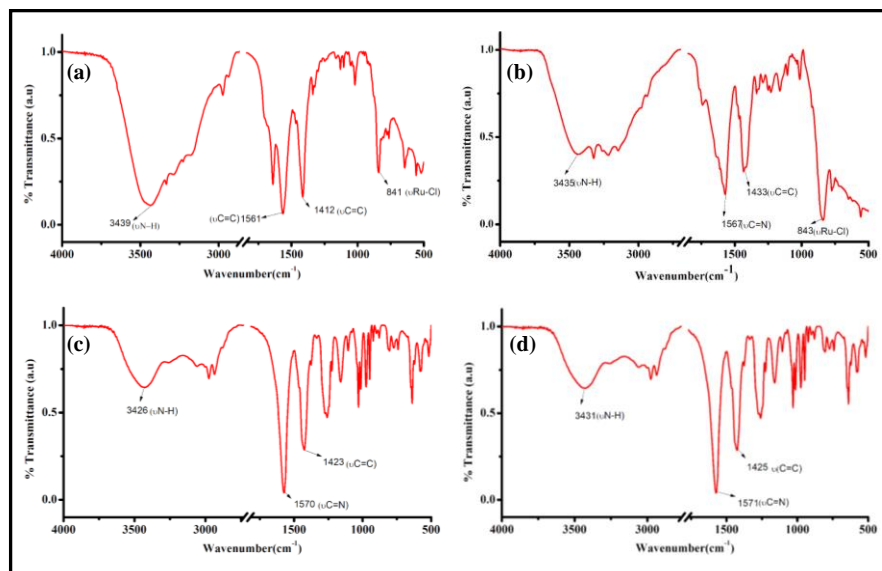


**Figure.2.13:** FTIR stretching frequencies (in KBr pallet) of (a) complex 1, (b) complex 2, (c) complex 3, and (d) complex 4, respectively

Structure of compounds **1** and **2** have been further confirmed by single crystal X-ray crystallography. Complexes **1** and **2** were crystallized in monoclinic and triclinic crystal arrangement having space group of  $P 1 21/n 1$  and  $P -1$ , respectively. Both the complexes possess a pseudo-octahedral geometry and the fluxional  $\pi$ -bonded arene ring occupies three coordination positions of the octahedron. In complexes **1** and **2**, the other two coordination sites are occupied by 2-aminomethyl pyridine ligand through N, N chelation. The sixth coordination position is occupied by the chloro ligand (Figure 2.14).

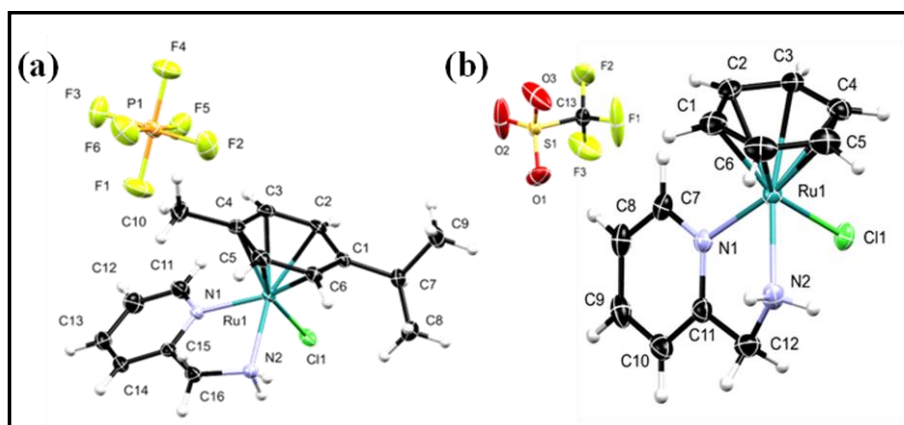


**Figure.2.14:** ORTEP diagram (50% thermal probability of ellipsoids) of (a) complex 1, and (b) complex 2, respectively

### 2.3.2 Stability study of the complexes

Investigation of the stability of the complexes in biological media is an important factor for the developing of the synthesized complexes as drug molecules [31,32]. All the complexes were dissolved in a 1% DMSO/PBS solution mixture, and their stability was monitored through UV-visible spectroscopy in a time period of 0, 24 and 48 hrs. No significant peak shift was observed in the absorption bands of the complexes, which clearly shows that complexes are stable in the biological medium. In biological studies, DMSO is a mainly used solvent for preparing metal complex stock solutions (Figure 2.15).

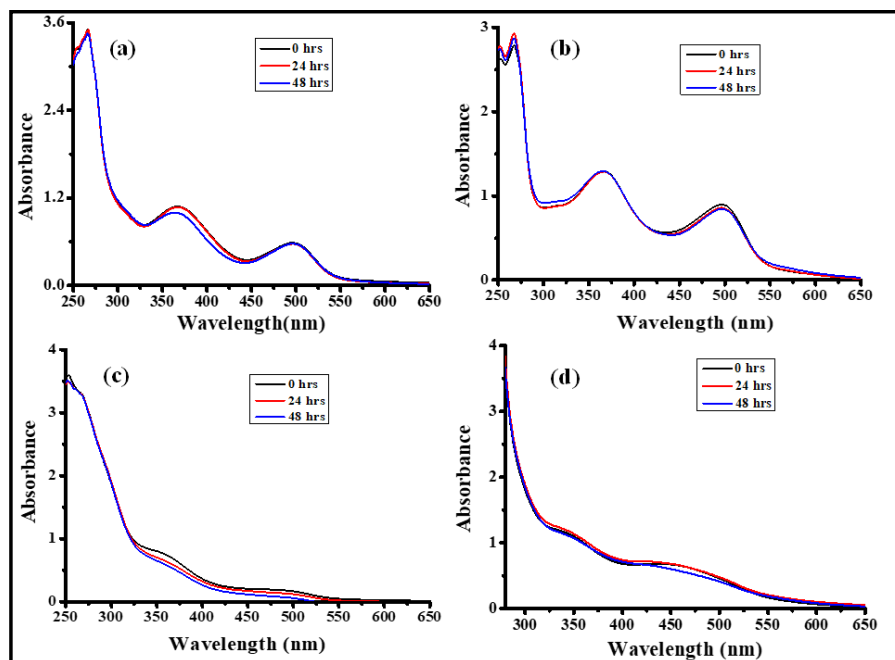


**Figure.2.15:** UV-visible spectra of complexes **1-4** in 1% DMSO-PBS mixture at a different time period 0, 24, and 48 hrs. (a) complex **1**, (b) complex **2**, (c) complex **3**, and (d) complex **4**

Therefore, the stability of complexes **3** and **4** was further confirmed through  $^1\text{H}$  NMR kinetics in DMSO- $d_6$  for 96 hrs with a time interval of 0, 24, 72, and 96 hrs, which shows no significant change in  $^1\text{H}$  NMR peaks for both complexes (Figure 2.16).

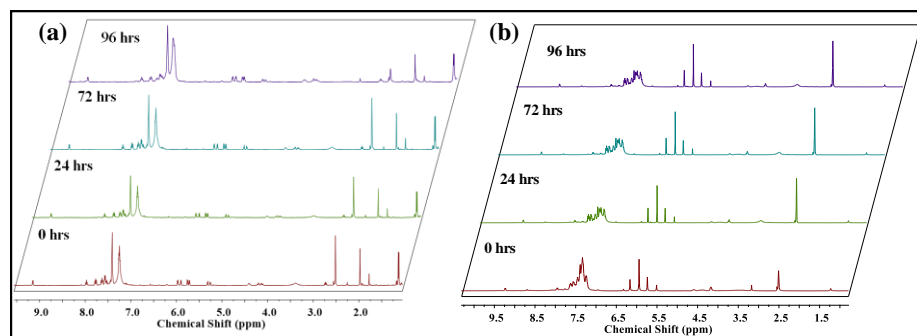


**Figure.2.16:** Time dependent  $^1\text{H}$  NMR spectra of (a) complex 3 and (b) complex 4 at different time interval 0, 24, 72, and 96 hrs.

### 2.3.3 Protein binding study

#### 2.3.3.1 Emission Spectra

Serum albumin protein (BSA or HSA) is the most abundant protein in the bloodstream, which helps in the transportation of biomolecules and drug molecules. Therefore, knowing the possible interactions between albumin proteins and drug molecules is always important. The existence of amino acids such as tryptophan, tyrosine, and phenylalanine are responsible for the intrinsic fluorescent nature of BSA and HSA [21,22]. Among the three amino acids, the intrinsic fluorescent nature of BSA and HSA is mainly observed because of tryptophan residues. Tryptophan quenching experiments were performed by fluorescence spectroscopy to investigate the binding ability of complexes **1-4** with proteins. In serum albumin protein (BSA and HSA), the tryptophan region and its localized domain are highly sensitive and as a consequence, in the presence of any external agent it can get easily disturbed and creates a change in the fluorescence intensity. To know the possible interactions with the ruthenium complexes fluorescence titration studies have been carried out using 10  $\mu\text{M}$  BSA/ HSA and varied concentrations of the compounds (0-100  $\mu\text{M}$ ) in the wavelength range of 290-500 nm ( $\lambda_{\text{ex}} = 280$  nm). Figure 2.17 and Figure 2.18 illustrate the decrease in the FL intensity of HSA/ BSA with the accumulation of metal complexes. A decrease in the FL intensity of proteins shows the interaction between proteins and metal complexes and this happens because of the energy transfer which takes place from the excited state of proteins to the metal complexes [33].

Fluorescence quenching data was obtained in terms of the Stern Volmer Constant ( $K_{SV}$ ), which is presented in Table 2.2. Compound **3** shows better interaction with the protein than any other complexes which might be due to the presence of methyl and isopropyl side chain group in the p-cymene ring and the incorporation of the  $PPh_3$  ligand, which can show better hydrophobic interactions *via* nonpolar residue in the protein chain pockets. Moreover, the bimolecular quenching constant  $K_q$  values have been obtained in the range of  $10^{12} \text{ M}^{-1}\text{s}^{-1}$ , indicating the involvement of static quenching [21].

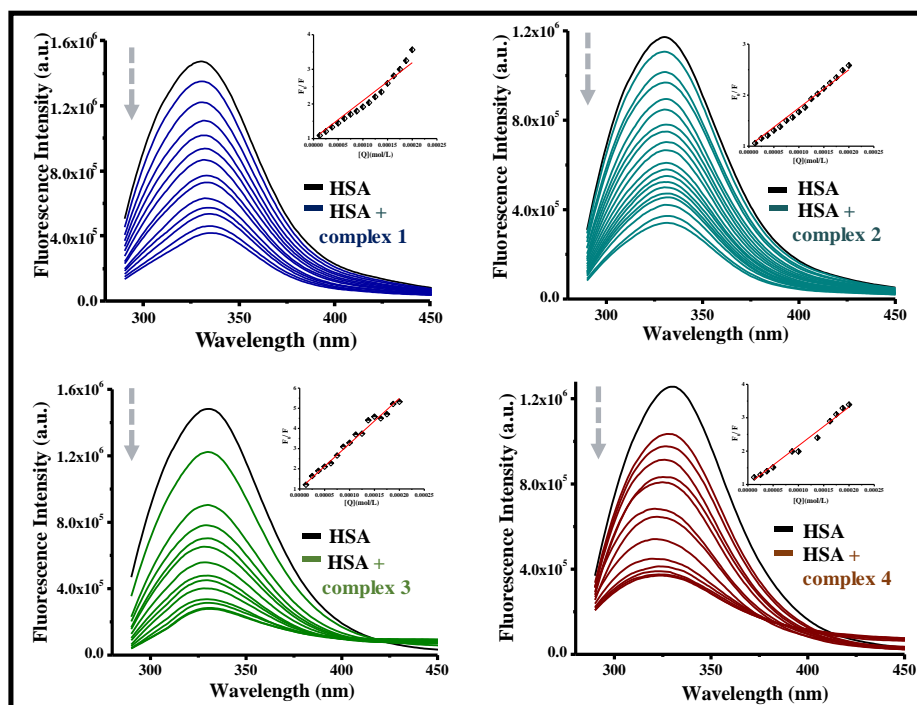


**Figure 2.17:** Fluorescence quenching spectra of HSA ( $10 \mu\text{M}$ ) at different concentrations ( $0\text{-}100 \mu\text{M}$ ) of complexes **1-4** at  $298 \text{ K}$ . Inset: Plots of  $F_0/F$  vs.  $[Q](\text{mol/L})$

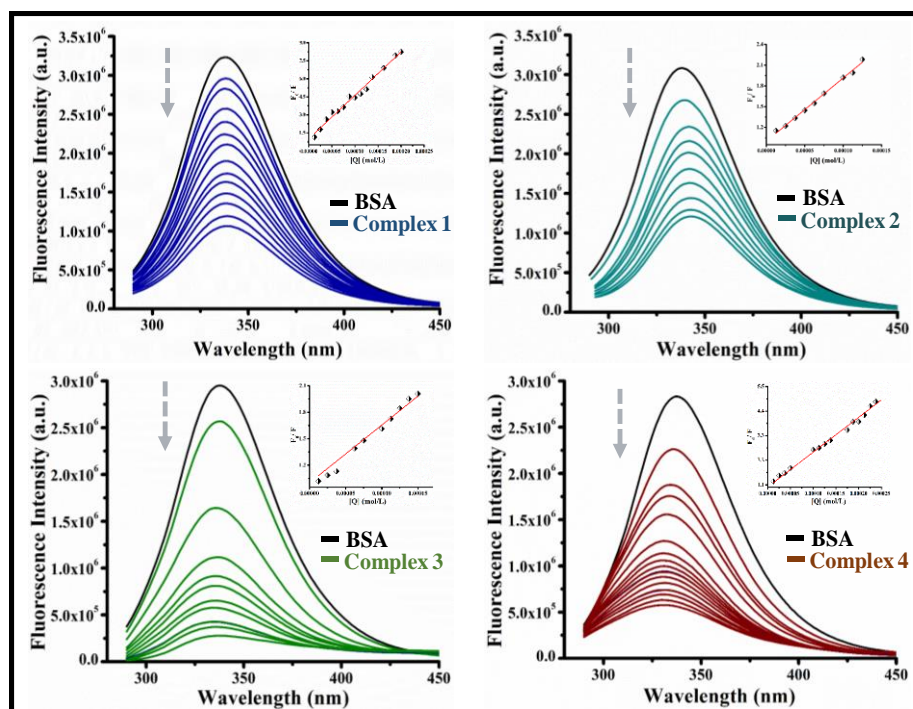


**Figure 2.18:** Fluorescence quenching spectra of BSA ( $10 \mu\text{M}$ ) at different concentrations ( $0\text{-}100 \mu\text{M}$ ) of complexes **1-4** at  $298 \text{ K}$ . Inset: Plots of  $F_0/F$  vs.  $[Q](\text{mol/L})$

**Table 2.2:** Parameters of SV constant, bimolecular quenching constant ( $K_q$ ), binding constant ( $K_a$ ) and number of binding site ( $n$ ) for HAS and BSA protein

System	$K_{sv} (\text{M}^{-1})$	$K_q (\text{M}^{-1}\text{s}^{-1})$	$K_a (\text{M}^{-1})$	$n$
<b>1-HSA</b>	$8.0 \times 10^3$	$1.2 \times 10^{12}$	$3.2 \times 10^4$	1.1
<b>2-HSA</b>	$7.4 \times 10^3$	$1.1 \times 10^{12}$	$1.9 \times 10^4$	1.1
<b>3-HSA</b>	$2.2 \times 10^4$	$3.5 \times 10^{12}$	$5.3 \times 10^4$	1.2
<b>4-HSA</b>	$7.7 \times 10^3$	$1.2 \times 10^{12}$	$3.3 \times 10^4$	1.1
<b>1-BSA</b>	$7.9 \times 10^3$	$1.2 \times 10^{12}$	$2.1 \times 10^4$	1.1
<b>2-BSA</b>	$6.5 \times 10^3$	$1.2 \times 10^{12}$	$1.2 \times 10^4$	1.0
<b>3-BSA</b>	$3.6 \times 10^4$	$5.8 \times 10^{12}$	$3.3 \times 10^5$	1.1
<b>4-BSA</b>	$7.6 \times 10^3$	$1.0 \times 10^{12}$	$7.5 \times 10^3$	1.0

### 2.3.3.2 Circular dichroism (CD) spectral studies

CD spectroscopy is a highly reliable and sensitive technique to investigate the change in the secondary structure of proteins after interaction with metallodrugs. Figure 2.19 and Figure 2.20, represent the interaction of BSA and HSA with different complexes. A negative band at 235 nm is observable for BSA and HSA because of  $n \rightarrow \pi^*$  transition in bare proteins which is a characteristic band of  $\alpha$ -helical proteins [21]. Upon addition of complexes with gradual increase in concentration, the spectra display decrease in the negative ellipticity value of the characteristic band of  $\alpha$ -helix structure showing the extent of conformational changes in the protein structure. The result shows that changes in the percentage value of  $\alpha$ -helical content of proteins are higher in the case of treatment with complexes **1** and **3** than complexes **2** and complex **4**. This may be due to the presence of p-cymene ring which have isopropyl and methyl substituents making the system more hydrophobic and inducing greater interactions [34].

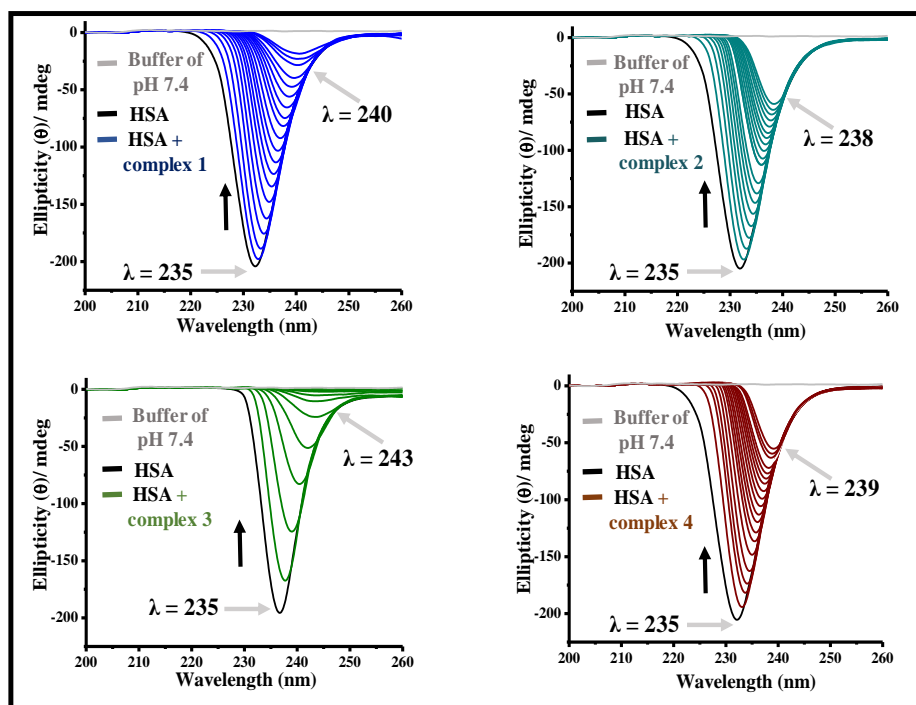


**Figure 2.19:** CD spectra of HSA ( $10 \mu\text{M}$ ) in absence or presence of complex in different concentration ( $0\text{-}100 \mu\text{M}$ ) at pH  $\sim 7.4$

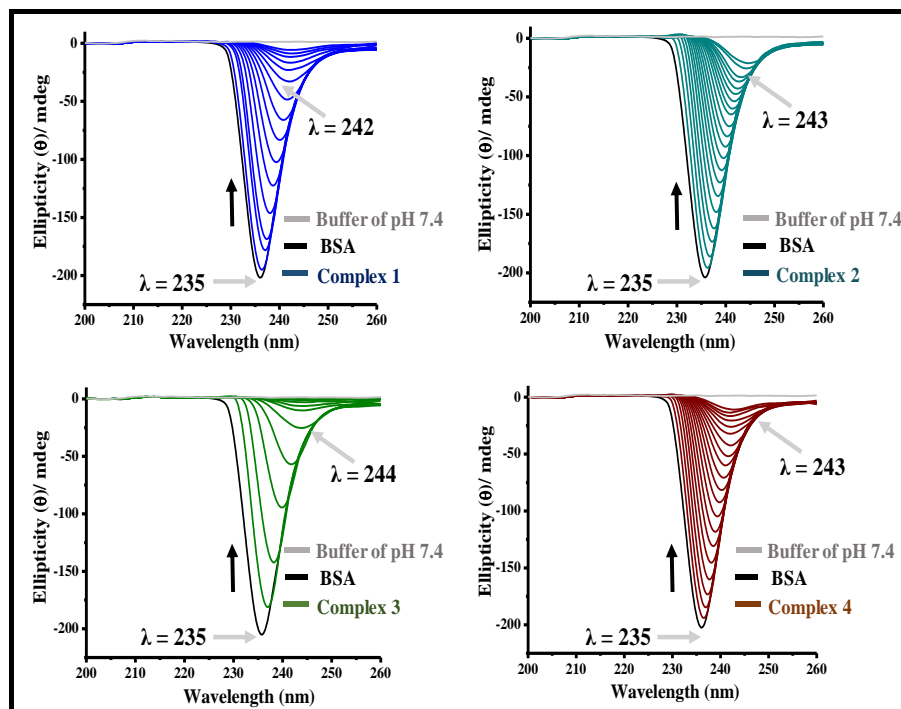


**Figure 2.20:** CD spectra of BSA protein ( $10 \mu\text{M}$ ) in absence or presence of complex in different concentration ( $0\text{-}100 \mu\text{M}$ ) at  $\text{pH} \sim 7.4$

### 2.3.4 DNA binding study

#### 2.3.4.1 Electronic absorption spectroscopy

UV-vis spectroscopy is the most convenient and beneficial technique to know the mode of interaction of complexes **1-4** with DNA. This technique evidenced the DNA-complex interaction through changes in absorbance intensity and absorption band position. Figure 2.21 demonstrate change in absorption spectra of complexes **1-4** in the course of titration with the increasing amount of CT-DNA. After the addition of CT-DNA, spectra of complexes **1-4** show an increase in optical density at a particular wavelength along with blue shift ( $\sim 9$  nm). An increase in the absorption intensity in a specific wavelength, i.e., hyperchromism in LMCT, was observed by the assemblage of DNA at complexes **1-4**. DNA absorption spectra of complexes **1-4** represent the hyperchromic tendency, which suggests non-intercalative binding between DNA and the complexes [35]. Furthermore, appreciable change in the band position, i.e., blue shift, exhibits a strong groove binding nature of complexes. This suggests that these complexes bind to DNA electrostatically *via* external

contact (surface binding having strong intercalative interactions) with the DNA duplex. The Benesi-Hildebrand equation is utilized to determine the intrinsic binding constant  $K_b$  values, which quantified the binding strength of complexes **1-4** with DNA (Table 2.3).

$$\frac{[\text{DNA}]}{(\varepsilon_a - \varepsilon_f)} = \frac{[\text{DNA}]}{(\varepsilon_b - \varepsilon_f)} + \frac{1}{K_b(\varepsilon_b - \varepsilon_f)}$$

where  $[\text{DNA}]$  is the concentration of DNA in base-pairs,  $\varepsilon_a$  is the apparent extinction coefficient calculated using absorbance/  $[\text{complex}]$ ,  $\varepsilon_f$  is the extinction coefficient of the complex in its free form, and  $\varepsilon_b$  is the extinction coefficient of the complex in the bound form. A slope value of  $1/(\varepsilon_b - \varepsilon_f)$  and an intercept of  $1/K_b(\varepsilon_b - \varepsilon_f)$  was determined by a straight line fitting using above equation. The ratio of slope to intercept gives the value of  $K_b$ .

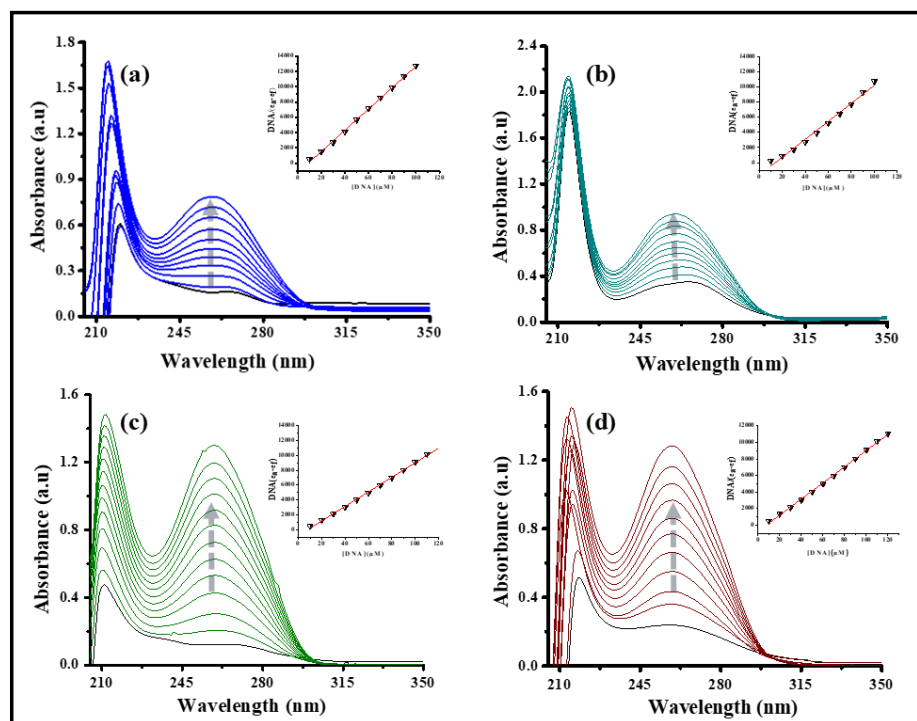


**Figure 2.21:** Electronic absorption spectra of only complexes **1-4** and with addition of CT-DNA. (a) complex **1**, (b) complex **2**, (c) complex **3**, and (d) complex **4**. Inset: Plots of  $[\text{DNA}]$  vs.  $[\text{DNA}]/\varepsilon_a - \varepsilon_f$  for the titration of CT-DNA with the complexes

**Table 2.3:** The values of intrinsic binding constant ( $K_b$ ) for the interaction between complexes and DNA

System	Wavelength (nm)	$K_b$ ( $M^{-1}$ )
Complex 1	265	$8.8 \times 10^4$
Complex 2	267	$1.7 \times 10^4$
Complex 3	269	$1.3 \times 10^5$
Complex 4	262	$1.0 \times 10^5$

#### 2.3.4.2 Competitive fluorometric DAPI displacement assay

Competitive fluorometric DAPI displacement assay were carried out to validate the binding mode of complexes **1-4** with DNA. DAPI is a blue fluorescent dye that preferentially binds to the AT-riched minor groove region of DNA. Adding a solution of DNA molecules into the DAPI solution increases FL intensity of DAPI dye by thirty-fold [36]. The emission spectra of DNA-DAPI solution with increasing concentrations of complexes **1-4** has been recorded. A noticeable decrease in the FL intensity of the DNA bound DAPI complex was observed upon the addition of complexes **1-4** as the DAPI molecules are displaced from their DNA binding sites (Figure 2.22). By using the Stern-Volmer equation, the linear Stern-Volmer quenching constant ( $K_{sv}$ ), bimolecular quenching rate constant ( $K_q$ ) and apparent binding constant value ( $K_a$ ) are calculated (Table 2.4) [37]. The magnitude of calculated values of  $K_{sv}$  is in the order of  $10^4$  for complex **3** and complex **4**, which indicates that complexes have good quenching efficiency and a remarkable degree of binding to DNA.

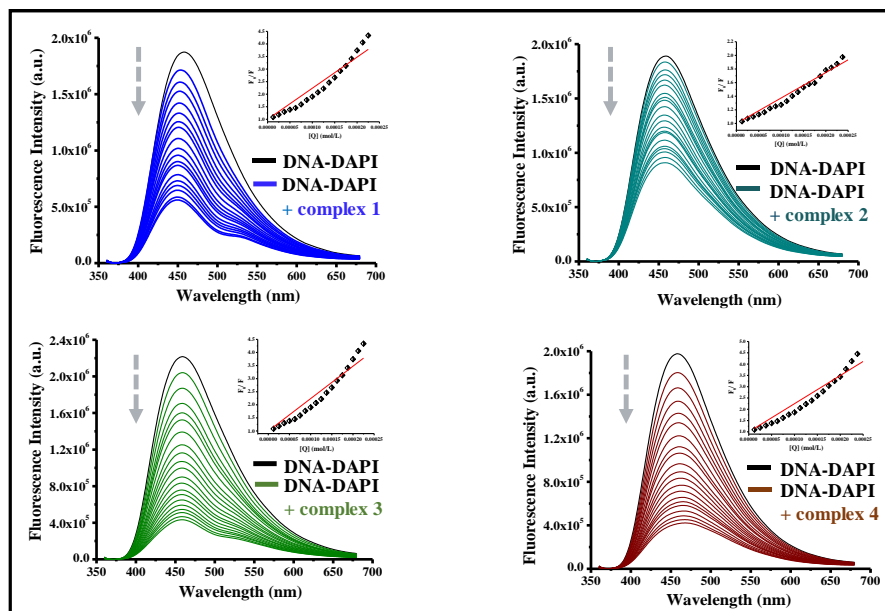


**Figure 2.22:** Fluorescence quenching spectra of DNA (0-100  $\mu\text{M}$ ) at gradually addition of complexes **1-4** at 298 K. Inset: Plots of  $F_0/F$  vs.  $[Q](\text{mol/L})$  for the titration of DNA with the complexes

**Table 2.4:** Absorption and emission spectral parameters of SV constant, bimolecular quenching constant, apparent binding constant for CT-DNA

Complex	$K_{sv} (\text{M}^{-1})$	$K_q (\text{M}^{-1}\text{s}^{-1})$	$K_a (\text{M}^{-1})$	$n$
<b>1</b>	$7.1 \times 10^3$	$1.1 \times 10^{12}$	$1.3 \times 10^6$	1.8
<b>2</b>	$3.5 \times 10^3$	$5.6 \times 10^{11}$	$1.5 \times 10^4$	1.1
<b>3</b>	$1.2 \times 10^4$	$1.9 \times 10^{12}$	$1.3 \times 10^5$	1.2
<b>4</b>	$1.2 \times 10^4$	$1.7 \times 10^{12}$	$7.5 \times 10^4$	1.2

### 2.3.5 *In vitro* cytotoxicity assay

#### 2.3.5.1 MTT assay

The preliminary DNA and protein binding studies motivated us to check the potency of our complexes as a growth inhibitor for various cancerous cell lines. To know the anticancer efficacy of our complexes, a colorimetric MTT assay was performed against HeLa and MCF-7 cancer cell lines that measure the mitochondrial dehydrogenase activity as an indication of cell viability. The

cytotoxic properties of complexes were analyzed with the help of a cell viability curve and with different concentration values of the complexes (0-100  $\mu\text{M}$ ). Figure 2.23 reveals that complexes **3** and **4** show better cytotoxicity against tested cancerous cell lines than complexes **1** and **2**. Complex **3** has shown the most cytotoxic effect against MCF-7 and HeLa cells. The Presence of triphenylphosphine ligand in the coordination sphere might help to increase the anticancer nature of compounds [38,39]. Furthermore, the presence of p-cymene group in the complex gives stronger hydrophobic interaction with targeted biomolecules. Complex **3** display  $\text{IC}_{50}$  values as low as  $3.41 \pm 2.87 \mu\text{M}$  and  $9.38 \pm 7.60 \mu\text{M}$  toward MCF-7 and HeLa cancer cell line, respectively. The cytotoxicity against normal cell line HEK 293 is found to be much lower as complexes **1-4** show much high  $\text{IC}_{50}$  values in the case in comparison to the cancerous cell lines. This results indicate that the activities of the complexes are the cancerous cell-specific (Table 2.5).

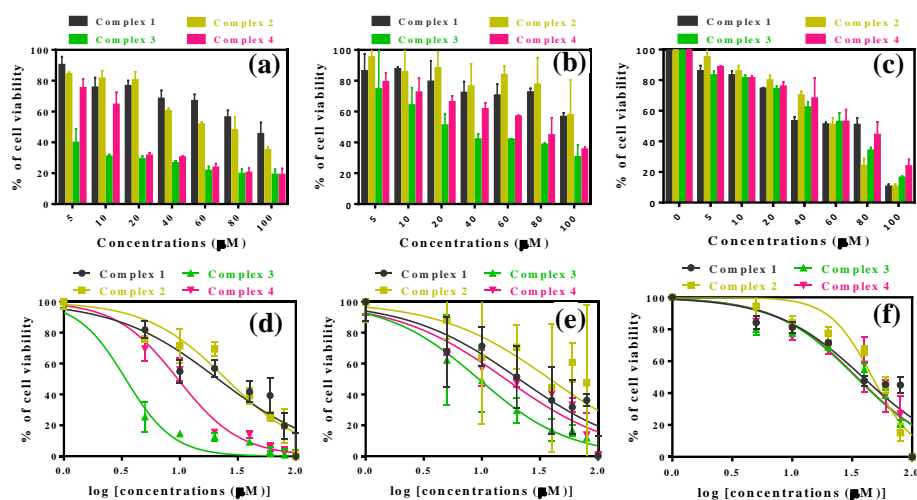


**Figure 2.23:** (a) Percentage of cell viability of all compounds against MCF-7 cell line (b) HeLa cell line (c) HEK 293 (normal cell line). Normalized log of concentrations of the compound doses and corresponding cell viabilities for respectively cancer cell lines (d) MCF-7 (e) HeLa cells (f) HEK 293 (normal cell line)

**Table 2.5:** *In vitro* cytotoxicity studies of synthesized complexes against HeLa and MCF-7 cancer cell line and comparison with HEK 293 (normal cell line) for 24 hrs incubation.  $IC_{50}$  values are in  $\mu M$

Complex	HeLa	MCF-7	HEK 293
1	$20.88 \pm 6.71$	$21.30 \pm 2.23$	$38.78 \pm 2.23$
2	$38.49 \pm 10.84$	$25.12 \pm 3.65$	$46.61 \pm 3.28$
3	$9.38 \pm 7.60$	$3.41 \pm 2.87$	$34.03 \pm 2.38$
4	$15.99 \pm 3.87$	$9.61 \pm 3.46$	$34.69 \pm 5.01$

### 2.3.6 Catalytic Oxidation of NADH

In various biocatalyzed processes, coenzyme nicotinamide adenine dinucleotide (NADH) and its oxidized form  $NAD^+$  maintain cellular metabolism, and the couple is also involved in numerous intracellular redox reactions [40]. The ratio between its oxidized ( $NAD^+$ ) and reduced (NADH) forms remains the central balance system for the redox status of the cells. A significant shift in the normal ratio of the oxidized and reduced form changes the cell redox balance and alters the cell metabolism, leading to cell malfunction. As catalysts was regulating the intracellular  $NAD^+/NADH$  ratio of cancerous cells, so to externally influence the redox balance can provide an alternative strategy for the treatment of cancer. Previously it was reported that half-sandwich Ir(III) and Ru(II) anticancer complexes can accept a hydride from NADH and promote the production of ROS, thus providing a pathway to an oxidant mechanism of action [41]. Herein, the catalytic activities of the synthesized complexes **1-4** are evaluated for NADH oxidation by UV-Vis spectroscopy. NADH ( $100 \mu M$ ) was taken as a control and was incubated with drug molecules in the solution of 5% MeOH and 95%  $H_2O$ . The change in the characteristic absorption peak of NADH at 339 nm during the reaction between complexes ( $1 \mu M$ ) and NADH ( $100 \mu M$ ) was observed and it was found to decreases slowly with increasing time intervals. This observation suggests the gradual conversion of NADH to  $NAD^+$  as  $NAD^+$  does not show any absorption peak at 339 nm (Figure 2.24). With the help of a change in UV-Vis absorption

spectra, the turnover numbers (TONs) for complexes **1-4** (Figure 2.25) are obtained. The result shows that all the ruthenium compounds are quite capable of catalyzing the oxidation of NADH to NAD<sup>+</sup>. The probable mechanism for oxidative catalytic conversion of NADH to NAD<sup>+</sup> by Ru(II) complexes **1-4** involves the transfer of hydride from NADH to the Ru(II) center and the formation of kinetically favorable six membered ring transition state. It happens *via* a ring slippage mechanism, creating a vacant hydride coordination site [42]. A plausible mechanism has been proposed for complex **1** having the best TON value (Scheme 2.2). UV-Vis data demonstrates that all complexes can accept an NADH hydride. The extent of conversion of NADH to NAD<sup>+</sup> depends not only on the arene ring but also on the lability of the leaving group [43]. Para-cymene ring shows faster conversion than benzene ring due to the presence of strong electron donating methyl substituent. Therefore, complex **1** showed the most rapid conversion among all the complexes and possessed the highest TON value. This clearly indicates the ruthenium complexes can disturb the balance of NAD<sup>+</sup>/NADH ratio and can provide a potential pathway to generate ROS and enhance the killing of cancer cells by an oxidative mechanism of action.

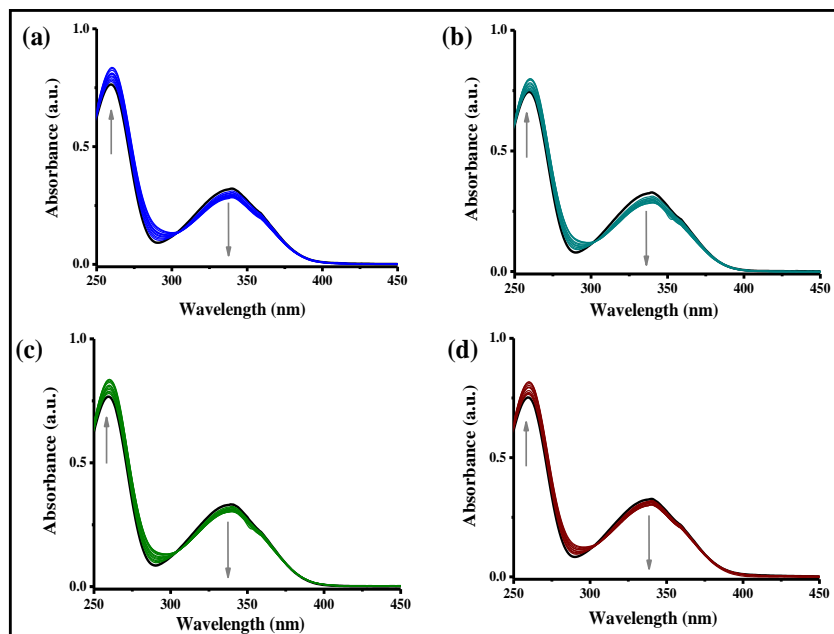


**Figure 2.24:** UV-visible spectra of complexes 1-4 ( $1 \mu\text{M}$ ) react with NADH ( $100 \mu\text{M}$ ). (a) complex 1, (b) complex 2, (c) complex 3, and (d) complex 4

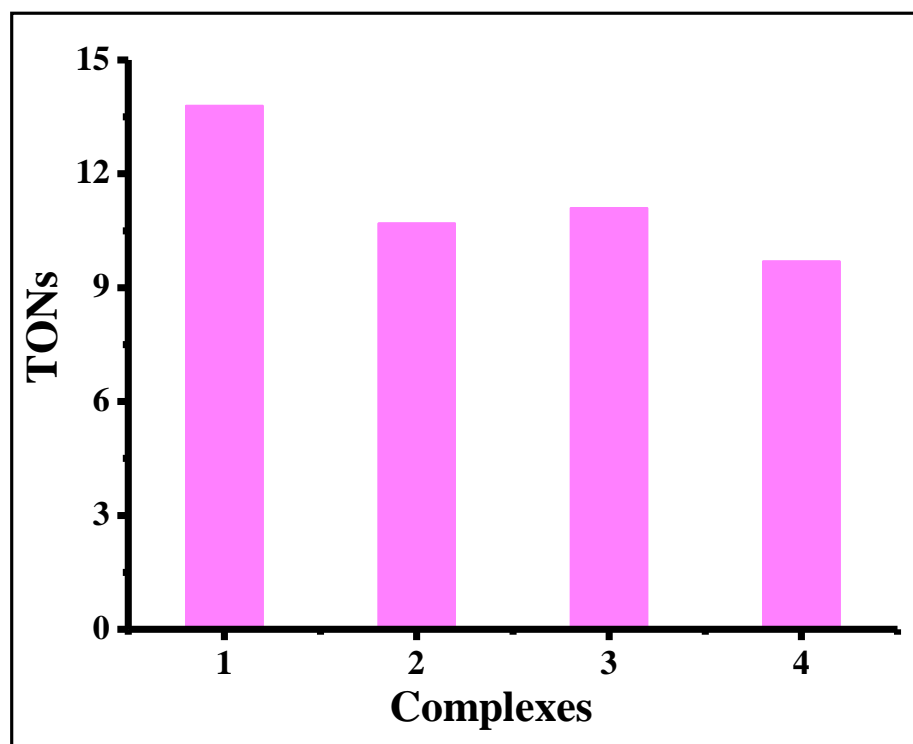
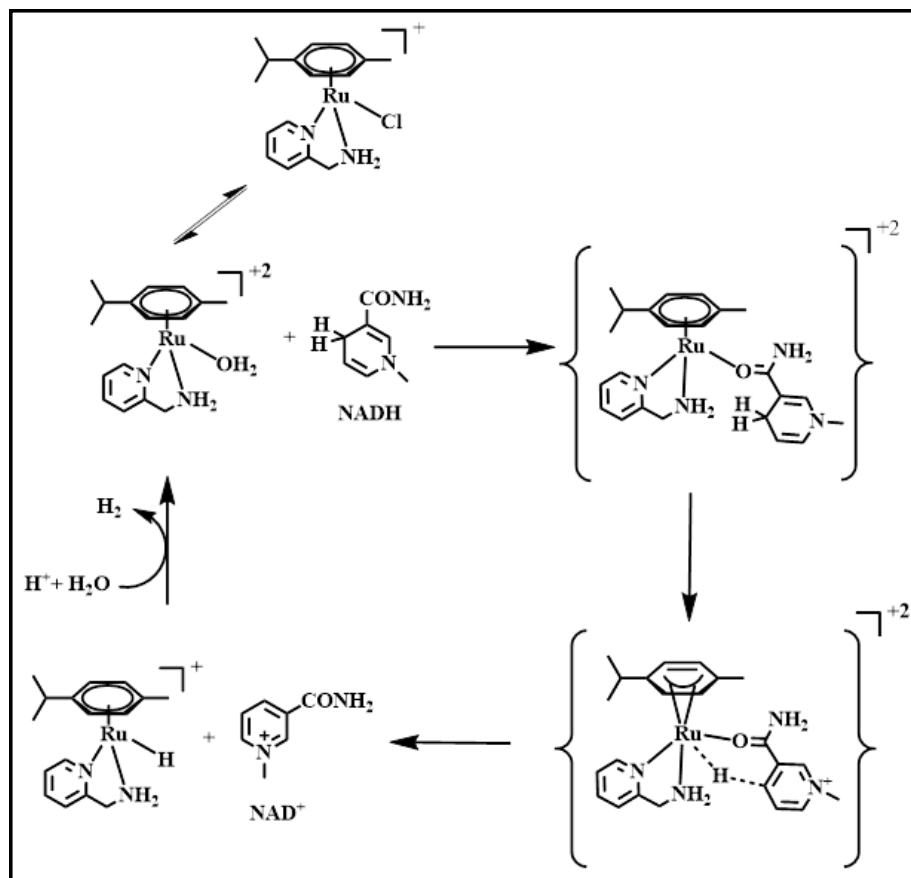


**Figure 2.25:** The turnover numbers (TONs) of complexes 1-4



**Scheme 2.2:** The probable mechanism of the catalytic oxidation of NADH to NAD<sup>+</sup> in presence of complex 1

### 2.3.7 Reactive Oxygen Species (ROS) generation

Reactive oxygen species (ROS) play valuable roles in regulating cell proliferation, signaling cell death, and mechanism of action of anticancer agents [44]. Uncontrolled and excessive production of reactive oxygen species (ROS) often leads to oxidative stress and can cause cell damage. Generation of high quantities of ROS cannot be tolerated by the cells as they have limited scavenging ability. This produces oxidative stress and damages various cellular components. Cancerous cells are often naturally under increased oxidative stress compared to normal cells because of abnormal cellular function [45]. Treatment with effective and selective anticancer agents can increase oxidative stress furthermore. Based on the previous reports of similar compounds which activate ROS generation, herein DCF-DA is utilized to investigate the potency of complexes **1-4** for inducing ROS generation in MCF-7 cells with the

concentration of the complexes with respective  $IC_{50}$  values. The data reveals that in treated cells there are significant increments in ROS generation in MCF-7 cells compared to untreated cells. Figure 2.26 represents the appearance of strong green fluorescence due to the overproduction of ROS when the cells are treated with **3** and **4**. The increased ROS levels in cells by the complexes might be related to the catalytic conversion of NADH to  $NAD^+$ .

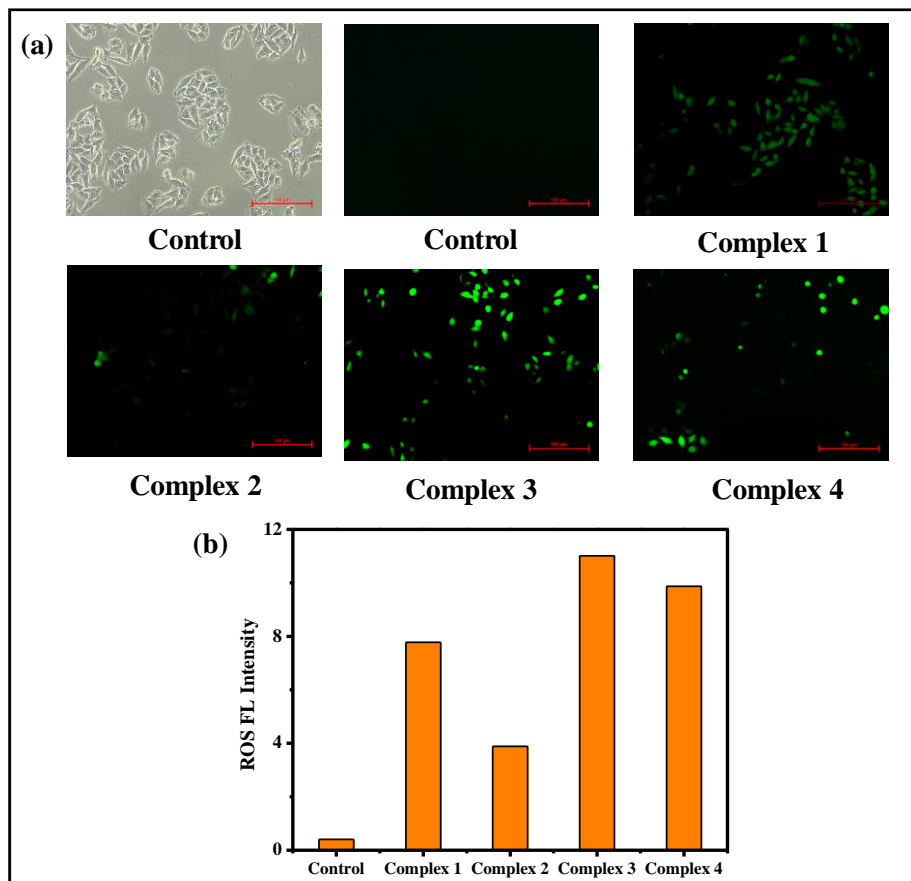


**Figure 2.26:** (a) Inverted microscopic image of ROS generation, treated and untreated MCF-7 cells through DCFH-DA fluorescence staining procedure.

(b) Fluorescence intensity graph of ROS

### 2.3.8 Apoptosis study with Hoechst staining method

It is reported that the significant morphological changes of nuclei, nuclear swelling, cell shrinkage or rounding, cytoplasmic blebbing, chromatin fragmentation, and condensation are the distinctive features of apoptotic cells [46]. These significant changes in cancer cells were evaluated by the Hoechst

staining method. As complex **3** and **4** show higher cytotoxicity, so MCF-7 cells are treated with **3** and **4** at their  $IC_{50}$  concentrations and the images of the cells are captured with the help of confocal microscopy. Figure 2.27 shows that treated cells are highly stained along with elongated filamentous morphological changes and condensed nuclei while untreated cells are evenly and lightly stained. After treatment, these morphological changes of nuclei are attributed to apoptosis in the treated cells.

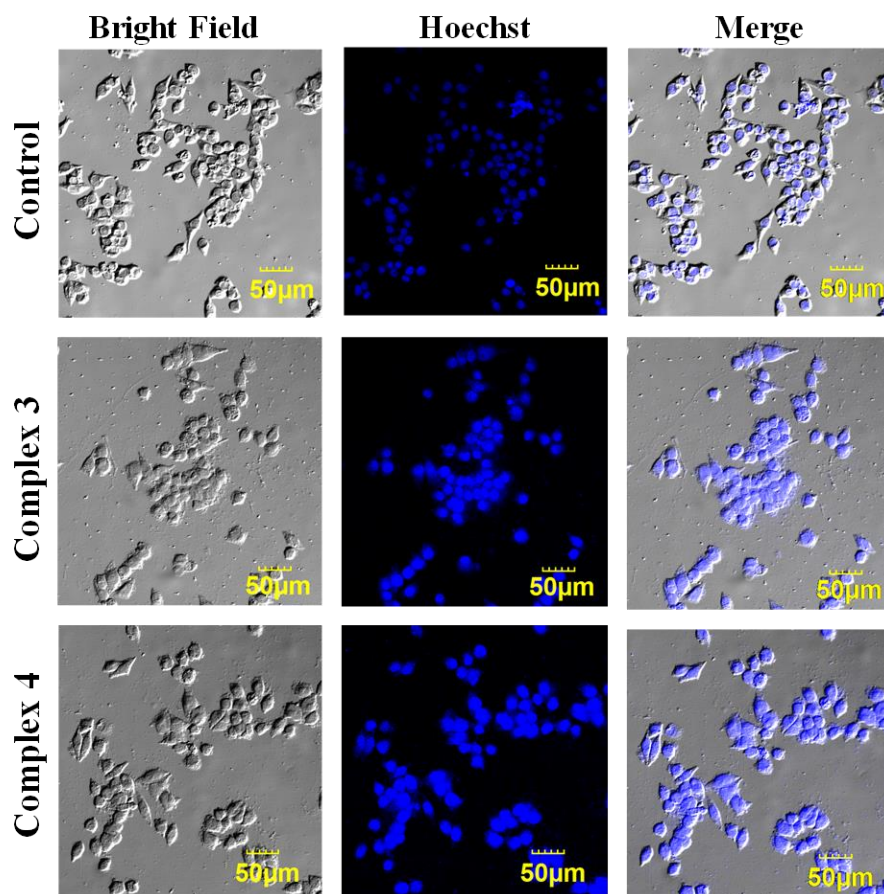


**Figure 2.27:** Confocal image of treated MCF-7 cells with complexes **3** and **4** stained by Hoechst dye

### 2.3.9 Density functional theory (DFT) Study

DFT study was performed to optimize the geometry and calculate the energies of HOMO and LUMO energy band gap and electronic communication of complexes **1-4**. Geometry parameters, calculated bond lengths and bond angles of complex **1** and **2** are found to be similar to those obtained from their single

crystal structures. Structures of complexes **3** and **4** have also been optimized by generating the expected structures (Figure 2.28). Gaussview 5.0 is utilized to generate contour plots for molecular orbitals of the complexes and frontier molecular orbital (HOMO and LUMO) energies for all the complexes are calculated (Figure 2.29). The interactions between DNA and complexes are compared for different complexes, considering the energy gap of the HOMO of DNA molecule and LUMO of the complexes [47]. It is well established that higher HOMO of the DNA favors transfers of “electron-cloud” to low-lying LUMO of the complexes indicating stronger interaction between DNA and the complex [48]. In this regard, it could be considered that the energy and population of LUMO of complexes **1-4** are the key factors to affect DNA binding. From Table 2.6 it is evident that the order of the energies of LUMO of complexes is  $\epsilon_L$  (**1**) >  $\epsilon_L$  (**2**) >  $\epsilon_L$  (**3**) >  $\epsilon_L$  (**4**) and  $\epsilon_{L+1}$  (**1**) >  $\epsilon_{L+1}$  (**2**) >  $\epsilon_{L+1}$  (**3**) >  $\epsilon_{L+1}$  (**4**) and  $\epsilon_{L+2}$  and  $\epsilon_{L+3}$  following the same order. It is noteworthy to mention that with an increase in the size of the arene ring (**1** and **3**) the LUMO energies increase because of the steric factor [49]. The theoretical calculations indicate the order of interaction of complexes **1-4** with DNA should be  $4 \sim 3 > 2 > 1$ . To some extent, these results are similar to the obtained experimental results. However, a number of other important factors, such as lipophilicity, H-bonding, variation of metal ions, rotational motions, etc., can also affect the interaction with DNA [50].

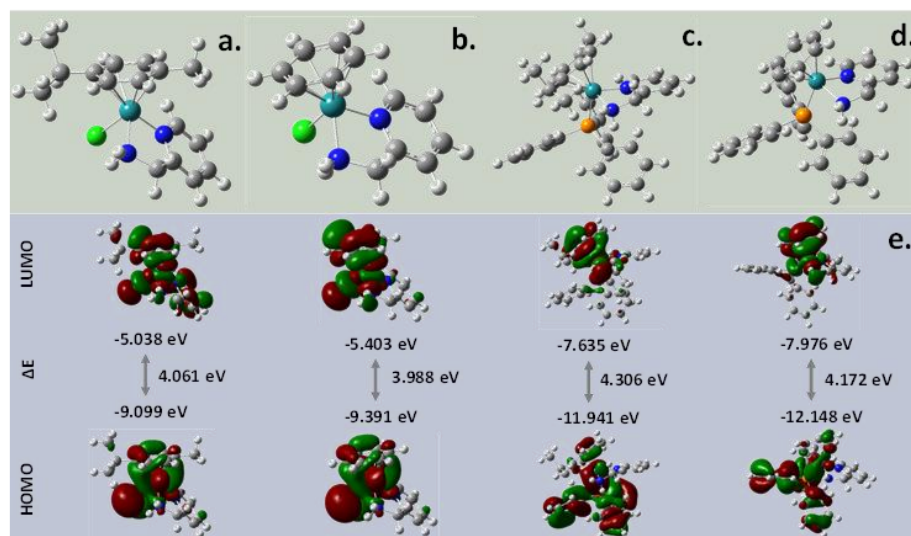


**Figure 2.28:** Frontier molecular orbitals of complexes and their HOMO-LUMO energy gaps (a) complex 1 (b) complex 2 (c) complex 3, and (d) complex 4

**Table 2.6.** HOMO, LUMO, and their population energy ( $\epsilon/\text{eV}$ ) of complexes 1-4.

Complexes	HOMO -3	HOMO -2	HOMO -1	HOMO	LUMO	LUMO +1	LUMO +2	LUMO +3
1	-10.412	-9.872	-9.411	-9.099	-5.038	-4.966	-4.675	-4.330
2	-10.689	-10.189	-9.694	-9.391	-5.403	-5.258	-4.981	-4.494
3	-12.188	-12.092	-12.037	-11.941	-7.635	-7.537	-7.354	-6.744
4	-12.374	-12.285	-12.210	-12.148	-7.976	-7.909	-7.547	-7.129

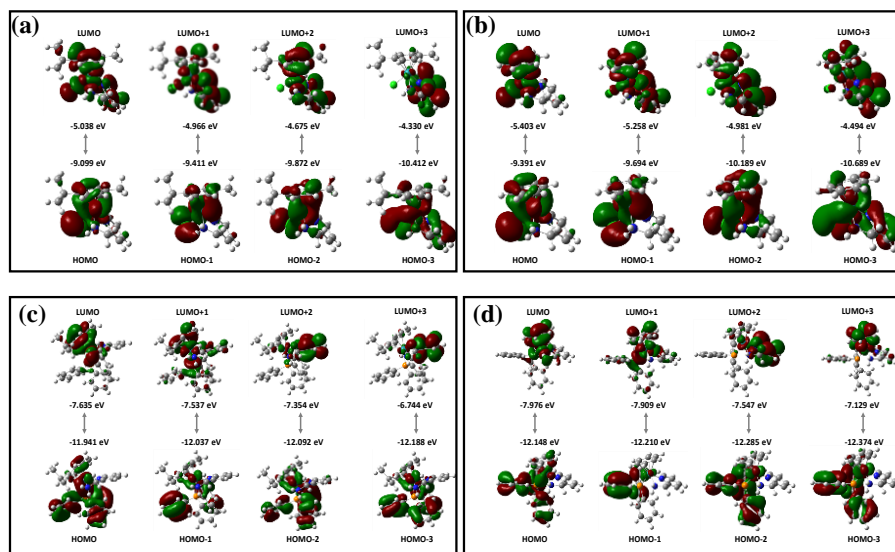


**Figure 2.29:** Frontier MOs contour plots of (a) complex 1 (b) complex 2 (c) complex 3 and (d) complex 4

## 2.4 Conclusion

In summary, four ruthenium(II) arene complexes **1-4** with 2-aminomethyl pyridine as coligand have been synthesized and characterized through different analytical tools. A combination of single crystal X-ray crystallography and DFT study confirms the structures with piano-stool geometry. Most of the complexes have shown binding towards biomolecules like serum albumin proteins and DNA. UV-Vis and DAPI displacement binding studies reveal the groove binding nature of the compounds. All the complexes have demonstrated significant cytotoxicity against HeLa and MCF-7 cancer cell lines with

compounds **3** and **4**, containing triphenylphosphine ligand, have shown better activity because of enhanced hydrophobicity in the compound. The compounds have shown specific activity against cancer cell lines as it remains non-cytotoxic against normal HEK cells. All the complexes have been found to be catalytically active to oxidize NADH to NAD<sup>+</sup>, which increases the ROS production within the cells and brings about apoptosis. Moreover, the Hoechst staining study confirms the signature morphological changes in cells due to apoptosis.

### **2.5 Declaration**

This chapter is adapted from Polyhedron., 2021, 207, 115379. (DOI: 10.1016/j.poly.2021.115379)

### **2.6 References**

- [1] Weilbaecher, K. N., Guise, T. A., & McCauley, L. K. (2011), Cancer to bone: a fatal attraction. *Nature Reviews Cancer*, 11(6), 411-425. (DOI: 10.1038/nrc3055).
- [2] Flight, M. H. (2011), A sweet blow for cancer cells. *Nature Reviews Drug Discovery*, 10(10), 734-734. (DOI: 10.1038/nrd3566).
- [3] Jeggo, P. A., Pearl, L. H., & Carr, A. M. (2016), DNA repair, genome stability and cancer: a historical perspective. *Nature Reviews Cancer*, 16(1), 35-42. (DOI: 10.1038/nrc.2015.4).
- [4] Weinberg, R. A. (1996). How cancer arises. *Scientific American*, 275(3), 62-70. (DOI: 10.1038/nrc.2015.4).
- [5] Tarabichi, M., Salcedo, A., Deshwar, A. G., Ni Leathlobhair, M., Wintersinger, J., Wedge, D. C., ... & Boutros, P. C. (2021), A practical guide to cancer subclonal reconstruction from DNA sequencing. *Nature methods*, 18(2), 144-155. (DOI: 10.1038/s41592-020-01013-2).
- [6] Carbone, M., Arron, S. T., Beutler, B., Bononi, A., Cavenee, W., Cleaver, J. E., ... & Yang, H. (2020), Tumour predisposition and cancer syndromes as models to study gene–environment interactions. *Nature Reviews Cancer*, 20(9), 533-549. (DOI: 10.1038/s41568-020-0265-y).

- [7] Gatti, A., Habtemariam, A., Romero-Canelón, I., Song, J. I., Heer, B., Clarkson, G. J., ... & Carcelli, M. (2018), Half-sandwich arene ruthenium (II) and osmium (II) thiosemicarbazone complexes: solution behavior and antiproliferative activity. *Organometallics*, 37(6), 891-899. (DOI: 10.1021/acs.organomet.7b00875).
- [8] Needham, R. J., Sanchez-Cano, C., Zhang, X., Romero-Canelón, I., Habtemariam, A., Cooper, M. S., ... & Sadler, P. J. (2017), In-Cell Activation of Organo-Osmium (II) Anticancer Complexes. *Angewandte Chemie International Edition*, 56(4), 1017-1020. (DOI: 10.1002/anie.201610290).
- [9] Soldevila-Barreda, J. J., Romero-Canelón, I., Habtemariam, A., & Sadler, P. J. (2015), Transfer hydrogenation catalysis in cells as a new approach to anticancer drug design. *Nature Communications*, 6(1), 6582. (DOI: 10.1038/ncomms7582).
- [10] Coverdale, J. P., Romero-Canelón, I., Sanchez-Cano, C., Clarkson, G. J., Habtemariam, A., Wills, M., & Sadler, P. J. (2018). Asymmetric transfer hydrogenation by synthetic catalysts in cancer cells. *Nature chemistry*, 10(3), 347-354. (DOI: 10.1038/nchem.2918).
- [11] Mandal, P., Kundu, B. K., Vyas, K., Sabu, V., Helen, A., Dhankhar, S. S., ... & Mukhopadhyay, S. (2018), Ruthenium (ii) arene NSAID complexes: inhibition of cyclooxygenase and antiproliferative activity against cancer cell lines. *Dalton transactions*, 47(2), 517-527. (DOI: 10.1039/C7DT03637J).
- [12] Banerjee, S., & Sadler, P. J. (2021), Transfer hydrogenation catalysis in cells. *RSC Chemical Biology*, 2(1), 12-29. (DOI: 10.1039/D0CB00150C).
- [13] Gatti, A., Habtemariam, A., Romero-Canelón, I., Song, J. I., Heer, B., Clarkson, G. J., ... & Carcelli, M. (2018), Half-sandwich arene ruthenium (II) and osmium (II) thiosemicarbazone complexes: solution behavior and antiproliferative activity. *Organometallics*, 37(6), 891-899. (DOI: 10.1021/acs.organomet.7b00875).
- [14] Thomas, J. C., & Peters, J. C. (2003), Zwitterionic and Cationic Bis (phosphine) Platinum (II) Complexes: Structural, Electronic, and Mechanistic Comparisons Relevant to Ligand Exchange and Benzene C-H Activation

Processes. *Journal of the American Chemical Society*, 125(29), 8870-8888. (DOI: 10.1021/ja0296071).

[15] Elmroth, S., Bugarcic, Z., & Elding, L. I. (1992), High-pressure stopped-flow study of kinetics and mechanism for complex formation reactions of tetraaquapalladium (II) and platinum (II) with thioethers in aqueous solution. *Inorganic Chemistry*, 31(17), 3551-3554. (DOI: 10.1021/ic00043a013).

[16] Prachayasittikul, S., Pingaew, R., Worachartcheewan, A., Sinthupoom, N., Prachayasittikul, V., Ruchirawat, S., & Prachayasittikul, V. (2017), Roles of pyridine and pyrimidine derivatives as privileged scaffolds in anticancer agents. *Mini Reviews in Medicinal Chemistry*, 17(10), 869-901. (DOI: 10.2174/1389557516666160923125801).

[17] Tian, M., Li, J., Zhang, S., Guo, L., He, X., Kong, D., ... & Liu, Z. (2017), Half-sandwich ruthenium (ii) complexes containing N<sup>^</sup> N-chelated iminopyridyl ligands that are selectively toxic to cancer cells. *Chemical Communications*, 53(95), 12810-12813. (DOI: 10.1039/C7CC08270C).

[18] Awasthi, M. K., & Singh, S. K. (2019), Ruthenium catalyzed dehydrogenation of alcohols and mechanistic study. *Inorganic Chemistry*, 58(21), 14912-14923. (DOI: 10.1021/acs.inorgchem.9b02691).

[19] (2013), SAINT V8.34A; Bruker AXS Inc.

[20] (2014), SHELXTL -2014/7; Bruker AXS Inc.

[21] Kundu, B. K., Pragti., Mobin, S. M., & Mukhopadhyay, S. (2020), Studies on the influence of the nuclearity of zinc (ii) hemi-salen complexes on some pivotal biological applications. *Dalton Transactions*, 49(43), 15481-15503. (DOI: 10.1039/D0DT02941F).

[22] Chhabra, V., Kundu, B. K., Ranjan, R., Mobin, S. M., & Mukhopadhyay, S. (2020), Coligand driven efficiency of catecholase activity and proteins binding study of redox active copper complexes. *Inorganica Chimica Acta*, 502, 119389. (DOI: 10.1016/j.ica.2019.119389).

[23] Das, M., Kundu, B. K., Tiwari, R., Mandal, P., Nayak, D., Ganguly, R., & Mukhopadhyay, S. (2018), Investigation on chemical protease, nuclease and catecholase activity of two copper complexes with flexidentate Schiff base

- ligands. *Inorganica Chimica Acta*, 469, 111-122. (DOI: 10.1016/j.ica.2017.09.013).
- [24] Kundu, B. K., Biswas, S., Mondal, A., Mazumdar, S., Mobin, S. M., & Mukhopadhyay, S. (2021), Unveiling the urease like intrinsic catalytic activities of two dinuclear nickel complexes towards the in situ syntheses of aminocyanopyridines. *Dalton Transactions*, 50(14), 4848-4858. (DOI: 10.1039/D1DT00108F).
- [25] Das, M., Biswas, A., Kundu, B. K., Charmier, M. A. J., Mukherjee, A., Mobin, S. M., ... & Mukhopadhyay, S. (2019), Enhanced pseudo-halide promoted corrosion inhibition by biologically active zinc (II) Schiff base complexes. *Chemical Engineering Journal*, 357, 447-457. (DOI: 10.1016/j.cej.2018.09.150).
- [26] Kundu, B. K., Ranjan, R., Mukherjee, A., Mobin, S. M., & Mukhopadhyay, S. (2019), Mannich base Cu (II) complexes as biomimetic oxidative catalyst. *Journal of Inorganic Biochemistry*, 195, 164-173. (DOI: 10.1016/j.jinorgbio.2019.03.023).
- [27] Yan, X. W., Xie, Y. R., Jin, Z. M., Hu, M. L., & Zhou, L. P. (2018), Three Arene-Ru (II) compounds of 2-halogen-5-aminopyridine: Synthesis, characterization, and cytotoxicity. *Applied Organometallic Chemistry*, 32(1), e3923. (DOI: 10.1002/aoc.3923).
- [28] Dixon, N. E., Lawrance, G. A., Lay, P. A., Sargeson, A. M., & Taube, H. (1990), Trifluoromethanesulfonates and Trifluoromethanesulfonato-O Complexes. *Inorganic Syntheses: Reagents for Transition Metal Complex and Organometallic Syntheses*, 28, 70-76. (DOI: 10.1002/9780470132593.ch16).
- [29] Mandal, P., Malviya, N., Da Silva, M. F. C. G., Dhankhar, S. S., Nagaraja, C. M., Mobin, S. M., & Mukhopadhyay, S. (2016), Fine tuning through valence bond tautomerization of ancillary ligands in ruthenium (II) arene complexes for better anticancer activity and enzyme inhibition properties. *Dalton Transactions*, 45(48), 19277-19289. (DOI: 10.1039/C6DT02969H).

- [30] Kundu, B. K., Mobin, S. M., & Mukhopadhyay, S. (2019), Mechanistic and thermodynamic aspects of a pyrene-based fluorescent probe to detect picric acid. *New Journal of Chemistry*, 43(29), 11483-11492. (DOI: 10.1039/C9NJ02342A).
- [31] Jeyalakshmi, K., Haribabu, J., Balachandran, C., Swaminathan, S., Bhuvanesh, N. S., & Karvembu, R. (2019), Coordination behavior of N, N', N''-trisubstituted guanidine ligands in their Ru-arene complexes: synthetic, DNA/protein binding, and cytotoxic studies. *Organometallics*, 38(4), 753-770. (DOI: 10.1021/acs.organomet.8b00702).
- [32] Subarkhan, M. K. M., Ramesh, R., & Liu, Y. (2016), Synthesis and molecular structure of arene ruthenium (II) benzhydrazone complexes: impact of substitution at the chelating ligand and arene moiety on antiproliferative activity. *New Journal of Chemistry*, 40(11), 9813-9823. (DOI: 10.1039/C6NJ01936F).
- [33] Annaraj, B., & Neelakantan, M. A. (2015), Synthesis, crystal structure, spectral characterization and biological exploration of water soluble Cu (II) complexes of vitamin B6 derivative. *European Journal of Medicinal Chemistry*, 102, 1-8. (DOI: 10.1016/j.ejmech.2015.07.041).
- [34] Kumar, R. R., Ramesh, R., & Malecki, J. G. (2018), Synthesis and structure of arene ruthenium (II) benzhydrazone complexes: Antiproliferative activity, apoptosis induction and cell cycle analysis. *Journal of Organometallic Chemistry*, 862, 95-104. (DOI: 10.1016/j.jorganchem.2018.03.013).
- [35] Anjomshoa, M., Fatemi, S. J., Torkzadeh-Mahani, M., & Hadadzadeh, H. (2014), DNA-and BSA-binding studies and anticancer activity against human breast cancer cells (MCF-7) of the zinc (II) complex coordinated by 5, 6-diphenyl-3-(2-pyridyl)-1, 2, 4-triazine. *Spectrochimica Acta Part A: Molecular and Biomolecular Spectroscopy*, 127, 511-520. (DOI: 10.1016/j.saa.2014.02.048).
- [36] Ramadevi, P., Singh, R., Jana, S. S., Devkar, R., & Chakraborty, D. (2015), Ruthenium complexes of ferrocene mannich bases: DNA/BSA interactions and cytotoxicity against A549 cell line. *Journal of Photochemistry*

and Photobiology A: Chemistry, 305, 1-10. (DOI: 10.1016/j.jphotochem.2015.02.010).

[37] Lakowicz, J. R. (Ed.). (2006), Principles of fluorescence spectroscopy. Boston, MA: springer US. (DOI: 10.1007/978-0-387-46312-4\_2).

[38] Delavault, A., Fronczek, F. R., Xu, W., & Srivastava, R. S. (2018), Ionic  $\eta^5$ -Cp-Ruthenium (II) complexes as potential anticancer agents. Journal of Organometallic Chemistry, 875, 29-34. (DOI: 10.1016/j.jorganchem.2018.08.027).

[39] Battogtokh, G., Choi, Y. S., Kang, D. S., Park, S. J., Shim, M. S., Huh, K. M., ... & Kang, H. C. (2018), Mitochondria-targeting drug conjugates for cytotoxic, anti-oxidizing and sensing purposes: current strategies and future perspectives. Acta Pharmaceutica Sinica B, 8(6), 862-880. (DOI: 10.1016/j.apsb.2018.05.006).

[40] Christensen, C. E., Karlsson, M., Winther, J. R., Jensen, P. R., & Lerche, M. H. (2014), Non-invasive in-cell determination of free cytosolic [NAD<sup>+</sup>]/[NADH] ratios using hyperpolarized glucose show large variations in metabolic phenotypes. Journal of Biological Chemistry, 289(4), 2344-2352. (DOI: 10.1074/jbc.M113.498626).

[41] Betanzos-Lara, S., Liu, Z., Habtemariam, A., Pizarro, A. M., Qamar, B., & Sadler, P. J. (2012), Organometallic ruthenium and iridium transfer-hydrogenation catalysts using coenzyme NADH as a cofactor. Angewandte Chemie, 124(16), 3963-3966. (DOI: 10.1002/ange.201108175).

[42] Liu, Z., Romero-Canelón, I., Qamar, B., Hearn, J. M., Habtemariam, A., Barry, N. P., ... & Sadler, P. J. (2014), The potent oxidant anticancer activity of organoiridium catalysts. Angewandte Chemie, 126(15), 4022-4027. (DOI: 10.1002/ange.201311161).

[43] Betanzos-Lara, S., Liu, Z., Habtemariam, A., Pizarro, A. M., Qamar, B., & Sadler, P. J. (2012), Organometallic ruthenium and iridium transfer-hydrogenation catalysts using coenzyme NADH as a cofactor. Angewandte Chemie, 124(16), 3963-3966. (DOI: 10.1002/ange.201108175).

- [44] Aggarwal, V., Tuli, H. S., Varol, A., Thakral, F., Yerer, M. B., Sak, K., ... & Sethi, G. (2019), Role of reactive oxygen species in cancer progression: molecular mechanisms and recent advancements. *Biomolecules*, 9(11), 735. (DOI: 10.3390/biom9110735).
- [45] Liou, G. Y., & Storz, P. (2010), Reactive oxygen species in cancer. *Free radical research*, 44(5), 479-496. (DOI: 10.3109/10715761003667554).
- [46] Schmid, I., Uittenbogaart, C., & Jamieson, B. D. (2007), Live-cell assay for detection of apoptosis by dual-laser flow cytometry using Hoechst 33342 and 7-amino-actinomycin D. *Nature Protocols*, 2(1), 187-190. (DOI: 10.1038/nprot.2006.458).
- [47] Liu, X. W., Li, J., Deng, H., Zheng, K. C., Mao, Z. W., & Ji, L. N. (2005), Experimental and DFT studies on the DNA-binding trend and spectral properties of complexes [Ru (bpy) 2L] 2+(L= dmdpq, dpq, and dcdpq). *Inorganica chimica acta*, 358(12), 3311-3319. (DOI: 10.1016/j.ica.2005.05.006).
- [48] Kurita, N., & Kobayashi, K. (2000), Density functional MO calculation for stacked DNA base-pairs with backbones. *Computers & chemistry*, 24(3-4), 351-357. (DOI: 10.1016/S0097-8485(99)00071-6).
- [49] Paitandi, R. P., Gupta, R. K., Singh, R. S., Sharma, G., Koch, B., & Pandey, D. S. (2014), Interaction of ferrocene appended Ru (II), Rh (III) and Ir (III) dipyrinato complexes with DNA/protein, molecular docking and antitumor activity. *European Journal of Medicinal Chemistry*, 84, 17-29. (DOI: 10.1016/j.ejmech.2014.06.052).
- [50] Zou, X. H., Ye, B. H., Li, H., Zhang, Q. L., Chao, H., Liu, J. G., ... & Li, X. Y. (2001), The design of new molecular" light switches" for DNA. *JBIC Journal of Biological Inorganic Chemistry*, 6, 143-150. (DOI: 10.1007/s007750000183).



## *Chapter 3*

*Pyrene based fluorescent Ru(II)-arene complexes towards significant biological applications: catalytic potential, DNA/protein binding, two photon cell imaging and in vitro cytotoxicity*

## **Chapter 3**

### **Pyrene based fluorescent Ru(II)-arene complexes towards significant biological applications: catalytic potential, DNA/protein binding, two photon cell imaging and in vitro cytotoxicity**

#### **3.1 Introduction**

The contribution of transition metal ion chemistry towards cancer therapy started with the introduction of cisplatin in treating of cancers of the ovary, lungs, testicles, bladder, and head and neck area about forty years ago [1]. After the initial success of platinum-based metallodrugs, it has been found that several drawbacks of this class of the complex need to be taken care of additionally [2]. Therefore, several metal ions loaded with various ligands within the coordination sphere have been tested as prospective metallodrugs in cancer chemotherapy widening the window of cellular targets [3]. Among them ruthenium complexes are found to be quite interesting as several of them have entered in clinical trial for further evaluation [4]. The advantages of the ruthenium complexes lie in the facts that they can show significant ligand exchange in biological systems. Furthermore, the introduction of aqueous solubility of the complexes can be achieved with the engagement of the hydrophilic ligands, and ruthenium is accessible in its different oxidation states. To understand the prospective mechanism of the anticancer metal complexes, using specific ligands to render fluorescent character to the metal complex is a standard technique[5]. Properties like intense emission, large stoke shift values, and extended emission lifetime can make them suitable as molecular imaging agent within the cell. A fluorescent chemotherapeutic agent is generally suitable for monitoring cellular distribution and reveals the mechanism of action.

As the effectiveness of a drug is determined by both the central metal atom and the surrounding ligands, a minimal change in the structure of ligand moieties

can produce a new drug. Therefore, special care must be taken while selecting the prospective ligands. Schiff bases are well known pharmacophores for a wide range of biological activities that interfere with normal cellular processes by forming intramolecular hydrogen bonds between the imine group and the active center of the cellular components [6]. Therefore, it is conceived that combining these biologically active Schiff base ligands with the ruthenium (II) arene moiety can invoke a synergistic effect that could be used to design effective metallodrugs for chemotherapy [7].

In this chapter a pyrene ring containing ligand is designed and synthesized and incorporated into a Ru(II)-arene scaffold to generate four ruthenium compounds with general formula [Ru(arene)LX] [arene = p-cymene, benzene; HL = (*E*)-*N'*-(pyren-1-ylmethylene)thiopene-2-carbohydrazide; X = Cl, N<sub>3</sub><sup>-</sup>] having significant emission properties. Different arene rings are utilized to explore the effectiveness of the hydrophobicity of the compound on cytotoxic behaviour and different anionic co-ligands are used to investigate their influences. The pyrene containing N, O donor Schiff base **HL** has an extended delocalized  $\pi$ -system which imparts unique photophysical character in the compounds. Extended delocalized  $\pi$ -system such as anthracene, perylene, naphthalene, and pyrene are excellent rigid molecular skeletons that are convenient for the development of highly fluorescent probes with two-photon excitation [8]. The synthesized compounds are investigated for their anticancer properties and their cytotoxicity is evaluated against different cell lines. Theoretical calculations have been performed by applying the B3LYP DFT approach to support the experimental observations [9,10,11,12]. A hybrid periodic DFT-D quantum mechanical (QM) method has been employed to obtain the equilibrium geometries of complexes **5** and **6**. A finite non-periodic molecular cluster modelling approach has been utilized to explore the reaction pathways, mechanisms, formation, and reaction barriers using a non-periodic DFT method to explain the experimental observation. It was found that the computed results agreed well with the experimental observation. The interaction of the compounds with DNA and plasma proteins (HSA/BSA) was

studied using UV–visible and fluorescence spectroscopy. Ruthenium(II) complexes have been explored as catalysts in order to investigate the transfer of hydrogen from NADH and its conversion into NAD<sup>+</sup>, and the cell migration inhibition study is also conducted. Furthermore, these complexes have also been tested to check their utility as two-photon cell imaging agents. The results suggest that these arene ring containing organometallic Ru(II) complexes are promising candidates for further investigation in cancer treatment.

### 3.2 Experimental Section

#### 3.2.1 Materials and methods

All the required chemicals were commercially accessible with highest quality analytical grade from Alfa Aesar and Sigma Aldrich, India. Biological reagents purchased from Himedia and Sisco Research Laboratories (SRL) were used without purification. The specifications of all the instruments used for analysis purpose were same as described in the section 2.2.1 of the chapter 2.

#### 3.2.2 Syntheses of compounds

##### 3.2.2.1 Synthesis of ligand, HL

The ligand synthesis is already reported in a previous work [13].

##### 3.2.2.2 Synthesis of complex 5 [Ru( $\eta^6$ -*p*-cymene)(L)Cl]

Complex 5 was synthesized through drop-by-drop addition of DMF solution of ligand, HL (0.11 g, 0.32 mmol) into the corresponding ruthenium dimer precursor, [( $\eta^6$ -*p*-cymene)RuCl<sub>2</sub>]<sub>2</sub> (0.1 g, 0.16 mmol) solution containing 10 ml of DMF solvent. The reaction mixture was stirred at room temperature for 4-5 hours to obtain a brownish coloured solution. The crude product was obtained by evaporating and drying the final mixture over a vacuum. The residue was recrystallized to grow suitable single crystals in DMF solvent by slow evaporation. Yield: 70%. <sup>1</sup>H NMR in (400.13 MHz, 298K, DMSO-*d*<sub>6</sub>)  $\delta$ : ppm, 9.51 (1H, s, Py-CH=N), 9.21 (1H, d, Py-H), 8.75 (2H, d, Py-H), 8.56 (4H, d, Py-H), 8.49 (2H, d, Py-H), 8.32 (1H, d, Th-CH), 7.77 (1H, d, Th-CH), 7.23 (1H, t, Th-CH), 6.17 (2H, d, CH of C<sub>6</sub>H<sub>4</sub>), 5.93 (2H, d, CH of C<sub>6</sub>H<sub>4</sub>), 2.96 (1H, sept, CH(CH<sub>3</sub>)<sub>2</sub>), 2.46 (3H, s, C<sub>6</sub>H<sub>4</sub>CH<sub>3</sub>), 1.43 (6H, d, CH(CH<sub>3</sub>)<sub>2</sub>) ppm. <sup>13</sup>C NMR (100.61 MHz, 298 K, DMSO-*d*<sub>6</sub>)  $\delta$  ppm: 162.8(C=O), 158.5(C=N),

132.6, 130.2, 129.9, 128.0, 127.9, 126.7, 124.8, 123.6, 102.0, 100.1, 85.6, 81.9, 80.6, 80.5(C<sub>Aromatic</sub>) and 36.2, 31.2, 22.2(C<sub>Aliphatic</sub>) ppm. FT-IR (KBr, cm<sup>-1</sup>): 1654 (amide), 1558 (C=N). ESI-MS (+ve mode): [Ru(η<sup>6</sup>-p-cymene)(L)]<sup>+</sup> : 589.1 (m/z). Calcd. elemental analysis (%) for C<sub>32</sub>H<sub>27</sub>ClN<sub>2</sub>ORuS: C, 61.58; H, 4.36; N, 4.49; S, 5.14. Found: C, 60.15; H, 4.32; N, 4.29; S, 5.02.

### 3.2.2.3 Synthesis of complex 6 [Ru(η<sup>6</sup>-benzene)(L)Cl]

Complex **6** was synthesized through drop by drop addition of DMF solution of ligand, **HL** (0.14 g, 0.4 mmol) into the corresponding ruthenium dimer precursor, [(η<sup>6</sup>-benzene)RuCl<sub>2</sub>]<sub>2</sub> (0.1 g, 0.2 mmol) solution containing 10 ml of DMF solvent. The reaction mixture was then stirred at room temperature for 4-5 hrs to get the brownish coloured solution. Crude product was obtained by evaporating and drying the final mixture over vacuum. Dark brown single crystals were obtained *via* slow evaporation method in DMF solvent over a period of few days. Yield: 70%. <sup>1</sup>H NMR (400.13 MHz, 298K, DMSO-*d*<sub>6</sub>) δ: ppm, 9.74 (1H, s, Py-CH=N), 9.28 (1H, d, Py-H), 8.49 (2H, d, Py-H), 8.38 (4H, d, Py-H), 8.36 (2H, d, Py-H), 8.22 (1H, d, Th-CH), 7.69 (1H, d, Th-CH), 7.17 (1H, t, Th-CH), 5.32 (6H, s, CH of C<sub>6</sub>H<sub>6</sub>) ppm. <sup>13</sup>C NMR (100.61 MHz, 298 K, DMSO-*d*<sub>6</sub>) δ ppm: 170.1(C=O), 158.9(C=N), 135.5, 132.6, 131.3, 130.3, 129.7, 128.8, 127.9, 126.8, 124.7 and 84.3(C<sub>Aromatic</sub>) ppm. ESI-MS (+ve mode): [Ru(η<sup>6</sup>-benzene)(L)]<sup>+</sup>: 532.0 (m/z). FT-IR (KBr, cm<sup>-1</sup>): 1643(amide), 1568(C=N). Calcd. elemental analysis (%) for C<sub>28</sub>H<sub>19</sub>ClN<sub>2</sub>ORuS: C, 59.20; H, 3.37; N, 4.93; S, 5.64. Found: C, 58.15; H, 3.32; N, 4.29; S, 5.16.

### 3.2.2.4 Synthesis of complex 7 [Ru(η<sup>6</sup>-p-cymene)(L)N<sub>3</sub>]

A through drop by drop addition of DMF solution of ligand, **HL** (0.11 g, 0.31 mmol) into ruthenium dimer *viz.* [(η<sup>6</sup>-p-cymene)Ru(N<sub>3</sub>)<sub>2</sub>]<sub>2</sub> (0.1 g, 0.15 mmol) solution containing 10 ml of DMF solvent furnished complex **7**. It was stirred at room temperature for 4-5 hrs and a brownish coloured solution was obtained. Crude product was collected by evaporating and drying the final mixture over vacuum. The residue was recrystallized in DMF solvent by slow evaporation. Yield: 65%. <sup>1</sup>H NMR (400.13 MHz, 298K, DMSO-*d*<sub>6</sub>) δ: ppm, 9.36 (1H, s, Py-CH=N), 9.06 (1H, d, Py-H), 8.60 (2H, d, Py-H), 8.42 (4H, d,

Py-H), 8.28 (2H, d, Py-H), 8.17 (1H, d, Th-CH), 7.58 (1H, d, Th-CH), 7.31 (1H, t, Th-CH), 6.02 (2H, d, CH of C<sub>6</sub>H<sub>4</sub>), 5.84 (2H, d, CH of C<sub>6</sub>H<sub>4</sub>), 2.84 (1H, sept, CH(CH<sub>3</sub>)<sub>2</sub>), 2.54 (3H, s, C<sub>6</sub>H<sub>4</sub>CH<sub>3</sub>), 1.26 (3H, d, CH(CH<sub>3</sub>)<sub>2</sub>) ppm. <sup>13</sup>C NMR (100.61 MHz, 298 K, DMSO-*d*<sub>6</sub>) δ ppm: 172.4(C=O), 152.0(C=N), 130.7, 128.1, 129.3, 128.9, 127.9, 126.7, 124.4, 100.8, 83.5, 82.3, 80.8(C<sub>Aromatic</sub>) and 31.2, 22.8, 18.9(C<sub>Aliphatic</sub>) ppm. FT-IR (KBr, cm<sup>-1</sup>): 1643 (amide), 1552 (C=N), 2135 (azide). ESI-MS (+ve mode): [Ru(η<sup>6</sup>-p-cymene)(L)]<sup>+</sup>: 589.1 (m/z). Calcd. elemental analysis (%) for C<sub>28</sub>H<sub>19</sub>N<sub>5</sub>ORuS: C, 60.94; H, 4.31; N, 11.10; S, 5.08. Found: C, 59.20; H, 4.12; N, 10.38; S, 4.80.

### 3.2.2.5 Synthesis of complex 8 [Ru(η<sup>6</sup>-benzene)(L)N<sub>3</sub>]

Complex **8** was synthesized in a similar method like complex **7** using [(η<sup>6</sup>-benzene) Ru(N<sub>3</sub>)<sub>2</sub>]<sub>2</sub> (0.1 g, 0.17 mmol) as ruthenium precursor. Yield: 65%. <sup>1</sup>H NMR (400.13 MHz, 298K, DMSO-*d*<sub>6</sub>) δ: ppm, 9.74 (1H, s, Py-CH=N), 9.26 (1H, d, Py-H), 8.54 (2H, d, Py-H), 8.51 (4H, d, Py-H), 8.49 (2H, d, Py-H), 8.36 (1H, d, Th-CH), 7.73 (1H, d, Th-CH), 7.19 (1H, t, Th-CH), 5.32 (6H, s, CH of C<sub>6</sub>H<sub>6</sub>) ppm. <sup>13</sup>C NMR (100.61 MHz, 298 K, DMSO-*d*<sub>6</sub>) δ ppm: 169.8(C=O), 158.6(C=N), 135.3, 132.4, 131.4, 130.1, 129.1, 127.6, 126.8, 124.1, 123.3 and 84.4(C<sub>Aromatic</sub>) ppm. FT-IR (KBr, cm<sup>-1</sup>): 1664 (amide), 1558 (C=N), 2033 (azide). ESI-MS (+ve mode): [Ru(η<sup>6</sup>-benzene)(L)]<sup>+</sup>: 532.0 (m/z). Calcd. elemental analysis (%) for C<sub>28</sub>H<sub>19</sub>N<sub>5</sub>ORuS: C, 59.53; H, 3.33; N, 12.19; S, 5.58. Found: C, 58.20; H, 3.12; N, 12.08; S, 5.50.

*Note: Ruthenium benzene azide dimer i.e. [(η<sup>6</sup>-benzene)Ru(N<sub>3</sub>)<sub>2</sub>]<sub>2</sub> is explosive in nature, needs to be handled carefully.*

## 3.2.3 X-ray crystallography

### 3.2.3.1 X-ray crystallography of complex 5 and 6

The description of instrumentation of X-ray crystallography for complex **5** and **6** is same as described in Section 2.2.3 of chapter 2.

## 3.2.4 Protein Binding Study

### 3.2.4.1 Competitive binding experiments

Protein binding experiments follow the procedure outlined in section 2.2.4.1 of chapter 2.

#### **3.2.4.2 Circular dichroic spectral studies**

Follow the same procedure outlined in section 2.2.4.2 of chapter 2 for circular dichroic spectral studies.

#### **3.2.5 DNA binding study**

##### **3.2.5.1 Absorption spectral studies**

DNA binding experiments follow the procedure outlined in section 2.2.5.1 of chapter 2.

##### **3.2.5.2 Competitive binding experiments**

Follow the same procedure outlined in section 2.2.5.2 of chapter 2 for competitive binding experiments.

#### **3.2.6 Evaluation of cytotoxicity**

The procedure for MTT assay is same as discussed in section 2.2.5.1 of chapter 2.

#### **3.2.7 Wound healing assay**

HeLa cells ( $1.5 \times 10^6$  per well) were seeded in 2.0 mL media in 6-well plates and allowed to attach and grow to form a confluent monolayer. Each well of the plates was marked with a horizontal line passing through the center of bottom in advance. Wounds were created perpendicular to the lines by 10  $\mu$ L tips, and unattached cells were removed by washing with PBS (pH = 7.4) [14]. Complexes **5-8** in DMEM with 1% FBS were added and cells were incubated at 37 °C under 5% CO<sub>2</sub> for imaging. DMEM with 1% FBS were used to suppress cell proliferation. Images were captured at t = 0 and 24 h at the same position of each well. Experiments were repeated for at least three times.

#### **3.2.8 Two-photon cell imaging analysis**

HeLa cells were plated at a density of  $5 \times 10^4$  in 6-well plates. They were allowed to grow at 37 °C in a humidified CO<sub>2</sub> incubator until they were 70-80 % confluent. Then cells were treated at IC<sub>50</sub> concentration of complexes **5-8** for 24 h. The culture medium was aspirated from each well and cells were gently rinsed thrice with PBS at room temperature [15]. Then equal volumes of cells from the control (untreated) were mixed with DAPI dye (1 $\mu$ g/mL).

Finally, the treated and untreated cells were viewed immediately with two-photon laser scanning microscope: excitation 790 nm for the blue channel.

### 3.2.9 Dual staining assay with Hoechst and PI

To further confirm the nucleus morphology, Hoechst 33258 and PI staining were used. The  $5 \times 10^4$  HeLa cells were placed on six-well plates (Nest; USA). The cells were treated with the corresponding IC<sub>50</sub> concentration of complexes **5-8** and incubated for 24 h. After the incubation period treated cells were stained with the Hoechst and PI dye with concentrations of 5 and 3  $\mu\text{g/mL}$ , respectively., it was followed by incubation for 60 min at 37 °C and washing with PBS thrice. The fluorescence was viewed with the help of Fluoview FV100 (OLYMPUS, Tokyo, Japan) confocal microscope using appropriate filters. (Hoechst 33258 and PI having excitation wavelengths of 378 and 535 nm and an emission wavelength of 457 and 617 nm, respectively).

### 3.2.10 Reactive Oxygen Species (ROS) generation

The procedure for generating reactive oxygen species (ROS) is identical to the one outlined in section 2.2.7 of chapter 2.

### 3.2.11 Methodology and Computational Details

#### 3.2.11.1 Periodic DFT Calculations

To obtain the equilibrium crystal structures and lattice parameters of both the Complex **5** and Complex **6**, the periodic hybrid density functional theory (DFT) method was employed. The equilibrium geometries with the bulk 3D crystal unit cells of these Complex **5** and Complex **6** were obtained by using first-principles based B3LYP-D3 (in short DFT-D) method employed in quantum chemistry *ab-initio* based CRYSTAL17 program i.e. suite code. Triple- $\zeta$  valence polarization (TZVP) quality Gaussian types of atomic basis sets (i.e. Gaussian types of atomic Orbitals (GTO)) of the Ru, S, Cl, N, O and C atoms were used in the present calculations. The equilibrium structures are shown. To get fine equilibrium geometry of the crystal structures of the complexes **5** and **6**, semi-empirical Grimme's 3rd order (-D3) dispersion corrections have been incorporated in the present DFT computations to take account weak van der Waals (vdW) interactions among various layers and

atoms of the crystals which cannot be avoided. A threshold value of  $10^{-7}$  a. u. was set to converge both the energy and density during the optimization. The importance of B3LYP-D3 method is that it provides excellent quality of geometry of the crystal structures and also the structures are less affected due to the spin contaminations in the calculation. For analysis and graphical representation of the optimized crystal structures VESTA visualization code has been used.

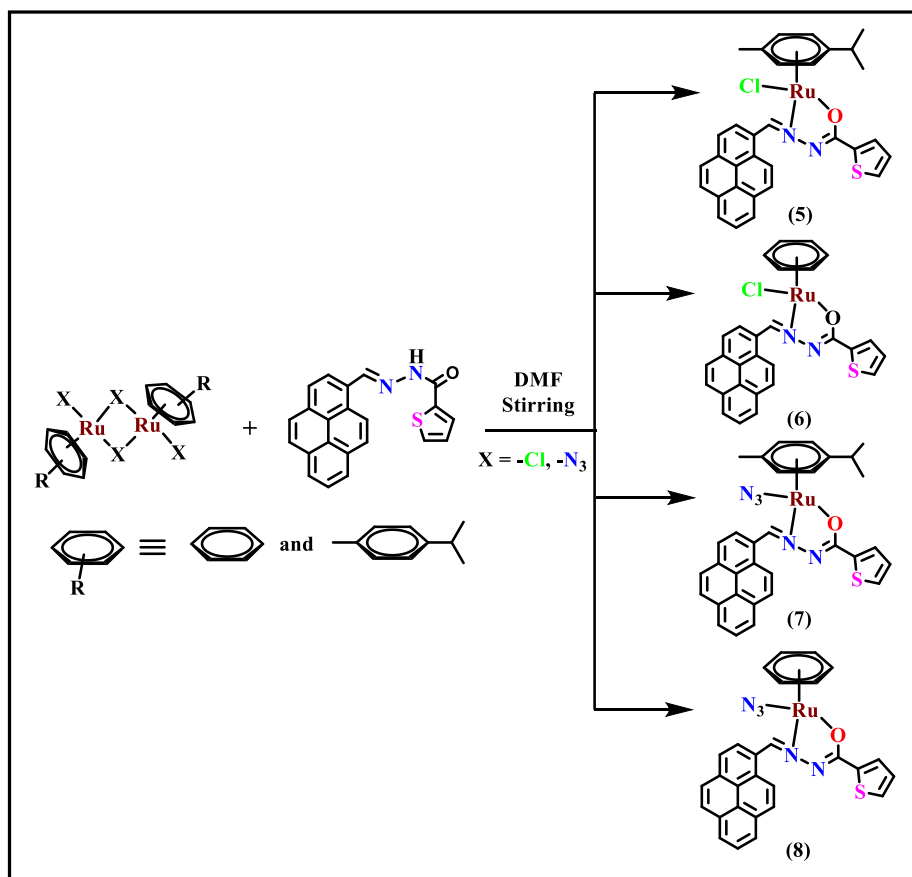
### 3.2.11.2 Non-periodic DFT Calculations

To explore the reaction mechanism involved in the formation of Ruthenium arene complexes, a theoretical and computational study was accomplished by employing the first-principle based hybrid quantum mechanical DFT method i.e. B3LYP considering a non-periodic molecular modeling. All the geometries of ligand HL, ruthenium dimers i.e.  $[(\eta^6\text{-p-cymene})\text{RuCl}_2]_2$ ,  $[(\eta^6\text{-benzene})\text{RuCl}_2]_2$ ,  $[(\eta^6\text{-p-cymene})\text{Ru}(\text{N}_3)_2]_2$ ,  $[(\eta^6\text{-benzene})\text{Ru}(\text{N}_3)_2]_2$  and ruthenium arene complexes (i.e. finite molecular cluster model systems of the complexes **5-6** i.e. Complex **5**, Complex **6**, Complex **7** and Complex **8**) were obtained by the same DFT method. The important stationary points on potential energy surface that is energy minima and first order saddle points (i.e., equilibrium transition states (TSs)) was investigated by employing the same DFT method in this study. All the electronic structure calculations and thermodynamic properties of the systems were calculated using B3LYP DFT method by with the Gaussian basis sets i.e., LANL2DZ with the Effective Core Potential (ECP) for the Ru atoms and the 6-31+G\* basis sets for the other atoms i.e., C, H, N, O, Cl and S atoms. The harmonic vibrational frequency analysis has been carried out to obtain the energy minima of the equilibrium geometries, and the imaginary frequencies were eliminated very carefully in the optimized stable structures. B3LYP method is the most popular method because of its accuracy and the equilibrium structures calculated by the B3LYP method are less influenced by the spin contamination in the present DFT calculations.

## 3.3 Results and discussion

### 3.3.1 Synthesis and characterization

The N, O chelating monobasic ligand was synthesized by the condensation reaction of equimolar amounts of thiophene-2-carboxylic hydrazide and 1-pyrenecarboxyaldehyde in ethanol as per the previously reported method [13]. Ruthenium arene complexes **5-8** were synthesized in good yields by the addition of one equivalent of ruthenium chloro- or azido-arene dimer with two equivalent of ligand **HL** in DMF and stirring the solution at room temperature for 4-5 hrs (Scheme 3.1). All four complexes are air stable and soluble in alcohols, DMSO, acetonitrile and moderately soluble in chlorinated solvents. Complexes **5-8** have been well characterized using various spectroscopic technique including  $^1\text{H}$  NMR, FT-IR, ESI-MS, UV-visible, fluorescence and the bulk purity was examined by elemental analysis (Figure 3.1- Figure 3.12).



**Scheme.3.1:** Synthetic path of complexes **5-8**

The proton NMR spectra ( $^1\text{H}$ ) of complexes **5-8** show significant aromatic proton peaks at 5.84-9.51 and typical azomethine proton peak in the region of

9.8- 9.2 ppm [16]. Compared to the free ligand, the absence of –NH proton around 12.06 ppm in complexes confirms the conversion to imidic form and ligation of the imidolate oxygen to the Ru(II) center. Complex **5** and **7** exhibit desired peaks in the region 5.84-6.17 ppm for p-cymene ring protons and 2.96-2.46, 2.36, and 1.11-1.02 ppm for the side chain protons of the p-cymene moiety. Complex **6** and **8** display singlet peak for benzene ring protons at 5.32 ppm [17].

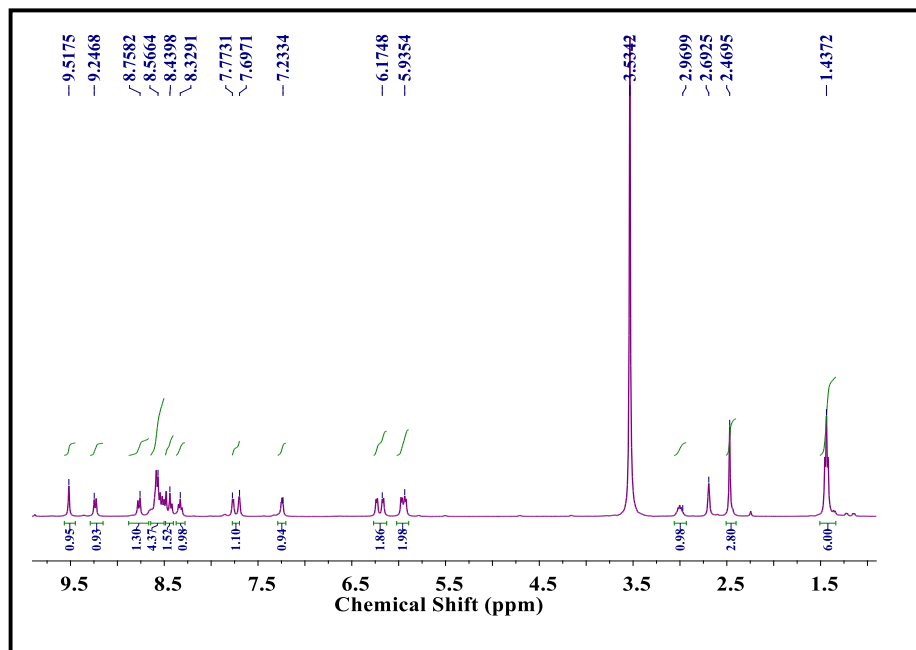


**Figure.3.1:**  $^1\text{H}$  NMR Spectra of Complex **5** in  $\text{DMSO-}d_6$  (400.13 MHz, 298K)

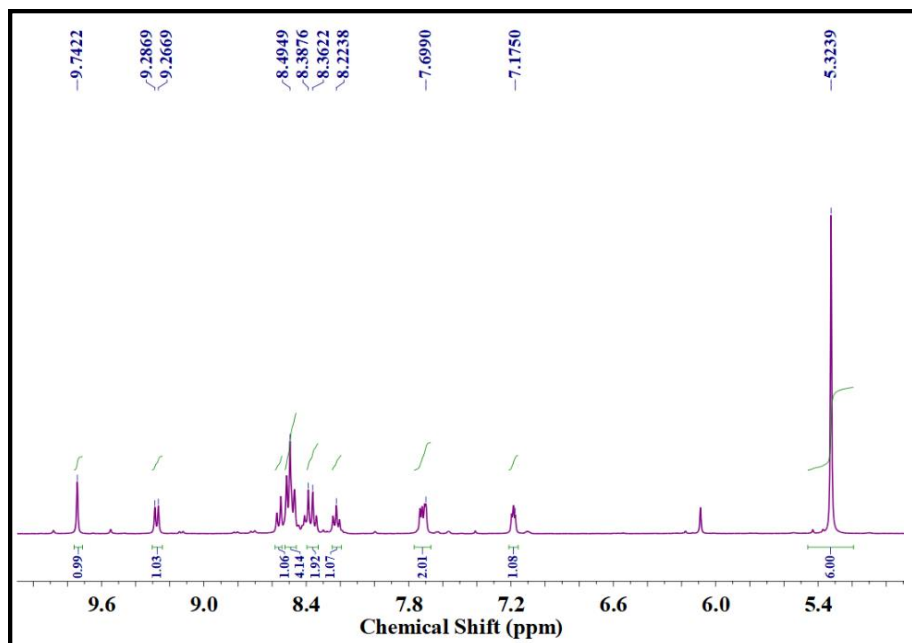


Figure.3.2:  $^1\text{H}$  NMR Spectra of Complex 6 in  $\text{DMSO-d}_6$  (400.13 MHz, 298K)

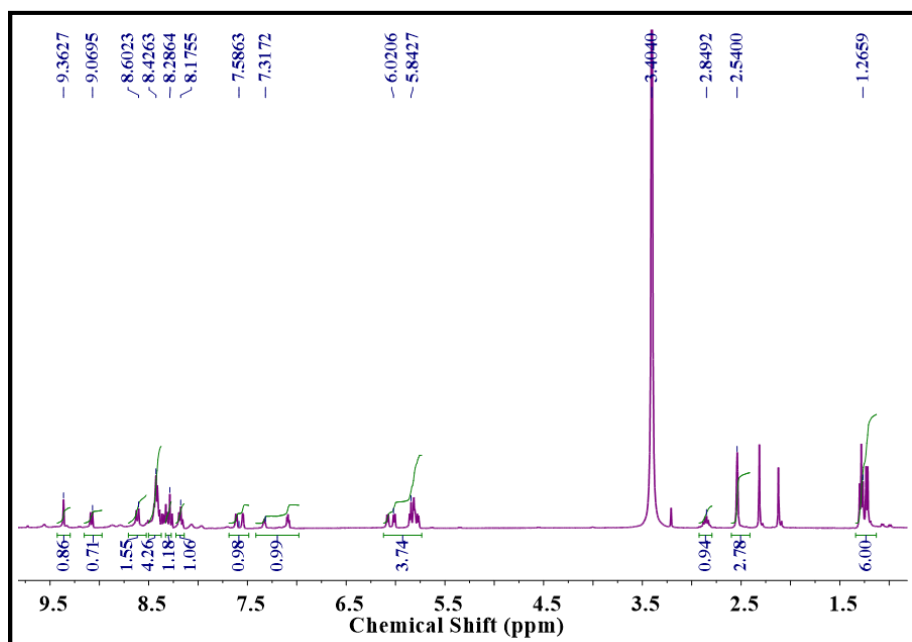


Figure.3.3:  $^1\text{H}$  NMR Spectra of Complex 7 in  $\text{DMSO-d}_6$  (400.13 MHz, 298K)

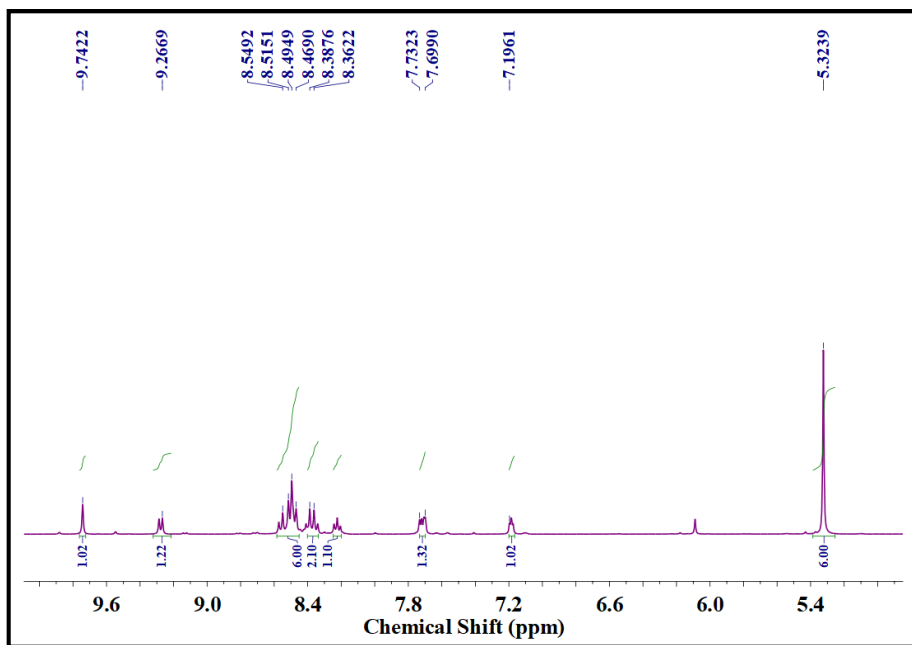


Figure.3.4:  $^1\text{H}$  NMR Spectra of Complex 8 in  $\text{DMSO-}d_6$  (400.13 MHz, 298K)

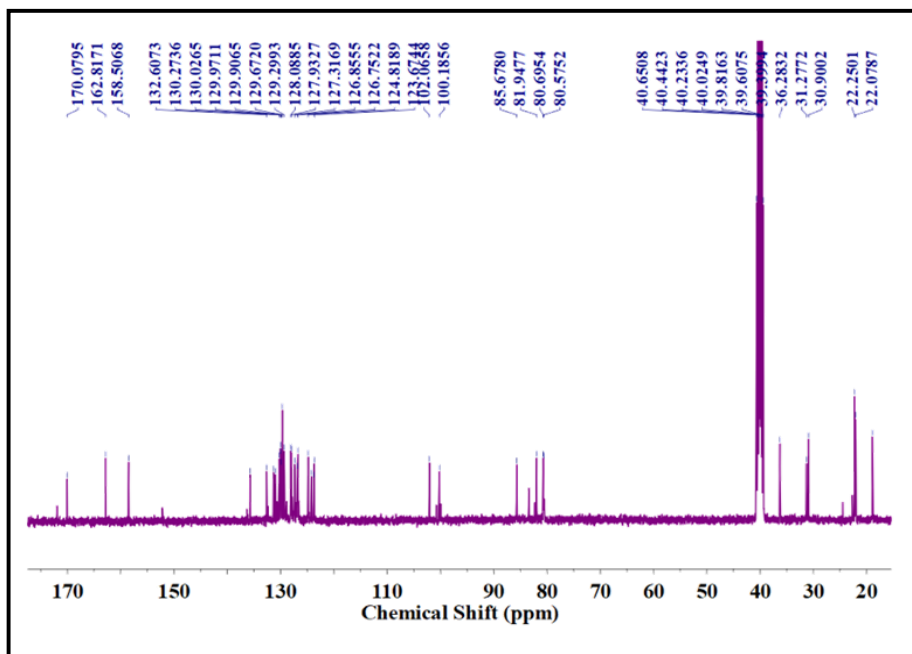


Figure.3.5:  $^{13}\text{C}$  NMR Spectra of Complex 5 in  $\text{DMSO-}d_6$  (400.13 MHz, 298K)

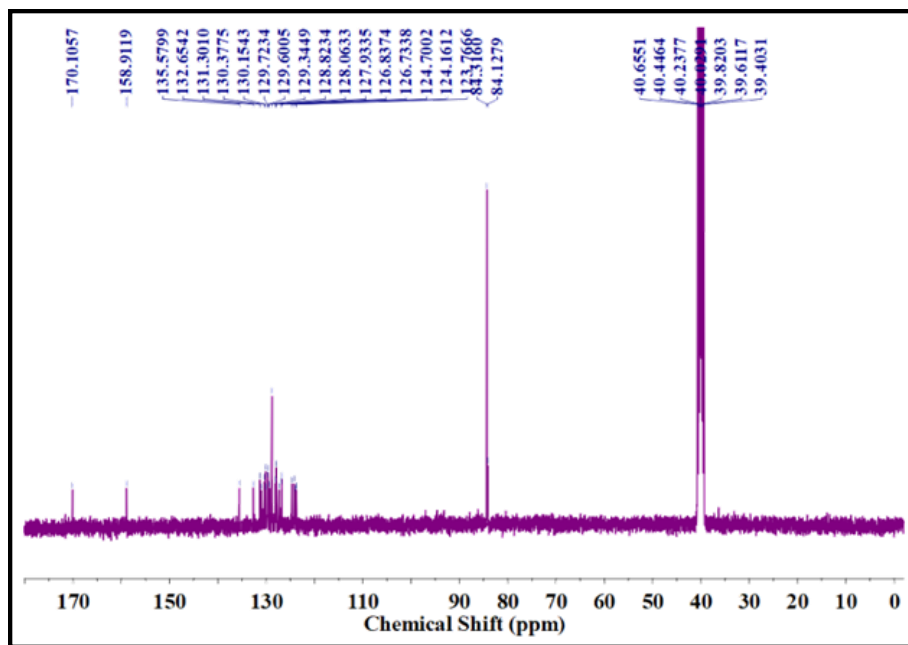


Figure.3.6:  $^{13}\text{C}$  NMR Spectra of Complex 6 in  $\text{DMSO-}d_6$  (400.13 MHz, 298K)

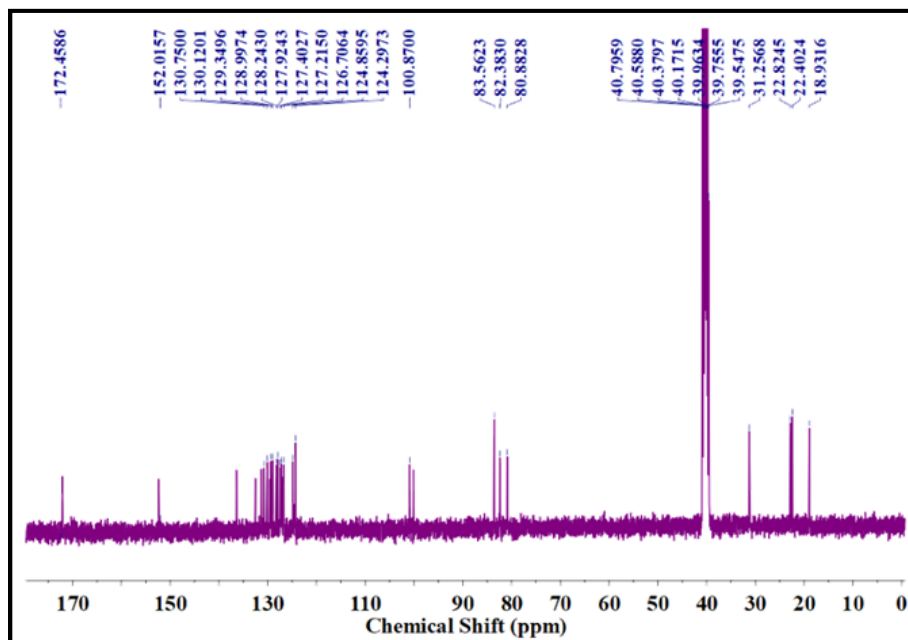
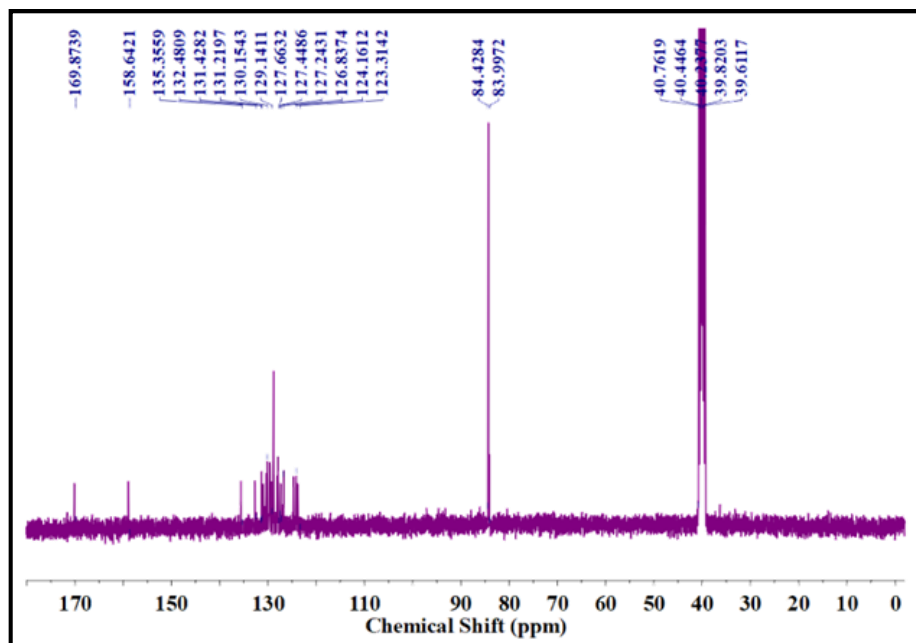
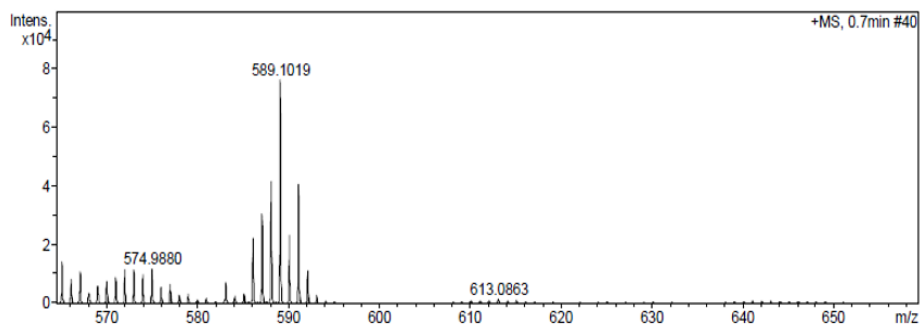


Figure.3.7:  $^{13}\text{C}$  NMR Spectra of Complex 7 in  $\text{DMSO-}d_6$  (400.13 MHz, 298K)



**Figure.3.8:**  $^{13}\text{C}$  NMR Spectra of Complex 8 in  $\text{DMSO-d}_6$  (400.13 MHz, 298K)



**Figure.3.9:** ESI-MS spectra of synthesized complex 5

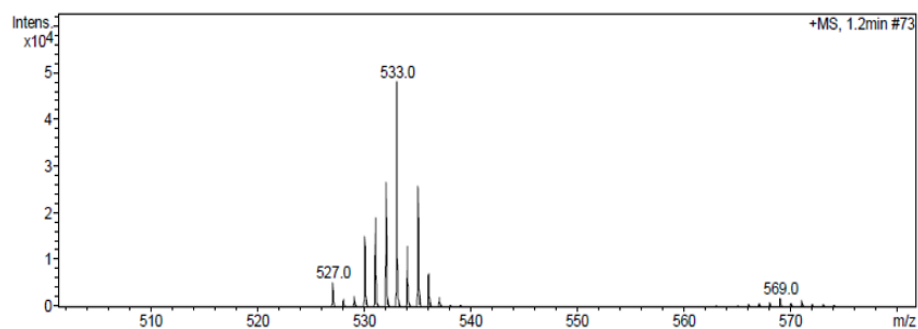


**Figure.3.10:** ESI-MS spectra of synthesized complex 6

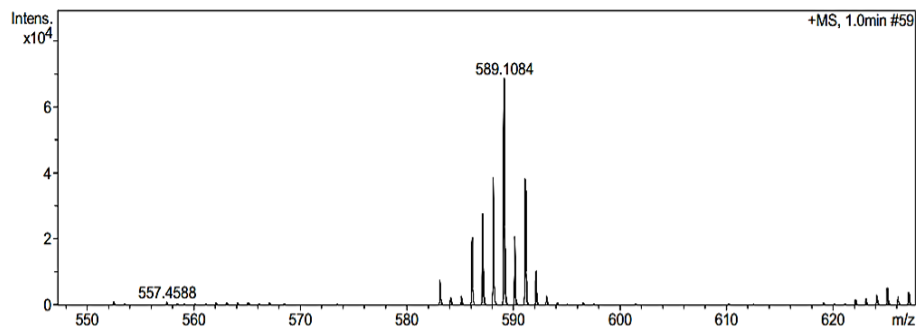


**Figure.3.11:** ESI-MS spectra of synthesized complex **7**

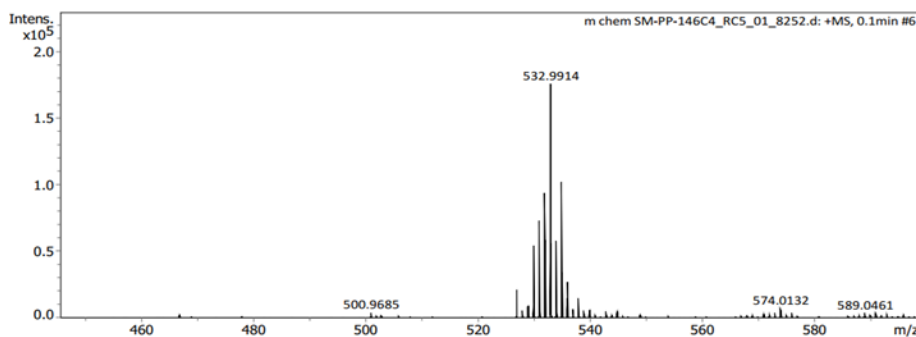


**Figure.3.12:** ESI-MS spectra of synthesized complex **8**

FTIR spectra of the ligand, **HL** display a characteristic band for N-H in the region of  $3221\text{ cm}^{-1}$  and also show two different absorption bands *viz.*  $\nu_{\text{C=O}}$  and  $\nu_{\text{C=N}}$  within the range  $1640\text{--}1700\text{ cm}^{-1}$  and  $1550\text{--}1650\text{ cm}^{-1}$  [13]. After complexation, in all of the IR spectra of Ru(II)-arene complexes **5-8**, the disappearance of  $\nu_{\text{N-H}}$  absorption band was observed due to the conversion of the ligand in imidic form and subsequent dissociation of the proton leads to oxygen coordination to the metal center. The  $1550\text{--}1650\text{ cm}^{-1}$  absorption band represents the azomethine nitrogen coordination to metal [18]. Complex **7** and complex **8** shows another characteristic sharp band for  $\nu_{\text{azide}}$  in the region of  $2033\text{ cm}^{-1}$  and  $2130\text{ cm}^{-1}$  which indicates the presence of azido functional group coordination with the metal center [19] (Figure 3.13).

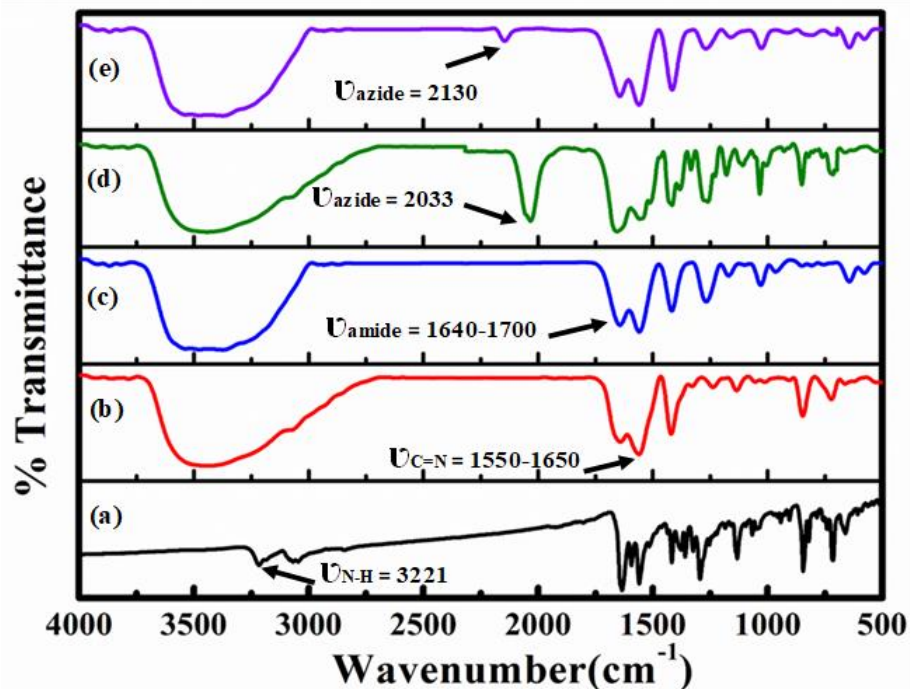


**Figure.3.13** FTIR stretching frequencies (in KBr pallet) of (a) **HL**, (b) complex 5, (c) complex 6, (d) complex 7 and (e) complex 8, respectively

Complexes **5-8** exhibit two absorption bands in the 283-385 nm range. The first relates to the ligand-centered transitions and has been characterized as  $\pi$ - $\pi^*$  transition with potential contributions from ligand (**HL**) moiety [18]. Like other Ru(II)-arene complexes, all exhibit a second highly intense absorption band in the 375-385 nm region due to the MLCT transition [20]. The fluorescence experiments of all complexes were carried out in a DMSO solution. All the complexes show emission maxima bands within 435-443 nm (Figure 3.14).

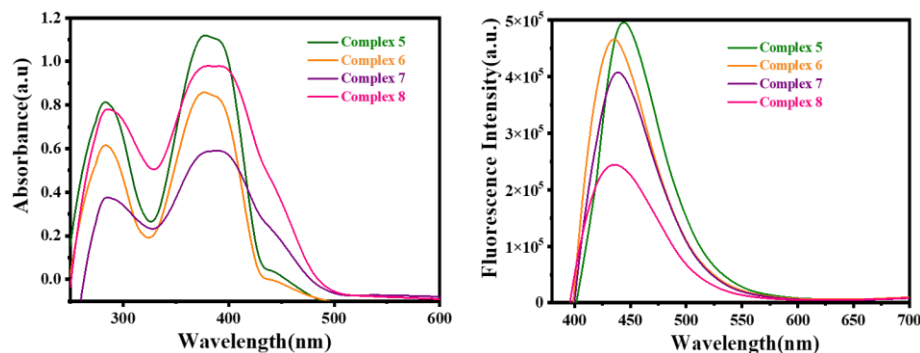


**Figure.3.14** (a) UV-Visible spectra, (b) emission spectra of complexes 5-8 in DMSO

### 3.3.2 X-ray crystallography study of complex 5 and 6

Single crystals of complexes **5** and **6** were obtained and characterized by single-crystal X-ray diffraction. However, it is pertinent to indicate that the crystal structure of complex **5** is communicated in a recent report [21]. Complex **5** and **6** were crystallized in monoclinic crystal arrangement having space groups of P 21 and C2/c, respectively. The crystal data and structure refinement data details are shown in Table 3.1, and the selected bond lengths and angles are summarized in Table 3.2. The crystal structures of complexes **5** and **6** display that the ligand coordinates with the ruthenium metal center in a bidentate manner through the azomethine nitrogen and imidolate oxygen, and two other coordination positions of the Ru metal center are occupied by chloride and arene group. The geometry of the ruthenium metal center is the pseudo-octahedral with a classical three-legged piano stool arrangement. In the complexes, three legs of the piano stool are formed by the ligand (HL) and chloro group, while the arene ring represents the seat. Extensive H-bonding interactions to build 2D and 3D polymeric frameworks are recorded. Complex **5** and **6** show a strong supramolecular network not only through hydrogen bonding (H4...C11, 2.825 Å, and H1...S3, 2.993 Å) but also via  $\pi \dots \pi$  stacking and CH... $\pi$  (2.881 Å) (Figure 3.15 - Figure 3.16).

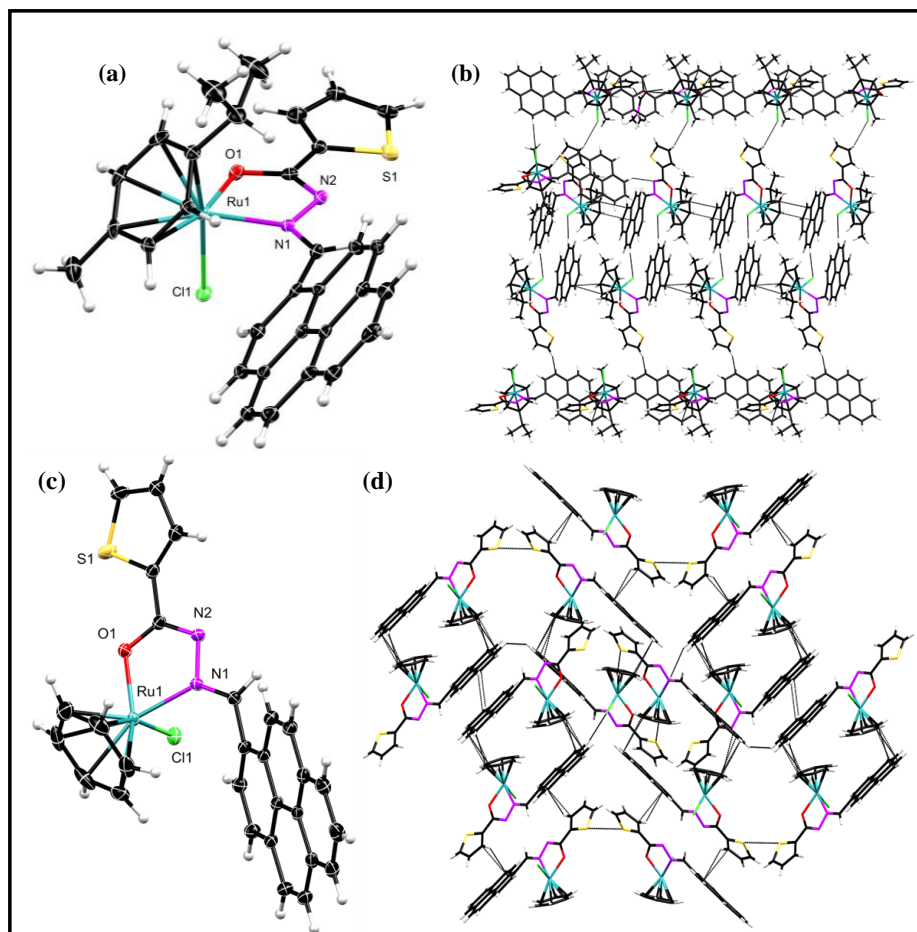


**Figure.3.15** ORTEP presentation of (a) complex 5 and (c) complex 6, at 50% thermal probability level. Supramolecular framework via intermolecular hydrogen bonding for (b) complex 5 and (d) complex 6

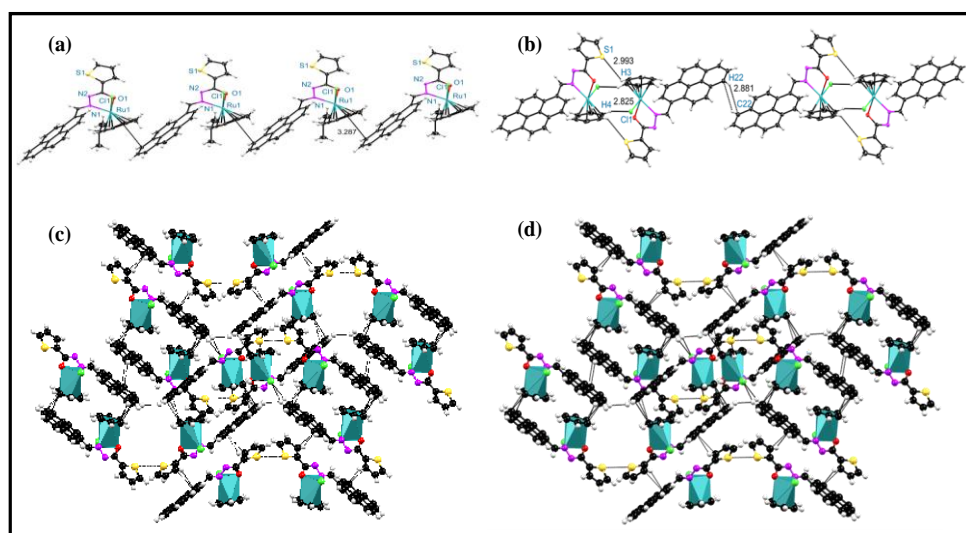


**Figure.3.16:** Crystal polymeric framework. (a) and (b) 2D framework of

complex 5 and complex 6. (c) and (d) Supramolecular interaction in complex 5 and 6 via intermolecular hydrogen bonding and CH... $\pi$  stacking interaction.

**Table 3.1:** Experimental crystal and structure refinement data of complex 5 and 6

Parameter	Complex 5	Complex 6
<b>Empirical Formula</b>	4(C <sub>32</sub> H <sub>27</sub> Cl N <sub>2</sub> O Ru S), 4(C <sub>3</sub> H <sub>7</sub> N O), H <sub>2</sub> O	C <sub>28</sub> H <sub>19</sub> Cl N <sub>2</sub> O Ru S
<b>Formula weight</b>	2806.94	568.03
<b>Crystal system</b>	monoclinic	monoclinic
<b>Space group</b>	<i>P</i> 21	<i>C</i> 2/ <i>c</i>
<b><i>a</i> (Å)</b>	11.0233(4)	24.1813(16)
<b><i>b</i> (Å)</b>	17.3526(6)	13.2549(9)
<b><i>c</i> (Å)</b>	16.4133(5)	14.7463(10)
<b><math>\alpha</math> (°)</b>	90	90
<b><math>\beta</math> (°)</b>	99.3076(9)	100.7758(16)
<b><math>\gamma</math> (°)</b>	90	90
<b><i>V</i> (Å<sup>3</sup>)</b>	3098.25(18)	4643.2(5)
<b><math>\lambda</math> (Å)</b>	0.71073	0.71073
<b><math>\rho_{\text{calcd}}</math> (g/cm<sup>3</sup>)</b>	1.504	1.625
<b><i>Z</i></b>	1	8
<b><i>T</i> (K)</b>	273	273
<b><math>\mu</math> (mm<sup>-1</sup>)</b>	0.698	0.906
<b>F(0 0 0)</b>	1442	2288
<b>Crystal size (mm<sup>3</sup>)</b>	0.04 x 0.06 x 0.10	0.06 x 0.08 x 0.12
<b>Theta ranges (°)</b>	2.9 to 28.3	3.0 to 29.6
<b><i>h/k/l</i></b>	-14,14/-23,23/-21,21	-33,33/-18,18/-20,20
<b>Goodness-of-fit (GOF)</b>	1.03	1.07
<b>Final <i>R</i> indices [<i>I</i> &gt; 2<math>\sigma</math>(<i>I</i>)]</b>	<i>R</i> 1 = 0.0277, w <i>R</i> 2 = 0.0681	<i>R</i> 1 = 0.0293, w <i>R</i> 2 = 0.0789
<b>R(int)</b>	0.029	0.038

<b>Largest peak and hole (eÅ<sup>-3</sup>)</b>	1.19 and -0.78	1.06 and -1.03
<b>CCDC No.</b>	<b>2092515</b>	<b>2092521</b>

*Table 3.2: Selected bond lengths (Å) and bond angles (°) of complexes 5 and 6*

<b>Complex 5</b>		<b>Complex 6</b>	
<b>Ru1-Cl1</b>	2.4025(11)	<b>Ru1-Cl1</b>	2.3985(6)
<b>Ru1-O1</b>	2.076(3)	<b>Ru1-O1</b>	2.0706(14)
<b>Ru1-N1</b>	2.090(3)	<b>Ru1-N1</b>	2.1044(15)
<b>Ru1-C1</b>	2.241(4)	<b>Ru1-C1</b>	2.177(2)
<b>Ru1-C2</b>	2.200(5)	<b>Ru1-C2</b>	2.188(2)
<b>Ru1-C3</b>	2.157(5)	<b>Ru1-C3</b>	2.180(2)
<b>Ru1-C4</b>	2.187(5)	<b>Ru1-C4</b>	2.186(2)
<b>Ru1-C5</b>	2.162(4)	<b>Ru1-C5</b>	2.167(2)
<b>Ru1-C6</b>	2.197(3)	<b>Ru1-C6</b>	2.188(2)
<b>N1-N2</b>	1.409(4)	<b>N1-N2</b>	1.408(2)
<b>O1-C11</b>	1.282(5)	<b>O1-C7</b>	1.290(2)
<b>Cl1-Ru1-O1</b>	85.01(9)	<b>Cl1-Ru1-O1</b>	85.80(4)
<b>Cl1-Ru1-N1</b>	86.45(9)	<b>Cl1-Ru1-N1</b>	86.22(4)
<b>Cl1-Ru1-C1</b>	90.51(9)	<b>Cl1-Ru1-C1</b>	126.50(7)
<b>Cl1-Ru1-C2</b>	109.71(13)	<b>Cl1-Ru1-C2</b>	96.33(6)
<b>Cl1-Ru1-C3</b>	145.67(11)	<b>Cl1-Ru1-C3</b>	89.40(7)
<b>Cl1-Ru1-C4</b>	167.15(13)	<b>Cl1-Ru1-C4</b>	110.37(7)
<b>Cl1-Ru1-C5</b>	129.33(10)	<b>Cl1-Ru1-C5</b>	146.95(8)
<b>Cl1-Ru1-C6</b>	98.74(9)	<b>Cl1-Ru1-C6</b>	163.72(6)
<b>O1-Ru1-N1</b>	76.66(13)	<b>O1-Ru1-N1</b>	76.54(5)
<b>O1-Ru1-C1</b>	129.25(14)	<b>O1-Ru1-C1</b>	147.10(8)
<b>O1-Ru1-C2</b>	98.65(16)	<b>O1-Ru1-C2</b>	162.70(8)
<b>O1-Ru1-C3</b>	88.75(15)	<b>O1-Ru1-C3</b>	125.27(8)
<b>O1-Ru1-C4</b>	107.83(15)	<b>O1-Ru1-C4</b>	95.25(8)

<b>O1-Ru1-C5</b>	144.30(12)	<b>O1-Ru1-C5</b>	88.61(7)
<b>O1-Ru1-C6</b>	165.80(15)	<b>O1-Ru1-C6</b>	110.42(7)
<b>N1-Ru1-C1</b>	153.57(14)	<b>N1-Ru1-C1</b>	97.40(7)
<b>N1-Ru1-C2</b>	162.92(15)	<b>N1-Ru1-C2</b>	120.68(8)
<b>N1-Ru1-C3</b>	124.78(13)	<b>N1-Ru1-C3</b>	157.39(8)
<b>N1-Ru1-C4</b>	96.84(15)	<b>N1-Ru1-C4</b>	161.15(9)
<b>N1-Ru1-C5</b>	94.04(14)	<b>N1-Ru1-C5</b>	123.97(8)
<b>N1-Ru1-C6</b>	117.11(15)	<b>N1-Ru1-C6</b>	98.69(7)

To support the experimental observation, a hybrid periodic DFT-D calculation is performed to predict the crystal structures of both the Complex **5** and Complex **6** as depicted in Figure 3.17, individually. These DFT-D computations reveal that the equilibrium lattice constants of the complex **5** are  $a = 10.415 \text{ \AA}$ ,  $b = 16.831 \text{ \AA}$ , and  $c = 14.887 \text{ \AA}$ , and the interfacial angles are  $\alpha = 90^\circ$ ,  $\beta = 151.96^\circ$  and  $\gamma = 90^\circ$ . The computational study shows that the complex **5** has *P21* monoclinic symmetry. The equilibrium bond lengths of the N-N, C-C, C-S, Ru-Cl, Ru-O, Ru-N, C-O and C-H are  $1.426 \text{ \AA}$ ,  $1.407 \text{ \AA}$ ,  $1.751 \text{ \AA}$ ,  $2.457 \text{ \AA}$ ,  $2.094 \text{ \AA}$ ,  $2.067 \text{ \AA}$ ,  $1.258 \text{ \AA}$ , and  $1.085 \text{ \AA}$ , respectively. Similarly, the equilibrium lattice constants of complex **6** are  $a = 24.049 \text{ \AA}$ ,  $b = 12.326 \text{ \AA}$  and  $c = 30.732 \text{ \AA}$ , and the interfacial angles are  $\alpha = 90^\circ$ ,  $\beta = 151.96^\circ$  and  $\gamma = 90^\circ$ . Computationally, it has been found that the crystal structure of the complex **6** has *C2/c* monoclinic symmetry, and the structure is thermodynamically stable. The equilibrium bond lengths of the N-N, C-C, C-S, Ru-Cl, Ru-O, Ru-N, C-O and C-H are  $1.425 \text{ \AA}$ ,  $1.408 \text{ \AA}$ ,  $1.753 \text{ \AA}$ ,  $2.443 \text{ \AA}$ ,  $2.080 \text{ \AA}$ ,  $1.301 \text{ \AA}$  and  $1.081 \text{ \AA}$ , respectively (Table 3.3). The computed lattice constants and various equilibrium bond lengths agree well with the experimental observation.

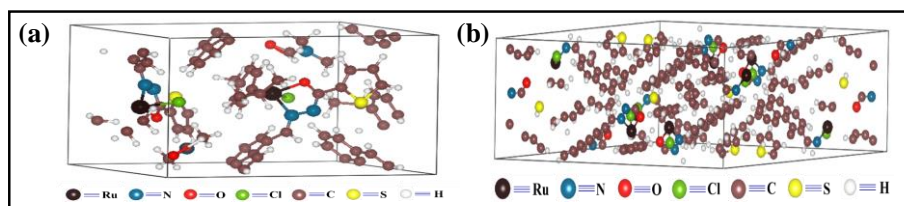


**Figure.3.17:** The equilibrium 3D bulk crystal structure of the Complex 5 and Complex 6 is depicted here, and the unit cell is highlighted by a cube

**Table 3.3:** Equilibrium structural parameters of the optimized crystal structure of the Complex 5 and complex 6

Lattice parameters in Å	Interfacial angles in degree (°)	Space group and Symmetry	Average bond distance between atoms (Å)							
			N-N	C-C	C-S	Ru-Cl	Ru-O	Ru-N	C-O	C-H
<b>Complex 5</b>										
a = 10.415, b = 16.831, c = 14.887	$\alpha = 90^\circ$ , $\beta = 90^\circ$ and $\gamma = 90^\circ$	P21 Monoclinic	1.426	1.407	1.751	2.457	2.094	2.067	1.258	1.085
<b>Complex 6</b>										
a = 24.049, b = 12.326, c = 30.732	$\alpha = 90^\circ$ , $\beta = 151.96^\circ$ $\gamma = 90^\circ$	C2/c Monoclinic	1.425	1.408	1.753	2.443	2.080	2.088	1.301	1.081

### 3.3.3 Stability studies

The investigation of the stability of the compounds under physiological conditions is an essential factor for almost all biological applications. Thus, an appropriate study was carried out by dissolving complexes **5-8** in a solution mixture of 1% DMSO/PBS and observing their stability in the time frame of 0 h, 6 h, 12 h, and 24 h via UV-visible spectroscopy. No substantial shifting or change in peaks was detected in the absorption spectra of the all the compounds, indicating the complexes' stability in biological medium (Figure 3.18).

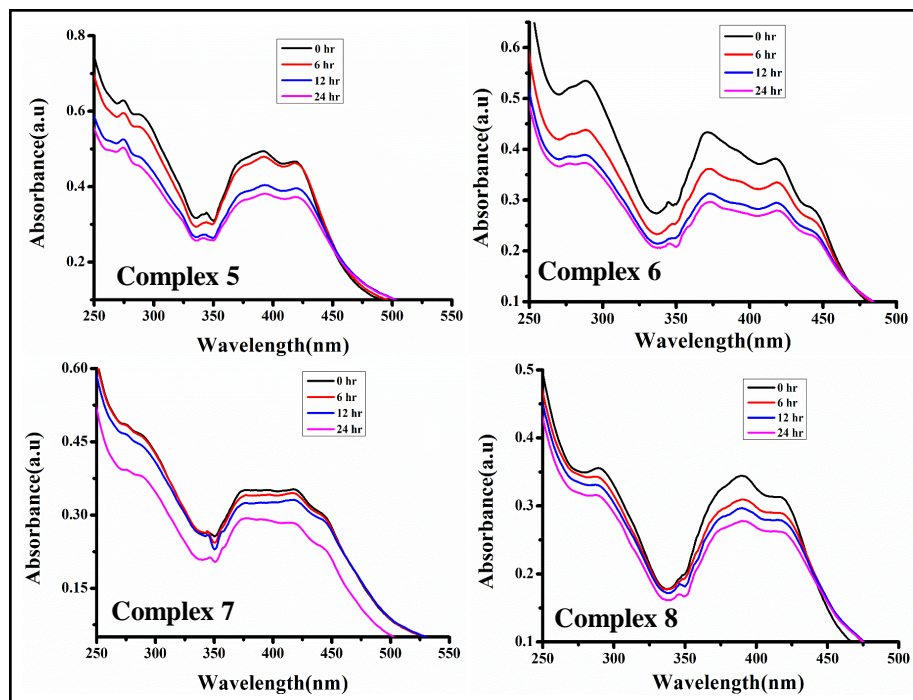


**Figure.3.18** Stability studies of the complexes 5-8 (1% DMSO in PBS Solution)

### 3.3.4 Protein binding study

#### 3.3.4.1 Emission Spectra

To understand the binding affinity of synthesized complexes with plasma protein, HSA and BSA are generally taken as model proteins. Serum albumin proteins have shown significant interaction with synthesized complexes because of their capability to transport the molecules through the bloodstream [22]. Fluorescence quenching experiment is carried out by the BSA and HSA protein (10  $\mu\text{M}$ ), where mainly the tryptophan residue contributes to the fluorescence. In the fluorescence titration studies, the FL intensity of BSA and HSA protein has been found to decrease continuously with an increase in the complexes concentration (5-50  $\mu\text{M}$ ) in the wavelength range of 290-500 nm ( $\lambda_{\text{ex}} = 280$  nm) (Figure 3.19 and Figure 3.20). The quantitative analysis of the binding affinity of complexes with protein is determined by employing the Stern-Volmer equation [17]. Stern-Volmer quenching constant of complex 5 ( $3.9 \times 10^5 \text{ M}^{-1}$  for HSA and  $1.9 \times 10^5 \text{ M}^{-1}$  for BSA) and complex 7 ( $1.5 \times 10^5 \text{ M}^{-1}$  for HSA and  $1.8 \times 10^5 \text{ M}^{-1}$  for BSA) are found to be higher than that of

complex **6** ( $1.2 \times 10^5 \text{ M}^{-1}$  for HSA and  $1.3 \times 10^5 \text{ M}^{-1}$  for BSA) and complex **8** ( $3.2 \times 10^4 \text{ M}^{-1}$  for HSA and  $2.7 \times 10^4 \text{ M}^{-1}$  for BSA) which may be ascribed to the presence of methyl side chain and isopropyl group in the p-cymene ring which can stabilize the hydrophobic interaction via nonpolar residue in protein chain pocket. In addition, the parameters of bimolecular quenching constant ( $k_q$ ), of approximately  $10^{12} \text{ M}^{-1}\text{s}^{-1}$  signifies the role of static quenching while in the range of  $10^{11} \text{ M}^{-1}\text{s}^{-1}$  stands for the dynamic quenching. The bimolecular quenching constants ( $k_q$ ) of all complexes **5-8** are found to be in the range of  $10^{12} \text{ M}^{-1}\text{s}^{-1}$  which signify the involvement of static quenching (Table 3.4).

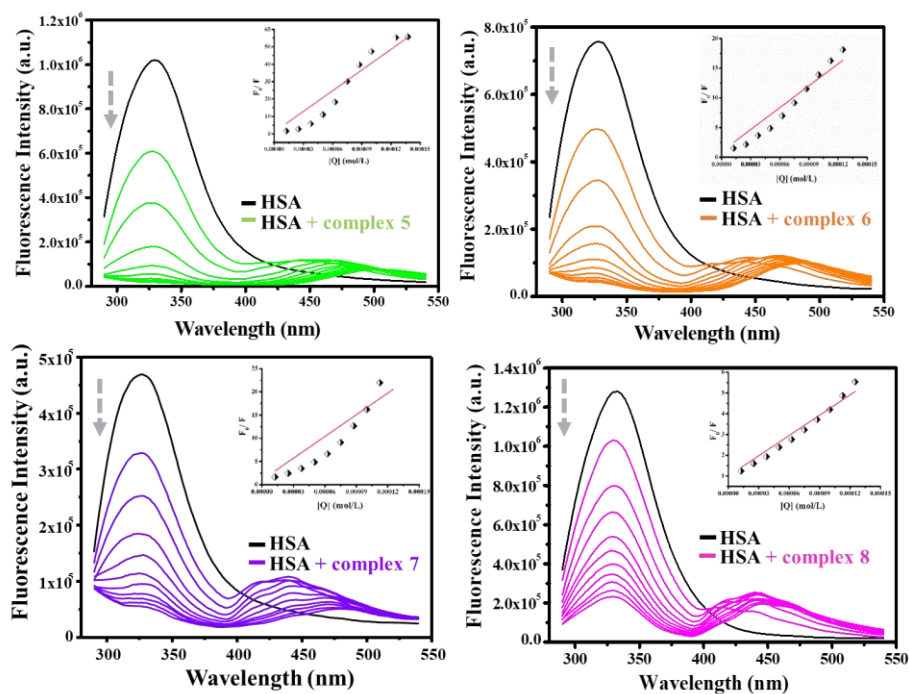


**Figure.3.19:** Emission titration spectra of HSA ( $10 \mu\text{M}$ ) in Tris-HCl buffer with complexes **5-8** ( $5\text{-}50 \mu\text{M}$ ) at  $298 \text{ K}$ . Inset: Plots of  $F_0/F$  vs.  $[Q](\text{mol/L})$  for HSA

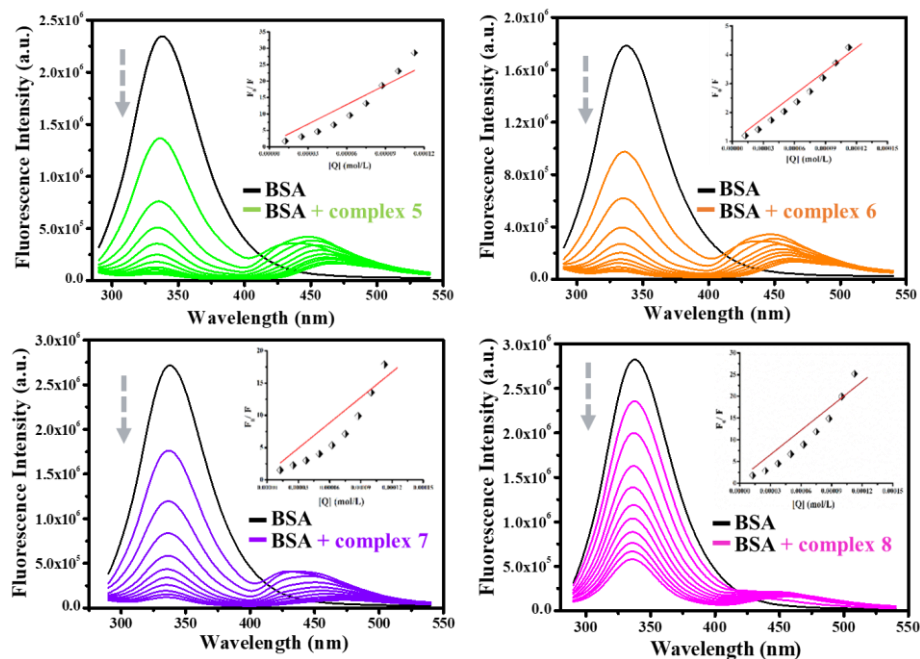


**Figure.3.20:** Emission titration spectra of BSA (10  $\mu\text{M}$ ) in Tris-HCl buffer with complexes 5-8 (5-50  $\mu\text{M}$ ) at 298 K. Inset: Plots of  $F_0/F$  vs.  $[Q]$ (mol/L) for BSA

**Table 3.4:** Determination of various spectral parameters to check the interaction of compounds with HSA and BSA protein

System	$K_{sv}$ ( $\text{M}^{-1}$ )	$k_q$ ( $\text{M}^{-1}\text{s}^{-1}$ )	$K_a$ ( $\text{M}^{-1}$ )	$n$
5-HSA	$3.9 \times 10^5$	$6.1 \times 10^{13}$	$5.1 \times 10^9$	2.02
6-HSA	$1.2 \times 10^5$	$1.9 \times 10^{13}$	$2.4 \times 10^7$	1.57
7-HSA	$1.5 \times 10^5$	$2.4 \times 10^{13}$	$4.8 \times 10^7$	1.63
8-HSA	$3.2 \times 10^4$	$5.1 \times 10^{12}$	$3.3 \times 10^5$	1.25
5-BSA	$1.9 \times 10^5$	$3.0 \times 10^{13}$	$1.3 \times 10^8$	1.69
6-BSA	$1.3 \times 10^5$	$2.1 \times 10^{13}$	$1.4 \times 10^7$	1.56
7-BSA	$1.8 \times 10^5$	$2.9 \times 10^{13}$	$3.7 \times 10^7$	1.62
8-BSA	$2.7 \times 10^4$	$4.3 \times 10^{12}$	$4.6 \times 10^4$	1.29

### 3.3.4.2 Circular dichroic spectroscopy studies

Circular Dichroism spectroscopy is a highly sensitive and informative technique for investigating changes in protein secondary structure during

protein-ligand interactions. As shown in Figure 3.21 and 3.22, bare proteins have a negative band at 235 nm attributed to  $n \rightarrow \pi^*$  transition which is characteristic of  $\alpha$ -helical proteins (BSA and HSA) [19]. To examine the conformational changes in the secondary structure of protein after the interaction with complexes, recorded the CD spectra which show a decrement in the negative ellipticity value of the helix structure, signifying the extent of conformational changes in the protein structure. When the complexes interact with the main polypeptide chain of the proteins, it breaks their H-bonding networks and the protein secondary structure (BSA/HSA) is destroyed. Apart from that, binding induces the extent of  $\alpha$ -helical content, which gradually decreases with a slight unfolding of the polypeptide chains of BSA/HSA. Based on the result, it is found that changes in the  $\alpha$ -helical content percentage values of proteins are higher in complexes **5** and **7** than complexes **6** and **8** because of the extra hydrophobicity factor associated with p-cymene ring. The result shows that  $\alpha$ -helical content of free HSA decrease from 68.39% to 2.61% (in the case of complex **5**) and 68.39% to 3.83% (in the case of complex **7**). For BSA  $\alpha$ -helical content decrease from 67.3% to 2.03% (in the case of complex **6**) and 67.3% to 3.42% (in the case of complex **8**).

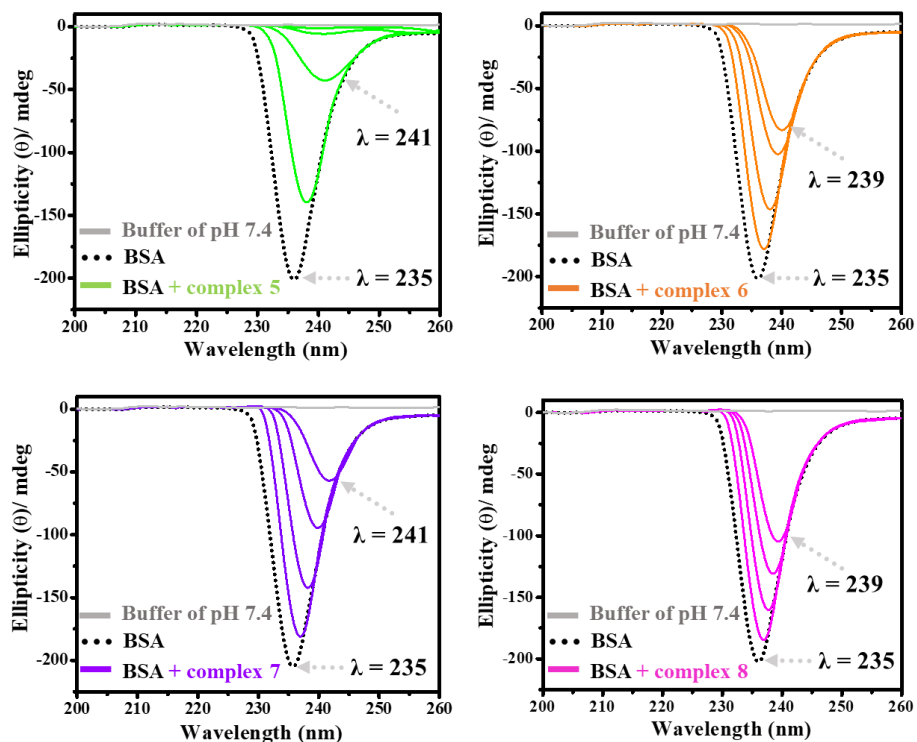


**Figure.3.21:** BSA proteins ( $10 \mu\text{M}$ ) Circular dichroism spectra with or without complex at different concentration (0-40  $\mu\text{M}$ )

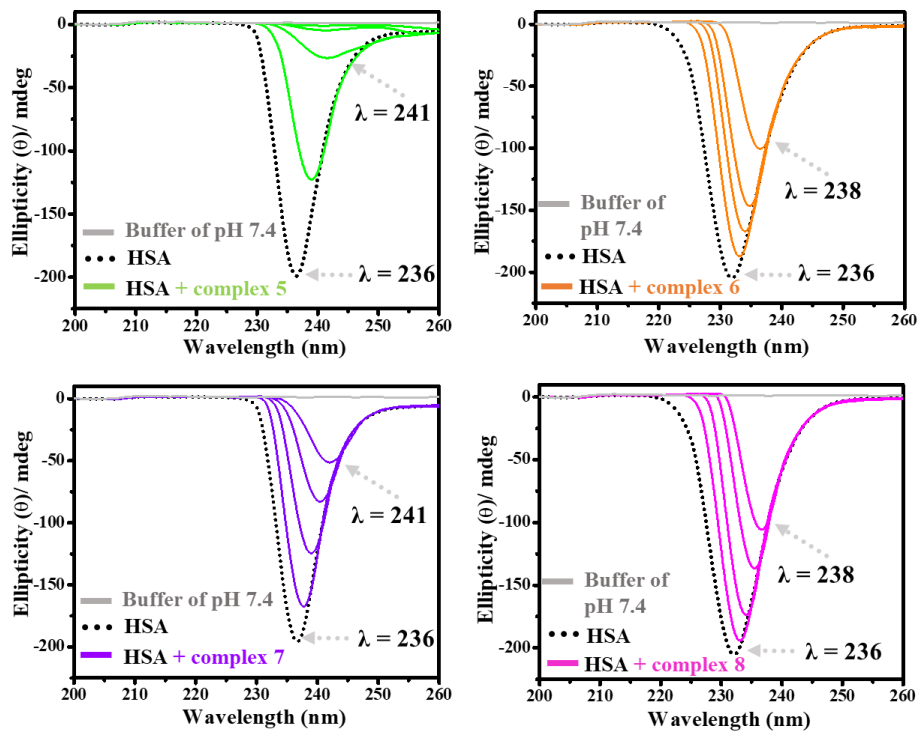


**Figure.3.22:** HSA proteins ( $10 \mu\text{M}$ ) Circular dichroism spectra with or without complex at different concentration (0-40  $\mu\text{M}$ )

### 3.3.5 DNA binding study

#### 3.3.5.1 Absorption spectroscopy

UV-visible spectroscopy is a reliable approach to knowing the interaction between synthesized small molecules with double-stranded DNA helix. Generally, upon spectroscopic titration of complexes to CT-DNA, two kinds of absorption spectral changes with hyperchromic (increased absorbance intensity) and hypochromic (decreased absorbance intensity) shifts are observed. The hypochromic effect arises due to DNA contraction, and hyperchromic shift results from conformational changes in DNA [23]. Complexes **5-8** display significant hyperchromic effect during spectroscopic titration with CT-DNA, signifying non-intercalative interaction. After gradually increasing the concentration of the complexes **5-8**, hyperchromic shifts occur indicating the existence of groove or electrostatic binding (Figure 3.23). The intrinsic binding constant ( $K_b$ ) of complexes-DNA adduct was examined by the Benesi-Hildebrand equation.

By using the Benesi-Hildebrand equation, the slope value of  $1/(\epsilon_b - \epsilon_f)$  and an intercept value of  $1/K_b(\epsilon_b - \epsilon_f)$  was determined by a straight line fitting. The value of  $K_b$  was determined by the ratio of slope to intercept (Table 3.5). The intrinsic binding constant ( $K_b$ ) values of all complexes range between  $10^5$ - $10^6$   $M^{-1}$ ; which indicates a strong binding interactions with DNA.

Moreover, the interaction between DNA and complexes **5-8** was investigated via the theoretical study (DFT), by calculating the energy gap of the HOMO of the DNA molecule and the LUMO of the complexes. It is well established that a higher HOMO of DNA favours transfers of “electron-cloud” to a low lying LUMO of a complex, indicating a stronger interaction between DNA and the complex [24]. In this regard, it could be considered that the energy of the LUMO and the population of the LUMO of complexes **5-8** are the key factors to affect DNA binding. Figure 3.24 clearly shows that order of the energies of the LUMOs of the complexes is:  $\epsilon_L$  (**8**) >  $\epsilon_L$  (**6**) >  $\epsilon_L$  (**5**) >  $\epsilon_L$  (**7**). The theoretical calculations indicate the order of interaction of complexes **5-8** with DNA should be **5 ~ 7** > **6** > **8**. To some extent, these results are similar to the

obtained experimental results. However, a number of other important factors, such as lipophilicity, H-bonding, variation of metal ions, rotational motions etc., can also affect the interaction with DNA [25].

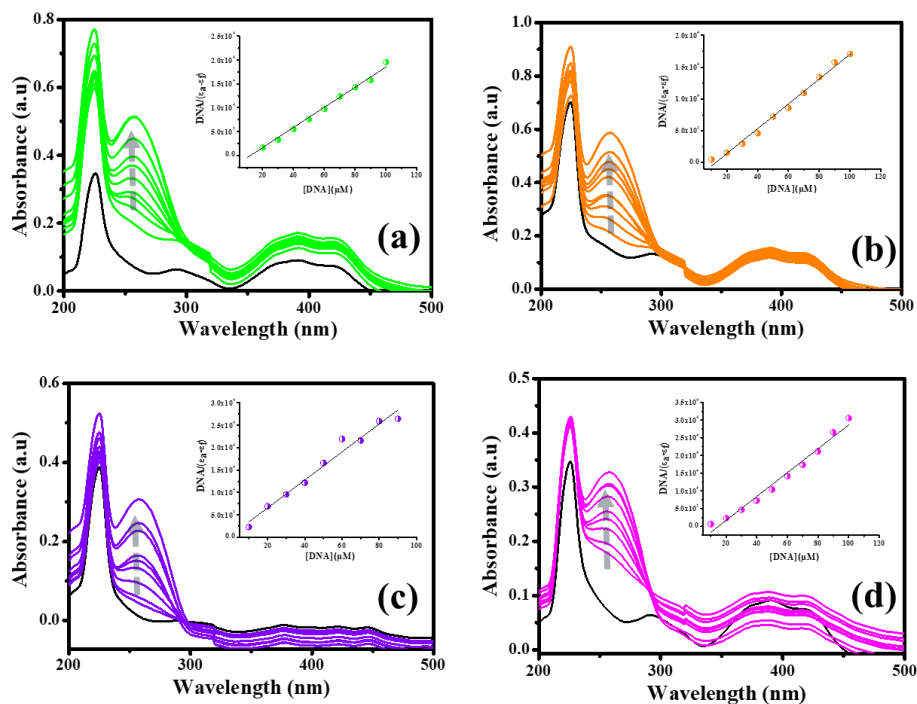


**Figure.3.23:** Absorption titration spectra of complexes 5-8 with CT-DNA (a) complex 5 (b) complex 6 (c) complex 7 and (d) complex 8. Inset: Plots of  $[DNA]$  vs.  $[DNA]/\epsilon_a - \epsilon_f$  for the titration of CT-DNA with the complexes

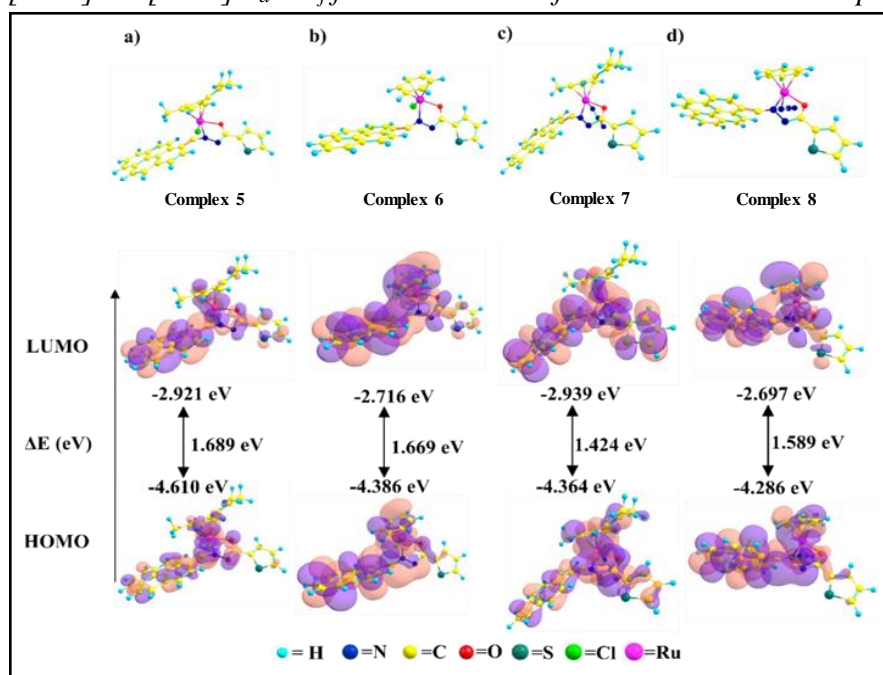


**Figure.3.24:** The molecular orbitals analysis of the optimized complexes and

their corresponding HOMO-LUMO energy gaps (a) complex 5 (b) complex 6 (c) complex 7, and (d) complex 8

### 3.3.5.2 Competitive fluorimetric DAPI displacement assay

A competitive binding assay with DAPI dye was used to examine the DNA-complexes interaction further. DAPI is a blue fluorescent dye with a phenylindole ring that binds to DNA minor grooves. After adding the DNA molecule into the DAPI dye solution, the FL intensity of DAPI dye increases approximately thirty times. Accordingly, the emission spectra of the DNA-DAPI solution were recorded as complex concentrations increased. It was noted that as the molecules of DAPI dye were replaced from their DNA binding sites by adding complexes 5-8, the FL intensity of the DNA-bound DAPI solution decreased (Figure 3.25). The Stern-Volmer equation can be used to calculate the Stern-Volmer quenching constants ( $K_{sv}$ ), apparent binding constant values ( $K_a$ ), and the bimolecular quenching rate constants ( $K_q$ ) (Table 3.5) [26]. For complexes 5-8, the calculated Stern-Volmer quenching constants ( $K_{sv}$ ) are found to be in the range of  $10^3$ - $10^4$ , reflecting that all complexes have significant quenching efficiency and intense interaction with DNA.

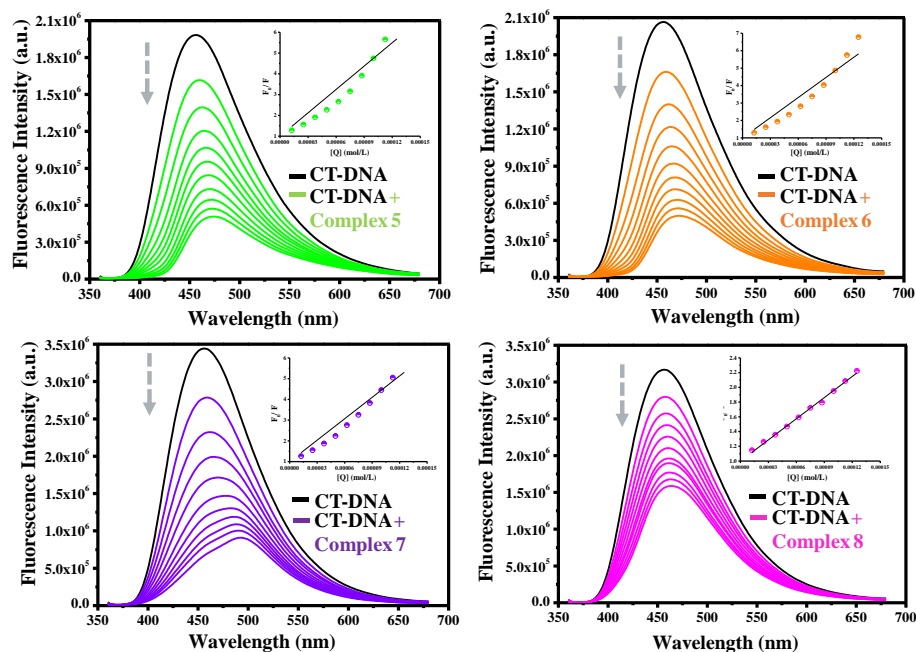


**Figure.3.25:** Fluorescence quenching spectra of DAPI-DNA with complexes 5-8 (0-50  $\mu$ M).

**Table 3.5** Emission<sup>a</sup> and absorption<sup>b</sup> spectral data of DNA interaction with titled compound

Complex	$K_{SV} (M^{-1})^a$	$K_q (M^{-1}S^{-1})^a$	$K_a (M^{-1})^a$	$K_b (M^{-1})^b$
<b>5</b>	$3.8 \times 10^4$	$6.2 \times 10^{12}$	$5.8 \times 10^5$	$1.8 \times 10^6$
<b>6</b>	$3.7 \times 10^4$	$6.0 \times 10^{12}$	$5.7 \times 10^5$	$5.6 \times 10^5$
<b>7</b>	$3.4 \times 10^4$	$5.5 \times 10^{12}$	$4.7 \times 10^7$	$3.7 \times 10^5$
<b>8</b>	$9.5 \times 10^3$	$1.5 \times 10^{12}$	$4.4 \times 10^3$	$1.3 \times 10^5$

<sup>a</sup>Determined by emission <sup>b</sup>Calculated via absorbance spectroscopy.

### 3.3.6 *In vitro* cytotoxicity assay (MTT assay)

The outcome of protein and DNA binding experiments stimulated the idea of checking the antiproliferative capability of synthesized compounds against various cancerous cells. The colorimetric MTT assay was used to evaluate the anticancer activity of all the complexes against the HeLa, A431, and MCF7 cells line. The cytotoxic result of complexes was analyzed by using the cell viability curve (Figure 3.26 and Figure 3.27) and signified with the concentration of the complexes (0-100  $\mu$ M). Compounds **5-8** show good cytotoxicity against the malignant cell lines. Among all complexes, complexes **5** and **6** show better anticancer efficacy than other complexes due to the presence of both chloride group and p-cymene moiety. The p-cymene group provides a stronger hydrophobic interaction with targeted biomolecules, and chloride plays a significant role in the water-halogen exchange reaction. Complex **5** shows low  $IC_{50}$  values signifying higher cytotoxicity toward HeLa, A431, and MCF7 cancer cell lines, respectively (Table 3.6). When tested with normal cell lines like HEK 293 (normal cell line), complexes **5-8** exhibit high  $IC_{50}$  values compared to cancerous cell lines, revealing significant cell selectivity. Interestingly complexes **5-8** exhibited a comparable range of inhibitory concentration ( $IC_{50}$ ) values to the commercially available cisplatin anticancer drug.

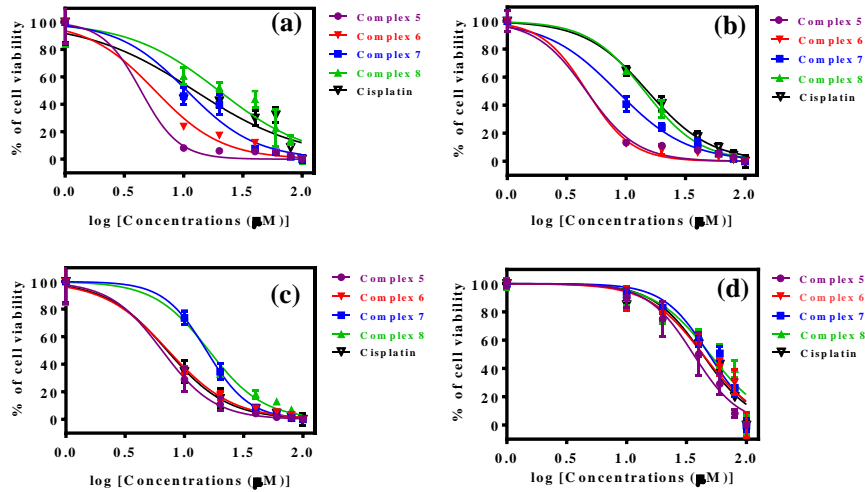


**Figure.3.26:** Cell viabilities curve of complexes 5-8 for respectively cancer cell lines (a) HeLa (b) A431 (c) MCF7 and (d) for HEK 293 (normal cell line)

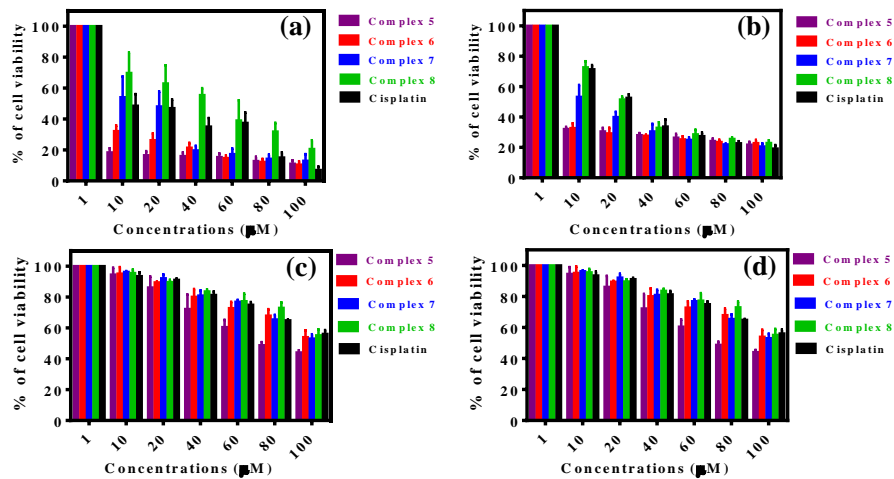


**Figure.3.27:** Cell viabilities curve of complexes 5-8 for respectively cancer cell lines (a) HeLa (b) A431 (c) MCF7 and (d) for HEK 293 (normal cell line)

**Table 3.6** *In vitro* anticancer efficacy of titled compounds against cancerous cell (HeLa, A431, MCF7) and compare with normal cell line (HEK 293) after 24 hours incubation at 37 °C, 5% CO<sub>2</sub>

IC <sub>50</sub> (μM) ± SD				
Complex	HeLa	A431	MCF7	HEK 293
<b>5</b>	<10	<10	6.48 ± 0.07	36.15 ± 0.64
<b>6</b>	<10	<10	7.28 ± 0.06	43.24 ± 0.51
<b>7</b>	10.65 ± 0.24	8.40 ± 0.07	15.32 ± 0.07	48.67 ± 0.33
<b>8</b>	19.78 ± 0.35	14.31 ± 0.06	16.06 ± 0.06	49.72 ± 0.40
<i>Cisplatin</i>	12.35 ± 0.26	15.61 ± 0.09	7.13 ± 0.09	43.08 ± 0.24

### 3.3.7 Inhibition of cell migration

Cell migration and invasion play a pivotal role in various biological processes, such as cancer growth and metastasis [27]. At a later period of cancer evolution, metastasis makes the disease more aggressive and difficult to contain. Malignant cancer cells have the potential to, migrate to non-malignant cells or tissues away from the primary tumour and proliferate there. Therefore, metastasis inhibition study is one of the vital research areas in advanced cancer treatment [28,29]. To evaluate compounds' effect on migration capacity, HeLa cells were treated with complexes **5-8** at their IC<sub>50</sub> values and analyzed for cell migration with time intervals. After 24 hr of drug treatment, treated cells showed little or no migration in the scratched wound region while PBS treated cells (without drug treatment) migrated to the scratched wound side significantly (Figure 3.28). Results obtained suggests that complexes **5-8** could reduce substantially the migratory ability of cancerous cells.

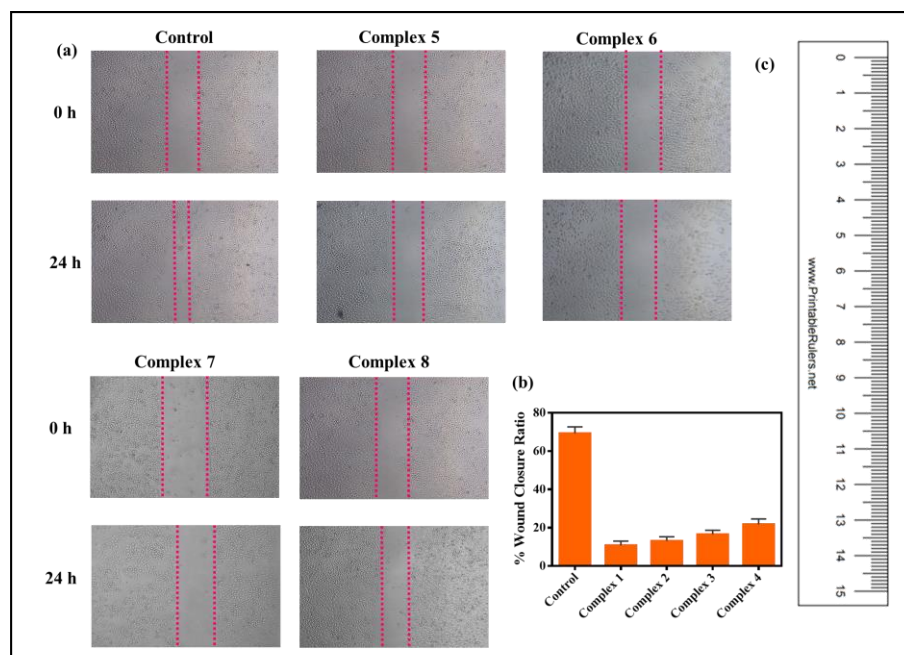


**Figure.3.28:** (a) Wound healing motility assay of HeLa untreated and treated cell with complexes 5-8, Image were taken at 0 and 24 h (b) Histogram of wound closure ratio of heal wound at 24 h (c) Measuring scale

### 3.3.8 NADH Catalytic Oxidation and generation of Reactive Oxygen Species (ROS)

In any biological system, reducing and oxidizing agents play an important role in maintaining the cell redox status for cell survival. In several biological and biocatalyzed processes such as cell death and energy metabolism, one redox couple nicotinamide adenine dinucleotide (NADH) and its oxidized form of  $\text{NAD}^+$  act as the coenzyme [30]. Previously it is reported that the anticancer half sandwich Ir(III) and Ru(II) arene complexes can take up a hydride from NADH and increase the production of ROS, thereby providing a pathway to an oxidant mechanism of cell death [31]. To investigate similar NADH catalytic activity of all complexes, 100  $\mu\text{M}$  NADH was incubated in a 10% MeOH + 90%  $\text{H}_2\text{O}$  solution as a control and the catalytic ability of all the complexes 5-8 with NADH was monitored through UV-Visible spectroscopy at 298 K in different time intervals. Since NADH has an absorbance at 339 nm, but  $\text{NAD}^+$  does not show an absorbance at 339 nm, it is straightforward to observe NADH to  $\text{NAD}^+$  catalytic conversion at the absorbance peak at 339 nm [32].

Turnover numbers (TONs) of complexes **5-8** were determined with the help of UV absorption spectra 15.52, 15.04, 11.64 and 10.19 are the values calculated for the complexes **5**, **6**, **7** and **8** respectively (Figure 3.29). The extent of conversion of NADH to NAD<sup>+</sup> depends not only on the arene ring but also on the lability of the leaving group. The complexes with para-cymene ring show a faster conversion than the benzene ring due to the presence of the strong electron donating methyl substituent; therefore, complex **5** shows the most rapid transformation among all the complexes and possesses the highest TON value. It shows that the ruthenium metal center can play an important role in reducing the catalytic activity and conversion of NADH to NAD<sup>+</sup>, thereby providing a potential pathway to produce ROS and increase cancer cell death via an oxidant mechanism [33]. Furthermore, the capacity of all complexes to cause ROS generation was evaluated by treating MCF7 cells with complexes close to their IC<sub>50</sub> values and using untreated MCF7 cells as a control. After examining the data, it was concluded that treated cells significantly increase the generation of ROS in MCF7 cells compared to the untreated cells (Figure 3.30).

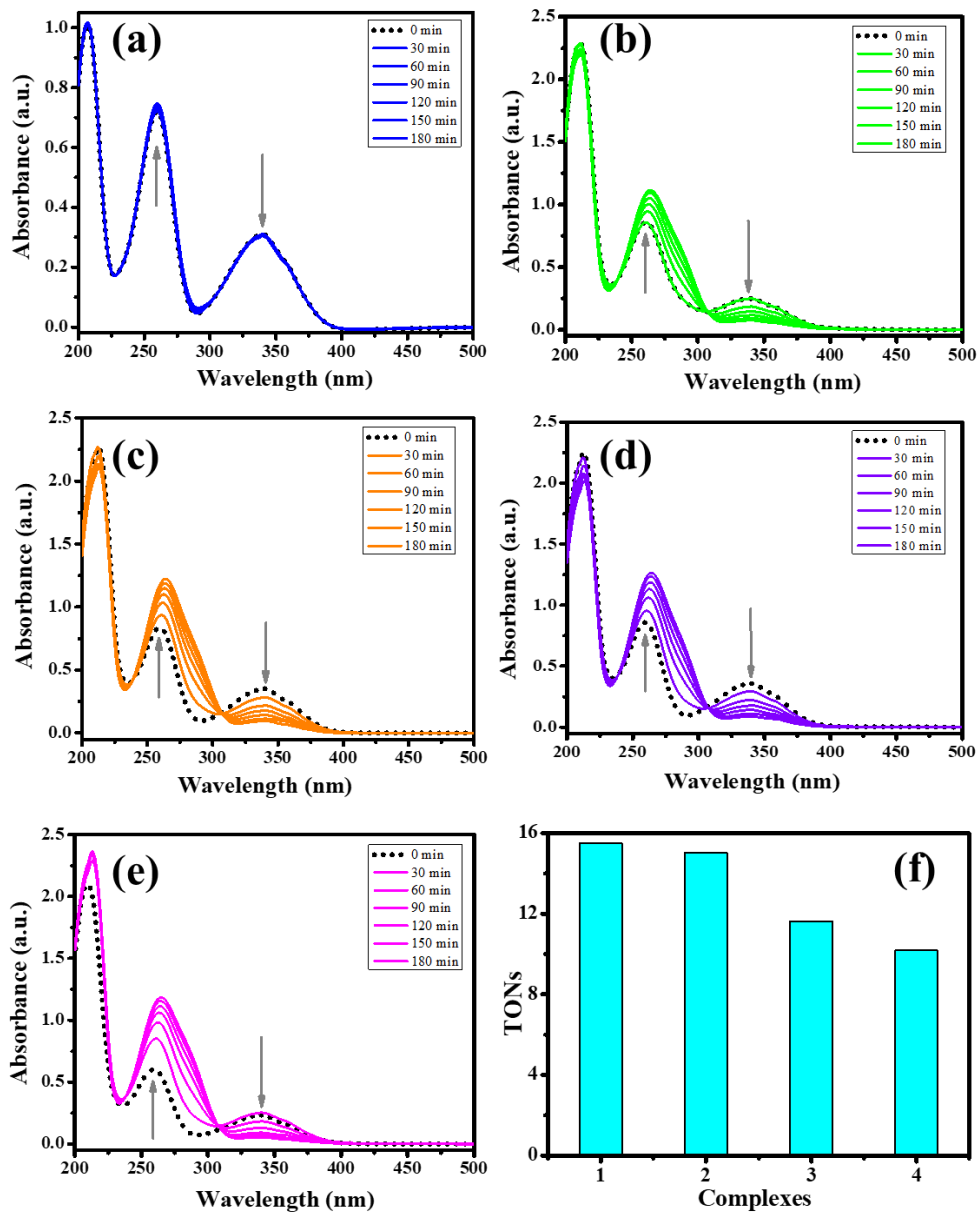


**Figure.3.29:** UV-visible spectra of complexes 5-8 ( $3 \mu\text{M}$ ) react with NADH ( $100 \mu\text{M}$ ) (a) only NADH (b) complex 5 (c) complex 6 (d) complex 7 (e) complex 8 and (f) Histogram graph of complexes 5-8 turnover numbers(TONs)

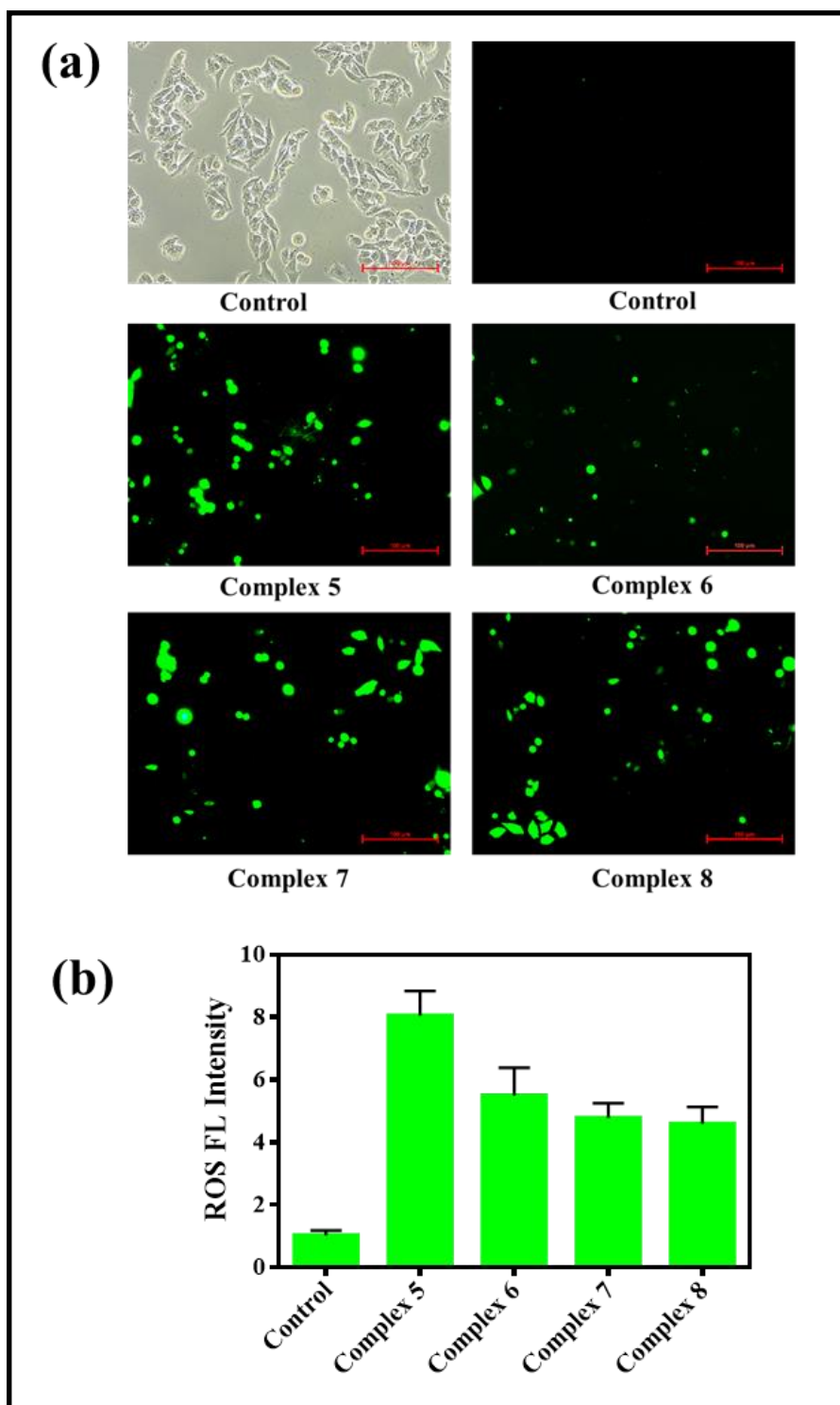
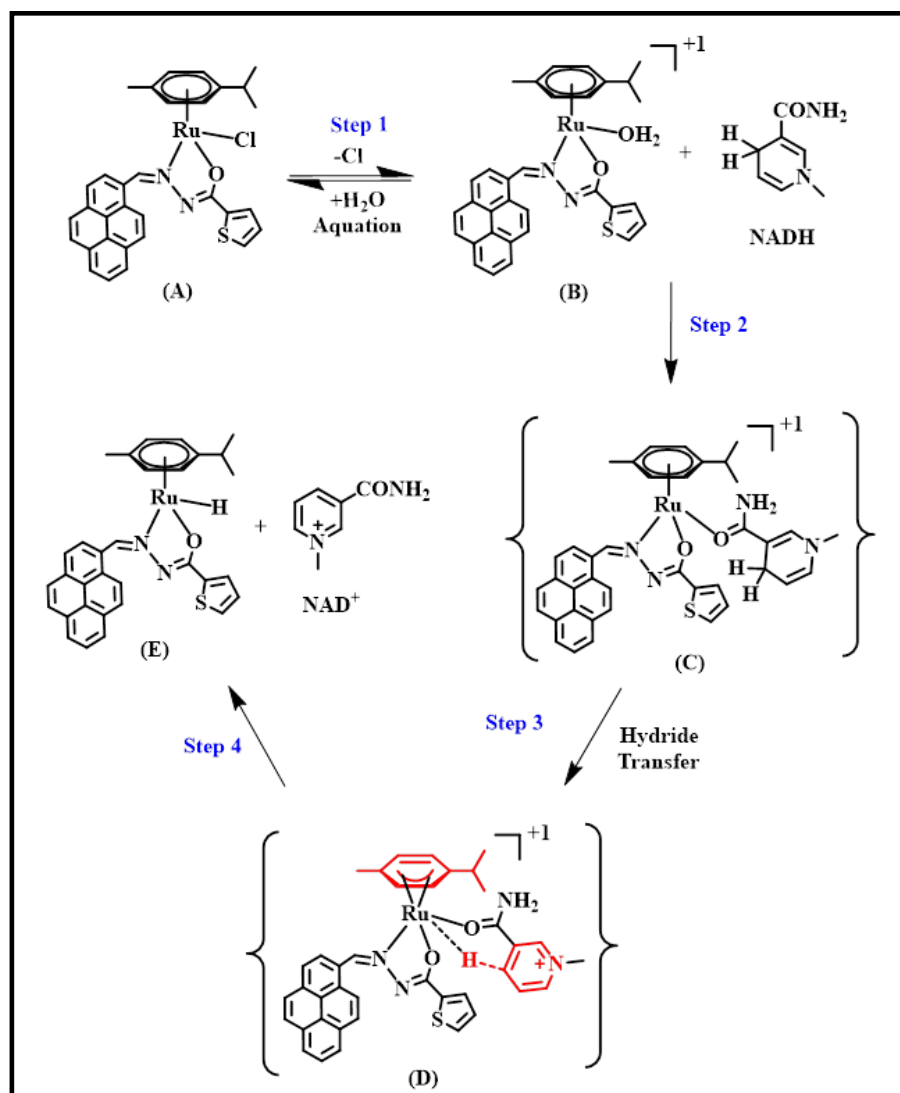


**Figure.3.30:** (a) Inverted microscopic image of ROS generation, treated and untreated HeLa cells through DCFH-DA fluorescence staining procedure (b) Fluorescence intensity graph of ROS

### 3.3.8.1 Theoretical Study of NADH Oxidation

The probable mechanism for the oxidative conversion of NADH to NAD<sup>+</sup> by Ru(II) complexes **5–8** involves the transfer of hydride from NADH to the Ru(II) center and the formation of the kinetically favored six membered ring transition state. It happens via a ring slippage mechanism, creating a vacant hydride coordination site. A plausible mechanism has been proposed for complex **5**, having the best TON value (Scheme 3.2). Density-functional theory (DFT) calculations were used to investigate the NADH oxidation pathway. Figure 3.31 represents the free energy diagram of the proposed mechanism and all the equilibrium geometries of reaction steps. In the first step of the reaction, to structure **A** whose free energy is set as 0.0 kcal/mol as a reference of the reaction, one H<sub>2</sub>O molecule is added and Cl<sup>-</sup> has been removed. Completion of this reaction gives the structure **B** and the detailed reaction pathways with the mechanism is shown in Figure 3.31 with the changes of free energy during the reactions. The equilibrium geometry of **B** is shown in Figure 3.31(b). This reaction involves a free energy change ( $\Delta G$ ) of about -40.21 kcal/mol. The next step of the reaction occurs with the addition of NADH to structure **B**, and the formation of structure **C** takes place by change of free energy ( $\Delta G$ ) about -2.21 kcal/mol. The equilibrium geometry of **C** is shown in Figure 3.31(c). These two reaction steps are thermodynamically favourable and spontaneous i.e., for the completion of these two steps, no additional energy is required. The next step proceeds from **C** to **D** by hydride transfer, and the free energy change in this step was calculated to be +12.26 kcal/mol. In the final step, NAD<sup>+</sup> is added to the structure **D**, and the formation of structure **E** takes place with the change of free energy +6.62 kcal/mol. The change in free energy of the last two steps is positive which means that for the completion of these two steps additional energy from outside is required. The equilibrium geometries of structures **D** and **E** are shown in Figure 3.31 (d) and (e), respectively.



*Scheme.3.2: The Probable mechanism of catalytic oxidation of NADH to NAD<sup>+</sup> for complex 5*

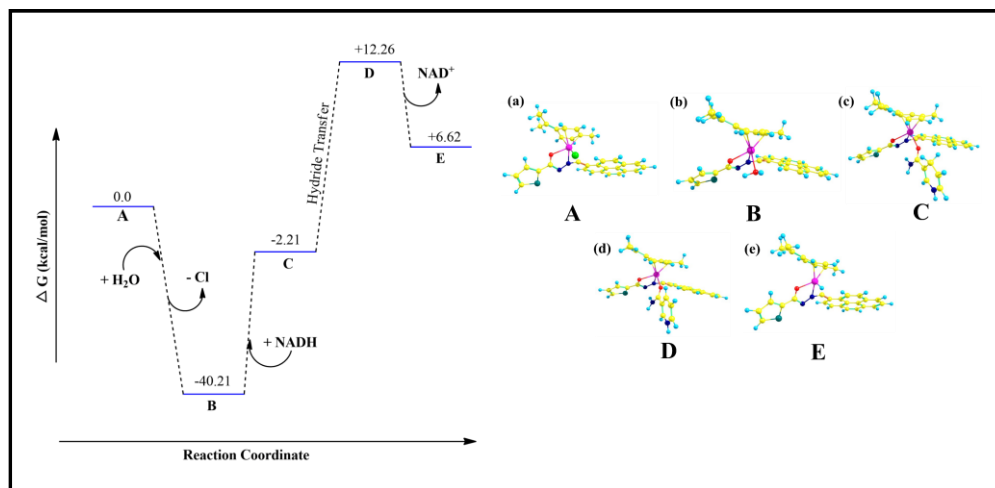


**Figure.3.31:** Reaction free energy profile diagram of the proposed mechanism for complex 5

### 3.3.9 Two-photon cell imaging study

Due to its low cell damage, ease of dynamic observation and high resolution, two-photon fluorescence cell imaging has attracted interest in the biological and medical fields [34]. Considering the above facts, the two-photon fluorescent cell imaging study in cancer (HeLa) cells was also carried out. HeLa cells were stained and treated with complexes **5-8** close to their  $IC_{50}$  values and captured the images of cell through the help of a confocal microscope. To correlate the imaging efficiency of synthesized compounds, DAPI dye was used as a positive control. After incubating HeLa cells with the complexes **5-8** for 24 hours, an excitation laser source of 790 nm was used to obtain two-photon fluorescence. The result displays significant uptake behaviour of complexes **5-8** into the treated cells with a bright blue emission and clear evidence of considerable morphological changes of nuclei, multinucleation and nuclear swelling together with the selective staining (Figure 3.32). Complexes **5-8** exhibit dual behaviour of good anticancer efficacy with two photon microscopic bio-imaging properties, making them promising candidates for cancer treatment in the future.

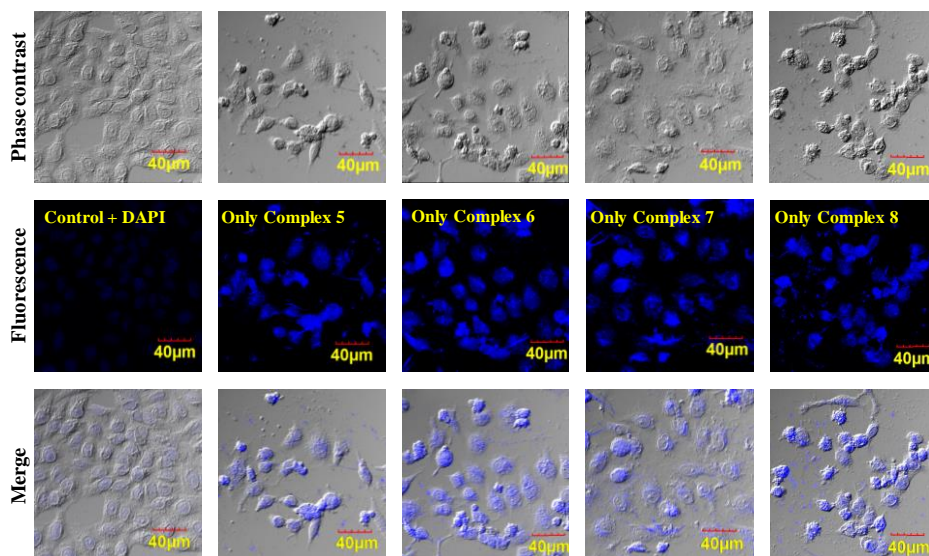


**Figure.3.32:** Two-photon confocal laser scanning microscopy images in HeLa cells (excitation at 790 nm)

### 3.3.10 Dual Staining (Hoechst/PI and AO/EtBr)

A fluorescence staining experiment with DNA binding dyes, namely Hoechst and PI, was done to investigate cell morphological changes during apoptosis after drug treatment. Hoechst dye is a cell-permeable dye that stains dead and live cells. In contrast, PI dye is membrane impermeable and generally precluded to live cells [35]. With the aid of the confocal microscopic technique, substantial changes were observed in the morphology of cancer cells after treating the cells with complexes **5-8**. The non-viable cell stain shows apoptotic nuclei with bright blue or intense red fluorescence with condensed and fragmented nuclei. In contrast, untreated cells show uniformly light blue fluorescence, which describes no nuclear disruption (Figure 3.33a). For further investigation, the dual staining assay with acridine orange/EtBr dye (5µg/mL) was done the same way as the Hoechst/PI dye staining experiment (Figure 3.33b). These experiments clearly show that drugs can potentially trigger apoptosis in cancer cells.

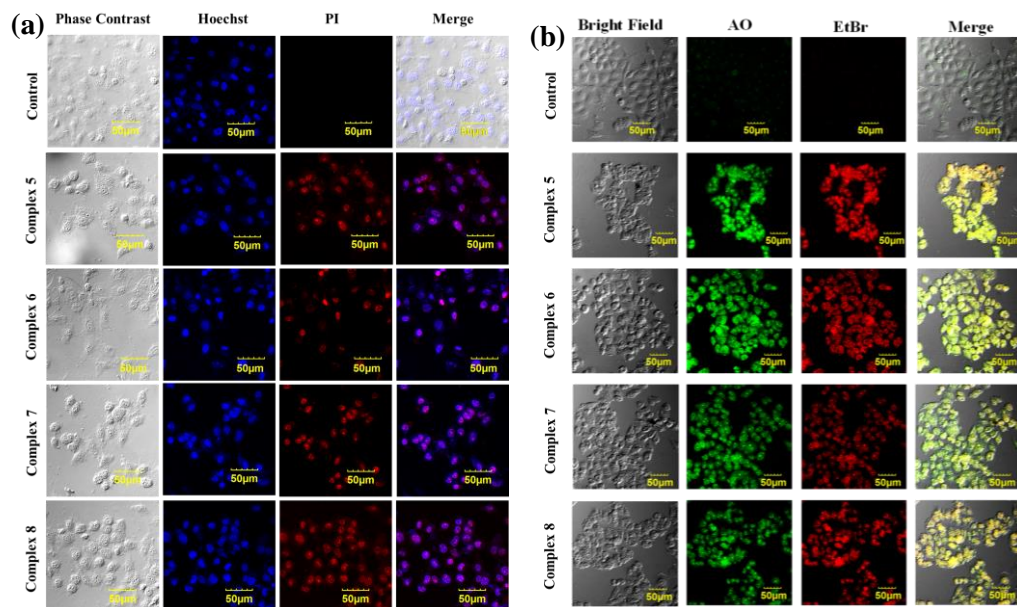


**Figure.3.33:** (a) Hoechst and PI, (b) Acridine orange and EtBr double staining confocal microscopy images of HeLa cells after complexes 5-8 treatment and cells without treatment as a control

### 3.3.11 Molecular docking study

A molecular docking study was performed to determine the binding sites and binding mode of interaction of synthesized compounds with biomolecule i.e. DNA and proteins (HSA and BSA). The dodecamer d(CGCGAATTCGCG)<sub>2</sub> (PDBID: 355D) duplex DNA sequence was employed. The cif files of complexes were obtained from their single crystal XRD analysis to have the exact conformation. To obtain the protein confirmation, the X-ray structure of HSA and BSA protein with PDB ID 5K2C and 3V03 were used. It clarifies from the docking profiles that complex **5** and complex **6** interact with the minor grooves region of DNA (binding energy = -8.5 kcal/mole for **5** and -8.8 kcal/mol for **6** and molecular docked profile of complex **5** and **6** with HSA and BSA are situated in the deep hydrophobic region of proteins, where the complexes are enclosed within the cavity by the polar and charged residues of the amino acids (Figure 3.34). The binding of BSA (binding energy = -7.9 kcal/mole for **5** and -7.7 kcal/mole for **6**) and HSA (binding energy = -9.0 kcal/mole for **5** and -8.0 kcal/mole for **6**) were found to be interacting with free

chloro groups of complexes. Vander Waals interactions and H-bonding are found to be the main driving forces of protein-complex interactions [36].

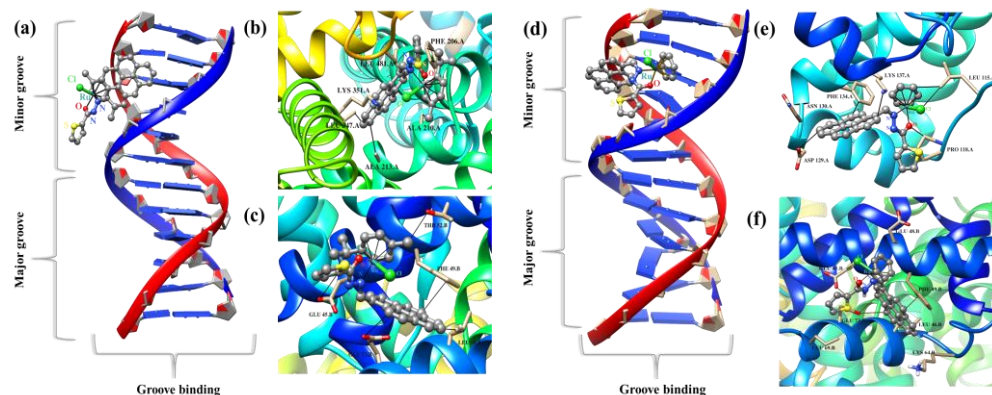


**Figure.3.34:** Docking images of complex 5 with (a) DNA (b) HSA and (c) BSA and complex 6 with (d) DNA (e) HSA and (f) BSA

### 3.3.12 Density functional theory (DFT) study

The finite molecular model system was constructed to explore the detailed chemical reactions and equilibrium structures of the complexes, and this model system has been developed to support the experiments. The equilibrium structures of molecular cluster models are depicted in (Figure 3.35). The equilibrium transition states (TSs) the appeared during the reactions are shown in Figure 3.36. According to the density functional theory calculations, all the equilibrium structures are thermodynamically stable, and the results are consistent with the experimental findings. The molecular modelling of the reaction pathways of formation of the four arene ruthenium (II) dimer complexes was used to explore the chemical reaction mechanisms and to explain the formation of the adducts, complexes, TSs and products by employing the first principles-based quantum mechanical (QM) DFT method. Thermodynamic and vibrational frequency calculations reveal that the products, Complex-5, Complex-6, Complex-7, and Complex-8, formed in the chemical reactions are thermodynamically and energetically stable, as no imaginary frequency is present in the equilibrium geometries of all the stable complexes and adducts (A-1, A-2, A-3, and A-4) as well. The adducts A-1, A-2, A-3 and A-4 are formed by the chemical reactions between the ligands and ruthenium arene dimers which are formed four complexes i.e., Complex 5, 6,

7, and 8, respectively, as products after completing the chemical reactions. A reaction between the ruthenium dimer complexes and the ligand HL formed the adducts, and they have been studied here to investigate the interactions during the initial step of the chemical reaction. To understand the chemical reaction mechanism, and the energy barriers in the reaction, the B3LYP DFT approach was used with the same level of theory to calculate the changes in enthalpy ( $\Delta H$ ) and relative Gibbs free energy ( $\Delta G$ ) in the reactions. The Figure 3.35 shows the reaction path, in which the transition states (TSs) show are intermediate state between adduct and product. Here, the complex 5 was formed via the Transition State-1 i.e.TS-1, with the reaction barriers ( $\Delta G$ ) 6.5 kcal/mol computed by the DFT method. Similarly, complex-6, 7 and 8 were formed via Transition States TS-2, 3, and 4, with the reaction barriers ( $\Delta G$ ) 6.9, 6.8 and 6.7 kcal/mol respectively. The TS-1, TS-2, TS-3 and TS-4 are connected between the adducts (A-1, A-2, A-3 and A-4) and corresponding products (Complex 5, Complex 6, Complex 7, and Complex 8) as displayed in the figure 3.36. The barrier energies of complexes were calculated with respect to the adducts. The barrier energy in terms of  $\Delta G$  of the complexes 5, 6, 7 and 8 are -6.3, -5.7, -6.7 and -6.8 kcal/mol; and  $\Delta H$  of the complexes are -7.0, -7.6, -6.24 and -7.0 kcal/mol, respectively, which indicate that the all the systems are thermodynamically stable. The DFT calculation presented here reveals that the reaction pathways are energetically favourable with a small reaction barrier about 6.5 – 6.9 kcal/mol.

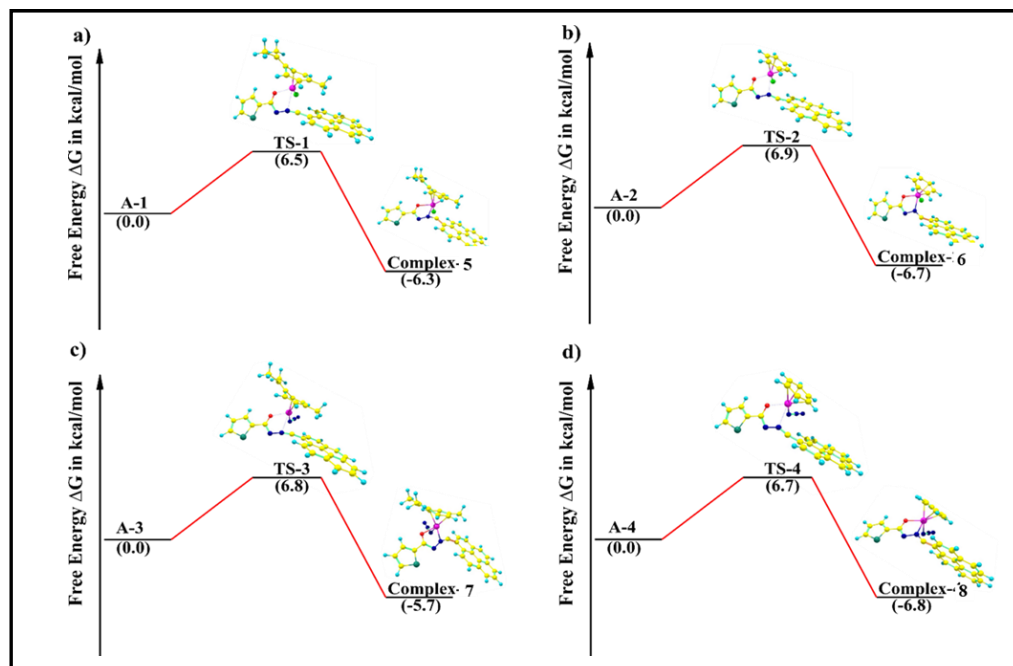


**Figure.3.35:** a) Reaction path of the  $[(\eta^6\text{-p-cymene})\text{RuCl}_2]_2$  and ligand, **HL** with adduct A-1, TS-1, and complex 5; b) reaction path of the  $[(\eta^6\text{-benzene})\text{RuCl}_2]_2$  and ligand, **HL** with adduct A-2, TS-2, and complex 6; c) reaction path of the  $[(\eta^6\text{-p-cymene})\text{Ru}(\text{N}_3)_2]_2$ , and ligand, **HL** with adduct A-3, TS-3, and complex 7; d) reaction path of the  $[(\eta^6\text{-benzene})\text{Ru}(\text{N}_3)_2]_2$  and ligand, **HL** with adduct A-4, TS-4, and complex 8 are shown here

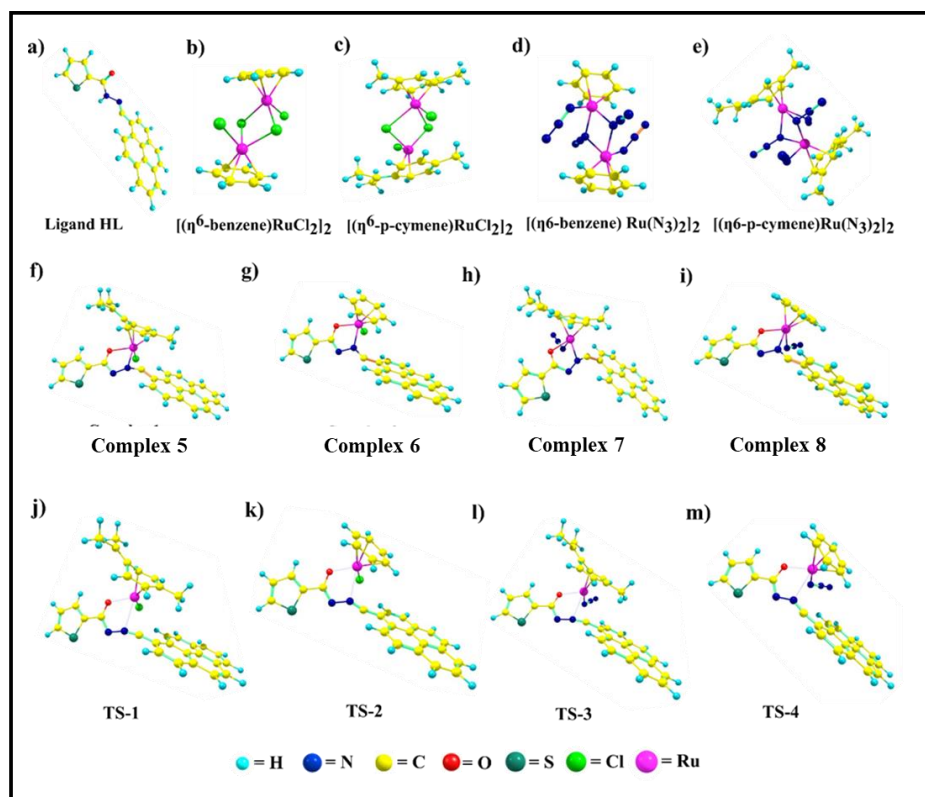


**Figure.3.36:** Equilibrium geometries computed by the DFT method are presented here; a) Ligand, HL, b)  $[(\eta^6\text{-benzene})\text{RuCl}_2]_2$ , c)  $[(\eta^6\text{-p-cymene})\text{RuCl}_2]_2$ , d)  $[(\eta^6\text{-benzene})\text{Ru}(\text{N}_3)_2]_2$ , e)  $[(\eta^6\text{-p-cymene})\text{Ru}(\text{N}_3)_2]_2$ , f) Complex 5, g) Complex 6, h) Complex 7, i) Complex 8, j) TS-1 is the transition state between A1 adduct and Complex 5 product. k) TS-2 is the transition state between A2 adduct and Complex 6 product. l) TS-3 is the transition state between A3 adduct and Complex 7 product. m) TS-4 is the transition state between A4 adduct and Complex 8 product

### 3.4 Conclusions

Four Ru(II) arene complexes have been synthesized and characterized through various spectroscopic techniques. The single crystal X-ray experiments revealed the molecular structure of the complexes with pseudo-octahedral geometry. The biological interaction studies of the complexes demonstrate significant binding of the compounds with DNA and protein (HSA, BSA). Through the DFT method, the interaction between DNA and complexes has been investigated by calculating the molecular orbitals (HOMO and LUMO) energy and the results found are in accordance with the obtained experimental

results. The *in vitro* anticancer efficacy of complexes **5** and **6** is found to be higher than complexes **7** and **8** towards HeLa, A549 and MCF7 cell lines. All the complexes can catalyze the oxidation of NADH to NAD<sup>+</sup> which increase ROS production causing cell deaths. Furthermore, a plausible mechanistic pathway for the conversion of NADH to NAD<sup>+</sup> has been explored through computational study (DFT) with the free energy diagram of the proposed mechanism and all the equilibrium geometries of reaction steps. Hoechst and PI dual staining were used to elaborate on the probable mechanism of cell death. It was observed that these complexes can exhibit their cytotoxicity through apoptosis. Meanwhile, complexes are found to be efficient in preventing cell migration which is one of the significant steps of metastasis.

### 3.5 Declaration:

This chapter is adapted from Dalton Transactions, 2022, 51(10), 3937-3953. (DOI: 10.1039/d1dt04093f)

### 3.6 References:

- [1] Pragti, Kundu, B. K., and Mukhopadhyay, S. (2021), *Coord. Chem. Rev.*, 448, 214169. (DOI: 10.1016/j.ccr.2021.214169).
- [2] Ndagi, U., Mhlongo, N., & Soliman, M. E. (2017), *Metal complexes in cancer therapy—an update from drug design perspective. Drug design, development and therapy*, 599-616. (DOI: 10.2147/DDDT.S119488).
- [3] Zaki, M., Arjmand, F., & Tabassum, S. (2016), *Current and future potential of metallo drugs: Revisiting DNA-binding of metal containing molecules and their diverse mechanism of action. Inorganica Chimica Acta*, 444, 1-22. (DOI: 10.1016/j.ica.2016.01.006).
- [4] Gatti, A., Habtemariam, A., Romero-Canelón, I., Song, J. I., Heer, B., Clarkson, G. J., ... & Carcelli, M. (2018), *Half-sandwich arene ruthenium (II) and osmium (II) thiosemicarbazone complexes: solution behavior and antiproliferative activity. Organometallics*, 37(6), 891-899. (DOI: 10.1021/acs.organomet.7b00875).

- [5] Fernández-Moreira, V., Thorp-Greenwood, F. L., & Coogan, M. P. (2010), Application of d6 transition metal complexes in fluorescence cell imaging. *Chemical communications*, 46(2), 186-202. (DOI: 10.1039/B917757D).
- [6] Ghanghas, P., Choudhary, A., Kumar, D., & Poonia, K. (2021), Coordination metal complexes with Schiff bases: Useful pharmacophores with comprehensive biological applications. *Inorganic Chemistry Communications*, 130, 108710. (DOI: 10.1016/j.inoche.2021.108710).
- [7] Nagalakshmi, V., Nandhini, R., Brindha, V., Krishnamoorthy, B. S., & Balasubramani, K. (2020), Half-sandwich ruthenium (II) complexes containing biphenylamine based Schiff base ligands: Synthesis, structure and catalytic activity in amidation of various aldehydes. *Journal of Organometallic Chemistry*, 912, 121175. (DOI: 10.1016/j.jorganchem.2020.121175).
- [8] Abeywickrama, C. S., Wijesinghe, K. J., Plescia, C. B., Fisher, L. S., Goodson, T., Stahelin, R. V., & Pang, Y. (2020), A pyrene-based two-photon excitable fluorescent probe to visualize nuclei in live cells. *Photochemical & Photobiological Sciences*, 19, 1152-1159. (DOI: 10.1039/d0pp00107d).
- [9] Lee, C., Yang, W., & Parr, R. G. (1988), *Phys. Rev. B: Condens. Matter Mater. Phys*, 37, 785–789. (DOI: 10.1103/PhysRevB.37.785).
- [10] Becke, A. D. (1992), Density-functional thermochemistry. I. The effect of the exchange-only gradient correction. *The Journal of chemical physics*, 96(3), 2155-2160.
- [11] Hui, J., Pakhira, S., Bhargava, R., Barton, Z. J., Zhou, X., Chinderle, A. J., ... & Rodríguez-López, J. (2018), Modulating electrocatalysis on graphene heterostructures: physically impermeable yet electronically transparent electrodes. *ACS nano*, 12(3), 2980-2990. (DOI: 10.1021/acsnano.8b00702).
- [12] Sinha, N., Deshpande, I., & Pakhira, S. (2019), Substituents Effects of Organic Linkers on Rotational Energy Barriers in Metal-Organic Frameworks. *ChemistrySelect*, 4(29), 8584-8592. (DOI: 10.1002/slct.201901278).
- [13] Kundu, B. K., Pragti, Reena, Mobin, S. M., & Mukhopadhyay, S. (2019), Mechanistic and thermodynamic aspects of a pyrene-based fluorescent probe

to detect picric acid. *New Journal of Chemistry*, 43(29), 11483-11492. (DOI: 10.1039/C9NJ02342A).

[14] Subarkhan, M. K. M., Ren, L., Xie, B., Chen, C., Wang, Y., & Wang, H. (2019), Novel tetranuclear ruthenium (II) arene complexes showing potent cytotoxic and antimetastatic activity as well as low toxicity in vivo. *European journal of medicinal chemistry*, 179, 246-256. (DOI: 10.1016/j.ejmech.2019.06.061).

[15] Li, J., Zeng, L., Xiong, K., Rees, T. W., Jin, C., Wu, W., ... & Chao, H. (2019), A biotinylated ruthenium (ii) photosensitizer for tumor-targeted two-photon photodynamic therapy. *Chemical Communications*, 55(73), 10972-10975. (DOI: 10.1039/C9CC05826E).

[16] Mandal, P., Kundu, B. K., Vyas, K., Sabu, V., Helen, A., Dhankhar, S. S., ... & Mukhopadhyay, S. (2018), Ruthenium (ii) arene NSAID complexes: inhibition of cyclooxygenase and antiproliferative activity against cancer cell lines. *Dalton transactions*, 47(2), 517-527. (DOI: 10.1039/C7DT03637J).

[17] Mandal, P., Malviya, N., Kundu, B. K., Dhankhar, S. S., Nagaraja, C. M., & Mukhopadhyay, S. (2018). RAPTA complexes containing N-substituted Tetrazole scaffolds: Synthesis, characterization and Antiproliferative activity. *Applied Organometallic Chemistry*, 32(3), e4179. (DOI: 10.1002/aoc.4179).

[18] Kumar, R. R., Ramesh, R., & Małeckı, J. G. (2018), Synthesis and structure of arene ruthenium (II) benzhydrazone complexes: Antiproliferative activity, apoptosis induction and cell cycle analysis. *Journal of Organometallic Chemistry*, 862, 95-104. (DOI: 10.1016/j.jorganchem.2018.03.013).

[19] Kundu, B. K., Pragti, Mobin, S. M., & Mukhopadhyay, S. (2020), Studies on the influence of the nuclearity of zinc (ii) hemi-salen complexes on some pivotal biological applications. *Dalton Transactions*, 49(43), 15481-15503. (DOI: 10.1039/D0DT02941F).

[20] Mandal, S., Kundi, V., Seth, D. K., Srikanth, K., & Gupta, P. (2014). Studies on ruthenium complexes of pyrene-appended Schiff base ligands. *Polyhedron*, 80, 290-297. (DOI: 10.1016/j.poly.2014.06.005).

- [21] Vinoth, G., Indira, S., Bharathi, M., Archana, G., Alves, L. G., Martins, A. M., & Bharathi, K. S. (2021), Catalytic conversion of 2, 4, 5-trisubstituted imidazole and 5-substituted 1H-tetrazole derivatives using a new series of half-sandwich ( $\eta^6$ -p-cymene) Ruthenium (II) complexes with thiophene-2-carboxylic acid hydrazone ligands. *Inorganica Chimica Acta*, 516, 120089. (DOI: 10.1016/j.ica.2020.120089).
- [22] Chaves, O. A., Fernandes, T. V. A., de Melos, J. L. R., Netto-Ferreira, J. C., & Echevarria, A. (2020), Elucidation of the interaction between human serum albumin (HSA) and 3, 4-methylenedioxyde-6-iodo-benzaldehyde-thiosemicarbazone, a potential drug for *Leishmania amazonensis*: Multiple spectroscopic and dynamics simulation approach. *Journal of Molecular Liquids*, 310, 113117. (DOI: 10.1016/j.molliq.2020.113117).
- [23] Mandal, S., Kundi, V., Seth, D. K., Srikanth, K., & Gupta, P. (2014). Studies on ruthenium complexes of pyrene-appended Schiff base ligands. *Polyhedron*, 80, 290-297. (DOI: 10.1016/j.poly.2014.06.005).
- [24] Kurita, N., & Kobayashi, K. (2000). Density functional MO calculation for stacked DNA base-pairs with backbones. *Computers & chemistry*, 24(3-4), 351-357. (DOI: 10.1016/S0097-8485(99)00071-6).
- [25] Zou, X. H., Ye, B. H., Li, H., Zhang, Q. L., Chao, H., Liu, J. G., ... & Li, X. Y. (2001), The design of new molecular" light switches" for DNA. *JBIC Journal of Biological Inorganic Chemistry*, 6, 143-150. (DOI: 10.1007/s007750000183).
- [26] Lakowicz, J. R. (2013), Principles of fluorescence spectroscopy. Springer Science & Business. Media. (DOI: 10.1007/s00216-007-1822-x).
- [27] Chambers, A. F., Groom, A. C., & MacDonald, I. C. (2002), Dissemination and growth of cancer cells in metastatic sites. *Nature Reviews Cancer*, 2(8), 563-572. (DOI: 10.1038/nrc865).
- [28] Liu, X., Hao, H., Ge, X., He, X., Liu, Y., Wang, Y., ... & Liu, Z. (2019). Triphenylamine-appended cyclometallated iridium (III) complexes: Preparation, photophysical properties and application in biology/luminescence

- imaging. *Journal of Inorganic Biochemistry*, 199, 110757. (DOI: 10.1016/j.jinorgbio.2019.110757).
- [29] Kundu, B. K., Praggi, Carlton Ranjith, W. A., Shankar, U., Kannan, R. R., Mobin, S. M., ... & Mukhopadhyay, S. (2021), Cancer-targeted chitosan–biotin-conjugated mesoporous silica nanoparticles as carriers of zinc complexes to achieve enhanced chemotherapy in vitro and in vivo. *ACS Applied Bio Materials*, 5(1), 190-204. (DOI: 10.1021/acsabm.1c01041).
- [30] Christensen, C. E., Karlsson, M., Winther, J. R., Jensen, P. R., & Lerche, M. H. (2014), Non-invasive in-cell determination of free cytosolic [NAD<sup>+</sup>]/[NADH] ratios using hyperpolarized glucose show large variations in metabolic phenotypes. *Journal of Biological Chemistry*, 289(4), 2344-2352. (DOI: 10.1074/jbc.M113.498626).
- [31] Betanzos-Lara, S., Liu, Z., Habtemariam, A., Pizarro, A. M., Qamar, B., & Sadler, P. J. (2012), Organometallic ruthenium and iridium transfer-hydrogenation catalysts using coenzyme NADH as a cofactor. *Angewandte Chemie*, 124(16), 3963-3966. (DOI: 10.1002/ange.201108175).
- [32] Du, Q., Guo, L., Tian, M., Ge, X., Yang, Y., Jian, X., ... & Liu, Z. (2018), Potent half-sandwich iridium (III) and ruthenium (II) anticancer complexes containing a P<sup>^</sup> O-chelated ligand. *Organometallics*, 37(17), 2880-2889. (DOI: 10.1021/acs.organomet.8b00402).
- [33] Xu, Z., Kong, D., He, X., Guo, L., Ge, X., Liu, X., ... & Liu, Z. (2018), Mitochondria-targeted half-sandwich ruthenium II diimine complexes: Anticancer and antimetastasis via ROS-mediated signalling. *Inorganic Chemistry Frontiers*, 5(9), 2100-2105. (DOI: 10.1039/C8QI00476E).
- [34] Ye, Q., Chen, S., Zhu, D., Lu, X., & Lu, Q. (2015), Preparation of aggregation-induced emission dots for long-term two-photon cell imaging. *Journal of Materials Chemistry B*, 3(15), 3091-3097. (DOI: 10.1039/C5TB00207A).
- [35] Sharma, G., Rana, N. K., Singh, P., Dubey, P., Pandey, D. S., & Koch, B. (2017), p53 dependent apoptosis and cell cycle delay induced by heteroleptic

complexes in human cervical cancer cells. *Biomedicine & Pharmacotherapy*, 88, 218-231. (DOI: 10.1016/j.biopha.2017.01.044).

[36] Annaraj, B., & Neelakantan, M. A. (2015), Synthesis, crystal structure, spectral characterization and biological exploration of water soluble Cu (II) complexes of vitamin B6 derivative. *European Journal of Medicinal Chemistry*, 102, 1-8. (DOI: 10.1016/j.ejmech.2015.07.041).

***Chapter 4***

***Chitosan-Biotin Conjugated pH Responsive Ru(II)  
Glucose Nanogel: A Dual Pathway of Targeting  
Cancer Cells and Self-Drug Delivery***



## **Chapter 4**

### **Chitosan-Biotin Conjugated pH Responsive Ru(II) Glucose Nanogel: A Dual Pathway of Targeting Cancer Cells and Self-Drug Delivery**

#### **4.1 Introduction**

In the world of nanotechnology, designing effective nanocarriers is a challenging task for drug delivery applications. These ideal nanocarriers must be biocompatible and biodegradable, and should have a long blood circulation time with a high drug-loading capacity [1,2]. To satisfy all such requirements, efforts are being made to customize amphiphilic polymers as effective drug-delivery agents based on the selectivity and stability of the systems. Among the polymer-based systems, the development of nanocarriers, particularly nanogels (NGs), offers distinct advantages over micelles, dendrimers, vesicles, and nanoparticles due to the spacious architecture that enables the incorporation of a greater amount of drugs, proteins, or other bioactive molecules [3,4]. As a soft nanomaterial, nanogels have drawn a lot of interest in the past few decades in the field of medicinal chemistry. Nanogels are materials with a unique structure consisting of crosslinked hydrogel particles and nanoparticles that can release drugs in a controlled manner under specific conditions [5,6]. Nanogels, with the advantage of nanoparticles and hydrogels, can be helpful in various applications, including drug delivery and biomedicine. Thus, these carriers offer a polymeric nanotechnology approach with exceptional advantages like high drug loading capacity, high stability, and responsiveness to a wide range of environmental stimuli, whereby they may contract or expand in response to a change in pH or temperature, resulting in the release of the drug under particular conditions [7].

In this context, herein, a novel system has been synthesized for targeting cancer cells using nanogels loaded with ruthenium complexes containing glucose rings in the associated ligand. NGs have been meticulously designed

and synthesized by incorporating three essential components to achieve specific targeting of cancer cells.

These components include mesoporous silica nanoparticles (MSNs), which provide:

- High drug loading capacity.
- Chitosan (CTS), which serves as a pH-responsive drug delivery gatekeeper.
- Biotin, which is a ligand for targeting cancer cells.

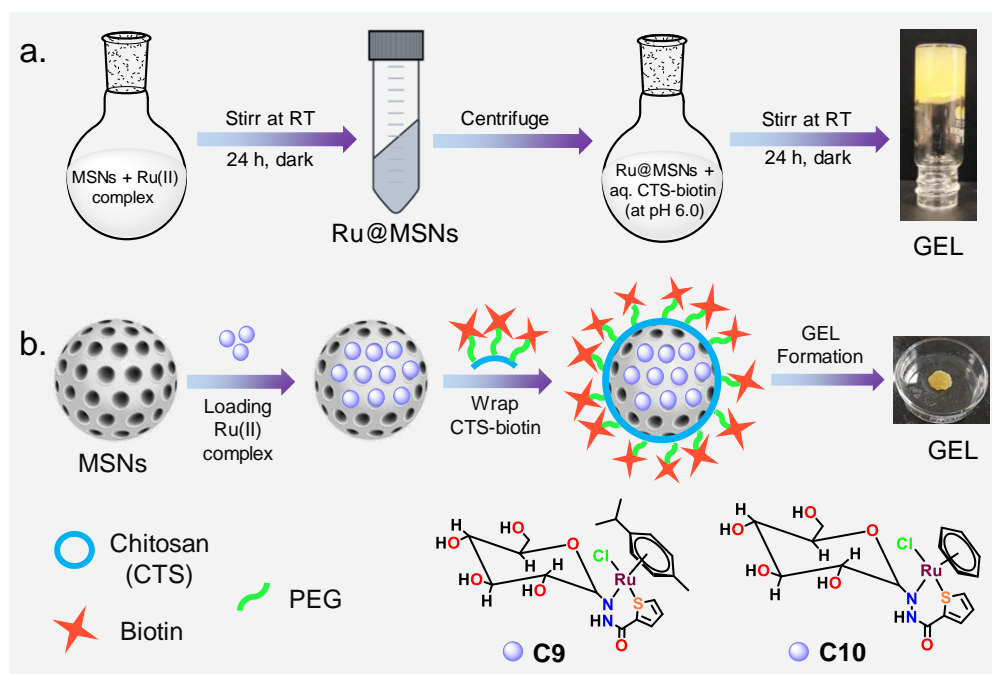
Drug-loaded mesoporous silica nanoparticles are employed in this approach due to their high pore volume, easy synthesis, simple functionalization, tunable pore morphologies, capability of high drug loading, biocompatibility, drugs protection from harsh environments, and ability to carry a variety of cargos within the porous core [8,9]. The use of biotin as a cancer cell-specific drug delivery system has shown promising results in recent studies. Biotin, also known as vitamin H, is an essential cellular micronutrient is crucial in various cellular functions, growth, and development. By utilizing biotin as a targeting agent, researchers have been able to deliver drugs specifically to cancer cells while minimizing toxicity to healthy cells. Biotin molecules are also known to bind favourably to the overexpressed biotin receptors of cancer cells [10,11]. Furthermore, the second most common polysaccharide after cellulose, chitosan, which can provide a variety of sites for attachment to molecules or ligands to target cancerous cells, is utilized here. Additionally, chitosan is useful in drug delivery systems due to its pH sensitivity, biodegradability, biocompatibility, non-toxicity, etc [12]. Chitosan can be chemically modified with various functional groups due to the active hydroxyl and amino groups in the molecular chains. Using different techniques and systems, such as alkaline or acidic systems, chitosan, and its derivatives have been converted into hydrogels with many desirable properties (Scheme 5.1). CTS acts as the "gatekeeper" for pH-responsive drug delivery in distinct pH environments: normal cells ~pH 7.4 and cancer cells ~pH 5.5. Chitosan, a natural biopolymer, acts as a linking agent between the MSNs and biotin by forming a bio-conjugate [13,14].

In the field of chemotherapeutic metallodrugs, researchers seek alternatives to platinum-based chemotherapy to reduce side effects, prevent drug resistance, and for economic viability. Ruthenium complexes have gained attention as anticancer agents due to their lower toxicity and ability to mimic iron's binding ability to biomolecules [15,16]. NAMI-A, KP1019, and NKP-1339 are leading ruthenium-based candidates and have entered clinical trials for further evaluation [17,18].

Keeping all the above facts in mind and continuous endeavors to develop ruthenium-based anticancer complexes, two ruthenium-based anticancer complexes have been designed and synthesized, employing a targeted ligand called **HGluL**. This ligand was obtained by the condensation of thiophene-2-carbohydrazide with D-glucose. As Cancer cells require glycolysis to generate energy, so they have a higher demand for simple sugars like D-glucose [19]. It is well known that polar molecules cannot pass through the impermeable cell membrane. Hence the glucose intake is regulated by specialized membrane transporters (GLUT and SGLT) [20]. These transporters facilitate D-glucose penetration because they are overexpressed in various cancer cells. Additionally, it offers a way to direct therapeutic or imaging agents specifically to cancer cells [21,22,23]. On the other hand, thiosemicarbazones are organic molecules that contain a thiosemicarbazide functional group ( $-C(=S)NHNH_2$ ). They have been extensively studied in medicinal chemistry due to their diverse biological activities, such as their antibacterial, antiviral, and antifungal properties [24]. Additionally, these molecules have displayed promising results in addressing cancer and have recently emerged as potential candidates for cancer therapy. Their ability to hinder tumor growth has been demonstrated in numerous preclinical models [25].

The novelty of a drug-loaded nanogel delivery system lies in its ability to target cancer cells in a dual way, which is a unique approach in the field of cancer drug delivery, allowing the delivery of the drug in cancer cells with precision. The dual mode ensures that if the cancer cell targeting delivery system fails to transport the complete cargo inside the cancer cells specifically,

the pre-released **HGluL**-based ruthenium compound will also target cancer cells through the GLUT receptor. The above feature is crucial as it improves the overall selectivity of the drug towards cancerous cells, which is critical for effective cancer therapy. The synthesized ruthenium(II) complexes derived from the ligand showed promising efficacy against various cell lines. These complexes were further loaded into the nanogel system for selective delivery. The accumulation of the drug within cancerous cells, with or without a delivery agent, was investigated, and morphological changes in cells were captured using confocal microscopy. Additionally, zebrafish culture was used to assess the practical applicability of the compounds and cardiac function was evaluated. Overall, the results demonstrate promising potential for further studies on nanogels loaded with ruthenium(II) anticancer agents.



**Scheme.4.1.** Diagrammatic illustration of (a) the synthesis of Ru(II) arene complex-loaded NGs, and (b) the gel formation strategy through the loading of Ru(II) arene complexes in MSNs followed by wrapping of CTS-biotin, where **C9**:  $[Ru(GluL)(p\text{-cymene})Cl]$  and **C10**:  $[Ru(GluL)(benzene)Cl]$ .

## 4.2 Experimental Section

### 4.2.1 Materials and methods

All the required chemicals were commercially accessible with highest quality analytical grade from Alfa Aesar and Sigma Aldrich, India. Biological reagents purchased from Himedia and Sisco Research Laboratories (SRL) were used without purification. The specifications of all the instruments used for analysis purposes were the same as described in section 2.2.1 of Chapter 2.

## 4.2.2 Syntheses of compounds

### 4.2.2.1 Synthesis of ligand, HGluL

To a stirred solution of D-glucose (0.54 g, 3.0 mmol) in 50 mL of methanol was added 2-thiophene carboxylic acid hydrazide (0.426 g, 3.0 mmol) and 0.3 mL of 10% HCl (aq.). The reaction mixture was refluxed for 6 hr. The resulting clear white solution was cooled to room temperature, and the solvent was removed under reduced pressure. The compound was purified by recrystallization in the water to obtain a white-colored solid product. Yield: 70%.  $^1\text{H}$  NMR in (400.13 MHz, 298K, DMSO- $d_6$ )  $\delta$ : ppm, 10.15 (1H, s, -NH (1) of -CONH), 7.91 (1H, d, Th-CH), 7.39 (1H, d, Th-CH), 7.19 (1H, t, Th-CH), 4.99 (1H, s, -NH (2)), 4.51-3.02 (11H, of glucose ring) ppm.  $^{13}\text{C}$  NMR (100.61 MHz, 298 K, DMSO- $d_6$ )  $\delta$  ppm: 161.6(C=O), 138.0, 131.6, 129.0 and 128.6 (C of thiophene ring), 91.4, 78.5, 77.1, 71.4, 70.8 and 61.7 (C of glucose ring) ppm. FT-IR (KBr,  $\text{cm}^{-1}$ ): 3428 ( $\nu_{\text{(NH)}}$ ), 3299 ( $\nu_{\text{(OH)}}$ ), 1631 ( $\nu_{\text{(C=O)}}$ ), 1080 ( $\nu_{\text{(C-O-C)}}$ ). ESI-MS (+ve mode): [ $\text{C}_{11}\text{H}_{16}\text{N}_2\text{O}_6\text{S} + \text{H}$ ] $^+$ : 305.1 (m/z). Calcd. elemental analysis (%) for  $\text{C}_{11}\text{H}_{16}\text{N}_2\text{O}_6\text{S}$ : C, 43.42; H, 5.30; N, 9.21; S, 10.54. Found: C, 43.52; H, 5.46; N, 9.30; S, 10.56.

### 4.2.2.2 Synthesis of complex C9 [Ru( $\eta^6$ -p-cymene)(GluL)Cl]

Complex **C9** was synthesized by the dropwise addition of MeOH: H<sub>2</sub>O solution of GluL (0.098 g, 0.4 mmol) in the methanolic solution of ruthenium p-cymene dimer (0.100 g, 0.2 mmol) and stirred it for 6 hr at room temperature. After that, the reaction mixture was filtered, by rotavapour the solvent was evaporated, and a brown-colored solid product was obtained, which was purified by the recrystallization method in DCM and methanol solution. Yield: 70%.  $^1\text{H}$  NMR in (400.13 MHz, 298K, DMSO- $d_6$ )  $\delta$ : ppm, 7.40 (1H, d, Th-CH), 7.28 (1H, d, Th-CH), 7.15 (1H, t, Th-CH), 5.82 (2H, d,

CH of C<sub>6</sub>H<sub>4</sub>), 5.77 (2H, d, CH of C<sub>6</sub>H<sub>4</sub>), 5.47 (1H, s, CH of glucose ring), 3.98-3.64 (11H, of glucose ring), 2.83 (1H, sept, CH(CH<sub>3</sub>)<sub>2</sub>), 2.09 (3H, s, C<sub>6</sub>H<sub>4</sub>CH<sub>3</sub>), 1.18 (6H, d, CH(CH<sub>3</sub>)<sub>2</sub>), ppm. <sup>13</sup>C NMR (100.61 MHz, 298 K, DMSO-*d*<sub>6</sub>) δ ppm: 161.6(C=O), 138.0, 131.5, 129.0 and 128.6 (C of thiophene ring), 106.8, 100.6, 86.8 and 85.8 (C<sub>aromatic</sub> of p-cymene), 78.2, 76.8, 71.1, 61.4 and 48.9 (C of glucose ring), 30.4, 21.9 and 18.1 (C<sub>aliphatic</sub> of p-cymene) ppm. FT-IR (KBr, cm<sup>-1</sup>): 3289 (ν(-OH)), 1635 (ν(-C=O)), 1017 (ν(-C-O-C)). ESI-MS (+ve mode): [C<sub>12</sub>H<sub>29</sub>ClN<sub>2</sub>O<sub>6</sub>RuS + H]<sup>+</sup>: 575.09 (m/z). Calcd. elemental analysis (%) for C<sub>12</sub>H<sub>29</sub>ClN<sub>2</sub>O<sub>6</sub>RuS: C, 43.94; H, 5.09; N, 4.88; S, 7.29. Found: C, 44.02; H, 5.19; N, 5.01; S, 7.50.

#### 4.2.2.3 Synthesis of complex C10 [Ru(η<sup>6</sup>- benzene)(GluL)Cl]

Complex **C10** was synthesized by the dropwise addition of MeOH: H<sub>2</sub>O solution of GluL (0.121 g, 0.4 mmol) in the methanolic solution of ruthenium benzene dimer (0.100 g, 0.2 mmol) and stirred it for 6 hr at room temperature. After stirring, the reaction mixture was filtered, the solution was evaporated by the rotavapour, and a brown-colored solid product was obtained, which was purified by the recrystallization method in DCM and methanol solution. Yield: 70%. <sup>1</sup>H NMR in (400.13 MHz, 298K, DMSO-*d*<sub>6</sub>) δ: ppm, 7.51 (1H, d, Th-CH), 7.36 (1H, d, Th-CH), 7.08 (1H, t, Th-CH), 5.81-5.79 (6H, s, CH of C<sub>6</sub>H<sub>6</sub>), 5.10 (1H, s, CH of glucose ring), 3.58-3.38 (10H, glucose ring), ppm. <sup>13</sup>C NMR (100.61 MHz, 298 K, DMSO-*d*<sub>6</sub>) δ ppm: 161.6(C=O), 138.0, 131.5, 129.0 and 128.6 (C of thiophene ring), 106.8, 100.6, 86.8 and 85.8 (C<sub>aromatic</sub> of p-cymene), 78.2, 76.8, 71.1, 61.4 and 48.9 (C of glucose ring), 30.4, 21.9 and 18.1 (C<sub>aliphatic</sub> of p-cymene) ppm. FT-IR (KBr, cm<sup>-1</sup>): 3295 (ν(-OH)), 1650 (ν(-C=O)), 1032 (ν(-C-O-C)). ESI-MS (+ve mode): [C<sub>12</sub>H<sub>29</sub>ClN<sub>2</sub>O<sub>6</sub>RuS+H]<sup>+</sup>: 519.0, [C<sub>17</sub>H<sub>21</sub>N<sub>2</sub>O<sub>6</sub>RuS]<sup>+</sup>: 483.0 (m/z). Calcd. elemental analysis (%) for C<sub>17</sub>H<sub>21</sub>ClN<sub>2</sub>O<sub>6</sub>RuS: C, 42.32; H, 4.39; N, .81; S, 6.64. Found: C, 42.52; H, 4.49; N, 5.99; S, 6.70.

#### 4.2.2.4 Preparation of Nanoparticles

The MSN-based nanoparticles were synthesized based on previous reports. Here, a short description has been added for the reference.

#### 4.2.2.4.1 Preparation of MSNs

Briefly, 1.0 g of CTAB and 0.28 g of NaOH were dissolved in 480 mL of distilled water and heated to 80°C with vigorous stirring. Next, 5.0 g of TEOS was added dropwise to the aforementioned solution with vigorous stirring and heated at 80°C for 2 h. Finally, the white precipitate obtained was washed with distilled water and methanol three times each and then dried under a high vacuum. The CTAB surfactant of the MSNs was removed with concentrated HCl at 80°C for 48 h. The resulting product was washed with ethanol and double-distilled water six times each and dried as mentioned above. The obtained product was denoted as MSNs.

#### 4.2.2.4.2 Synthesis of Drug-Loaded Ru(II)GLUL C9/C10@MSNs

50 mg of MSN particles was added to 5 mL of C9 and C10 solution (10 mg/mL). The mixed solution was stirred for 24 h at room temperature in the dark. The product was collected by centrifugation and vacuum-drying to obtain C9/C10@MSN particles. The loading capacity (LC) of C9 and C10 in MSNs was determined by the weight and UV/vis spectrophotometry methods and calculated with the following formula.

For weight method:  $LC = (m_1 - m_0) / m_1$

Here,  $m_0$  and  $m_1$  are the weights of MSNs before and after loading, respectively.

#### 4.2.2.4.3 Preparation of Chitosan and Biotin Conjugates (CTS-Biotin)

Biotin-PEG-NHS was joined to CTS by conjugating NHS to the -NH<sub>2</sub> group on CTS to obtain CTS-biotin. In brief, CTS (50 mg) and Biotin-PEG-NHS (10 mg) were reacted in dry tetrahydrofuran (THF) (10 mL) at room temperature for 24 h and then CTS-biotin was collected by centrifugation and vacuum drying.

#### 4.2.2.4.4 Synthesis of drug loaded *insitu* gel formation (GC9 & GC10)

Twenty millilitres of 2% w/v CTS-biotin acetic acid aqueous (10% v/v) solution was prepared, and the pH was adjusted to 6.0 with 1 M NaOH; then, C9/C10@MSNs was added to it and stirred for 24 h at room temperature in the

dark it resulted formation of gels. Thus the resulting product **C9@MSNs-CTS-Biotin (GC9)** and **C10@MSNs-CTS-Biotin (GC10)** were obtained.

### **4.2.3 Experimental Methods**

#### **4.2.3.1 Theoretical Study**

In order to understand the geometry of the molecules, stability of the compounds, and electronic communication with ligand (**HGluL**), for complexes **C9** and **C10**, DFT calculations are carried out. Structures of **C9** and **C10** have been optimized by the generation of the expected structures. Both complexes have piano stool pseudo-octahedral geometry where three positions around Ru metal are being coordinated through arene rings, two sides are coordinated through bidentate ligand, and the remaining side is occupied by chloride. Gaussview 5.0 is utilized to generate contour plots for molecular orbitals of the ligand and complexes, and frontier molecular orbital (HOMO and LUMO) energies for all the compounds are calculated.

#### **4.2.3.2 *In vitro* drug release**

For determination of the drug release profile, 5 mg of **GC9** and **GC10** were suspended in 20 ml of PBS at different pH values with constant shaking at 37°C in a hard glass tube. At a specific time following incubation, 0.5 mL of the supernatant was taken out from the glass tube and the same volume of fresh PBS was replaced. All samples were investigated by UV-vis spectrophotometry.

#### **4.2.3.3 Cytotoxic assay**

The procedure for MTT assay is same as discussed in section 2.2.6 of chapter 2.

#### **4.2.3.4 Western blotting**

The procedure was done according to previously published methods (10.1039/D2RA01919A). Briefly, the  $4 \times 10^5$  HeLa cells were seeded into the 6-well plate for 24 h. The next day HeLa cells were dealt with the **C9**, **C10**, **GC9** and **GC10** at the IC<sub>50</sub> values for 24 h. The cell lysates were then collected for western blot analysis. After briefly being washed with 1X PBS, the cells

were lysed in the RIPA lysis buffer (1 M Tris pH 7.4, 2 M NaCl, 0.1 M EDTA, 1 M PMSF, protease inhibitor cocktail, 100 mM DTT and 1 mM sodium orthovanadate, Triton-X-100, and Glycerol) and stored in  $-80^{\circ}\text{C}$ . The proteins were separated in 15% SDS-PAGE gel electrophoresis and then transferred to the nitrocellulose membrane (Bio-Rad). The membrane was blocked for 1 h at room temperature in 1X PBST, containing 5% of skimmed milk. Followed by membrane was then incubated with the primary antibody (1:1000) at  $4^{\circ}\text{C}$  overnight on shaking condition. Next, the membrane was incubated with HRP-conjugated anti-rabbit/anti-mouse IgG secondary antibodies for 2 h at room temperature. The membrane was developed using standard chemiluminescent substrate (BioRad) and images were captured on a Fusion Solo S chemidoc system (Vilber).  $\beta$ -actin was applied as a loading control. Band intensities were measured using Image J software (NIH) with respect to  $\beta$ -actin.

#### **4.2.3.5 *In vitro* cellular uptake by ICP-OES analysis**

For quantitative analysis of cellular uptake HeLa and HEK293 cells were seeded in 10 cm dishes with  $10^6$  cells in 10 ml PBS solution and allowed to attach for 24 h. The cells were then treated with complex **C9** and **C10**, nanogels **GC9** and **GC10** at  $10\ \mu\text{M}$  for 4 h at  $37^{\circ}\text{C}$  in  $\text{CO}_2$  incubator. At the end of the incubation, the collected cells were digested with mixed acid ( $\text{HNO}_3:\text{HClO}_4 = 3:1$ ) for 2 h at  $180^{\circ}\text{C}$ . Then the concentration of ruthenium in the cells was examined with inductively coupled plasma optical emission spectrometry (ICP-OES) analysis. The uptake in cancer and normal cells was expressed as the amount of Ru ( $\mu\text{g}$ ).

#### **4.2.3.6 Reactive Oxygen Species (ROS) generation**

The procedure for generating reactive oxygen species (ROS) is identical to the one outlined in section 2.2.7 of chapter 2.

#### **4.2.3.7 Hoechst staining assay**

HeLa cancer cell line were plated at a density of  $5 \times 10^4$  in 6-well plates. They were allowed to grow at  $37^{\circ}\text{C}$  in a humidified  $\text{CO}_2$  incubator until they were 70-80% confluent. Then cells were treated  $\text{IC}_{50}$  concentration of synthesized compounds for 24 h. The culture medium was aspirated from each well and

cells were gently rinsed thrice with PBS at room temperature. Then equal volumes of cells from control (untreated) were mixed with 10  $\mu$ L Hoechst 33258 dye. Finally, the compounds and dye-treated cells were viewed immediately with a confocal microscope: excitation  $340 \pm 20$  nm for the blue channel.

#### **4.2.3.8 Dual staining assay with Acridine orange and EtBr**

To validate the nucleus morphology, an AO/EtBr staining procedure was conducted. The  $5 \times 10^4$  HeLa cells were placed on six-well plates (Nest; USA). The cells were treated with the corresponding  $IC_{50}$  concentration of the synthesized compounds followed by incubation for 24 h. After the incubation period treated cells were stained with the acridine orange and ethidium bromide dye with concentrations of 5 and 3  $\mu$ g/mL, respectively, followed by incubation for 15 min at  $37^\circ\text{C}$  and washing with PBS thrice. The fluorescence was viewed with the help of Fluoview FV100 (OLYMPUS, Tokyo, Japan) confocal microscope using appropriate filters.

#### **4.2.3.9 Wound healing assay**

The procedure for wound healing assay is identical to the one outlined in section 3.2.7 of chapter 3.

#### **4.2.3.10 *In vivo* assessment using zebrafish embryos**

##### **4.2.3.10.1 Zebrafish Husbandry**

Wild type Zebrafish (*Danio rerio*) was maintained in a 14:10 light: dark cycle under optimum conditions at  $28^\circ\text{C}$ . The experiments were performed under the guidelines of the institutional bioethical committee and complied with the ARRIVE guidelines following the U.K. Animals (Scientific Procedures) Act, 1986 and associated guidelines. The adult zebrafish were bred in a breeding tank and the embryos were collected.

##### **4.2.3.10.2 Zebrafish toxicity studies**

The embryos were exposed to different concentrations (10, 25, 50, 100, 200, 400, 800, 1200, and 1600  $\mu$ M) of **GC9** and **GC10**. The mortality, hatching rate, morphology, and heartbeat rate were observed till 72 hours postfertilization (hpf) according to the OECD guidelines. Any developmental

changes, such as deformities in the tail, spine, edema, and change in the heartbeat, were observed using a stereo microscope. Working standards of the solutions were prepared using distilled water and diluted in an E3 medium. Statistical analysis was performed using Origin 8 for determination of LD<sub>50</sub> values

#### **4.2.3.10.3 Heartbeat analysis of the zebrafish embryos**

The heartbeat of the zebrafish larvae was analyzed at 48 hpf, and the percentage change in a heartbeat was calculated with respect to control. **GC9** and **GC10** were incubated to check the influence of the compounds on heartbeat rate when compared to the control.

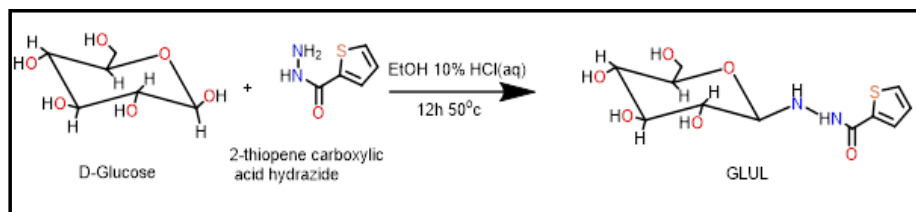
#### **4.2.3.10.4 Differential AO/PI apoptosis staining assay**

AO/PI double staining was performed at 96-hpf on the embryos exposed to 10, 25, 50, 100, 200, 400, 800, 1200 and 1600  $\mu$ M of **GC9**, and **GC10**. Briefly, zebrafish embryos were incubated with 10  $\mu$ g/mL AO and 10  $\mu$ g/mL PI for 15 min in the dark. Then they were washed three times with an E3 medium and visualized using a stereo microscope. AO: acridine orange.

### **4.3 Results and discussion**

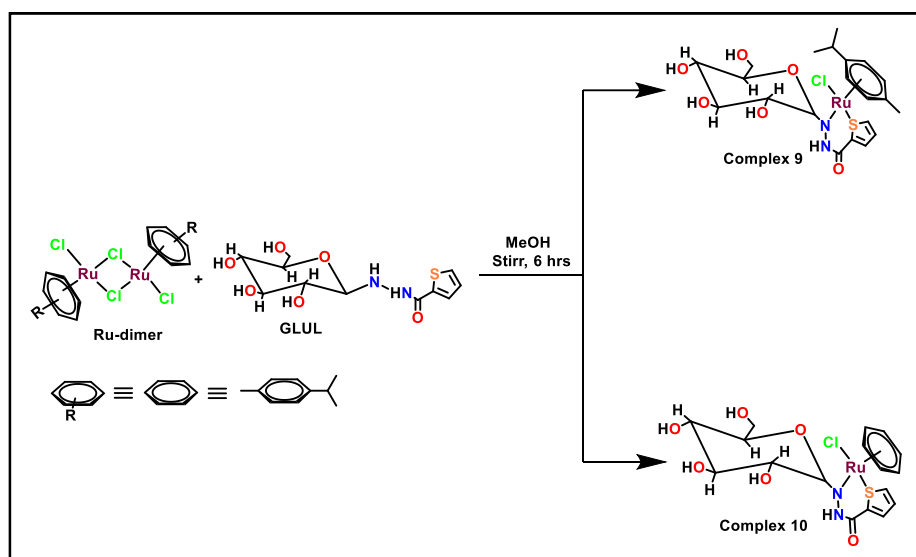
#### **4.3.1 Preparation and characterization of glucose-based Ru anticancer drug and delivery systems**

Glucose is a naturally occurring and abundant sugar in the human body, which makes it an ideal choice as a ligand for targeting glucose transporters, such as GLUT. These transporters are responsible for the glucose uptake from the bloodstream into cells, and their dysregulation is linked to various diseases, including diabetes and cancer. Glucose-based ligands are designed to mimic the structure of glucose, allowing them to bind to the GLUT transporter with high affinity and specificity. This enables them to selectively target cells that overexpress GLUT transporters, such as cancer cells. Therefore, in this Chapter a new water-soluble glucose-based ligand named **HGluL** is synthesized and characterized. The ligand was prepared through the condensation of 2-thiophenecarbohydrazide and D-glucose in ethanol, using an acid catalysis method (Scheme 4.2) [26].



**Scheme 4.2.** Synthesis of Glucose ring conjugated ligand (**HGluL**).

The monomeric Ru(II) complexes (**C9**: attached to *p*-cymene, and **C10**: benzene substitution) were obtained upon refluxing the ligand (**HGluL**) in presence of Ru(II) dimer of either *p*-cymene or benzene (Scheme 4.3).



**Scheme 4.3.** Synthesis of Glucose ring conjugated Ru(II) arene complexes.

Both complexes are soluble in DMSO, acetone, methanol, DMF, dichloromethane, chloroform, acetonitrile, and benzene. They are found to be hygroscopic, and light brown in color. The **HGluL** and the corresponding complexes **C9** and **C10** were characterized using various analytical techniques, including ESI-MS, NMR, elemental analysis, FTIR, and UV-vis. Further, the theoretical DFT study was used to validate the structure and geometry of the ligand and complexes. In the  $^1\text{H}$  NMR spectrum of ligand, peaks between 7.91-7.19 ppm show the presence of a thiophene ring [27], the peaks between 4.99-3.02 ppm display the existence of resonating glucose ring, and the signal at 10.1 ppm exhibit presence of -NH. Likewise, the proton signals between 5.82-5.77 display the presence of *p*-cymene ring and 2.83, 2.09, and 1.18 ppm for the side chain of *p*-cymene ring and 5.97-5.79 the benzene ring in the

corresponding complexes **C9** and **C10** [28]. From the mass spectroscopic data analysis, the molecular peaks of synthesized compounds were observed, confirming the formation of the desired products. Ligand shows band at 3428 and 3299  $\text{cm}^{-1}$  for  $\nu_{(-\text{NH})}$  and  $\nu_{(-\text{OH})}$ , and at 1631 and 1080  $\text{cm}^{-1}$  for  $\nu_{(\text{C}=\text{O})}$  and  $\nu_{(\text{C}-\text{O}-\text{C})}$ , respectively [29]. In complex **C9** and **C10**, the band at 3428  $\text{cm}^{-1}$   $\nu_{(-\text{NH})}$  disappeared, which shows that Ru metal gets coordinated through the N, S-donor sites of the ligand in a bidentate manner and validates the structures of the complexes. The absorption spectra of three compounds, namely **HGluL**, **C9**, and **C10**, were recorded in a DMSO solution. The ligand exhibited a single absorption band at 265 nm, indicating the promotion of an electron from a non-bonding orbital to a higher energy level ( $n-\pi^*$ ). On the other hand, the metal complexes **C9** and **C10** showed two distinct absorption bands at 260 nm and 375 nm. The higher energy absorption band at 375 nm is attributed to a metal-to-ligand charge transfer (MLCT) transition, where an electron is transferred from a metal d-orbital to a ligand  $\pi^*$ -orbital (Figure 4.1- Figure 4.10).

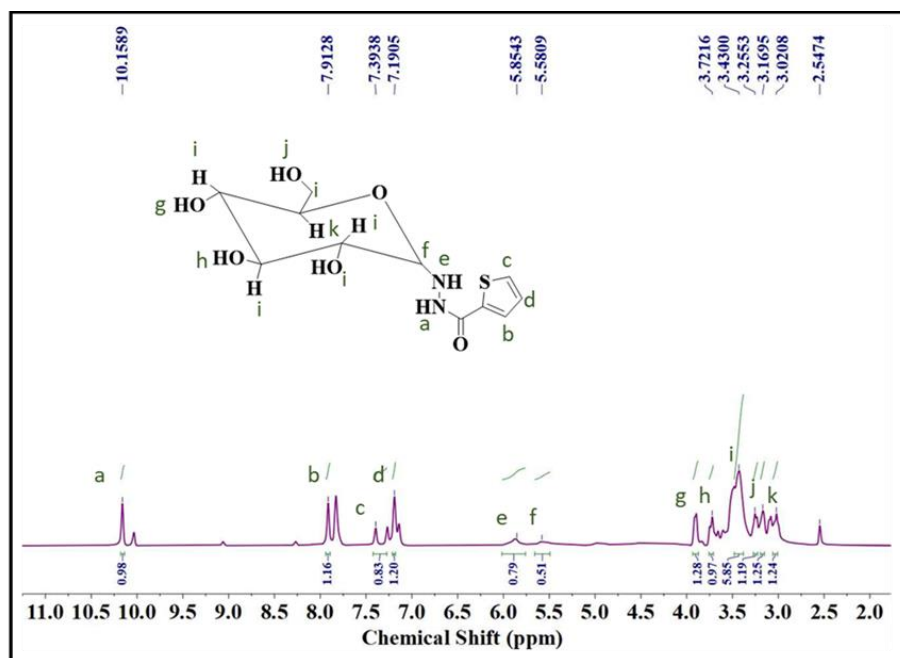


**Figure 4.1:**  $^1\text{H}$  NMR Spectra of ligand **GluL** in  $\text{DMSO}-d_6$  (400.13 MHz, 298K)

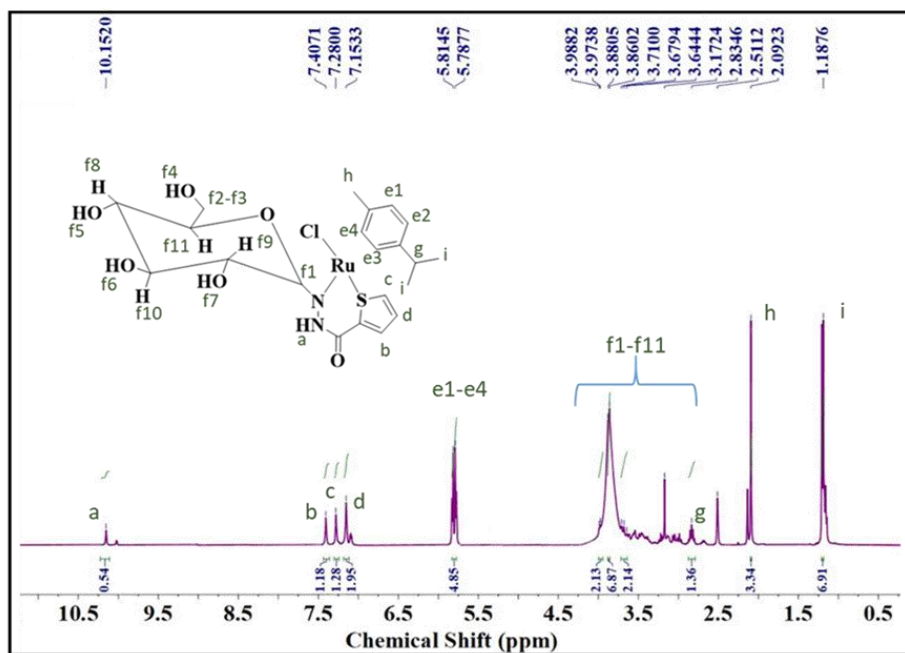


Figure 4.2:  $^1\text{H}$  NMR Spectra of complex 9 in  $\text{DMSO-}d_6$  (400.13 MHz, 298K)

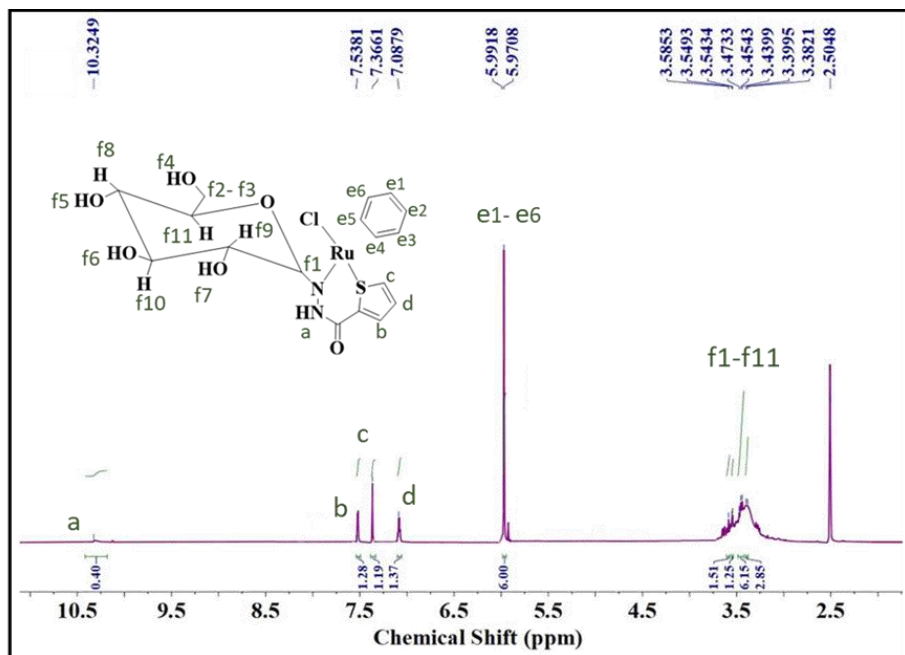


Figure 4.3:  $^1\text{H}$  NMR Spectra of complex 10 in  $\text{DMSO-}d_6$  (400.13 MHz, 298K)

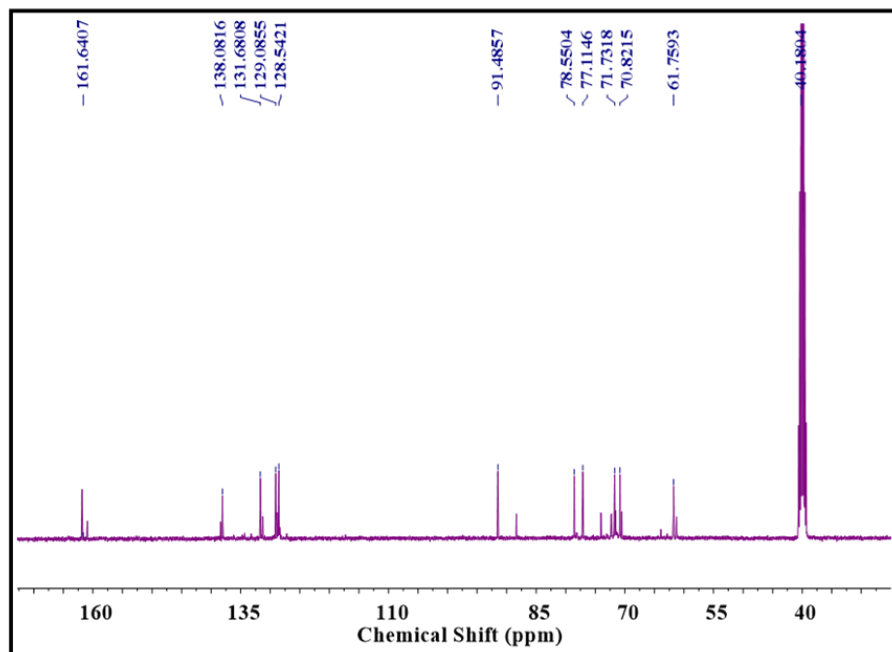


Figure 4.4:  $^{13}\text{C}$  NMR Spectra of ligand **GluL** in  $\text{DMSO-}d_6$  (400.13 MHz, 298K)

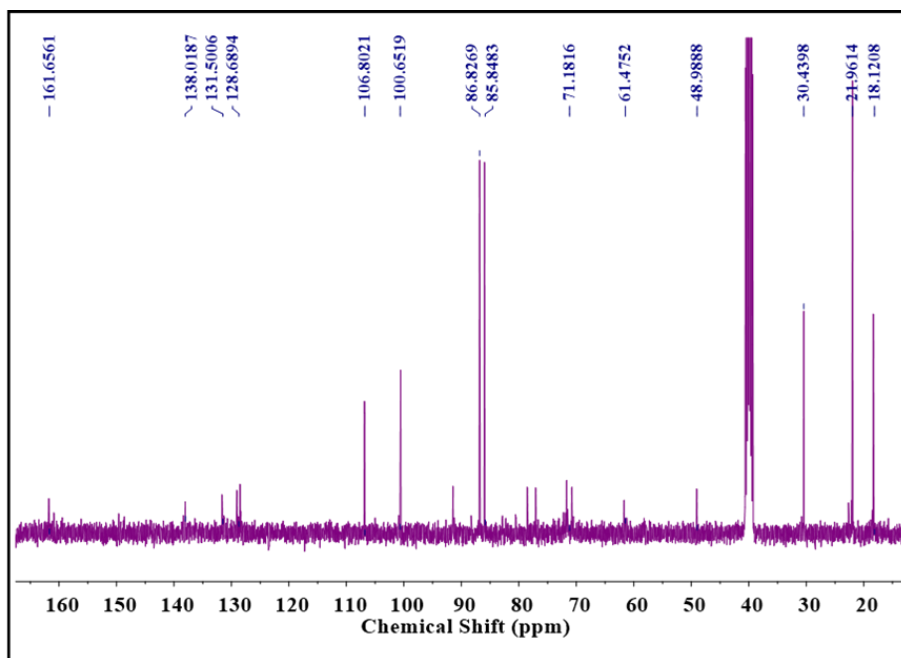


Figure 4.5:  $^{13}\text{C}$  NMR Spectra of complex **9** in  $\text{DMSO-}d_6$  (400.13 MHz, 298K)

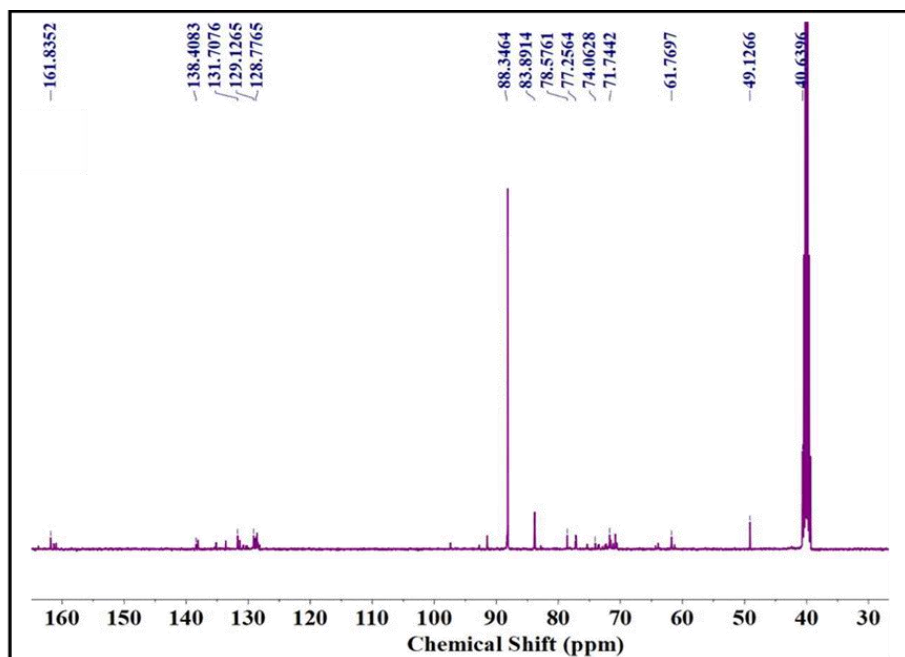


Figure 4.6:  $^{13}\text{C}$  NMR Spectra of complex **10** in  $\text{DMSO-}d_6$  (400.13 MHz, 298K)

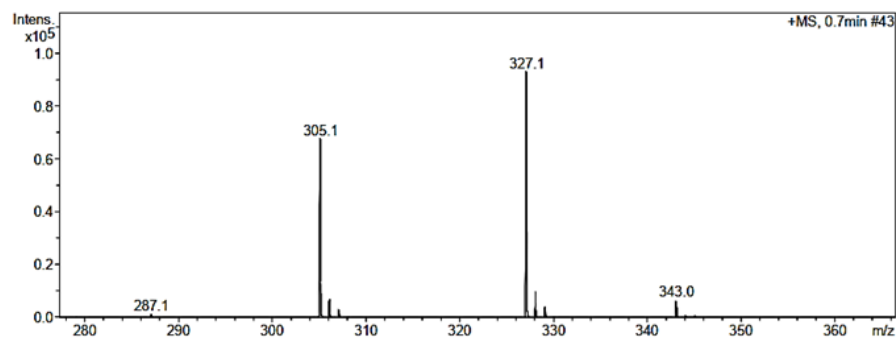


Figure 4.7. ESI-MS data for ligand (**HGLuL**) at room temperature.

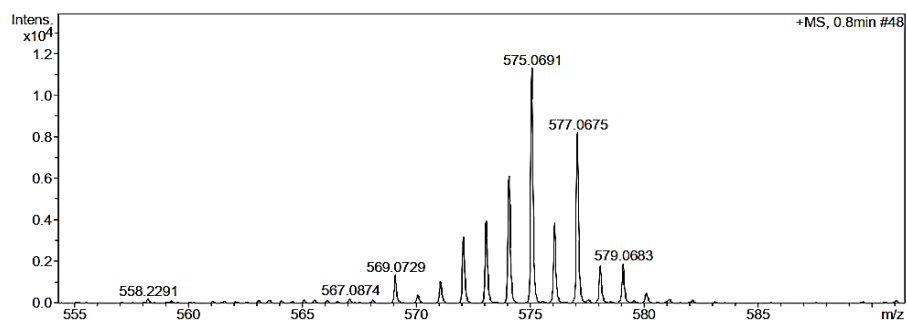
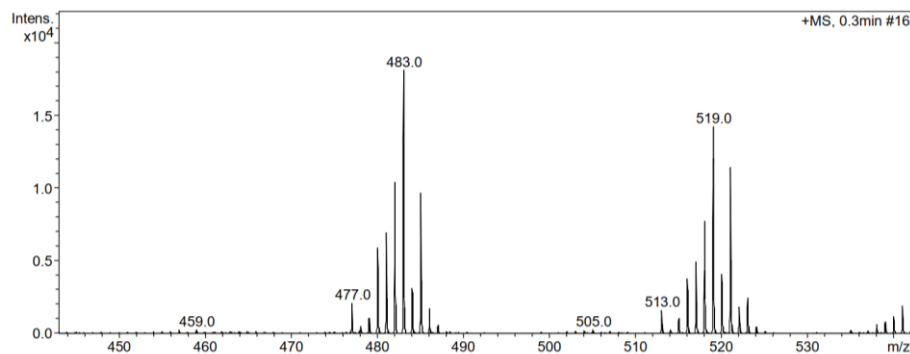
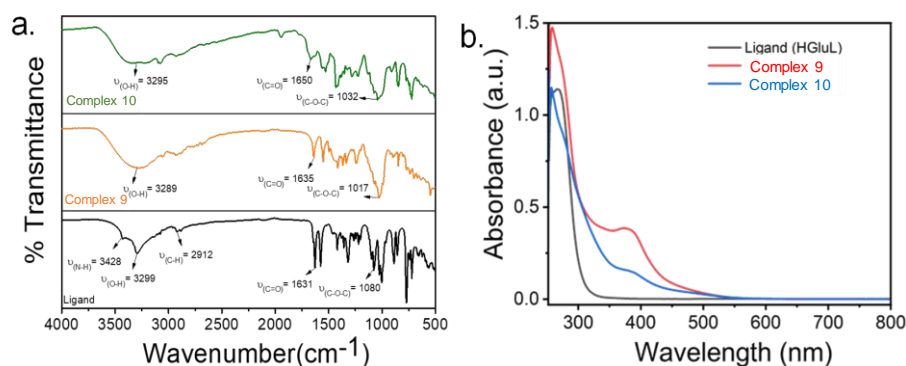


Figure 4.8. ESI-MS data for complex **C9** at room temperature.



**Figure 4.9.** ESI-MS data for complex **C10** at room temperature.



**Figure 4.10.** (a) FTIR Spectra and (b) UV-vis spectra of ligand (**HGluL**), **C9** and **C10**.

Furthermore, the structure and geometry of the complexes were optimized through DFT studies. The geometry of both complexes is found to be pseudo-octahedral, and the arene fluxional  $\pi$ -bonded ring occupies three coordination positions., The GluL occupies the other two coordination sites in complexes **C9** and **C10** *via* N, S chelation, and the chloro ligand takes up the sixth coordination position (Figure 4.11). Estimated bond lengths and angles are described in Table 4.1 for synthesized compounds.

For biological studies, the stability of the compounds was examined in DMSO, considering its wide use for preparing metal complex stock solutions. The stability of complexes was confirmed through  $^1\text{H}$  NMR in DMSO- $d_6$  over 48 hrs, with time intervals of 0, 24, and 48 h; this showed no significant change in the  $^1\text{H}$  NMR peaks for either complex (Figure 4.12).

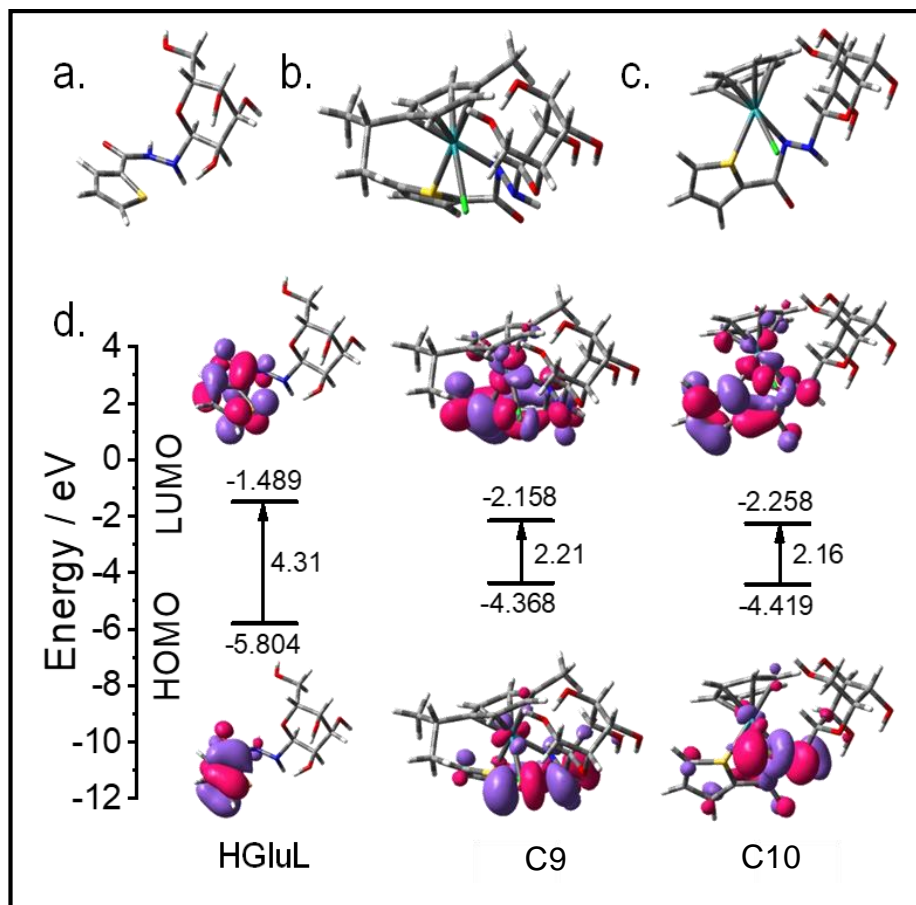
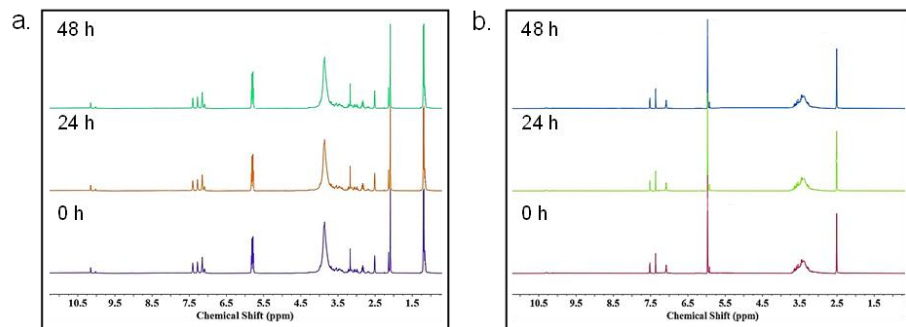


**Figure 4.11.** Geometry optimized structure of (a) **HGLuL**, (b) **C9**, and (c) **C10**. The Stuttgart/Dresden (SDD) basis set and effective core potential were used for the Ru atom, and 6-311 G\* basis set was applied for H, C, O, N, S, and Cl. (d) Calculated frontier molecular orbitals viz HOMO and LUMO of **HGLuL**, **C9**, and **C10** (Isovalue = 0.04).

**Table 4.1.** Selected bond lengths (Å) and bond angles (°) for Ligand (HGluL), C9 and C10 (calculated data).

Bond length (Å)	Ligand (HGluL) Cal.	Complex 1 (C1) Cal.	Complex 2 (C2) Cal.
C1 <sub>(thiophene)</sub> -S	1.72709	1.54921	1.55312
C4 <sub>(thiophene)</sub> -S	1.75130	1.36968	1.34176
N1-N2	1.39763	1.24204	1.26997
C1 <sub>(thiophene)</sub> =C2 <sub>(thiophene)</sub>	1.36937	1.40155	1.39423
C3 <sub>(thiophene)</sub> =C4 <sub>(thiophene)</sub>	1.37721	1.41227	1.41414
C=O	1.23358	1.25835	1.25840
Ru-Cl	-	2.2299	2.2300
Ru-N1	-	1.9468	1.9968
Ru-S	-	2.2604	2.2456
Ru-C1	-	2.05875	2.0531
Ru-C2	-	2.07449	2.0722
Ru-C3	-	2.09212	2.0915
Ru-C4	-	2.05722	2.0548
Ru-C5	-	2.07046	2.0675
Ru-C6	-	2.08965	2.0854
Bond angles (°)	Ligand (HGluL) Cal.	Complex 1 (C1) Cal.	Complex 2 (C2) Cal.
C1-S-C4	91.60160	106.19025	105.93057
N1-N2-C	124.10961	124.62211	129.05690
C4-C5=O	120.40600	122.53618	119.91971
Cl-Ru-S	-	60.3988	60.9423
Cl-Ru-N1	-	46.8186	65.5188
S-Ru-N1	-	47.6793	79.6184



Figure

**4.12.** Time dependent stability study of (a) complex **9** (b) complex **10** at different time interval 0 h, 24 h and 48 h.

The synthesized ruthenium(II) complexes have been tested for their anticancer properties against different cancer cell lines. It was observed that both compounds could show significant cytotoxicities (*vide infra*). In order to achieve targeted delivery of the newly synthesized compound for cancer treatment, a composite system consisting of three key components: complex-loaded mesoporous silica nanoparticles, chitosan act as a pH-responsive drug delivery gatekeeper, and biotin act as a cancer cell-targeting ligand is developed. Interestingly, this system formed a drug-loaded nanogel, presumably due to the chemically crosslinked hydrogen bonding and electrostatic interaction between the encapsulated glucose moiety of the complexes and the amine group of chitosan. To confirm the specificity of the developed system, similar experiments were performed separately with Ru-arene-dimer, only the ligand **HGluL**, and our previously synthesized ruthenium complexes. However, it was found that gel not formed with these compounds, except for **HGluL**, which formed a runny gel with low mechanical strength (Figure 4.13). Our results suggest that our composite system is highly specific for gel formation.

**HGluL**



**Figure 4.13.** Digital images of Gel formation of a. reported Ru complex (not forming gel) b. ligand HGluL (runny gel formed) c. Ru-dimer (not forming gel).

The delivery systems are characterized by various analytical methods, such as SEM, BET, TGA, UV-vis, XPS, and gel formation is confirmed by the rheological study. Drug-loaded nanoparticles and the formation of gels can be clearly seen by FE-SEM analysis. The uniform sheet-like morphology of the gels is observable by SEM. Moreover, SEM images of nanogels display embedded drug-loaded nanoparticles at a 100 nm scale. HR-TEM images were utilized to confirm the presence of drug-loaded nanoparticles within the gels. Further, the elemental composition in drug-loaded nanoparticles is verified using EDS analysis and mapping study (Figure 4.14-Figure 4.15).

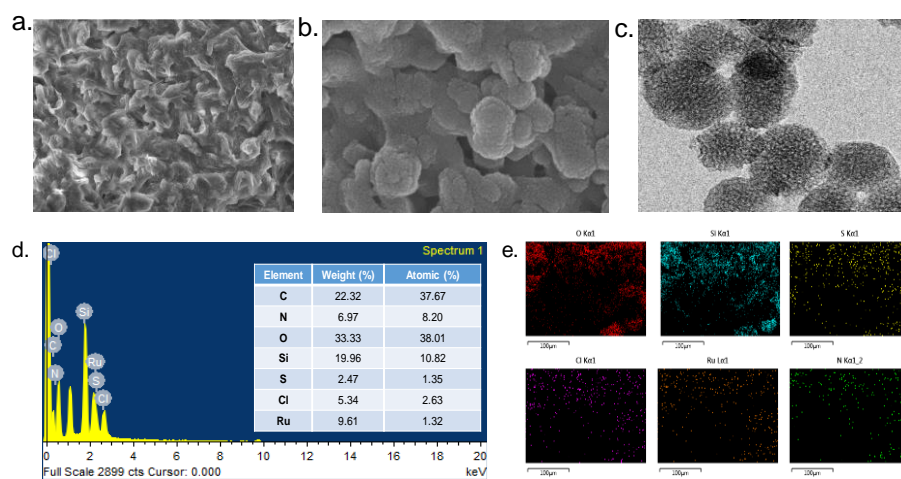


**Figure 4.14.** FE-SEM images of NGs: (a) GC9 at 10  $\mu\text{m}$ , and (b) magnified range of GC9 at 100 nm. (c) HR-TEM image of GC9. (d) EDS analysis (e) mapping data of C9@MSNs, showcasing the elemental composition.

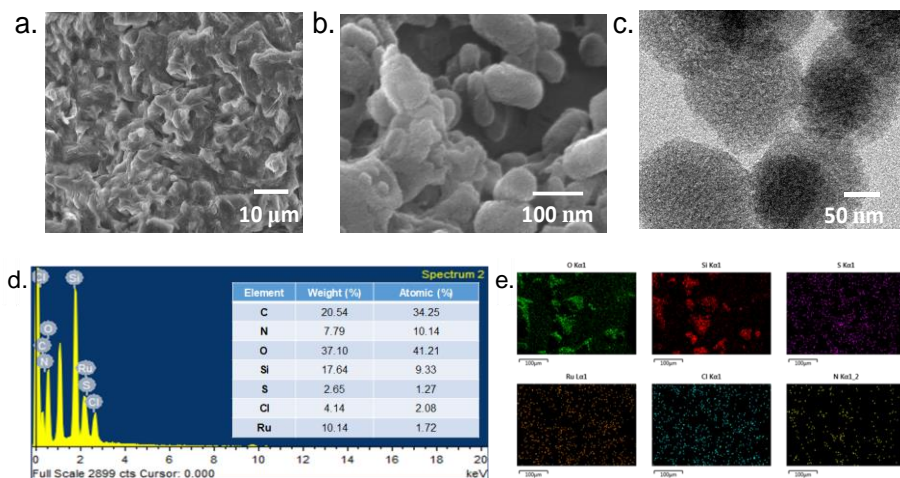


**Figure 4.15.** FE-SEM images of NGs: (a) **GC10** at 10  $\mu\text{m}$ , and (b) magnified range of **GC10** at 100 nm. (c) HR-TEM image of **GC10**. (d) EDS analysis (e) mapping data of **C10@MSNs**, showcasing the elemental composition.

Surface area calculations of drug-loaded nanoparticles and nanogels were performed using the obtained measurements from the BET isotherm. The surface area decreased considerably from 965.7m<sup>2</sup>/g (MSNs) to 885.0m<sup>2</sup>/g (**C9@MSNs**) and 104.1m<sup>2</sup>/g (**GC9**) in case of **C9**, and to 909.5 m<sup>2</sup>/g (**C10@MSNs**) and 347.3m<sup>2</sup>/g (**GC10**) for **C10**, respectively. Similar to this, the pore volumes in BET also decreased from 1.88 cm<sup>3</sup>/g (MSNs) to 1.76 cm<sup>3</sup>/g (**C9@MSNs**) and 0.31 cm<sup>3</sup>/g **GC9** for **C9** and to 1.81 cm<sup>3</sup>/g (**C10@MSNs**) and 1.00 cm<sup>3</sup>/g **GC10** in case of **C10**, respectively (Figure 4.16- Figure 4.17). The result demonstrates that drug-loaded nanoparticles (**C9** and **C10**) have been successfully loaded into a gel matrix. This is significant because it suggests that the nanoparticles can be used as a drug delivery system, where the gel matrix can provide a sustained release of the drug over time.

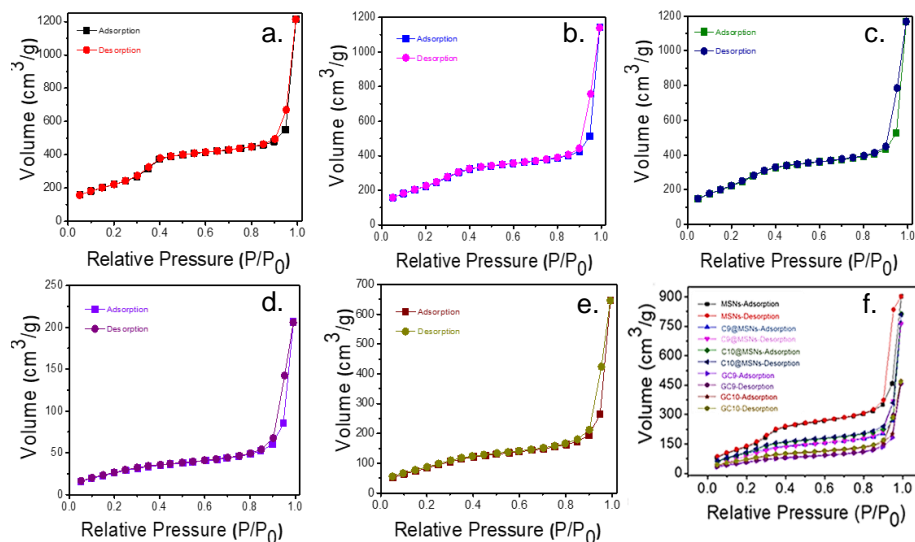


**Figure 4.16.**  $N_2$  adsorption isotherms of (a) MSNs, (b) C9@MSNs, (c) C10@MSNs, (d) GC9 and, (e) GC10.

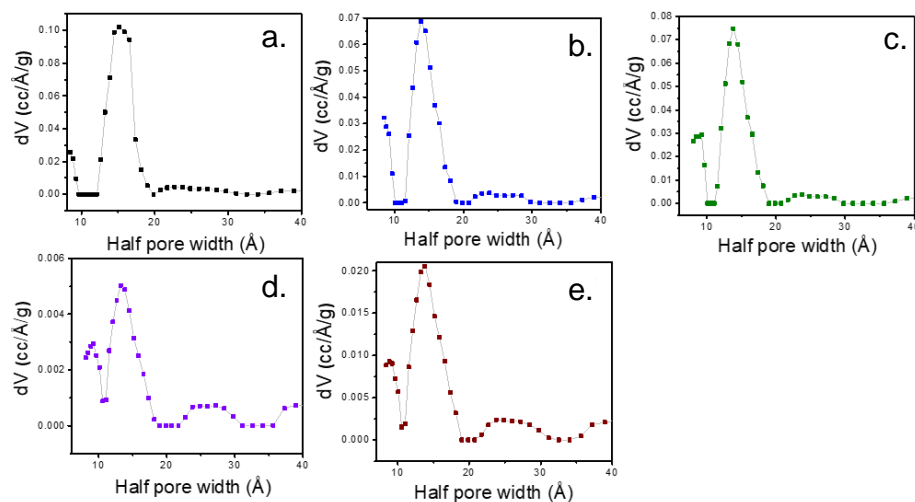


**Figure 4.17.** Pore size distribution curve analyzed by BET method for (a) MSNs, (b) C9@MSNs, (c) C10@MSNs, (d) GC9, and (e) GC10.

By using FTIR spectroscopy, the successful encapsulation of complexes was further verified. Si-O-Si antisymmetric vibration band of MSNs has been found in the range of  $1065-1092\text{ cm}^{-1}$ , whereas biotin's carboxylic C=O stretching vibration has been observed around  $1621\text{ cm}^{-1}$  [30]. Besides, three new bands of GC9 and GC10 in the region of  $2033-2043\text{ cm}^{-1}$ ,  $1498-1546\text{ cm}^{-1}$  and,  $1636-1641\text{ cm}^{-1}$  were ascribed to C-H and C=C stretching vibration on benzene and cymene, and C=O stretching present in the complexes. Additionally, the UV-vis peaks in GC9 and GC10 at 260 nm and 378 nm,

respectively, reveal the characteristic peaks for complexes **C9** and **C10**, supporting the successful drug loading in the core. TGA profile of drug delivery systems demonstrates that up to 150 °C, drug delivery systems are thermally stable, and no significant weight loss occurred other than the removal of water molecules that have adhered to surfaces. Further verification of these findings was carried out using X-ray photoelectron spectroscopy (XPS), which offers details on the valence state of metal ions, stereochemical configurations, and multiplicity of electrons. The XPS data of **GC9** and **GC10** demonstrate that **C9** and **C10** were successfully loaded inside the NGs. All the elements found in the NGs are identified by XPS spectra from the XPS survey. The presence of -N-H is confirmed with a peak at 401.0 eV in N1s, and the presence of -C=O with a peak at 531.0 eV in O1s, and C=C at 284.3 eV in C1s, respectively. Similarly, Ru 3d<sub>5/2</sub> (Cl), and Ru 3d<sub>5/2</sub> give the HRD-XPS peaks at 282.4/283.8 eV, and 282.0/283.1 eV for **GC9** and **GC10**, respectively, which reveal the presence of Ru-Cl and Ru-N in the NGs [31]. All of these results also support the successful drug-loading into the NGs (Figure 4.18- Figure 4.20).

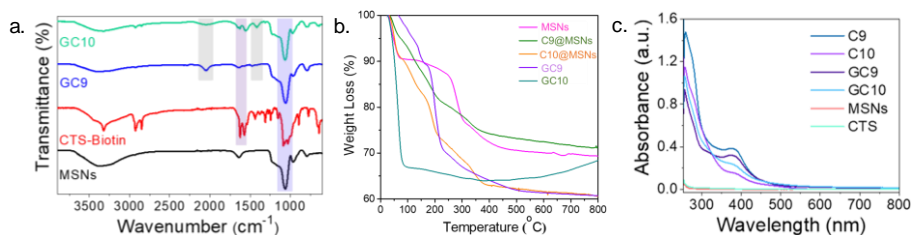


**Figure 4.18.** (a) FTIR spectra of MSNs, CTS-Biotin, GC9, and GC10. (b) TGA graph in the temperature range of 0-800 oC of synthesized compounds. (c) UV-vis spectra of MSNs, CTS, C9, C10, GC9, and GC10 in PBS at pH~7.4.

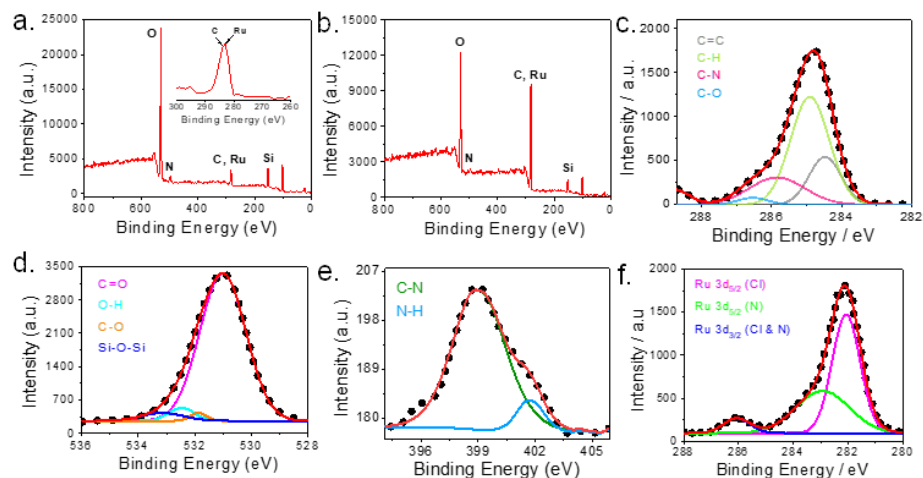


**Figure 4.19.** X-ray photoelectron spectroscopic (XPS) analysis of drug delivery systems (NGs). Representation of XPS survey spectra of (a) GC9, and (b) GC10, respectively. High resolution deconvoluted XPS spectra of (c) C1s (d) O1s, (e) N1s, and (f) Ru 3d<sub>3/2</sub>, and Ru 3d<sub>5/2</sub> in case of GC9.

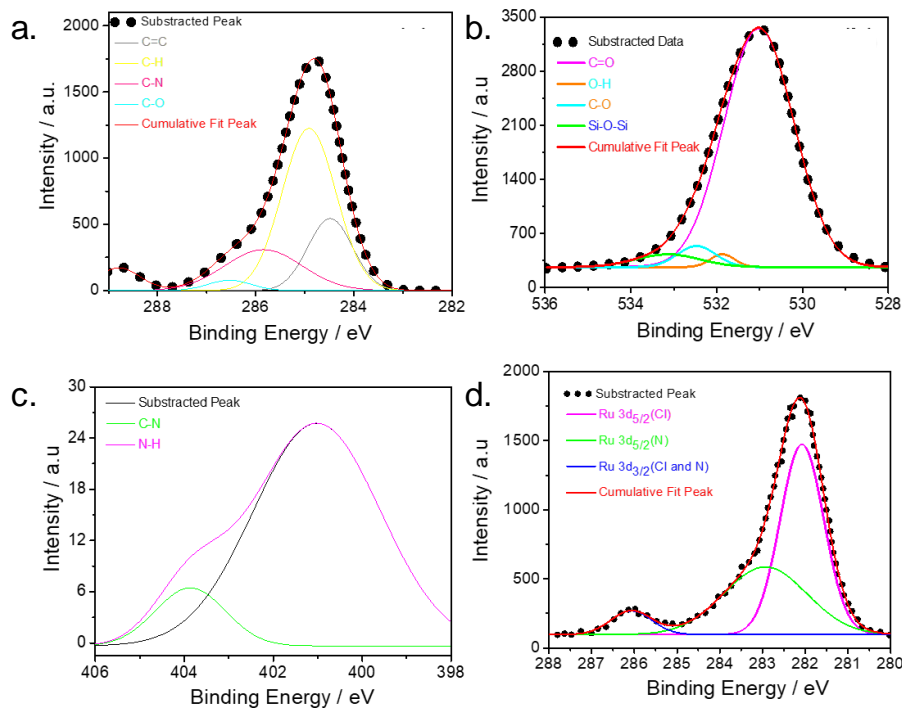


**Figure 4.20.** High resolution deconvoluted XPS spectra of (a) C1s, (b) O1s, (c) N1s, and (d) Ru 3d<sub>3/2</sub>, and Ru 3d<sub>5/2</sub> in case of GC10.

### 4.3.2 Rheology Study for confirmation of gels formation

It is essential to understand the mechanical strength of the material to evaluate the rigidity of the material for potential applications, so rheological

experiments have been performed. The average storage modulus ( $G'$ ) in **GC9** and **GC10** was found to be 520 Pa and 553 Pa, respectively, higher than the loss modulus ( $G''$ ), indicating moderate gel strength. There is no crossover point found for either gel. In the experiment, the gel had a higher dynamic frequency sweep storage modulus ( $G'$ ) than loss modulus ( $G''$ ), demonstrating the viscoelastic nature of the material. The rigidity of the gel was demonstrated by  $G' - G''$  values that were positive over the entire sweep range (Figure 4.21).

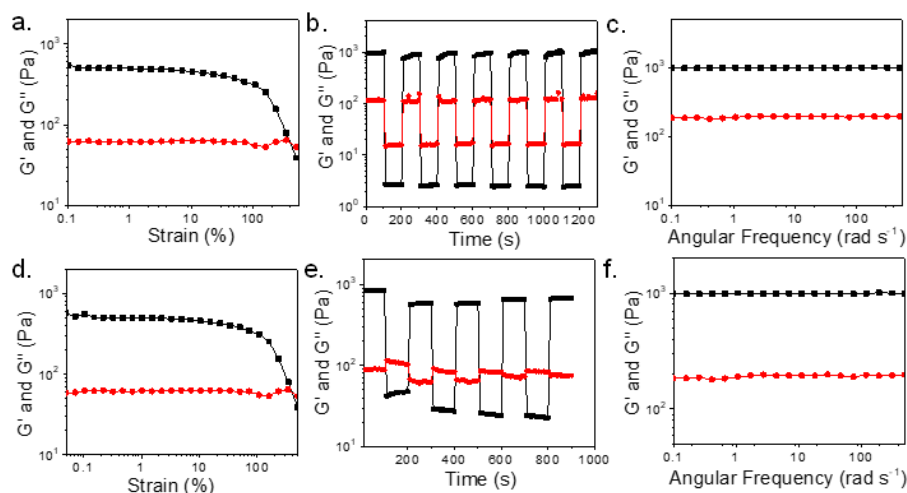


**Figure 4.21.** (a) Linear viscoelastic graph, (b) time-oscillation strain-sweep experiment, and (c) dynamic frequency sweep of **GC9**. (d) Linear viscoelastic graph, (e) time-oscillation strain-sweep experiment, and (f) dynamic frequency sweep of **GC10**. '■' and '●' denote the storage modulus ( $G'$ ), and loss modulus ( $G''$ ), respectively.

### 4.3.3 Solvent dependency of nanogels formation

Gels are formed due to weak interactions, such as hydrogen bonding and  $\pi$ - $\pi$  stacking, that can be easily changed by exposing them to different conditions or solvent systems. As a result, the nature of the gel formation was assessed in the presence of various solvent systems. In this work, the gelation was investigated with respect to the common laboratory solvents. Here, seven different solvent systems (10% DMSO, 10% ethanol, 10% DMF, 10% ACN, 100% water and 100% acetic acid with respect to gel formation solvent 10% acetic acid) were used to check the gel formation in similar conditions. It was noticed that gel gets formed only with the 10% aqueous acetic acid solution. It

observed that some solvent systems, such as 100% acetic acid and 10% ethanol, show colloidal solution, but other solvent systems show transparent solution except pure aqueous solution in which compounds settled down in the bottom. Therefore, it was concluded that the formation of gels depends on the solvent systems (Figure 4.22).

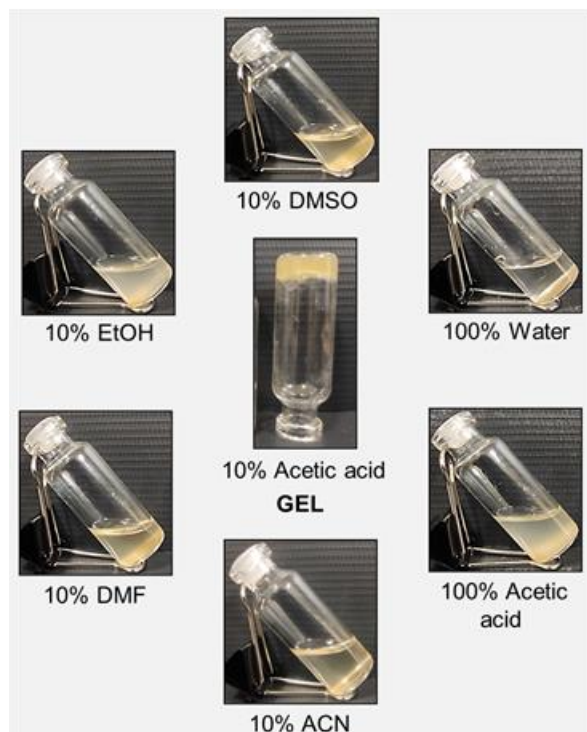


**Figure 4.22.** Digital images of nanogel formation captured by a handheld camera under different solvent conditions.

#### 4.3.4 Effect on NADH catalytic activity

In various biological processes, the pair of coenzymes NADH/NAD<sup>+</sup>, the reduced and oxidized form, play a very significant role in maintaining the cell redox status for its survival. The substantial changes in the equilibrium between the reduced and oxidized form of coenzymes (NADH/NAD<sup>+</sup>) alter the redox balance of the cell and affect the metabolism, which causes the cell to malfunction. With the help of catalysts, disrupting this intracellular redox balance in cancer cells can offer an alternative path for cancer treatment. Earlier studies have shown that half-sandwich Ru(II) and Ir(III) anticancer complexes can take a hydride from NADH that can promote the production of ROS, opening a pathway to an oxidation mode of action [32]. With the help of

UV-vis spectroscopy, the catalytic ability of **C9** and **C10** was investigated with the incubation of 100  $\mu\text{M}$  NADH. The NADH shows one absorption band at 339 nm, but after the addition of **C9** and **C10** (3  $\mu\text{M}$ ), the band at 339 nm gradually disappeared with time (0 $\rightarrow$ 210 min), which suggests the conversion of NADH to  $\text{NAD}^+$ . TON values were calculated through time-dependent absorption spectra and the values were found to be 17.4 and 15.4 for **C9** and **C10**, respectively. These TON values suggest that ruthenium complexes **C9** and **C10** have the capability to reduce the NADH and convert it into  $\text{NAD}^+$ . It can disrupt the  $\text{NAD}^+/\text{NADH}$  equilibrium and offer a potential pathway to generate ROS and enhance the killing of cancer cells by an oxidative mechanism of action [33] (Figure 4.23).

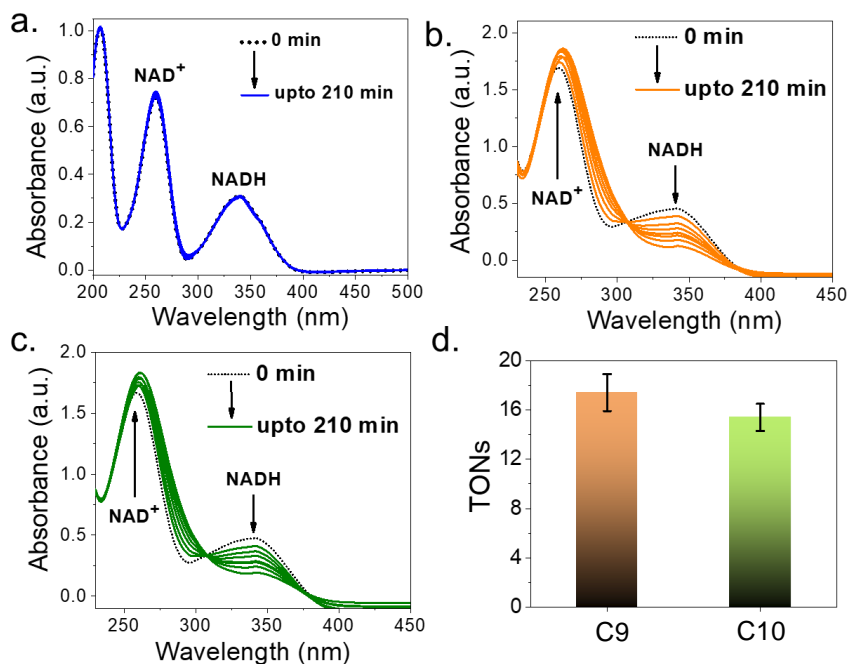


**Figure 4.23.** UV-vis spectra of the mixture of Ru(II) complex (3  $\mu\text{M}$ ), and NADH (100  $\mu\text{M}$ ) in PBS buffer at pH~7.4. (a) Self-catalysis of NADH in absence of **C9** and **C10**. (b) Time-dependent absorption spectra of NADH catalysis in presence of **C9**. (c) Linear curve fitting of NADH absorption maxima at 339 nm in presence of **C9**. (d) Time-dependent absorption spectra of NADH catalysis in presence of **C10**. (e) Linear curve fitting of NADH

absorption maxima at 339 nm in presence of **C10**. (f) The histogram representing the turnover numbers (TONs) of NADH catalysis by **C9** and **C10**.

### 5.3.5 Anticancer activity of core complexes and drug loaded nanogel

To evaluate the antiproliferative effect of complexes (**C9** and **C10**) and the loaded NGs on cancer cells and normal cells, three cancer cell lines HeLa, MCF7, A431, and a normal cell line HEK 293, were taken and treated with **C9** and **C10** and drugs loaded nanogels for 24 hrs. The outcomes demonstrated that both drug-loaded nanogels exhibit higher cytotoxicity than the free complexes **C9** and **C10**. The  $IC_{50}$  values of **C9**, **C10**, **GC9** and **GC10** were recorded as  $15.01 \pm 0.73$ ,  $24.05 \pm 0.56$ ,  $7.50 \pm 0.45$ , and  $10.17 \pm 0.62$   $\mu$ M against HeLa cell, respectively,  $15.52 \pm 0.35$ ,  $23.92 \pm 0.29$ ,  $10.61 \pm 0.38$  and  $12.53 \pm 0.34$   $\mu$ M against MCF 7 cell line respectively, and for normal cell line (HEK 293)  $IC_{50}$  values were  $51.32 \pm 0.63$ ,  $48.98 \pm 0.63$ ,  $60.29 \pm 0.32$  and  $58.60 \pm 0.57$   $\mu$ M respectively (Figure 4.24 and Table 4.2). The results indicated that drug-loaded cancer cell targeting nanogels, **GC9** and **GC10** showed higher cytotoxicity against cancer cell lines and lower cytotoxicity against normal cell lines due to the presence of cancer cell targeting biotin component in the gel, which can easily get recognized by cancer cells via integrin receptors that overexpressed in cancer cells. It can be concluded that the strategically designed cancer cell targeting nanogels enhanced the efficacy of **C9** and **C10** while encapsulated in gel matrices containing biotin components.

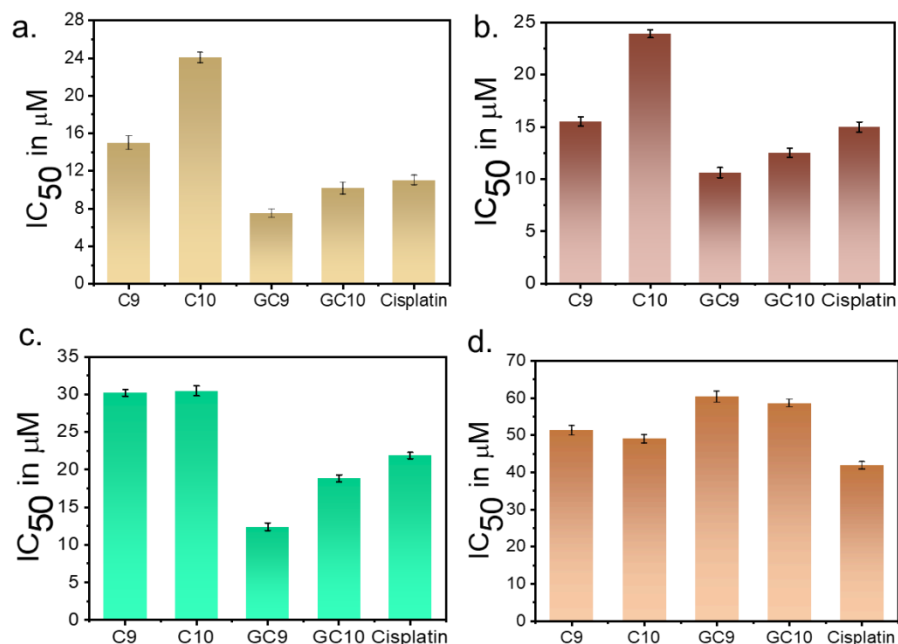


**Figure 4.24.**  $IC_{50}$  values of various cancer cells after the treatment of **C9**, **C10**, **GC9**, **GC10**, and positive control viz cisplatin. A temperature of 37 °C and 5%  $CO_2$  were thoroughly maintained during 24 h of incubation period. The histograms represent the  $IC_{50}$  values of the treated: (a) HeLa cervical cancer, (b) MCF7 breast cancer, (c) A431 epidermoid cancer cell, and (d) human embryonic HEK-293 kidney normal cell lines.

**Table 4.2.**  $IC_{50}$  values of complexes and NGs (**GC9** and **GC10**) against cancer cell line as well as normal cell line.

System	$IC_{50}$ ( $\mu$ M)			
	HeLa	MCF 7	A431	HEK 293
<b>Complex 9</b> ( <b>C9</b> )	15.01 $\pm$	15.52 $\pm$	30.20 $\pm$	51.32 $\pm$
	0.73	0.35	0.35	0.63
<b>Complex 10</b> ( <b>C10</b> )	24.05 $\pm$	23.92 $\pm$	30.46 $\pm$	48.98 $\pm$
	0.56	0.29	0.56	0.63
<b>GC9</b>	7.50 $\pm$	10.61 $\pm$	12.42 $\pm$	60.29 $\pm$
	0.45	0.38	0.41	0.32
<b>GC10</b>	10.17 $\pm$	12.53 $\pm$	18.86 $\pm$	58.60 $\pm$
	0.62	0.34	0.36	0.57

<b>Cisplatin</b>	11.04 ±	14.99 ±	21.87 ±	41.88 ±
	0.51	0.39	0.33	0.25

#### 4.3.6 Drug loading capacity and pH-mediated drug release study

The critical factors determining the drug activity of nanogels are drug loading capacity and release behaviour. The drug loading capacities of **GC9** and **GC10** are approximately 39.1% (19.5 mg/50 mg) and 35.9% (17.9 mg/50 mg), respectively, according to the weight measurement method. The investigation of pH-mediated drug release behavior is crucial for the development of effective drug delivery systems. In this study, the release behavior of drug-loaded nanogels **GC9** and **GC10** was examined in different pH environments. The nanogels were suspended in PBS at pH values 7.4 and 5.5 to mimic the normal tissue environment and tumor microenvironment, respectively.

The results presented in Figure 4.25a, indicate that the release ratios of both nanogels in acidic environments ~pH 5.5 are almost identical, with both releasing approximately 12.9% of their contents within the first six hours. The release amount quickly rises over time, reaching 76.8% and 73.4% for **C9** and **C10**, respectively, at 96 hours. In neutral environments with a pH of 7.4, the release rates of **C9** and **C10** from a nanogel system were found to be 22.2% and 20.2%, respectively, over a period of 96 hours. The different release behaviours of nanogel systems under neutral and acidic conditions were possibly caused by the wrapping of pH-responsive biopolymer CTS. The stability of CTS in neutral conditions allows for the encapsulation of drugs within the system, protecting them from degradation and improving their bioavailability. However, the protonation of amino groups in acidic conditions can cause to trigger drug release at specific sites. This pH-responsive behavior has been exploited to develop targeted drug delivery systems that release drugs only at the desired location, minimizing side effects and maximizing therapeutic efficacy. In this case, the conformation of CTS was transformed, and subsequently, rapid leaking of the complexes from the delivery system was observed [34]. As a result, the release of **C9** and **C10** from nanogels is found to

be pH dependent, with lower pH values providing more release of the cargo from gel system. However, it should be noted that under acidic and neutral conditions, nanogels demonstrate a distinct capacity for controlled release. Because of the hydrogen bonds between complexes and the remaining amino groups on the surface of the nanoparticles, **C9** and **C10** were released from the nanogel system more quickly when the pH was acidic. The amino groups were protonated in an acidic environment, causing the hydrogen bonds to break and the release of **C9** and **C10** occur more quickly. The above results showed that the nanogel system could control the release of complexes in an acidic environment, demonstrating the feasibility of controlling the release of drugs around tumour tissues but not in normal cells because of the pH differences. These results help to hypothesize that the pH-responsive drug release behaviour endowed the nanogels with significant anticancer drug delivery properties (Figure 4.25).

#### **4.3.7 *In vitro* cellular uptake study**

A drug to act as a cytotoxic agent must cross the cell membrane, which is composed of lipids and various proteins that control the substances that can enter the cell. Subsequently, cellular uptake is crucial for a targeted and efficient mode of treatment. Complexes have two pathways for entering the cell: endocytosis and active transport, both of which require energy for their processes. Complexes can also enter the cell through passive and facilitated diffusion, which does not rely on cellular energy [35]. This innovative approach of using target-based drug-loaded carriers has shown great potential in cancer treatment. By specifically targeting the overexpressed integrin receptor in cancer cell membranes, these carriers can increase the cellular uptake of drugs through an active transport process. This Chapter investigates the cellular uptake patterns of newly synthesized complexes, **C9** and **C10**, along with biotin-conjugated nanogels loaded with a drug targeting cancer cells, **GC9** and **GC10**. For the cellular uptake of these complexes in both breast cancer cells (MCF7) and normal cells (HEK 293) is studied by Inductively Coupled Plasma Atomic Emission Spectroscopy (ICP-AES). The

experimentally obtained values are found to be 0.324, 0.326, 0.372, and 0.360 in MCF7 cancer cells and 0.058, 0.072, 0.040, and 0.045  $\mu\text{g}/10^6$  in HEK 293 normal cells for **C9**, **C10**, **GC9**, and **GC10**, respectively (Figure 5.25b). Compared to normal cell viz HEK-293, cancer cell viz MCF7 were found to have higher intracellular ruthenium concentrations of synthesized compounds. Additionally, the results demonstrated that both nanogels, **GC9** and **GC10**, showed higher uptakes in MCF7 with respect to the core complexes **C9** and **C10** in the cancer cells. Interestingly the trends are found to be reversed in the normal cell line. From the above observation, it is concluded that biotin-conjugated targeted nanogels selectively deliver more drugs inside the cancerous cells than normal cells, which makes them potential candidates as drug-delivering agents for the cancerous cells.

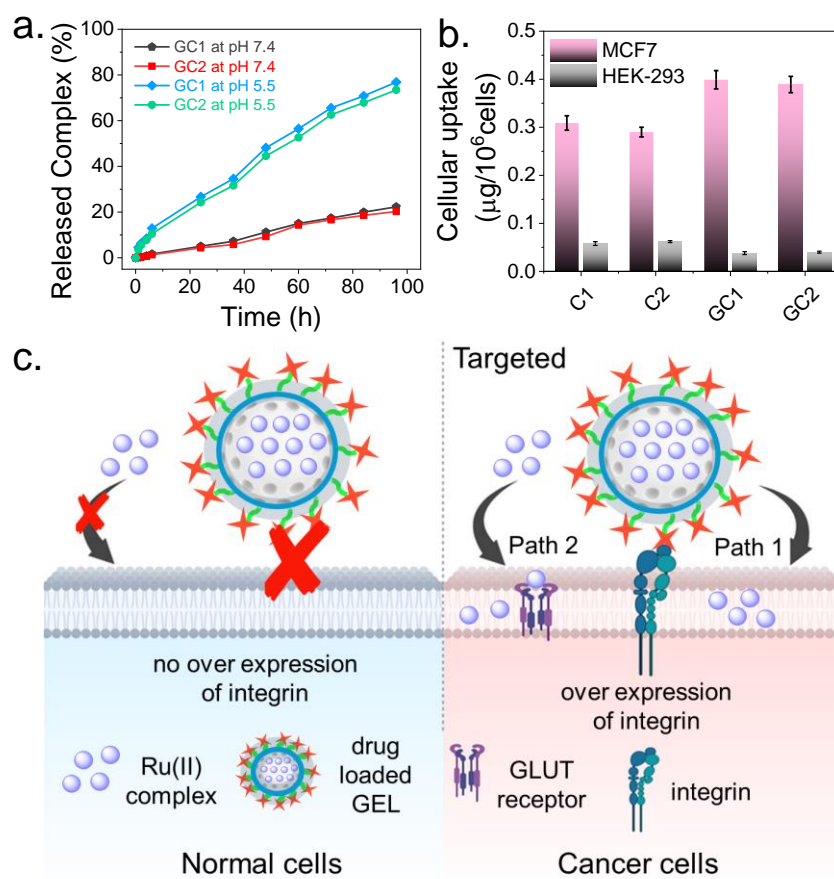


**Figure 4.25.** (a) Drug release profile of nanogels measured via UV-vis analysis under different pH environments. (b) Cellular uptake profile of **C9**,

*C10, GC9, and GC10 in MCF7 cancer, and HEK-293 normal cells. (b) Illustrating drug release mechanism from NGs to cancer, and normal cells.*

#### **4.3.8 Protein immunoblotting assay**

To better assess the actual mechanism of cancer cell deaths mediated by synthesized compounds, the expression level of apoptotic proteins associated with apoptosis was analyzed by western blotting. The expression level of cleaved caspase-3 was examined. The intrinsic and extrinsic pathways play an essential role in activating the caspase cascade, a common characteristic biological feature during apoptosis [36,37]. After exposing the HeLa cells to synthesized compounds for 24 hr at their close to IC<sub>50</sub> values, western blot results showed the cleavage of caspase-3. On the other hand, the expression level of anti-apoptotic protein BCL-XL was markedly inhibited by the **C9**, **C10**, **GC9**, and **GC10**. It is interesting to note that **C9** encapsulated in the gel exerted the lowest IC<sub>50</sub> value among the tested compounds and even with the lower concentration the caspase-3 cleavage and BCL-XL inhibitory activity of **GC9** was not different from the **C9**, which suggests encapsulation of **C9** in the gel resulted into the improved biological efficacy of the complex. Taken altogether, obtained results exhibited that the apoptosis in HeLa cells mediated by **C9**, **C10**, **GC9**, and **GC10** occurred through the caspase-dependent pathway (Figure 4.26).

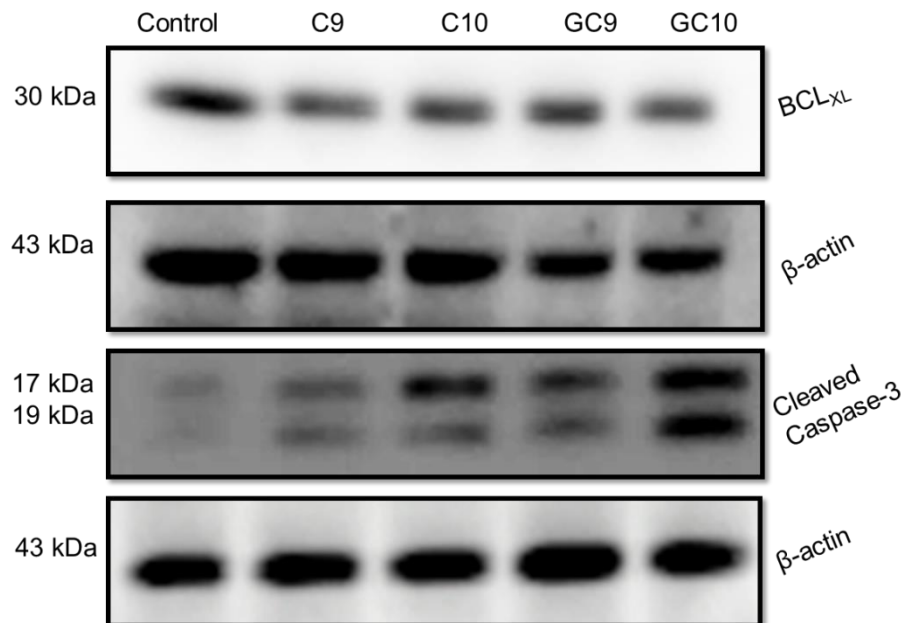


**Figure 4.26.** Representation of Western blotting experiments to examine the expression levels of proteins associated to apoptosis (e.g.,  $BCL_{XL}$  and Cleaved caspase-3) in HeLa cancer cells. The  $IC_{50}$  concentrations were used to perform the blotting experiments, such as **C9** ( $15.01 \mu M$ ), **C10** ( $24.05 \mu M$ ), **GC9** ( $7.50 \mu M$ ), and **GC10** ( $10.17 \mu M$ ) exposing through a period of 24 h.

#### 4.3.9 Metastasis Inhibition Assay

Malignant tumor cells can migrate and survive in non-malignant tissue and affect normal cells also, which causes a severe problem in the treatment of cancer [38]. Therefore, inhibition of migratory cells plays a vital role in chemotherapeutic drugs in the treatment of metastatic cancer. A study of the anti-metastatic potential in terms of the anti-migratory effect of drugs is extremely helpful in this regard. Thus, the anti-migration ability of synthesized compounds in MCF7 cancer cells was evaluated using a wound-healing assay. Results show that the treated cells reduced the migratory effect of cancer cells, whereas control cells (untreated) fill the space of the created wound. The wound closure ratios are 16.6%, 26.4%, 6.6%, and 7.8% for **C9**, **C10**, **GC9**, and **GC10**, respectively, while for untreated cells wound closure ratio is 75%. The outcome demonstrates that the compounds under consideration have the

potential to affect cancer cell metastasis, which is useful for cancer therapy (Figure 4.27).

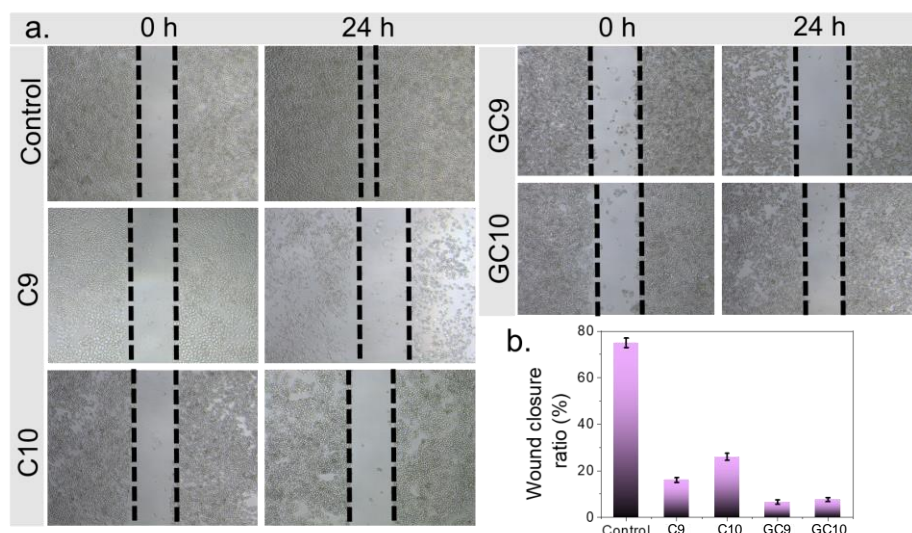


**Figure 4.27.** (a) Depiction of wound healing assay in MCF7 cancer cells having incubation period of 24 h. Control experiment represents the wound closure without treating any compound. (b) Histogram summarizing the percentage wound closure ratio of treated and untreated MCF7 cancer cells.

#### 4.3.10 ROS production in cancer cells

Reactive oxygen species (ROS) production plays a crucial role in various biological processes, including controlling the proliferation of cells, cellular apoptosis, and the mechanism of cell death. Cancer cells generate more spatially concentrated ROS than normal cells, stimulating the cell signaling pathways required for cellular transformation and carcinogenesis. Increased oxidative stress in cancer cells is caused by excessive ROS production and low levels or deactivation of antioxidant machinery. The ability of tumour cells to control the expression of endogenous antioxidant enzymes prevents the steady level of ROS from rising above the critical level, which would otherwise result in tumour cell death. However, nanogel-based targeted chemotherapy may be an effective way to increase anticancer efficacy for cancer cell death. Here, HeLa cells were treated and incubated with complexes and nanogels (at 10  $\mu\text{M}$ ) for 24 hours. The production of ROS was determined through the DCF-

DA assay, and the result shows the excessive production of ROS. This indicates that one of the reasons for cancer cell death while being treated with anticancer drugs is the overproduction of ROS, which leads to apoptosis (Figure 4.28a). ROS formation appears when the two acetate linkages of non-fluorescent DCF-DA are broken, resulting in green fluorescence-based DCF [39]. In Figure 4.28b, concentration-dependent fluorescence microscopic images of HeLa cancer cells treated with **GC9** are presented at two different concentrations (b1: 20  $\mu\text{M}$  and b2: 30  $\mu\text{M}$ ). Figure 4.28c, indicates a higher fluorescence intensity of ROS generation in **GC9** compared to the other compounds, exhibiting a greater capacity for ROS production in **GC9**.

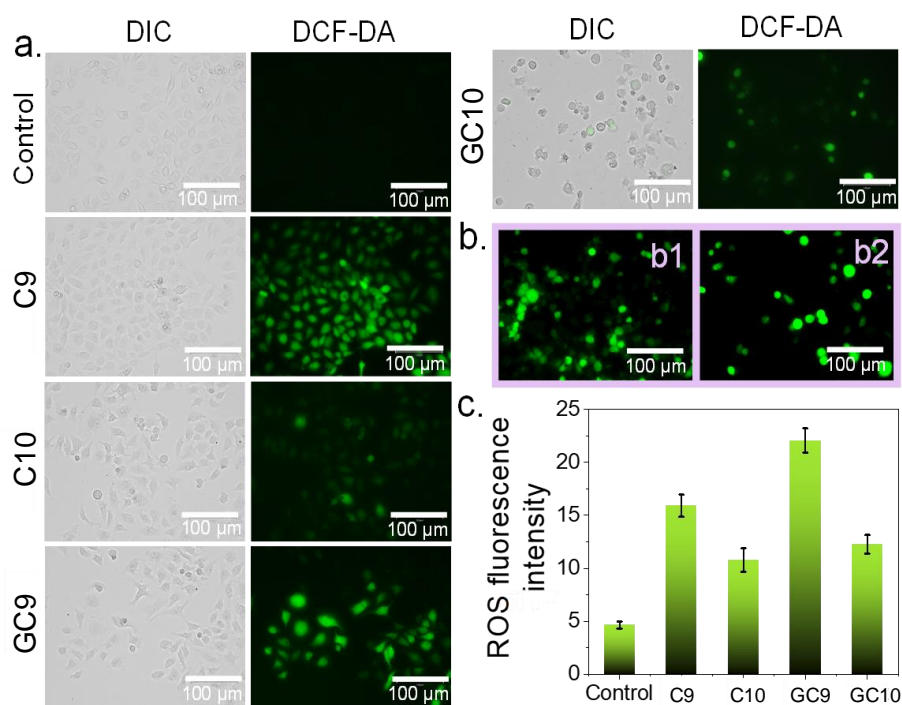


**Figure 4.28.** (a) Fluorescence microscopic images showing ROS generation in HeLa cancer cells after treating with **C9**, **C10**, **GC9**, and **GC10** (10  $\mu\text{M}$ ). Untreated control does not emit green fluorescence. The acronym ‘DIC’ stands for differential interference contrast. (b) Concentration dependent fluorescence microscopic images of **GC9** treated HeLa cancer cells (b1: 20  $\mu\text{M}$ , and b2: 30  $\mu\text{M}$ ). (c) The normalized ROS intensity calculated using ImageJ programme. Standard deviations are provided for three independent events.

### 4.3.11 Cell Morphology study via Hoechst Staining

Apoptosis is the main factor for cell death after treating cancer cells with our compounds. It indicates substantial nuclei morphological changes, cytoplasmic blebbing, chromatin condensation, and nuclear swelling. Such morphological changes in cells can be identified with the help of Hoechst staining. Through the Hoechst staining assay, the nuclear morphology changes of cells induced by the treatment of complexes and nanogels were evaluated. Consequently, the Hoechst staining assay was performed in HeLa cells using  $IC_{50}$  concentrations of complexes and nanogels [40]. Changes in the morphology were observed with the help of confocal microscopy and presented in Figure 4.29a. Furthermore, the changes in the morphology of the cells after **GC9** treatment at different concentrations (Figure 4.29b and 4.29c) were recorded. The untreated cells are found to be evenly and lightly stained; however, the treated cells can be observed with multinucleation, condensed nuclei, and chromatin fragmentation.

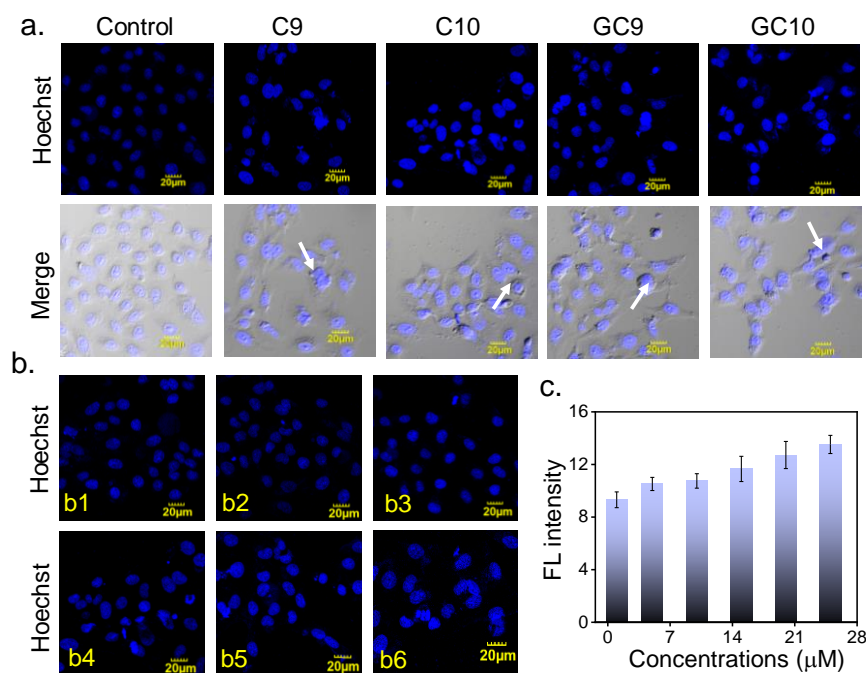


**Figure 4.29.** (a) Confocal images of treated and untreated HeLa cancer cells stained with Hoechst. Arrows indicate morphological changes of nucleus. (b) Treated HeLa cancer cells along with Hoechst staining at different

concentration of **GC9** (b1: 1  $\mu\text{M}$ , b2: 5  $\mu\text{M}$ , b3: 10  $\mu\text{M}$ , b4: 15  $\mu\text{M}$ , b5: 20  $\mu\text{M}$ , and b6: 25  $\mu\text{M}$ ). (c) Concentration dependent fluorescence intensity plot of treated cells, using ImageJ programme.

#### 4.3.12 Acridine Orange/EtBr dual staining assay

Using DNA-binding dyes like Acridine orange and EtBr, changes in the nuclear morphology during apoptosis were further explored. A cell-permeant nucleic acid binding dye called acridine orange can bind to DNA, stain living and dead cells, and emit green fluorescence. While EtBr, a red fluorescence dye, can stain only dead cells due to cell impermeability to live cells [41]. With the help of confocal microscopy, the morphological disruptions in cancer cells were studied after treating cancer cells with synthesized compounds close to their  $\text{IC}_{50}$  values. As shown in Figure 4.30, bright green fluorescence is emitted by acridine orange, staining both viable and apoptotic nuclei, while EtBr produced intense red fluorescence, staining only dead cells with fragmented and condensed nuclei. Additionally, untreated cells exhibit evenly light green emission and no red fluorescence, indicating no disruption in the nucleus. These findings clearly show that drug-loaded nanogels have the potential to induce apoptosis in cancer cells. To confirm the practical applicability of the synthesized nanogels, an *in vivo* approach was also used in addition to *in vitro* investigation. Same as *in vitro*, dual staining (acridine orange and propidium iodide) assay was utilized for *in vivo* imaging, and the results demonstrated that cellular apoptosis prevails over necrosis (Figure 4.31a). This study demonstrates the potential of compounds to be used in practical applications at lower concentrations. It also provides insights into the mechanisms by which they exert their effects, leading to further research.

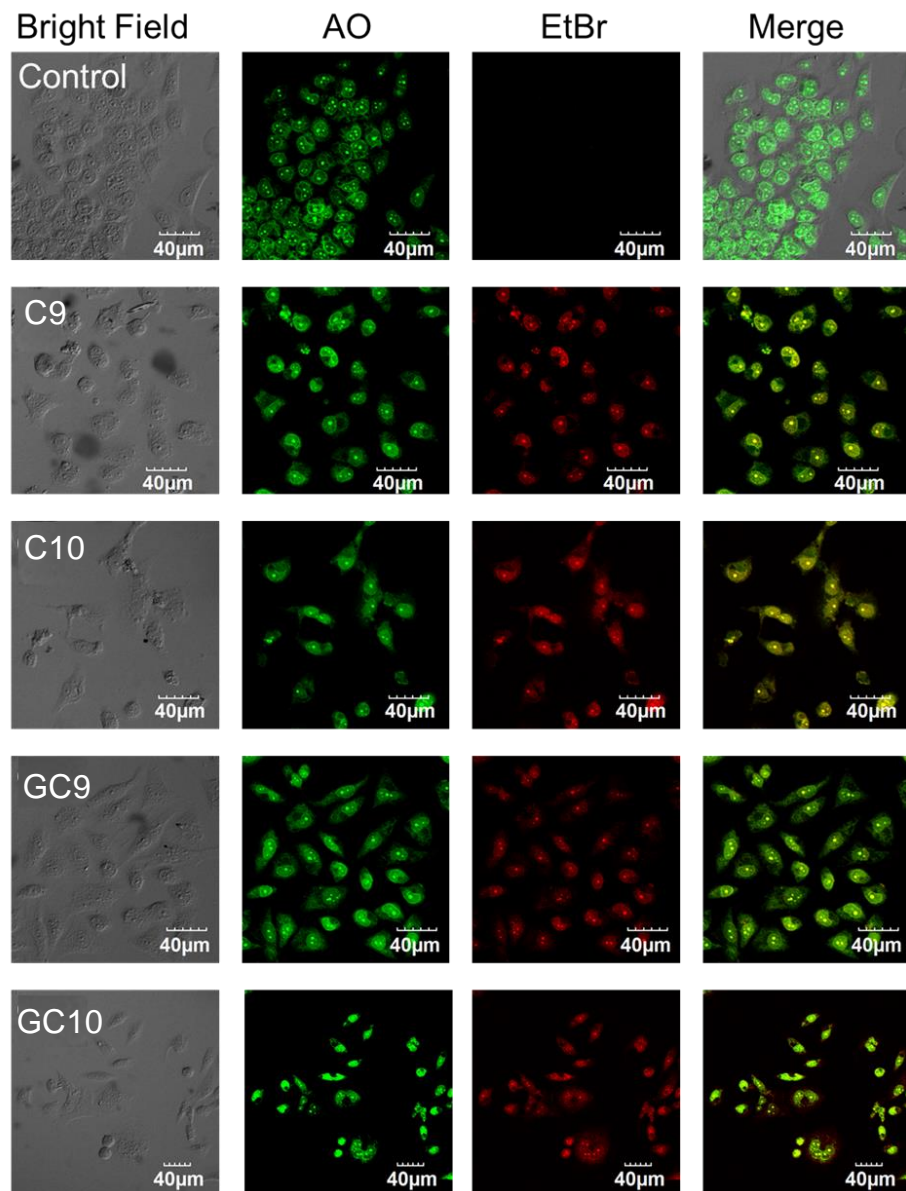


**Figure 4.30.** Confocal Images analysis of HeLa treated cells with synthesized compounds and untreated cells as a control, stained with AO/EtBr

#### 4.3.13 Quantification of toxicity in zebrafish embryos: *in vivo* study

Zebrafish (*Danio rerio*) are now viewed as an appropriate animal model for phenotype-based drug discovery due to their high DNA homology similarity to humans, rapid development, high fertility, and transparency. Because of DNA similarity with humans, it is a beneficial bioassay tool for toxicological studies and allows for high-quality *in vivo* confirmation of drug targets [42]. Following OECD guidelines [43], used embryos of zebrafish and exposed

them to different concentrations of drug-loaded nanogels **GC9** and **GC10** (10, 25, 50, 100, 200, 400, 800, 1200, and 1600  $\mu\text{M}$ ) to notice their rate of hatching, mortality, morphology, and heartbeat rate until 72 hours after fertilization (hpf). Drug-loaded nanogels **GC9** and **GC10** have shown promising results as a drug delivery system, with lethal dose concentration values of 1185.93  $\mu\text{M}$  and 823.03  $\mu\text{M}$ , respectively. Controlled release of the drug over an extended period can improve efficacy and reduce the frequency of administration (Figure 4.31b). The rate of heartbeat in the larvae and the percentage change from controls after compound treatment were analysed at 48 hpf. Both nanogels showed higher heart rates than controls (Figure 4.31c). After 24 hours, the hatching rate for both nanogels was 100% at a concentration of 100  $\mu\text{M}$ , whereas there was no hatchability observed at a concentration of  $\geq 400$   $\mu\text{M}$ . For both nanogels, no noticeable deformities were found at  $\leq 400$   $\mu\text{M}$  concentration (Figure 4.31d). The results on cardiac function show that overall toxicity is low, supporting further research on drug-loaded nanogels **GC9** and **GC10** for further evaluation as chemopreventive and chemotherapeutic agents.

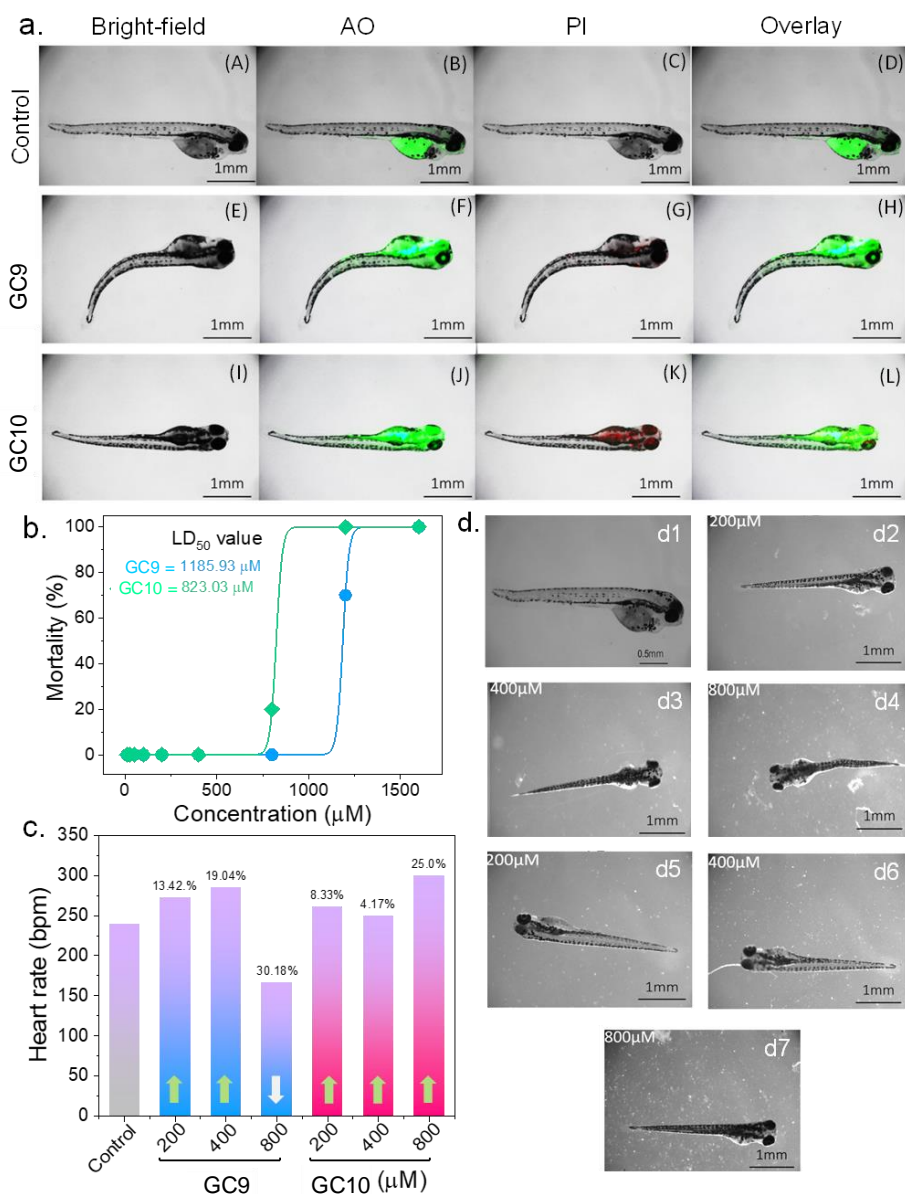


**Figure 4.31.** (a) *In vivo* zebrafish dual staining (AO/PI) assay after treatment with drug loaded nanogels at 72 hpf. (A) control larvae of Zebrafish; (B) AO-stained zebrafish control larvae emitting green fluorescence; (C) no red fluorescence in control larvae when stained with PI; (D) dual stained merged image of zebrafish showing only green emission at 72 hpf. (E) 800 µM of **GC9** treated zebrafish showing deformities; (F), and (G) are zebrafish images stained with AO, and PI, respectively treated with 800 µM of **GC9**. (H) is the merged image of (F), and (G) indicating live, and dead cells. (I) Zebrafish deformities upon treating 800 µM of **GC10**. (J), and (K) are zebrafish images

stained with AO, and PI, respectively treated with 800  $\mu\text{M}$  of **GC10**. (H) is the merged image of (F), and (G) indicating live, and dead cells. No such deformations were observed at  $\text{LD}_{50}$  concentrations. (b) Determining toxicity ( $\text{LD}_{50}$ ) of nanogels in zebrafish embryos at different concentrations of **GC9**, and **GC10** (10, 25, 50, 100, 200, 400, 800, 1200, and 1600  $\mu\text{M}$ ). (c) Heartbeat rate (in bpm) percentage bar chart of control, **GC9** and **GC10**. Arrows indicates increase or decrease heartbeat rate percentage when compared to control. Control represents by first bar, next three represents the **GC9** treated zebrafish embryos with increase heartbeat rate of 13.42 %, and 19.04 % at 200, and 400  $\mu\text{M}$  and decrease heartrate 30.18 % at 800  $\mu\text{M}$ . The last three bar represents the **GC10** treated zebrafish embryos with increase heartbeat rate of 8.33 %, 4.17 %, and 25.0 % at 200, 400, and 800  $\mu\text{M}$ , respectively. (d) Malformations observed in zebrafish embryos at 48 hpf after treatment with **GC9**, and **GC10**. Where (d1) control zebrafish, (d2, d3 and d5, d6) embryos treated with 200  $\mu\text{M}$  and 400  $\mu\text{M}$  of **GC9** and **GC10** showing no observable deformities, (d4 and d7) embryos treated with 800  $\mu\text{M}$  of **GC9** and **GC10** displaying stunned growth, blood congestion, edema, stunted growth, tail, and head malformation after 48 hpf.

#### 5.3.14 Self-healing nature of gel

Biomaterials from plants and animals exhibit an innate natural self-healing property. Gels have been identified as probable candidates that can mimic self-healing properties. The rheological time oscillation sweep (TOS)/strain sweep experiment has confirmed that these gels can heal themselves even after experiencing significant damage. The minimum and maximum applied strains with a constant angular frequency of 10 rad/s observed during the experiment show that these gels can withstand substantial mechanical stress without losing their self-healing properties. Furthermore, the incorporation of metal complexes into the gel matrix has been shown to enhance their mechanical strength and durability. Four cycles of TOS tests were conducted in both gels with periodic low (0.5% strain) and high (100% strain) strains applied at intervals of 200 seconds. The current study investigated the mechanical

properties of a nanogel under different strain levels. In step one, the nanogel was subjected to a low strain (0.5%) below its deformation level, resulting in the formation of a stable cross-linked gel structure, as indicated by the greater storage modulus ( $G'$ ) than the loss modulus ( $G''$ ). In step two, a higher strain (100% strain) was applied to the same nanogel after 200 seconds, causing the destruction of the cross-linked system within the gel matrix, as evidenced by a smaller  $G'$  value compared to  $G''$ . Step three demonstrated the recovery of the broken cross-linked system, with the sol transformed back into a gel within 200 seconds upon applying a low strain (0.5% strain) again. The nanogel exhibited a sol-gel-sol transition for four continuous cycles, indicating the regeneration of noncovalent and metal-ligand interactions. Notably, even after seven cycles, the gel strength showed no significant change. This suggests that the gel can maintain its shape and structure over time, which is an important characteristic for the development of advanced drug delivery systems.

Further, gels were taken out and divided into two halves on a petri dish. Then, with only a light press, the two pieces were reassembled and left untouched. Rhodamine B dye was used to stain one side of the joined gel. Furthermore, gels were cut into small pieces and brought into close contact, where they self-healed at the point where they were separated, resulting in a bridge made of alternate dye-doped and undoped gel. Generally, after 60 min, gels were found to be self-healed entirely (Figure 4.32).

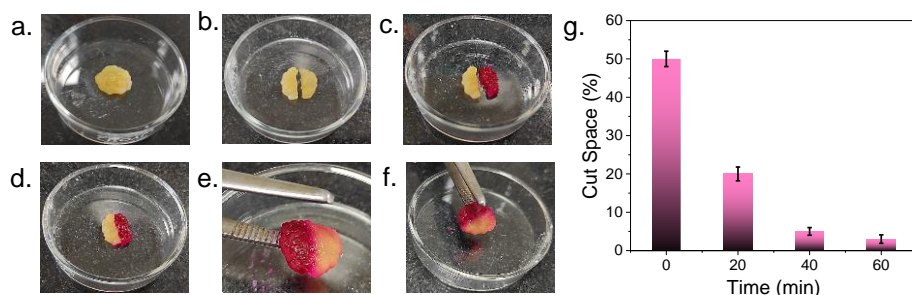


**Figure 4.32.** Self-healing nature of NGs recorded with a handheld camera. Images depict: (a) gel **GC9**, (b) gel separated into two pieces, (c) one side of the gel doped with a red dye, (d) doped and undoped sides start healing on contact, (e) 30 min, and (f) 60 min after the contact showing entirely self-

*healed nature of the gel. (g) Histogram representing increment of self-healing with time.*

#### **4.4 Conclusion**

In this Chapter, a novel drug delivery system (nanogels) that targets cancer cells and releases drugs in response to changes in pH levels, minimizing side effects and maximizing effectiveness is reported. The fabricated nanogels are loaded with synthesized glucose ring conjugated ruthenium (II) arene complexes as anticancer agents. The incorporation of glucose rings is to strategize the selective uptake of the complexes by cancerous cells to GLUT receptors. The core ruthenium complexes demonstrated improved cytotoxicity against different cancerous cell lines. Though the ruthenium complexes have shown significant selectivity towards cancerous cells, they can be further improved when loaded into the nanogels. The drug delivery system (NGs) which is used for this purpose is a combination of chitosan and biotin biopolymers that helps in targeted drug delivery. Bioconjugation with biotin promotes higher accumulation in cancer cells via receptor-mediated endocytosis, whereas pH-triggered release of ruthenium complexes has been achieved using chitosan. Core ruthenium complexes increase intracellular ROS production because they can catalyze the oxidation of NADH to NAD<sup>+</sup>. ROS can damage the DNA in the cell nucleus and trigger an intrinsic pathway (DNA damage-mediated pathway) for cellular apoptosis. Remarkably, all the results show that drug-loaded nanogels support the increased selectivity of ruthenium complexes between cancer and normal cells, subsequently establishing an improved anticancer property. The efficacy of this strategy presents a unique opportunity to investigate more practical and affordable drug delivery systems in the future.

#### **4.5 References**

[1] Mitchell, M. J.; Billingsley, M. M.; Haley, R. M.; Wechsler, M. E.; Peppas, N. A.; Langer, R. (2021), Engineering Precision Nanoparticles for Drug Delivery. *Nat Rev Drug Discov*, 20 (2), 101–124. (DOI: 10.1038/s41573-020-0090-8).

- [2] De, R.; Mahata, M. K.; Kim, K.-T. (2022), Structure-Based Varieties of Polymeric Nanocarriers and Influences of Their Physicochemical Properties on Drug Delivery Profiles. *Advanced Science* 9 (10), 2105373. (DOI: 10.1002/advs.202105373).
- [3] Mauri, E.; Perale, G.; Rossi, F. (2018), Nanogel Functionalization: A Versatile Approach to Meet the Challenges of Drug and Gene Delivery. *ACS Appl. Nano Mater.*, 1 (12), 6525–6541. (DOI: 10.1021/acsanm.8b01686).
- [4] Singh, A. P.; Biswas, A.; Shukla, A.; Maiti, P. (2019), Targeted Therapy in Chronic Diseases Using Nanomaterial-Based Drug Delivery Vehicles. *Sig Transduct Target Ther*, 4 (1), 1–21. (DOI: 10.1038/s41392-019-0068-3).
- [5] Wang, H.; Picchio, M. L.; Calderón, M. (2022), One Stone, Many Birds: Recent Advances in Functional Nanogels for Cancer Nanotheranostics. *WIREs Nanomedicine and Nanobiotechnology*, 14 (4), e1791. (DOI: 10.1002/wnan.1791).
- [6] Molina, M.; Asadian-Birjand, M.; Balach, J.; Bergueiro, J.; Miceli, E.; Calderón, M. (2015), Stimuli-Responsive Nanogel Composites and Their Application in Nanomedicine. *Chemical Society Reviews*, 44 (17), 6161–6186. (DOI: 10.1039/C5CS00199D).
- [7] Wang, H.; Gao, L.; Fan, T.; Zhang, C.; Zhang, B.; Al-Hartomy, O. A.; Al-Ghamdi, A.; Wageh, S.; Qiu, M.; Zhang, H. (2021), Strategic Design of Intelligent-Responsive Nanogel Carriers for Cancer Therapy. *ACS Appl. Mater. Interfaces*, 13 (46), 54621–54647. (DOI: 10.1021/acсами.1c13634).
- [8] Zhou, S.; Zhong, Q.; Wang, Y.; Hu, P.; Zhong, W.; Huang, C.-B.; Yu, Z.-Q.; Ding, C.-D.; Liu, H.; Fu, J. (2022), Chemically Engineered Mesoporous Silica Nanoparticles-Based Intelligent Delivery Systems for Theranostic Applications in Multiple Cancerous/Non-Cancerous Diseases. *Coordination Chemistry Reviews*, 452, 214309. (DOI: 10.1016/j.ccr.2021.214309).
- [9] García-Fernández, A.; Sancenón, F.; Martínez-Mañez, R. (2021), Mesoporous Silica Nanoparticles for Pulmonary Drug Delivery. *Advanced Drug Delivery Reviews*, 177, 113953. (DOI: 10.1016/j.addr.2021.113953).

- [10] Li, J.; Zeng, L.; Xiong, K.; W. Rees, T.; Jin, C.; Wu, W.; Chen, Y.; Ji, L.; Chao, H. (2019), A Biotinylated Ruthenium( II ) Photosensitizer for Tumor-Targeted Two-Photon Photodynamic Therapy. *Chemical Communications*, 55 (73), 10972–10975. (DOI: 10.1039/C9CC05826E).
- [11] Wang, H.; Chang, J.; Shi, M.; Pan, W.; Li, N.; Tang, B. (2019), A Dual-Targeted Organic Photothermal Agent for Enhanced Photothermal Therapy. *Angewandte Chemie*, 131 (4), 1069–1073. (DOI: 10.1002/ange.201811273).
- [12] Tian, B.; Hua, S.; Tian, Y.; Liu, J. (2020), Chemical and Physical Chitosan Hydrogels as Prospective Carriers for Drug Delivery: A Review. *J. Mater. Chem. B*, 8 (44), 10050–10064. (DOI: 10.1039/D0TB01869D).
- [13] Rasool, A., Rizwan, M., Islam, A., Abdullah, H., Shafqat, S. S., Azeem, M. K., ... & Bilal, M. (2021), Chitosan-Based Smart Polymeric Hydrogels and Their Prospective Applications in Biomedicine. *Starch-Stärke*, 2100150. (DOI: 10.1002/star.202100150).
- [14] Li, Z., Huang, J., & Wu, J. (2021), pH-Sensitive nanogels for drug delivery in cancer therapy. *Biomaterials science*, 9(3), 574-589. (DOI: 10.1039/D0BM01729A).
- [15] Liu, J., Lai, H., Xiong, Z., Chen, B., & Chen, T. (2019), Functionalization and cancer-targeting design of ruthenium complexes for precise cancer therapy. *Chemical Communications*, 55(67), 9904-9914. (DOI: 10.1039/C9CC04098F).
- [16] Pragti, Kundu, B. K., & Mukhopadhyay, S. (2021), Target based chemotherapeutic advancement of ruthenium complexes. *Coordination Chemistry Reviews*, 448, 214169. (DOI: 10.1016/j.ccr.2021.214169).
- [17] Trondl, R., Heffeter, P., Kowol, C. R., Jakupec, M. A., Berger, W., & Keppler, B. K. (2014), NKP-1339, the first ruthenium-based anticancer drug on the edge to clinical application. *Chemical Science*, 5(8), 2925-2932. (DOI: 10.1039/C3SC53243G).
- [18] Thota, S., Rodrigues, D. A., Crans, D. C., & Barreiro, E. J. (2018), Ru (II) compounds: next-generation anticancer metallotherapeutics?. *Journal of*

medicinal chemistry, 61(14), 5805-5821. (DOI: 10.1021/acs.jmedchem.7b01689).

[19] Dey, S., Murmu, N., Mondal, T., Saha, I., Chatterjee, S., Manna, R., ... & Giri, B. (2022), Multifaceted entrancing role of glucose and its analogue, 2-deoxy-D-glucose in cancer cell proliferation, inflammation, and virus infection. *Biomedicine & Pharmacotherapy*, 156, 113801. (DOI: 10.1016/j.biopha.2022.113801).

[20] Vaidya, S. P., & Patra, M. (2023), Platinum glycoconjugates: "Sweet bullets" for targeted cancer therapy?. *Current Opinion in Chemical Biology*, 72, 102236. (DOI: 10.1016/j.cbpa.2022.102236).

[21] Patra, M., Johnstone, T. C., Suntharalingam, K., & Lippard, S. J. (2016), A potent glucose-platinum conjugate exploits glucose transporters and preferentially accumulates in cancer cells. *Angewandte Chemie*, 128(7), 2596-2600. (DOI: 10.1002/ange.201510551).

[22] Patra, M., Awuah, S. G., & Lippard, S. J. (2016), Chemical approach to positional isomers of glucose-platinum conjugates reveals specific cancer targeting through glucose-transporter-mediated uptake in vitro and in vivo. *Journal of the American Chemical Society*, 138(38), 12541-12551. (DOI: 10.1021/jacs.6b06937).

[23] Bononi, G., Iacopini, D., Cicio, G., Di Pietro, S., Granchi, C., Di Bussolo, V., & Minutolo, F. (2021), Glycoconjugated metal complexes as cancer diagnostic and therapeutic agents. *ChemMedChem*, 16(1), 30-64. (DOI: 10.1002/cmdc.202000456).

[24] Gupta, S., Singh, N., Khan, T., & Joshi, S. (2022), Thiosemicarbazone derivatives of transition metals as multi-target drugs: A review. *Results in Chemistry*, 100459. (DOI: 10.1016/j.rechem.2022.100459).

[25] Bisceglie, F., Tavone, M., Mussi, F., Azzoni, S., Montalbano, S., Franzoni, S., ... & Pelosi, G. (2018), Effects of polar substituents on the biological activity of thiosemicarbazone metal complexes. *Journal of Inorganic Biochemistry*, 179, 60-70. (DOI: 10.1016/j.jinorgbio.2017.11.009).

- [26] Bonaccorso, C., Grasso, G., Musso, N., Barresi, V., Condorelli, D. F., La Mendola, D., & Rizzarelli, E. (2018), Water soluble glucose derivative of thiocarbohydrazone acts as ionophore with cytotoxic effects on tumor cells. *Journal of Inorganic Biochemistry*, 182, 92-102. (DOI: 10.1016/j.jinorgbio.2018.01.019).
- [27] Pragti, Kundu, B. K., Upadhyay, S. N., Sinha, N., Ganguly, R., Grabchev, I., Pakhira, S., & Mukhopadhyay, S. (2022), Pyrene-based fluorescent Ru (II)-arene complexes for significant biological applications: Catalytic potential, DNA/protein binding, two photon cell imaging and in vitro cytotoxicity. *Dalton Transactions*, 51(10), 3937-3953. (DOI: 10.1039/D1DT04093F).
- [28] Pragti, Kundu, B. K., Sonkar, C., Ganguly, R., & Mukhopadhyay, S. (2021), Modulation of catalytic and biomolecular binding properties of ruthenium (II)-arene complexes with the variation of coligands for selective toxicity against cancerous cells. *Polyhedron*, 207, 115379. (DOI: 10.1016/j.poly.2021.115379).
- [29] Wiercigroch, E., Szafraniec, E., Czamara, K., Pacia, M. Z., Majzner, K., Kochan, K., ... & Malek, K. (2017), Raman and infrared spectroscopy of carbohydrates: A review. *Spectrochimica Acta Part A: Molecular and Biomolecular Spectroscopy*, 185, 317-335. (DOI: 10.1016/j.saa.2017.05.045).
- [30] Kundu, B. K., Pragti, Carlton Ranjith, W. A., Shankar, U., Kannan, R. R., Mobin, S. M., ... & Mukhopadhyay, S. (2021), Cancer-targeted chitosan–biotin-conjugated mesoporous silica nanoparticles as carriers of zinc complexes to achieve enhanced chemotherapy in vitro and in vivo. *ACS Applied Bio Materials*, 5(1), 190-204. (DOI: 10.1021/acsabm.1c01041).
- [31] Morgan, D. J. (2015), Resolving ruthenium: XPS studies of common ruthenium materials. *Surface and Interface Analysis*, 47(11), 1072-1079. (DOI: 10.1002/sia.5852).
- [32] Betanzos-Lara, S., Liu, Z., Habtemariam, A., Pizarro, A. M., Qamar, B., & Sadler, P. J. (2012), Organometallic ruthenium and iridium transfer-hydrogenation catalysts using coenzyme NADH as a cofactor. *Angewandte Chemie*, 124(16), 3963-3966. (DOI: 10.1002/ange.201108175).

- [33] Xu, Z., Kong, D., He, X., Guo, L., Ge, X., Liu, X., ... & Liu, Z. (2018), Mitochondria-targeted half-sandwich ruthenium II diimine complexes: Anticancer and antimetastasis via ROS-mediated signalling. *Inorganic Chemistry Frontiers*, 5(9), 2100-2105. (DOI: 10.1039/C8QI00476E).
- [34] He, L., Huang, Y., Zhu, H., Pang, G., Zheng, W., Wong, Y. S., & Chen, T. (2014), Cancer-targeted monodisperse mesoporous silica nanoparticles as carrier of ruthenium polypyridyl complexes to enhance theranostic effects. *Advanced Functional Materials*, 24(19), 2754-2763. (DOI: 10.1002/adfm.201303533).
- [35] Dougherty, P. G., Sahni, A., & Pei, D. (2019), Understanding cell penetration of cyclic peptides. *Chemical Reviews*, 119(17), 10241-10287. (DOI: 10.1021/acs.chemrev.9b00008).
- [36] Asadi, M., Taghizadeh, S., Kaviani, E., Vakili, O., Taheri-Anganeh, M., Tahamtan, M., & Savardashtaki, A. (2022), Caspase-3: structure, function, and biotechnological aspects. *Biotechnology and Applied Biochemistry*, 69(4), 1633-1645. (DOI: 10.1002/bab.2233).
- [37] Singh, S., Sahadevan, R., Roy, R., Biswas, M., Ghosh, P., Kar, P., ... & Sadhukhan, S. (2022), Structure-based design and synthesis of a novel long-chain 4''-alkyl ether derivative of EGCG as potent EGFR inhibitor: in vitro and in silico studies. *RSC advances*, 12(28), 17821-17836. (DOI: 10.1039/D2RA01919A).
- [38] Fares, J., Fares, M. Y., Khachfe, H. H., Salhab, H. A., & Fares, Y. (2020). Molecular principles of metastasis: a hallmark of cancer revisited. *Signal transduction and targeted therapy*, 5(1), 28. (DOI: 10.1038/s41392-020-0134-x).
- [39] Dai, X., Zhang, B., Zhou, W., & Liu, Y. (2020), High-efficiency synergistic effect of supramolecular nanoparticles based on cyclodextrin prodrug on cancer therapy. *Biomacromolecules*, 21(12), 4998-5007. (DOI: 10.1021/acs.biomac.0c01181).
- [40] Malviya, N., Sonkar, C., Ganguly, R., Bhattacharjee, D., Bhabak, K. P., & Mukhopadhyay, S. (2019), Novel approach to generate a self-deliverable Ru

(II)-based anticancer agent in the self-reacting confined gel space. *ACS applied materials & interfaces*, 11(50), 47606-47618. (DOI: 10.1021/acsami.9b17075).

[41] Atale, N., Gupta, S., Yadav, U. C. S., & Rani, V. (2014), Cell-death assessment by fluorescent and nonfluorescent cytosolic and nuclear staining techniques. *Journal of microscopy*, 255(1), 7-19. (DOI: 10.1111/jmi.12133).

[42] Cassar, S., Adatto, I., Freeman, J. L., Gamse, J. T., Iturria, I., Lawrence, C., ... & Zon, L. I. (2019), Use of zebrafish in drug discovery toxicology. *Chemical research in toxicology*, 33(1), 95-118. (DOI: 10.1021/acs.chemrestox.9b00335).

[43] Busquet, F., Strecker, R., Rawlings, J. M., Belanger, S. E., Braunbeck, T., Carr, G. J., ... & Halder, M. (2014), OECD validation study to assess intra-and inter-laboratory reproducibility of the zebrafish embryo toxicity test for acute aquatic toxicity testing. *Regulatory Toxicology and Pharmacology*, 69(3), 496-511. (DOI: 10.1016/j.yrtph.2014.05.018).



*Chapter 5*

*Cancer-Targeted Chitosan–Biotin Conjugated  
Mesoporous Silica Nanoparticles as Carriers of  
Zinc Complexes to Achieve Enhanced  
Chemotherapy In Vitro and In Vivo*

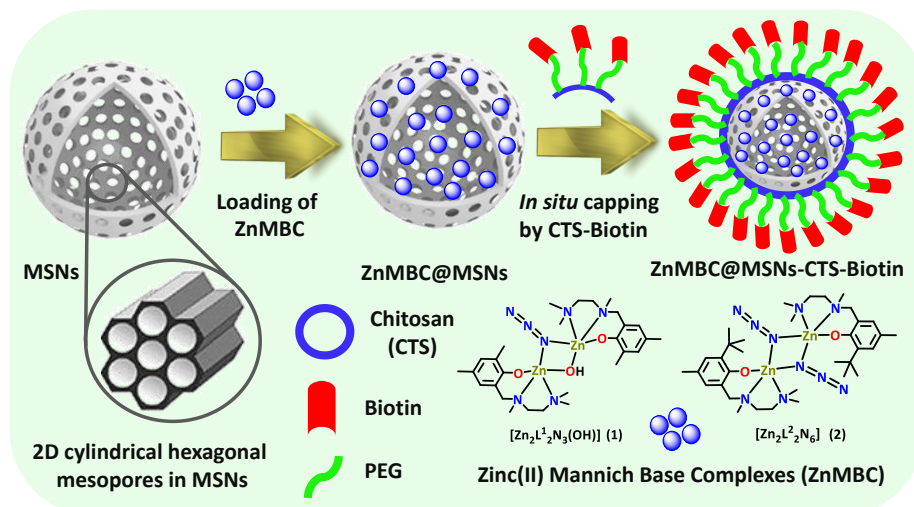
## **Chapter 5**

# **Cancer-Targeted Chitosan–Biotin Conjugated Mesoporous Silica Nanoparticles as Carriers of Zinc Complexes to Achieve Enhanced Chemotherapy In Vitro and In Vivo**

### **5.1 Introduction**

The primary reason for the high mortality rate of cancer patients, which is about 20.2% of the total death per annum, is mostly due to the lack of controlled, selective, and targeted drug delivery to cancer cells [1]. Therefore, the design of anticancer drug delivery systems is of great interest, as many of the drugs in the clinic cause severe toxic side effects due to nonspecific cytotoxicity, outweighing the therapeutic effect. Consequently, targeted nanodrug delivery systems are being developed with the help of a wide array of functional materials like metals, oxides, polymers, liposomes, semiconductors, micelles, and nanoparticle-based drug formulations combined with peptide or surface-antibody tagging, with the advantages like photochemical internalization, ultrasound stimulation etc. to enhance not only the therapeutic efficiency but also to suppress the toxic side effects [2,3]. Among these anticancer drugs carriers, MSNs have been well recognized as excellent disease-detection and drug delivery systems owing to their high pore volume, tunable pore morphologies, straightforward synthesis, facile functionalization, high drug loading capability, protection of drugs from harsh environment, biocompatibility, and capacity to carry disparate payloads (molecular drugs, proteins, other nanoparticles) within the porous core [4,5]. The endowed bioconjugation or easy surface modification property of MSNs helps them become an ideal vehicle for drug release, delivery, diagnosis, and imaging [6,7,8]. Also, to overcome the insolubility problem of hydrophobic anticancer drugs, using MSNs is a decent option [9]. Interestingly, the cytotoxicity of anticancer platinum drugs was found to be enhanced using

MSNs by ascertaining localized drug delivery though the mechanistic actions remain elusive [10]. Despite several advantages of MSNs, controlled drugs release is still a big challenge. In recent reports, an efficient agent biotin (vitamin H, a crucial cellular micronutrient accountable for numerous general cellular functions, growth, and development) has been considered for cancer cell-specific drug delivery as biotin conjugates as biotin molecules can preferentially bind to the overexpressed biotin receptors of cancer cells [11,12,13]. Now, introducing chitosan (CTS) can bridge biotin and MSNs through bioconjugation to produce smart delivery systems. The role of CTS is crucial because it is the second-most abundant polysaccharide after cellulose, having a vast number of amino groups on its chain which offers various sites of attachment to the cancer targeting molecule/ligand. Furthermore, its pH-sensitive biodegradability, biocompatibility, non-toxic nature, etc., make it significant for drug delivery systems (Scheme 5.1) [14,15]. Keeping in mind the pH distinction between normal (pH~7.4) and cancer (pH~5.5) cells, CTS can act as a “gatekeeper” for pH-tunable drug delivery.



**Scheme.5.1:** Schematic demonstration of the synthesis of zinc(II) nanodrug candidates.

In the realm of chemotherapeutic metallodrugs, scientists are constantly looking to go beyond platinum complex-based chemotherapy to combat drug resistance, reduce side effects, and economically viable options [16]. As an essential element for humans, zinc (Zn), which exists in all life forms, acquires

several commendatory properties (e.g., low toxicity and high coordination number) appropriate for rational anticancer drug design and other medicinal applications. Owing to such importance, irregularity of its homeostasis can lead to various diseases, which can be further linked to cancer development [17,18]. Numerous zinc-mediated complexes have been documented over the years for their pivotal biological activities in preventing infectious diseases. Among diverse medicinal applications, Zn(II) complexes have been revealed to be appealing as anticancer drugs with minimum side effects or as photosensitizers in photodynamic therapy. Recently, FDA approved two zinc-based histone deacetylase (HDAC) inhibitors such as depsipeptide (in 2009) and suberoylanilide hydroxamic acid (in 2006), for the treatment of cancers [19]. Among the various options of zinc-binding ligands, Mannich base-driven complexes received immense attention recently due to their unique properties, namely easy synthetic pathways, high stability, and flexible structures for fine-tuning to obtain compounds with promising *in vitro* and *in vivo* cytotoxic activities [20,21]. Several reports have also observed that higher nuclearity in metal complexes can help in obtaining more cytotoxic species, and using an ancillary bridging ligand, e.g., azide, can be an excellent choice to produce complexes with higher nuclearity [18]. Herein, two new azide-bridged zinc Mannich base complexes have been synthesized to get evaluated as core drug candidates for the *in vitro* treatment of a series of human cancer cells viz. breast cancer MCF7, cervical carcinoma HeLa, alveolar basal epithelial A549 (lung), and epidermoid carcinoma A431. In addition, selective drug administration inside cancer cells was quantified using ICP-OES, and the corresponding morphological changes at the cellular level were investigated via two-photon microscopy. Further emphasis has also been given to *in vivo* zebrafish culture to check the practical applicability of titled compounds because it has emerged in cardiac research that it can display anatomical resemblance to the human heart. Besides, to determine the lethal dose (LD50) responses in normal zebrafish embryos, the heartbeat of the larvae has been

analyzed in assessing cardiac function since discrepancies in heart rhythm can be the reason or consequence of hidden pathological heart conditions [22].

Thus, in this chapter, the main objectives are to determine whether it is possible to design improved anticancer zinc candidates and improve the therapeutic index of antitumor nanodrugs using pH-triggered CTS. Furthermore, the interaction between peptide/protein, say biotin and overexpressed  $\alpha\beta3$  integrin receptor of cancer cells is exploited for better drug delivery of the zinc payload, and it is investigated if zinc nanodrug agents are suitable for in vivo administration.

## **5.2 Experimental Section**

### **5.2.1 Materials and methods**

All the chemical reagents were commercially accessed with highest quality analytical grade mostly from Sigma Aldrich and used without further purification. The reagents, concentrated HCl, diethyl ether, magnesium sulfate, and zinc acetate dihydrate were supplied from Merck. 4% formaldehyde, ethanol (EtOH), dimethyl sulfoxide (DMSO), polyethylene glycol (PEG), cetyltrimethylammonium bromide (CTAB), biotin, chitosan (CTS), N-hydroxysuccinimide (NHS), and tetraethyl orthosilicate (TEOS) were obtained by Sisco Research Laboratories Pvt. Ltd. Cis-platin, doxorubicin hydrochloride (DOX), 5-fluorouracil (5-FU), and dichlorodihydrofluorescein diacetate (DCF-DA) were purchased from Tokyo Chemical Industry (TCI). Deionized water (Millipore, 18 M $\Omega$ ) was used to prepare buffer or physiological mediums. pH was measured using TOSHCON INDUSTRIES Pvt. LTD., AJMER. NMR ( $^1\text{H}$  and  $^{13}\text{C}$ ), ESI-MS/HRMS, and FTIR have been recorded in an AVANCE III 400 Ascend Bruker BioSpin, MicroTOF-Q II, and BRUKER TENSOR 27 instruments, respectively. Thermo Scientific FLASH 2000 (Flash EA1112), and METTLER TOLEDO were used for determining C, H, N and S contents, and thermogravimetric analysis (TGA; N $_2$  atmosphere, 0-800  $^\circ\text{C}$ , heating rate of 10 $^\circ\text{C min}^{-1}$ ). Photophysical properties such as UV-Vis, Fluorescence, and TCSPC were performed in Perkin-Elmer lambda-650 (Model: Cary 100), Horiba JobinYvon (Model: FM-100) made Fluoromax-4p, and HORIBA Jobin

Yvon picosecond (model Fluorocube-01-NL) spectrophotometers, respectively. For microscopic techniques, Carl zeiss Libra 200FE, Supra55 Zeiss, Nikon (Model: TS100 Eclipse, Hg lamp), and Olympus confocal microscopes were utilized to analyze HRTEM, FE-SEM, fluorescence, and two photon images. Raman, PXRD, and BET were recorded in a CCD detector based Jobin Yvon T64000, Rigaku SmartLab, and NOVA 1200 (Quanta Chrome) equipment, respectively. XPS, and ICP-OES PHI were measured through a Physical Electronics made 5000 VersaProbe III (Mg-K $\alpha$  X-rays,  $h\nu = 1253.6$  eV), and “Perkin Elmer”- ELAN DRC-e instruments, respectively.

## 5.2.2 Syntheses of compounds

### 5.2.2.1 Synthesis of Mannich base ligands (HL<sup>1</sup> and HL<sup>2</sup>)

Two Mannich bases have been synthesized as described in our previous report [23,24]. The spectroscopic characterization of the two ligands is given below.

#### 5.2.2.2 Synthesis of 2,4-Dimethyl-6-[(2'-dimethyl aminoethyl)-methylamino]methyl-phenol (HL<sup>1</sup>)

Molecular Weight: 236.36 g/mol. Yield: 2.10 g, 8.9 mmol, 83% (reactant, 10.7 mmol). <sup>1</sup>H NMR (400.13 MHz, 298K, CDCl<sub>3</sub>, in ppm):  $\delta$  2.211 (3H, s, -CH<sub>3</sub> Ar), 2.220 (3H, s, -CH<sub>3</sub> Ar), 2.256 (6H, s, -N(CH<sub>3</sub>)<sub>2</sub>), 2.285 (2H, s, -NCH<sub>2</sub> Ar), 2.512 and 2.589 (2H+2H, t, -NCH<sub>2</sub>CH<sub>2</sub>N-), 3.618 (3H, s, -N(CH<sub>3</sub>)), 4.875 (1H, s, ArOH), 6.628 (1H, s, ArH), 6.859 (1H, s, ArH), <sup>13</sup>C NMR (100.61 MHz, 298 K, CDCl<sub>3</sub>, in ppm):  $\delta$  15.710, 20.401, 41.830, 45.544, 54.687, 56.938, 60.753, 121.261, 124.594, 126.777, 127.292, 130.463, 153.501. Anal. Calculated for C<sub>14</sub>H<sub>24</sub>N<sub>2</sub>O: C, 71.14 %; H, 10.24%; N, 11.85%. Found: C, 71.26%; H, 10.32%; N, 11.72%. FTIR (in KBr pallette,  $\nu$  in cm<sup>-1</sup>): 1475 ( $\nu$ C-H, Scissoring, s), 1245 ( $\nu$ C-N, s). ESI-MS in HPLC MeOH (+ve mode, m/z): {C<sub>14</sub>H<sub>24</sub>N<sub>2</sub>O + H}<sup>+</sup>: 237.20 (100%). UV/Vis in HPLC H<sub>2</sub>O: ( $\lambda_{\max}$ , nm): 284

#### 5.2.2.3 Synthesis of 2-Methyl-4-t-butyl-6-[(2'-dimethyl aminoethyl)-methylamino]methyl-phenol (HL<sup>2</sup>)

Molecular Weight: 278.44 g/mol. Yield: 2.39 g, 8.6 mmol, 80% (reactant, 10.7 mmol). <sup>1</sup>H NMR (400.13 MHz, 298K, CDCl<sub>3</sub>, in ppm):  $\delta$  1.397 (9H, s, -t-Bu Ar), 2.205 (6H, s, -N(CH<sub>3</sub>)<sub>2</sub>), 2.228 (3H, s, -CH<sub>3</sub> Ar), 2.298 (3H, s, -N(CH<sub>3</sub>)),

2.466 and 2.539 (2H+2H, t, -NCH<sub>2</sub>CH<sub>2</sub>N-), 3.631 (2H, s, -NCH<sub>2</sub> Ar), 6.637 (1H, s, ArH), 6.973 (1H, s, ArH), <sup>13</sup>C NMR (100.61 MHz, 298 K, CDCl<sub>3</sub>, in ppm): δ 21.166, 29.941, 34.932, 42.095, 46.026, 54.573, 57.409, 62.201, 122.447, 126.981, 127.237, 127.609, 136.595, 154.821. Anal. Calculated for C<sub>17</sub>H<sub>30</sub>N<sub>2</sub>O: C, 73.33 %; H, 10.86%; N, 10.06%. Found: C, 73.16%; H, 10.91%; N, 9.89%. FTIR (in KBr pallette,  $\nu$  in cm<sup>-1</sup>): 1447 ( $\nu$ C-H, Scissoring, s), 1242 ( $\nu$ C-N, s). ESI-MS in HPLC MeOH (+ve mode, m/z): {C<sub>17</sub>H<sub>30</sub>N<sub>2</sub>O + H}<sup>+</sup>: 279.24 (100%). UV/Vis in HPLC H<sub>2</sub>O: ( $\lambda_{\max}$ , nm): 282.

#### 5.2.2.4 Synthesis of complex Zn<sub>2</sub>L<sup>1</sup><sub>2</sub>N<sub>3</sub>(OH) (ZnMBC 11)

152  $\mu$ L triethylamine (1.0 mmol) was added to a solution of **HL**<sup>1</sup> (0.236 g, 1.0 mmol) followed by mixing with a 20 mL methanolic solution of Zn(OAc)<sub>2</sub>·2H<sub>2</sub>O (0.219 g, 1.0 mmol) and NaN<sub>3</sub> (0.078 g, 1.2 mmol) to stir under inert atmosphere for 4 h. The colourless microcrystalline solid was obtained by filtration. Needle-shaped transparent single crystals were obtained through vapor diffusion method in MeOH: DEE solvent after 3-4 days. Molecular Weight: 660.49 g/mol. Yield: 0.541 g, 0.82 mmol, 82%. Anal. Calculated (%) for C<sub>28</sub>H<sub>46</sub>N<sub>7</sub>O<sub>3</sub>Zn<sub>2</sub>: C, 50.92; H, 7.17; N, 14.84; Found (%): C, 51.08; H, 7.31; N, 14.66. ESI-MS in HPLC H<sub>2</sub>O (+ve mode, m/z): {[Zn<sub>2</sub>L<sup>1</sup><sub>2</sub>N<sub>3</sub>(OH)] + H<sub>2</sub>O + H<sup>+</sup>}<sup>+</sup>: 679.97 (100%) and {C<sub>28</sub>H<sub>46</sub>N<sub>7</sub>O<sub>3</sub>Zn<sub>2</sub> + H<sub>2</sub>O + H<sup>+</sup>}<sup>+</sup>: 743.19 (100%). FTIR (in KBr,  $\nu$  in cm<sup>-1</sup>): 2918 { $\nu$ C-H, (m)}, 2084 { $\nu$ N=N=N, stretching, (s, sh)}, 1026 { $\nu$ C-O, phenolic, (s)}, 518 { $\delta$ Zn-O-Zn, (m)}. UV/Vis in HPLC H<sub>2</sub>O: ( $\lambda_{\max}$ , nm): 285.

#### 5.2.2.5 Synthesis of complex Zn<sub>2</sub>L<sup>2</sup><sub>2</sub>(N<sub>3</sub>)<sub>2</sub> (ZnMBC 12)

Complex **12** was also synthesized in a similar procedure as adopted for complex **11**. **HL**<sup>2</sup> (0.278 g, 1.0 mmol) has only been used in place of ligand **HL**<sup>1</sup>. The mixture was stirred for 4 h under inert atmosphere and recrystallized by slow evaporation of methanol at room temperature. Block-shaped transparent single crystals were found after 4-5 days through vapor diffusion method in MeOH: DEE solvent. Molecular Weight: 769.67 g/mol. Yield: 0.684 g, 0.89 mmol, 89%. Anal. Calculated (%) for C<sub>34</sub>H<sub>58</sub>N<sub>10</sub>O<sub>2</sub>Zn<sub>2</sub>: C, 53.06; H, 7.60; N, 18.20; Found (%): C, 52.88; H, 7.39; N, 18.35. ESI-MS in HPLC

H<sub>2</sub>O (+ve mode, m/z): {[Zn<sub>2</sub>L<sub>2</sub>(N<sub>3</sub>)<sub>2</sub>] + H<sub>2</sub>O + K<sup>+</sup>}<sup>+</sup>: 827.28 (100%). FTIR (in KBr,  $\nu$  in cm<sup>-1</sup>): 2903 { $\nu_{C-H}$ , (m)}, 2079 { $\nu_{N=N=N}$ , stretching, (s, sh)}, 1023 { $\nu_{C-O}$ , phenolic, (s)}, 516 { $\delta_{Zn-O}$ , (sh)}. UV/Vis in HPLC H<sub>2</sub>O: ( $\lambda_{max}$ , nm): 281.

Where, the above abbreviations define; (s) = strong; (m) = medium and (sh) = sharp band.

### 5.2.2.6 Preparation of Nanoparticles

The MSN-based nanoparticles were synthesized based on previous reports [25]. Here, a short description has been added for the reference.

#### 5.2.2.6.1 Preparation of MSNs

Briefly, 1.0 g of CTAB and 0.28 g of NaOH were dissolved in 480 mL of distilled water and heated to 80 °C with vigorous stirring. Next, 5.0 g of TEOS was added dropwise to the solution with vigorous stirring and heated at 80 °C for 2 h. Finally, the white precipitate was washed with distilled water and methanol three times each and dried under high vacuum. The CTAB surfactant of the MSNs was removed with concentrated HCl at 80 °C for 48 h. The resulting product was washed with ethanol and double-distilled water six times each and dried as mentioned above. The obtained product was denoted MSNs.

#### 5.2.2.6.2 Synthesis of Drug-Loaded ZnMBC 11/12@MSNs

50 mg of MSN particles was added to 5 mL of ZnMBC 11/12 solution (10 mg/mL). The mixed solution was stirred for 24 h at room temperature in the dark. The product was collected by centrifugation and vacuum-drying to obtain ZnMBC 11/12@MSN particles. The loading capacity (LC) of ZnMBC in MSNs was determined by the weight and UV/vis spectrophotometry methods and calculated with the following formula

$$\text{For weight method: } LC = (m_1 - m_0)/m_1 \quad (1)$$

Here,  $m_0$  and  $m_1$  are the weights of MSNs–biotin before and after loading, respectively.

#### 5.2.2.6.3 Preparation of Chitosan and Biotin Conjugates (CTS-Biotin)

Biotin-PEG-NHS was joined to CTS by conjugating NHS to the -NH<sub>2</sub> group on CTS to obtain CTS-Biotin. In brief, CTS (50 mg) and Biotin-PEG-NHS (10 mg) were reacted in dry tetrahydrofuran (THF) (10 mL) at room temperature

for 24 h and then CTS-Biotin was collected by centrifugation and vacuum drying.

#### 5.2.2.6.4 Synthesis of drug loaded ZnMBC 11/12@MSNs-CTS-Biotin

Twenty milliliters 2% w/v CTS-Biotin acetic acid aqueous (10% v/v) solution was prepared, and the pH was adjusted to 6.0 with 1 M NaOH, then ZnMBC 1/2@MSNs was added into it and stirred for 24 h at room temperature in the dark. The mixture was centrifuged, suspended, washed with deionized water twice, and dried. Then the resulting product ZnMBC 11/12@MSNs-CTS-Biotin was obtained. The concentration of ZnMBC 11/12 in the nanomaterials was determined by weight method:

$$LC = m_0/m_1 \quad \dots(2)$$

Herein,  $m_0$  and  $m_1$  mean the weight of ZnMBC 11/12 in ZnMBC 11/12@MSNs and the weight of obtained ZnMBC 11/12@MSNs-CTS-Biotin.

#### 5.2.2.6.5 Preparation of amino-functionalized MSNs (MSNs-NH<sub>2</sub>)

The surface of MSNs was functionalized with amine groups by treatment with APTES. MSNs (50 mg) were dispersed in 100 mL of ethanol, followed by the addition of 100  $\mu$ L of APTES. Then the solution was refluxed for 4 h. MSNs-NH<sub>2</sub> was then collected by centrifugation and vacuum drying.

#### 5.2.2.6.6 Synthesis of Biotin modified MSNs delivery system (MSNs-Biotin)

The Biotin-PEG-NHS was joined to MSNs by conjugating N-hydroxysuccinimide (NHS) onto MSNs-NH<sub>2</sub> to obtain MSNs-Biotin. In brief, MSNs-NH<sub>2</sub> (50 mg) and Biotin-PEG-NHS (10 mg) was reacted in dry THF (10 mL) at room temperature for 24 h, and then MSNs-Biotin were collected by centrifugation and vacuum drying.

#### 5.2.2.6.7 Synthesis of CTS modified MSNs delivery system (MSNs-CTS)

Twenty millilitre 2% w/v CTS acetic acid aqueous (10% v/v) solution was prepared and the pH was adjusted to 6.0 with 1 M NaOH, then MSNs was added into it and stirred for 24 h at room temperature in dark. The mixture was centrifuged, suspended, washed with deionized water twice and dried. Then the resulting products MSNs-CTS was obtained.

#### 5.2.2.6.8 Synthesis of drug loaded ZnMBC 11/12@MSNs-Biotin

To obtain the ZnMBC 11/12@MSNs-Biotin particles, 50 mg of the MSNs-Biotin particles was added to 5 mL of the ZnMBC solution (10 mg/mL). The mixed solution was stirred for 24 h at room temperature in the dark, and then collected by centrifugation and vacuum drying. The loading capacity (LC) of the nanomaterials was determined following aforementioned equations (1, 2).

#### 5.2.2.6.9 Synthesis of drug loaded ZnMBC 11/12@MSNs-CTS

Twenty milliliters of 2% w/v CTS acetic acid aqueous (10% v/v) solution was prepared, and the pH was adjusted to 6.0 with 1 M NaOH, then ZnMBC 11/12@MSNs was added into it and stirred for 24 h at room temperature in the dark. The mixture was centrifuged, suspended, washed with deionized water twice, and dried. Then the resulting product ZnMBC 11/12@MSNs-CTS was obtained.

### 5.2.3 X-ray crystallography

Single crystal X-ray structural studies of ZnMBC 11 and ZnMBC 12 were elucidated on a CCD Agilent Technologies (Oxford Diffraction) SUPER NOVA diffractometer. Data for both the compounds were collected at 293 K using a graphite-monochromated  $\text{CuK}\alpha$  radiation ( $\lambda_{\alpha} = 0.71073 \text{ \AA}$ ). The strategy for the data collection was evaluated by using the CrysAlisPro CCD software. The data were collected using the standard 'phi-omega scan techniques and scaled and reduced using CrysAlisPro RED software. The structures were solved by direct methods using SHELXS-97 and refined by full matrix least-squares with SHELXL-97, refining on  $F^2$ . The positions of all the atoms were obtained by direct methods. All non-hydrogen atoms were refined anisotropically. The remaining hydrogen atoms were placed in geometrically constrained positions and refined with isotropic temperature factors, generally  $1.2U_{\text{eq}}$  of their parent atoms.

### 5.2.4 Experimental Methods

#### 5.2.4.1 Stability studies in DMSO/DMEM medium

For the stability studies, all complexes were dissolved in 5% DMSO/95% DMEM at ca.  $1 \times 10^{-4} \text{ M}$ , and their electronic spectra were recorded in the

range allowed by the solvents at set time intervals. The samples used in the measurements were protected from light sources and were stored at room temperature between measurements.

#### **5.2.4.2 DNA binding study**

##### **5.2.4.2.1 Absorption spectral studies**

DNA binding experiments were done following the procedure outlined in section 2.2.5.1 of chapter 2.

##### **5.2.4.2.2 Competitive binding experiments**

It was done by following the same procedure outlined in section 2.2.5.2 of chapter 2 for competitive binding experiments.

#### **5.2.4.3 Protein binding assay**

##### **5.2.4.3.1 Absorption spectral studies**

The stock solutions of Bovine serum albumin (BSA) and Human serum albumin (HSA) proteins were prepared in TRIS-HCl buffer (pH ~7.4). Concentrated stock solutions of ZnMBC **11** and ZnMBC **12** were prepared by dissolving them separately in TRIS-HCl buffer and diluted suitably to get the required concentrations. An aqueous solution (2 mL) of BSA or HSA protein (10  $\mu$ M) was titrated by successive additions of the respective complexes (0-100  $\mu$ M). Interaction with proteins is also monitored by measuring the increment of the absorption band at 278 nm in UV-Vis spectroscopy through successive addition of 0-100  $\mu$ M of ZnMBC **11** and ZnMBC **12** in 10  $\mu$ M protein solutions.

##### **5.2.4.3.2 Competitive binding experiments**

Protein binding experiments follow the procedure outlined in section 2.2.4.1 of chapter 2.

#### **5.2.4.4 Evaluation of cytotoxicity**

The procedure for MTT assay is same as discussed in section 2.2.5.1 of chapter 2.

#### **5.2.4.5 *In vitro* cellular uptake by ICP-OES analysis**

For quantitative analysis of cellular uptake, A549, HeLa, MCF7, A431 and HEK293 cells were seeded in 10 cm dishes with 106 cells in 10 ml PBS

solution and allowed to attach for 24 h. The cells were then treated with ZnMBC 11/12, and ZnMBC 11/12@MSNs-CTS-Biotin at 10  $\mu$ M (concentration of ZnMBC) for 4 h at 37 °C in CO<sub>2</sub> incubator. At the end of the incubation, the collected cells were digested with mixed acid (HNO<sub>3</sub>:HClO<sub>4</sub> = 3:1) for 2 h at 180 °C. Then the concentration of Zn in the cells was examined with inductively coupled plasma optical emission spectrometry (ICP-OES) analysis. The uptake in cancer and normal cells was expressed as the amount of Zn ( $\mu$ g).

#### **5.2.4.6 Wound healing assay**

The procedure for wound healing assay is same as discussed in section 3.2.7 of chapter 3.

#### **5.2.4.7 Two photon analysis**

4',6-diamidino-2-phenylindole (DAPI) staining coupled with two photon confocal was carried out to check the nuclear disruption inside cells during cellular apoptosis. Different cancerous cell lines such as A549, HeLa, and MCF-7 were plated at a density of  $5 \times 10^4$  in 6-well plates. They were allowed to grow at 37 °C in a humidified CO<sub>2</sub> incubator until they were 70-80 % confluent. Then cells were treated with IC<sub>50</sub> concentration of nanodrugs for 24 h. The culture medium was aspirated from each well and cells were gently rinsed thrice with PBS at room temperature. Then equal volumes of cells from the control (untreated nanodrugs) were mixed with 10  $\mu$ L dye of DAPI. Finally, the nanoconjugates, and dye treated cells were viewed immediately with a two-photon laser scanning microscope: excitation  $690 \pm 20$  nm for the blue channel.

#### **5.2.4.8 Dual staining assay with Hoechst and PI**

The procedure for dual staining assay is same as discussed in section 3.2.9 of chapter 3.

#### **5.2.4.9 Measurement of intracellular reactive oxygen species (ROS) generation**

The procedure for generating reactive oxygen species (ROS) is identical to the one outlined in section 2.2.6 of chapter 2.

### **5.2.5 *In vivo* assessment using zebrafish embryos**

#### **5.2.5.1 Zebrafish Husbandry**

Wildtype Zebrafish (*Danio rerio*) was maintained in a 14:10 light: dark cycle under optimum conditions at 28 °C. The experiments were performed under the guidelines of the institutional bioethical committee and complied with the ARRIVE guidelines following the U.K. Animals (Scientific Procedures) Act, 1986 and associated guidelines. The adult zebrafish were bred in a breeding tank and the embryos were collected.

#### **5.2.5.2 Zebrafish toxicity studies**

The embryos were exposed to different concentrations (10, 25, 50, 100, 200, 400, 800, 1200 and 1600 µM) of ZnMBC 1@MSNs-CTS-Biotin, and ZnMBC 12@MSNs-CTS-Biotin. The mortality, hatching rate, morphology and heart beat rate were observed till 72 hours postfertilization (hpf) according to the OECD guidelines. Any developmental changes such as deformities in the tail, spine, edema and change in heart beat were observed using a stereo microscope. Working standards of the solutions were prepared using distilled water and diluted in an E3 medium. Statistical analysis was performed using Origin 8 for the determination of LD<sub>50</sub> values.

#### **5.2.5.3 Heartbeat analysis of the zebrafish embryos**

The heartbeat of the zebrafish larvae was analysed at 48 hpf, and the percentage change in a heartbeat was calculated with respect to control. ZnMBC 11@MSNs-CTS-Biotin, and ZnMBC 12@MSNs-CTS-Biotin were incubated to check the influence of the compounds on heartbeat rate when compared to the control.

#### **5.2.5.4 Differential AO/PI apoptosis staining assay**

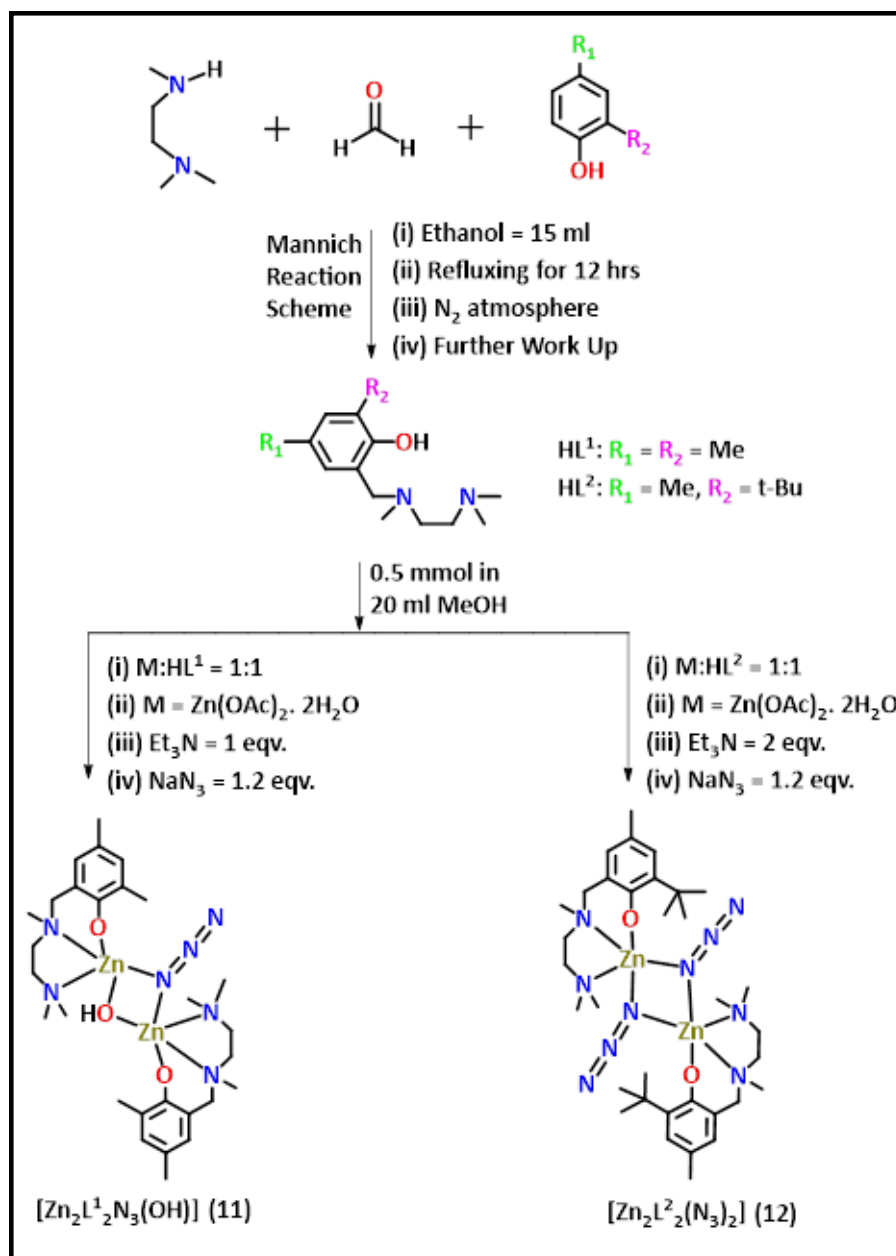
AO/PI double staining was performed at 96-hpf on the embryos exposed to 10, 25, 50, 100, 200, 400, 800, 1200, and 1600 µM of ZnMBC 11@MSNs-CTS-Biotin, and ZnMBC 12@MSNs-CTS-Biotin. Briefly, zebrafish embryos were incubated with 10 µg/mL AO and 10 µg/mL PI for 15 min, in the dark. They were washed three times with E3 medium and visualized using a stereo microscope. AO: acridine orange.

***Precaution!** Azide salts are explosive in nature. Proper protections should be taken while using in the laboratory. A very small portion of it was considered during complexation reactions as well as biomedical applications.*

### **5.3 Results and discussion**

#### **5.3.1 Preparation and characterization of drug delivery systems**

Ligands **HL**<sup>1</sup> and **HL**<sup>2</sup>, synthesized by a conventional Mannich base condensation method, are further utilized for the production of core drug agents (**ZnMBC 11** and **ZnMBC 12**) after metalation with  $\text{Zn}(\text{OAc})_2 \cdot 2\text{H}_2\text{O}$  (Scheme 5.2).



**Scheme.5.2:** Synthesis of Mannich base ligands and core drug candidates

Various analytical methods such as NMR, ESI-MS, elemental analysis, FTIR spectroscopy, and UV-vis spectrophotometry were used to characterize the Mannich bases and the corresponding complexes. ZnMBC **11** and ZnMBC **12** show a sharp band for bridging azide at about 2079–2084 cm<sup>-1</sup> (Figure 5.1-Figure 5.9).

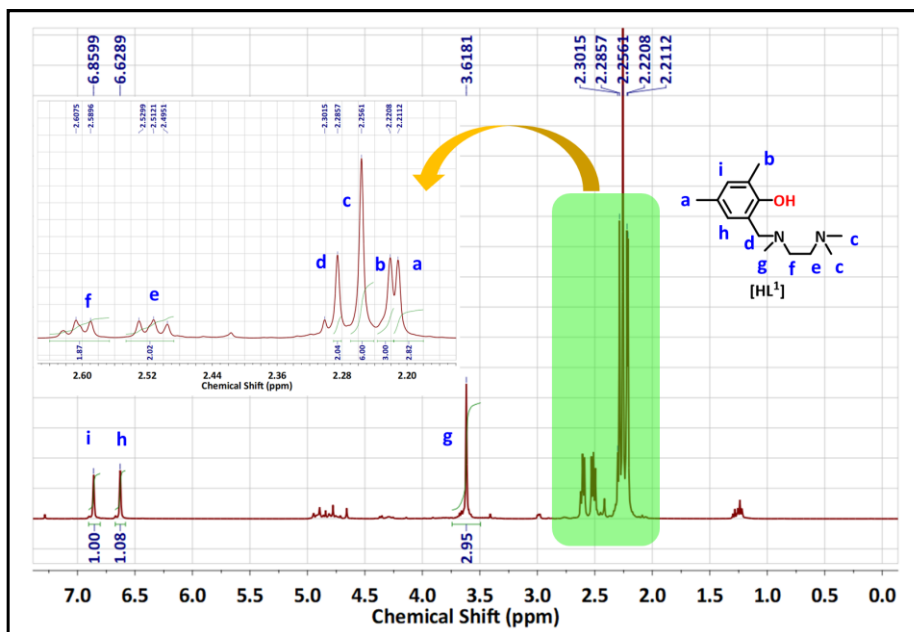


Figure 5.1:  $^1\text{H}$  NMR Spectra of  $\text{HL}^1$  in  $\text{CDCl}_3$  (400.13 MHz, 298K)

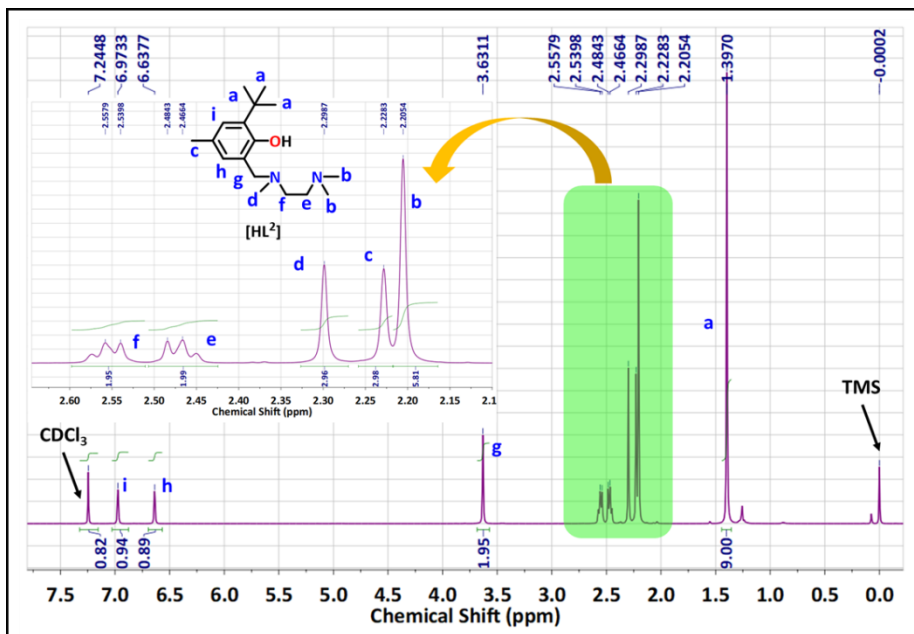


Figure 5.2:  $^1\text{H}$  NMR Spectra of  $\text{HL}^2$  in  $\text{CDCl}_3$  (400.13 MHz, 298K)

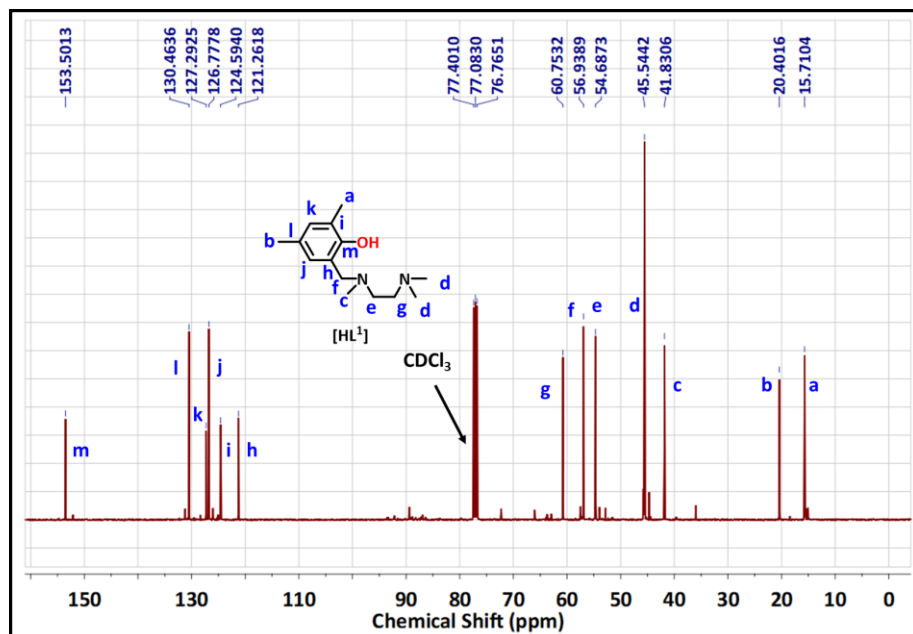


Figure.5.3:  $^{13}C$  NMR Spectra of  $HL^1$  in  $CDCl_3$  (400.13 MHz, 298K)

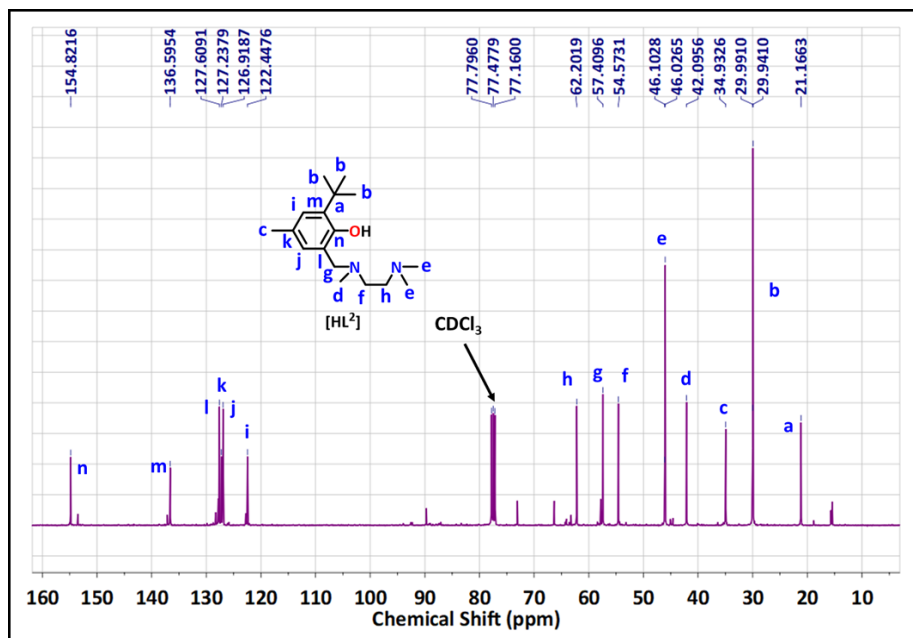


Figure.5.4:  $^{13}C$  NMR Spectra of  $HL^2$  in  $CDCl_3$  (400.13 MHz, 298K)

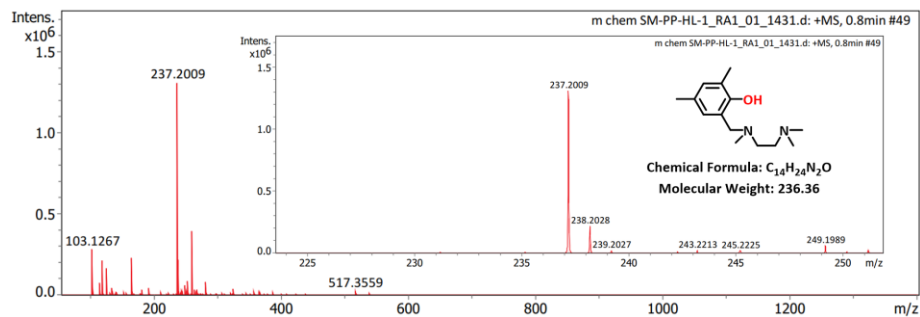


Figure 5.5: ESI-MS data of  $HL^1$  at room temperature.

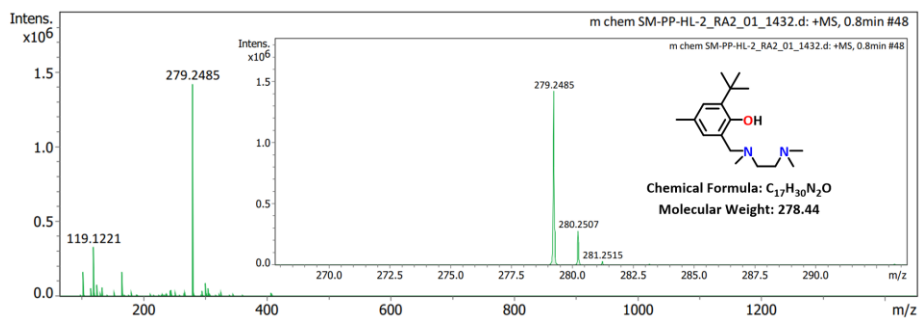


Figure 5.6: ESI-MS data of  $HL^2$  at room temperature.

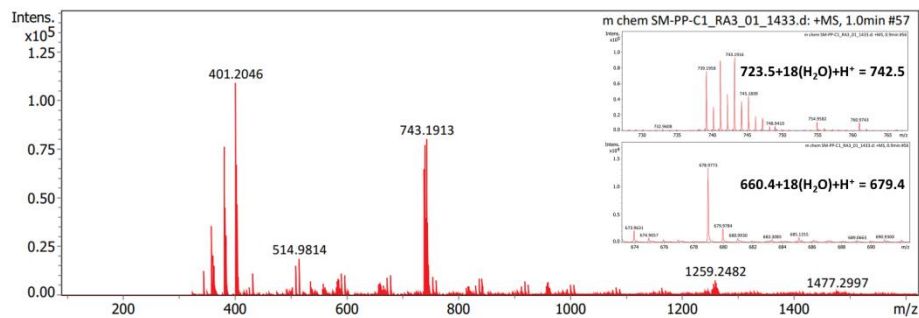
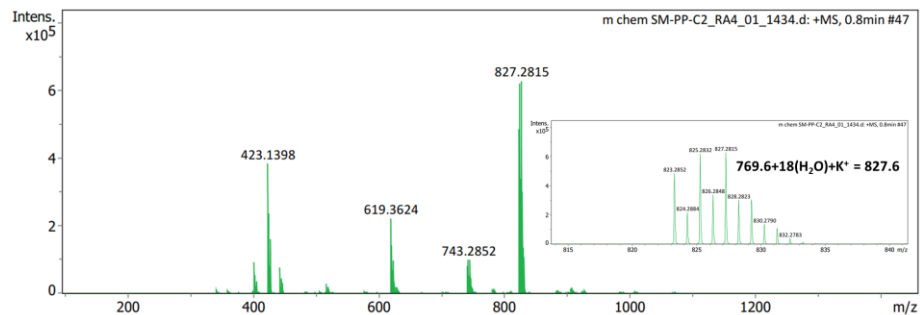
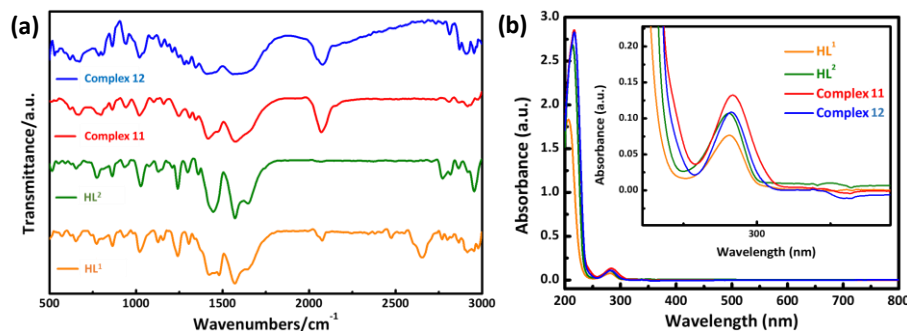


Figure 5.7: ESI-MS data of complex **11** at room temperature.



**Figure.5.8:** ESI-MS data of complex **12** at room temperature.



**Figure.5.9:** (a) FTIR stretching frequencies of  $HL^1$ ,  $HL^2$ ,  $Zn_2L^1_2(N_3)(OH)$  (**11**) and  $Zn_2L^2_2(N_3)_2$  (**12**) (b) UV-Visible transitions of ligands and complexes ( $10 \mu M$  in HPLC DMSO- $H_2O$  (1:9) solvent at  $25^\circ C$ ).

Also, single crystal XRD was employed to elucidate the exact solid-state structure and the refinement parameters of ZnMBC **11**, and ZnMBC **12**. In both cases the Mannich base ligands bind the metal ion in a tridentate fashion with one phenolic O and two amino N atoms getting coordinated to the zinc(II) center. The distorted square pyramidal structure of **11** gets satisfied with the help of a bridging azido ( $N_3^-$ ) group in the fourth position and the fifth position is occupied by a bridging phenolic-OH group. On the other hand, two bridging azido ( $N_3^-$ ) groups were involved in furnishing the square pyramidal geometry around zinc(II) in the case of **12**. The symmetrical ZnMBC **11** (CCDC: 2097274) and ZnMBC **12** (CCDC: 1488858) were crystallized in an orthorhombic and monoclinic crystal system having the space group of  $Pnm a$  and  $P2_1/c$ , respectively. The crystal structures and packing diagrams of ZnMBC **11**, and ZnMBC **12**, present the 2D polymeric networks formed by the strong hydrogen bond interaction between  $O1H...O111$  and  $H12A...O333$  of

closest water of crystallization (bond distances of 2.743 and 2.596 Å, respectively) in complexes (Figure 5.10, Table 5.1-5.2).

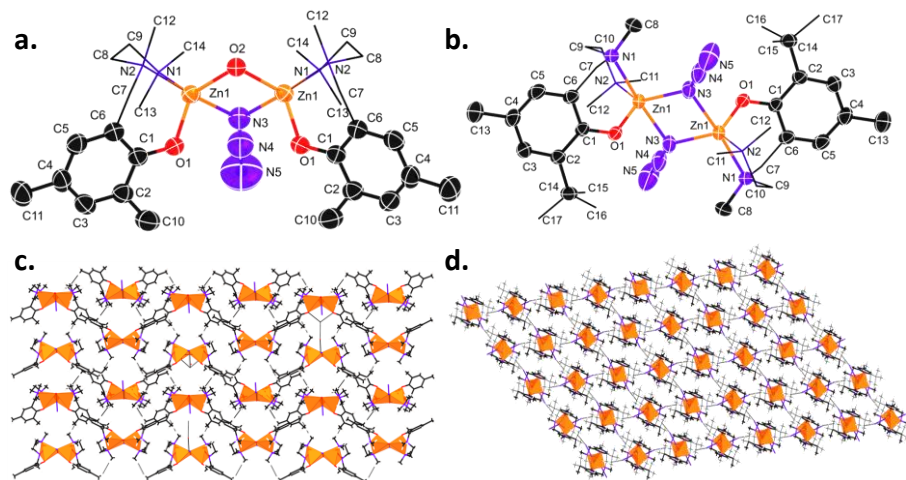


**Figure.5.10:** The Oak Ridge Thermal Ellipsoid Plot (ORTEP) (ellipsoids with 50% thermal probability level) of ZnMBC (a) **11**, and (b) **12**. Omitting hydrogens and wireframe as the style occasionally used for simplicity. Formation of three-dimensional supramolecular framework via hydrogen bond interactions in (c) **11**, and (d) **12**.

**Table.5.1.** Crystallographic information and structure refinement parameters for ZnMBC **11**, and ZnMBC **12**.

Parameter	Complex 11	Complex 12
Empirical Formula	C <sub>28</sub> H <sub>46</sub> N <sub>7</sub> O <sub>3</sub> Zn <sub>2</sub> + 4O	C <sub>34</sub> H <sub>58</sub> N <sub>10</sub> O <sub>2</sub> Zn <sub>2</sub>
Formula weight	723.46	769.64
Crystal system	Orthorhombic	Monoclinic
Space group	<i>P n m a</i>	<i>P 21/c</i>
<i>a</i> (Å)	13.0990(3)	13.5811(6)
<i>b</i> (Å)	22.9389(7)	7.7937(4)
<i>c</i> (Å)	12.0270(4)	18.3035(9)
$\alpha$ (°)	90	90
$\beta$ (°)	90	95.882(5)
$\gamma$ (°)	90	90
<i>V</i> (Å <sup>3</sup> )	3613.83(18)	1927.17(16)

$\lambda$ (Å)	0.71073	0.71073
$\rho_{\text{calcd}}$ (mg m <sup>-3</sup> )	1.330	1.326
<i>Z</i>	4	4
<i>T</i> (K)	293(2)	293(2)
$\mu$ (mm <sup>-1</sup> )	1.376	1.288
<b>F(0 0 0)</b>	1516	816
<b>Crystal size (mm<sup>3</sup>)</b>	0.28 × 0.24 × 0.21	0.26 × 0.21 × 0.17
<b>Theta ranges (°)</b>	2.905 to 24.998	3.016 to 32.356
<i>h/k/l</i>	-15,15/-27,27/-14,14	-20,19/-11,11/-24,27
<b>Reflections collected</b>	29428	22451
<b>Independent reflections</b>	3269	6388
<i>T<sub>max</sub></i> and <i>T<sub>min</sub></i>	1.00000 and 0.66169	1.00000 and 0.30177
<b>Data/restraints/parameters</b>	3269 / 0 / 219	6388 / 0 / 225
<b>Goodness-of-fit (GOF)</b>	1.147	1.143
<b>Final <i>R</i> indices [<i>I</i> &gt; 2σ(<i>I</i>)]</b>	<i>R</i> 1 = 0.0866, <i>wR</i> 2 = 0.2251	<i>R</i> 1 = 0.0509, <i>wR</i> 2 = 0.1393
<b><i>R</i> indices (all data)</b>	<i>R</i> 1 = 0.1111, <i>wR</i> 2 = 0.2649	<i>R</i> 1 = 0.0712, <i>wR</i> 2 = 0.1779
<b>Extinction coefficient</b>	0.037(4)	0.054(4)
<b>Largest peak and hole (eÅ<sup>-3</sup>)</b>	2.507 and -1.315	1.282 and -0.861
<b>CCDC No.</b>	<b>2097274</b>	<b>1488858</b>

**Table.5.2.** Selected bond lengths (Å) and bond angles (deg) of ZnMBC 11, and ZnMBC 12.

Complex 11	Parameters	Complex 12	Parameters
Zn(1)-O(1)	1.940(3)	Zn(1)-O(1)	1.9167(15)
Zn(1)-O(2)	1.962(3)	Zn(1)-N(3)	2.0309(18)
Zn(1)-N(1)	2.149(4)	Zn(1)-N(2)	2.1412(19)
Zn(1)-N(2)	2.219(4)	Zn(1)-N(1)	2.2257(17)
Zn(1)-N(3)	2.228(5)	Zn(1)-N(3)#1	2.2924(18)
O(1)-C(1)	1.332(5)	O(1)-C(1)	1.331(2)
O(2)-Zn(1)#1	1.962(3)	N(1)-C(9)	1.478(3)
N(1)-C(9)	1.467(7)	N(1)-C(8)	1.479(3)
N(1)-C(14)	1.481(8)	N(1)-C(7)	1.484(3)
N(1)-C(13)	1.491(7)	N(2)-C(12)	1.486(3)
N(2)-C(8)	1.483(6)	N(2)-C(10)	1.486(3)
N(2)-C(12)	1.487(6)	N(2)-C(11)	1.489(3)
N(2)-C(7)	1.491(7)	N(3)-N(4)	1.201(3)
N(3)-N(4)	1.149(9)	N(3)-Zn(1)#1	2.2925(18)
N(3)-Zn(1)#1	2.228(5)	N(4)-N(5)	1.132(3)
N(4)-N(5)	1.157(13)	O(1)-Zn(1)-N(3)	117.71(8)
O(1)-Zn(1)-O(2)	123.12(16)	O(1)-Zn(1)-N(2)	120.87(7)
O(1)-Zn(1)-N(1)	113.34(15)	N(3)-Zn(1)-N(2)	121.08(9)
O(2)-Zn(1)-N(1)	123.28(17)	O(1)-Zn(1)-N(1)	92.91(7)
O(1)-Zn(1)-N(2)	92.43(14)	N(3)-Zn(1)-N(1)	100.76(7)
O(2)-Zn(1)-N(2)	99.50(15)	N(2)-Zn(1)-N(1)	82.42(8)
N(1)-Zn(1)-N(2)	82.32(17)	O(1)-Zn(1)-N(3)#1	93.55(7)
O(1)-Zn(1)-N(3)	92.71(17)	N(3)-Zn(1)-N(3)#1	77.30(8)
O(2)-Zn(1)-N(3)	79.70(16)	N(2)-Zn(1)-N(3)#1	93.15(8)
N(1)-Zn(1)-N(3)	93.38(18)	N(1)-Zn(1)-N(3)#1	173.41(7)
N(2)-Zn(1)-N(3)	174.30(18)	C(1)-O(1)-Zn(1)	123.06(12)
C(1)-O(1)-Zn(1)	125.9(3)	C(9)-N(1)-Zn(1)	104.18(13)
Zn(1)#1-O(2)-Zn(1)	107.4(2)	C(8)-N(1)-Zn(1)	115.38(15)
C(9)-N(1)-Zn(1)	107.2(3)	C(7)-N(1)-Zn(1)	106.44(12)
C(14)-N(1)-Zn(1)	114.0(3)	C(12)-N(2)-Zn(1)	108.69(15)

Now, in order to successfully deliver the chemotherapeutic drug, MSNs were synthesized as outlined in Scheme 5.1, and characterized by various analytical techniques (e.g., HR-TEM, SEM, BET, TGA, UV-Vis, XPS, Raman, etc).

The drug loading capacity of MSNs and the surface modification by CTS-Biotin can be seen from the FE-SEM and HR-TEM analysis. The diffraction patterns explicate the amorphous nature of the drug delivery systems, whereas the particle size was found to be in the range of  $50 \pm 4$  nm. The drug loading or CTS-Biotin conjugation did not influence the dispersity and size of MSNs (Figure 5.11).

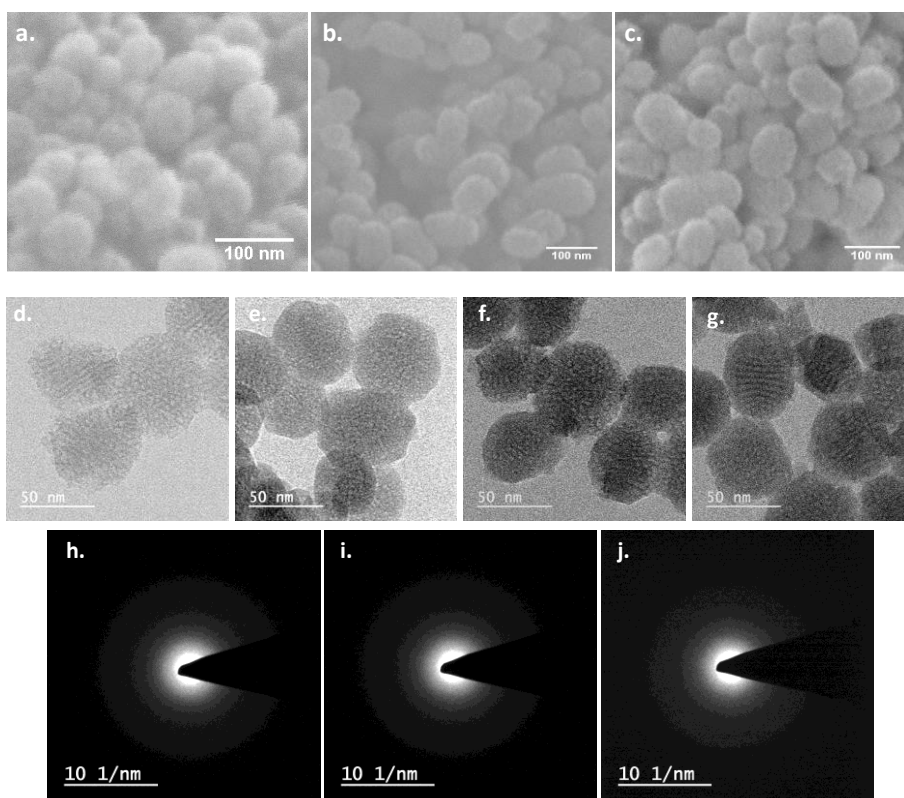


**Figure.5.11:** FE-SEM diagrams of (a) free MSNs, (b) ZnMBC loaded MSNs, i.e., (11)@MSNs, and (c) functionalization of ZnMBC loaded MSNs with CTS-Biotin, i.e., (11)@MSNs-CTS-Biotin. (d-g) HRTEM profiles of MSNs, (11)@MSNs, (11)@MSNs-CTS-biotin, and (12)@MSNs-CTS-biotin. (h-j)

Corresponding diffraction patterns of MSNs-based drug candidates using HR-TEM.

The BET surface areas of the drug loaded functionalized MSNs, as calculated from the nitrogen adsorption-desorption isotherms, diminished significantly from 676.6 m<sup>2</sup>/g (MSNs) to 472.5 m<sup>2</sup>/g ((**11**)@MSNs) and 278.9 m<sup>2</sup>/g ((**11**)@MSNs-CTS-Biotin) in case of ZnMBC **11** and to 405.4 m<sup>2</sup>/g ((**12**)@MSNs) and 232.8 m<sup>2</sup>/g ((**12**)@MSNs-CTS-Biotin) for ZnMBC **12**, respectively. Similarly, the pore volumes in BET also reduced from 1.39 cm<sup>3</sup>/g (MSNs) to 1.25 cm<sup>3</sup>/g ((**11**)@MSNs) and 0.73 cm<sup>3</sup>/g ((**11**)@MSNs-CTS-Biotin) for ZnMBC **11** and to 1.18 cm<sup>3</sup>/g ((**12**)@MSNs) and 0.71 cm<sup>3</sup>/g ((**12**)@MSNs-CTS-Biotin) in case of ZnMBC **12**, respectively (Figure 5.12-5.13, and Table 5.3). This outcome successfully demonstrates the loading of ZnMBC into the nanoparticles.

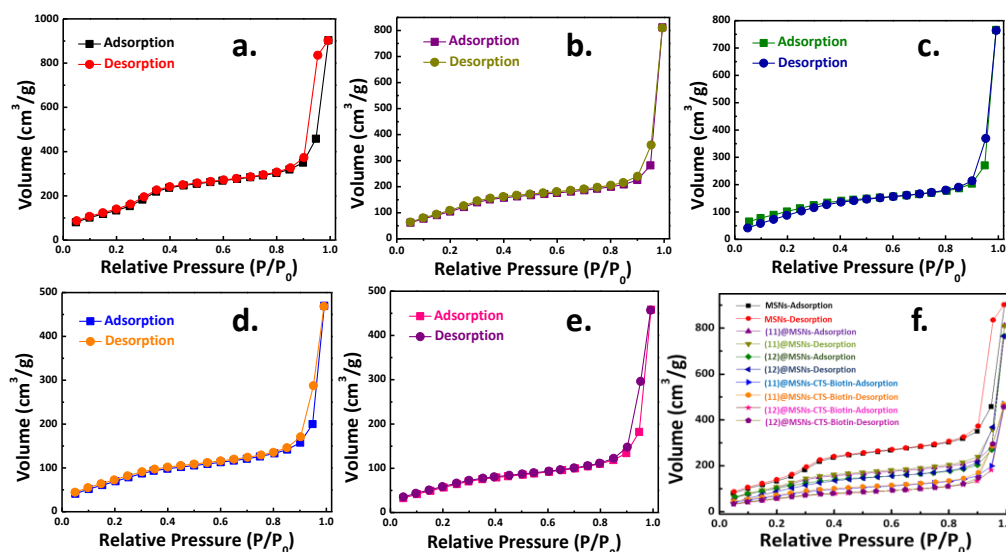


**Figure.5.12:** N<sub>2</sub> adsorption isotherms of (a) MSNs, (b) (**11**)@MSNs, (c) (**12**)@MSNs, (d) (**11**)@MSNs-CTS-Biotin, (e) (**12**)@MSNs-CTS-Biotin, and (f) Combine data of BET isotherms.

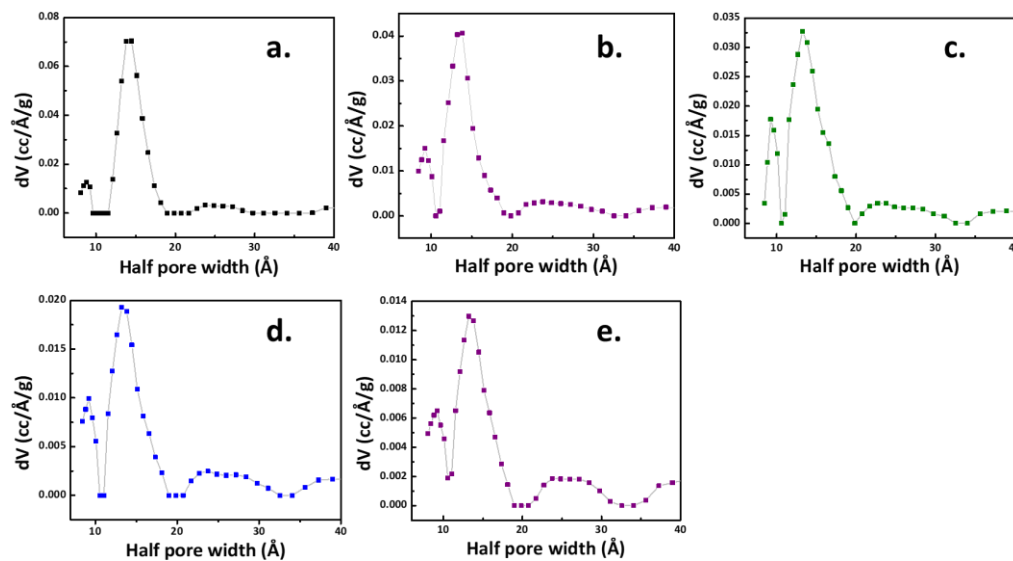


**Figure.5.13:** Pore size distribution curve analyzed by BET/DFT method for (a) MSNs, (b) (11)@MSNs, (c) (12)@MSNs, (d) (11)@MSNs-CTS-Biotin, and (e) (12)@MSNs-CTS-Biotin.

**Table.5.3.** BET adsorption results of nanocarrier and drug delivery systems.

Entry	N <sub>2</sub> adsorption isotherm		
	Multi Point BET (m <sup>2</sup> /g)	Langmuir Surface Area (m <sup>2</sup> /g)	Total Pore Volume (cc/g)
MSNs	676.6	3341.6	1.39
(11)@MSNs	472.5	1876.5	1.25
(12)@MSNs	405.4	1789.1	1.18
(11)@MSNs-CTS- Biotin	278.9	1306.1	0.73
(12)@MSNs-CTS- Biotin	232.8	1218.8	0.71

TGA profiles confirm the thermal stability of drug delivery systems up to 150 °C, as no considerable weight loss occurred except for the removal of surface-adsorbed water molecules (Figure 5.14).

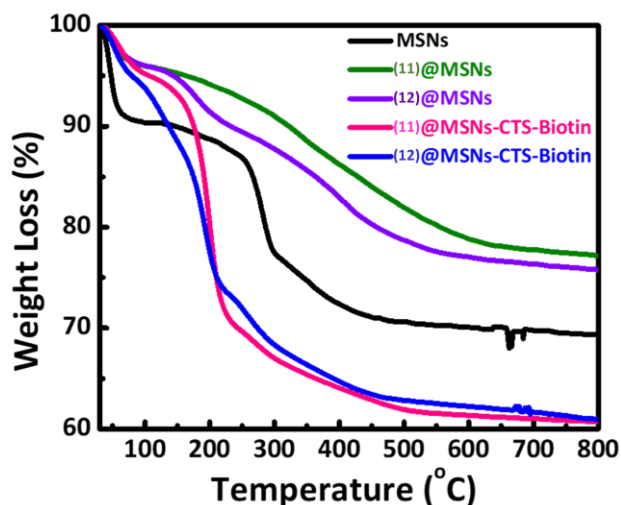


**Figure.5.14:** TGA curves in the temperature range of 0–800 °C.

Moreover, the fruitful loading of the core drug agents is further proved by corroborating the UV-Vis spectrum of **(11)**@MSNs-CTS-Biotin and **(12)**@MSNs-CTS-Biotin at 285 nm and 281 nm, respectively with **11** and **12**. The successful conjugation of CTS-Biotin to MSNs was further authenticated by FTIR spectroscopy. The antisymmetric vibration of Si-O-Si of MSNs has been assigned in the region of 1065-1092  $\text{cm}^{-1}$ , whereas that of carboxylic C=O stretching vibration of biotin is in the region of 1631  $\text{cm}^{-1}$ . The stretching band of C=O group for ZnMBC (**11/12**)@MSNs-Biotin was assigned to 1718  $\text{cm}^{-1}$ . Similarly, the bands 3360  $\text{cm}^{-1}$  and 1630  $\text{cm}^{-1}$  correspond to the N-H stretching and bending of ZnMBC (**11/12**)@MSNs-CTS. Besides, four new bands of (**11/12**)@MSNs-CTS-Biotin in the region of 2903-2918  $\text{cm}^{-1}$ , 2079-2084  $\text{cm}^{-1}$ , 1023-1026  $\text{cm}^{-1}$ , and 516-518  $\text{cm}^{-1}$  were ascribed to C-H stretching vibration on benzene, azide stretching, C-O stretching due to phenolic group, and Zn-O stretching vibration, respectively. Beside the peaks that come from ZnMBC, two significant peaks in Resonance Raman spectroscopy have been identified at 977  $\text{cm}^{-1}$  and 1059  $\text{cm}^{-1}$  arised out of  $\nu_{\text{symmetric}}$  (Si-O-Si bending) and  $\nu_{\text{symmetric}}$  (SiO<sub>4</sub> framework) stretching of MSNs [26, 27,28]. Moreover, the bridging azide stretching, and the strong C-H stretching vibration of benzene fall in the range of 2186 and 2938  $\text{cm}^{-1}$ , respectively (Figure 5.15).

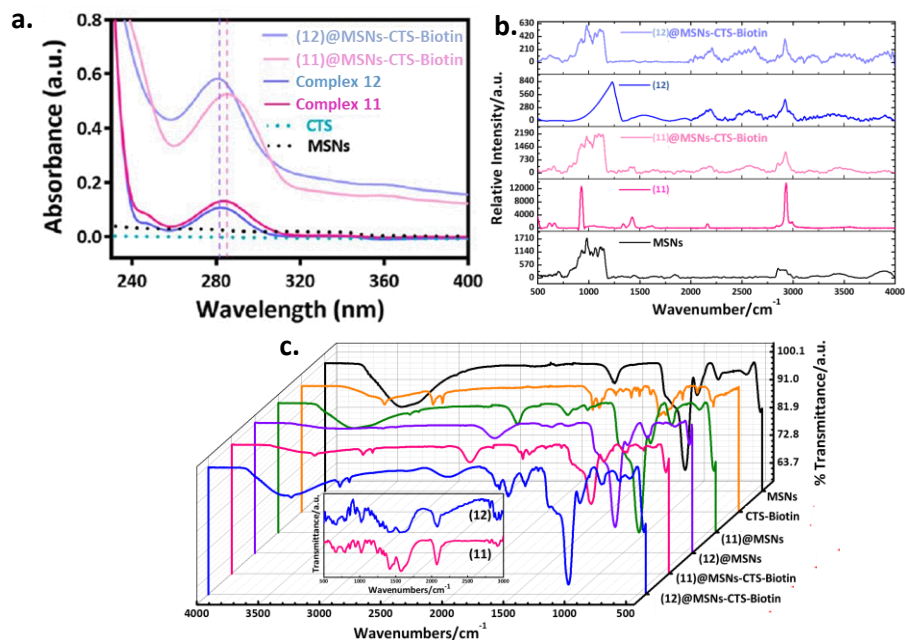


**Figure.5.15:** (a) UV-Visible spectra of ZnMBC and drug delivery systems in PBS buffer medium (b) Relative Raman spectra of nanocarrier and drug candidates (c) FTIR spectra of core drug candidates (inset) and drug delivery systems.

These results were further verified by X-ray photoelectron spectroscopy (XPS), which provides information about the valence state of metal ions, stereochemical configurations, along with the multiplicity of electrons. Figure 5.16 and Figure 5.17 summarize the XPS data of (11)@MSNs-CTS-Biotin, and (12)@MSNs-CTS-Biotin, respectively, which confirms the successful loading of ZnMBC inside the supercages of MSNs. The XPS survey spectra provide information on all the elements present in the nanodrugs. Briefly, azide can be assigned at 400.4 eV in N1s, Zn-O at 529.6 eV in O1s, and C-O at 287.2 eV in C1s, respectively. Similarly, Zn 2p<sub>3/2</sub>, and Zn 2p<sub>1/2</sub> give the HRD-XPS peaks at 1021.3/1021.6 eV, and 1044.3/1044.7 eV for ZnMBC 11/12, respectively, which signify the presence of Zn-O or Zn(OH) in the nanodrugs (Table 5.4). Taken together, these outcomes establish the successful assembly of (11/12)@MSNs-CTS-Biotin system.

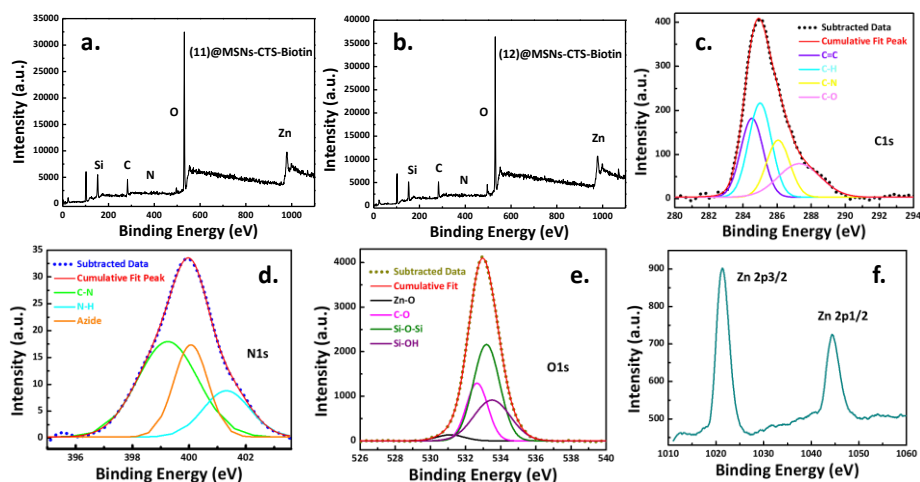


**Figure.5.16:** (a-b) Survey spectrum of drug delivery systems by X-ray photoelectron spectroscopic (XPS) analysis. High resolution deconvoluted XPS spectra of (c) C1s, (d) N1s, (e) O1s, and (f) Zn 2p1/2, and Zn 2p3/2 in case of (11)@MSNs-CTS-Biotin. Representation implies the subtracted data in dots and cumulative peak fitting in lines.

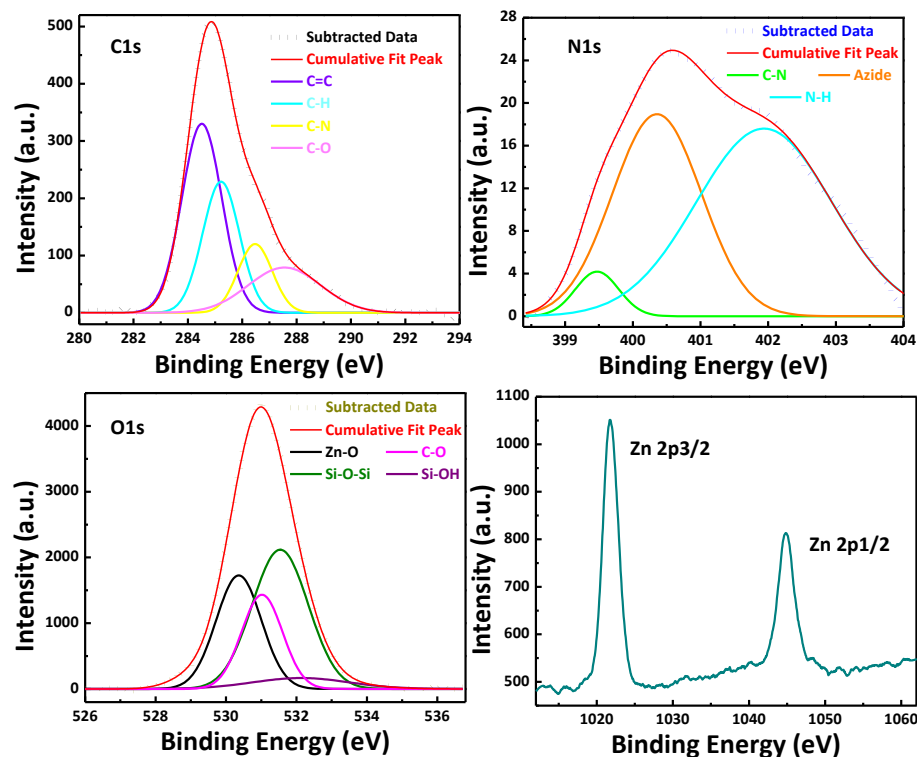


**Figure.5.17:** High resolution deconvoluted XPS spectra of C1s, N1s, O1s, and Zn 2p1/2, and Zn 2p3/2 in case of (12)@MSNs-CTS-Biotin. Representation indicates the subtracted data in dots and cumulative peak fitting in lines.

**Table.5.4.** Binding energies (in eV) of **(11)**@MSNs-CTS-Biotin, and **(12)**@MSNs-CTS-Biotin through XPS interpretation.

<b>Binding Energy (eV)</b>						
<b>Drug delivery systems</b>	<b>C (1s)</b>	<b>N (1s)</b>	<b>O (1s)</b>	<b>Zn (2p3/2)</b>	<b>Zn (2p1/2)</b>	<b>Δ2p</b>
<b>(11)</b> @MSNs-CTS-Biotin	284.89	400.08	532.81	1021.37	1044.38	23.01
<b>(12)</b> @MSNs-CTS-Biotin	284.81	400.38	531.17	1021.69	1044.77	23.08

### 5.3.2 Drug loading and pH-based delivery

Nanomaterials-based drug action demands efficient drug loading capacity and release factors. It was found that nanosystems **(11)**@MSNs-CTS-Biotin and **(12)**@MSNs-CTS-Biotin have drug loading capacity of about 42.6% (21.3 mg/50 mg), and 44.2% (22.1 mg/50 mg), respectively. On the other, **(1)**@MSNs-CTS, **(2)**@MSNs-CTS, **(11)**@MSNs-Biotin, and **(12)**@MSNs-Biotin showed a drug loading capacity of 33.7% (16.8 mg/50 mg), 35.4% (17.7 mg/50 mg), 26.9% (13.4 mg/50 mg), and 29.8% (14.9 mg/50 mg), respectively. In order to explore the pH-based drug release profile, the nanodrugs **(11/12)**@MSNs-CTS-Biotin, **(11/12)**@MSNs-CTS and **(11/12)**@MSNs-Biotin were suspended in PBS buffer at pH~ 7.4 and 5.5, respectively, mimicking the normal and cancer microenvironment in this work. As depicted in Figure 5.18, under acidic environments (pH~ 5.5), the release ratios up to 4 h are almost same (10.1%) for both nanosystems **(11/12)**@MSNs-CTS-Biotin. Meanwhile, ZnMBC **12** were leaked out in a slightly faster rate from **(12)**@MSNs-CTS-Biotin in comparison to its analogous ZnMBC **11** from **(11)**@MSNs-CTS-Biotin 27.6% and 25.6% release are observed in 24 h, respectively. In addition, the drug release (pH~ 5.5) from **(11)**@MSNs-CTS, **(12)**@MSNs-CTS, **(11)**@MSNs-Biotin, and **(12)**@MSNs-Biotin were 18.7%, 20.2%, 14.9%, and 16.7%, respectively. With

time the release amount sharply increases up to 75.4% and 72.5% in the case of ZnMBC **12**, and ZnMBC **11** whereas that of **(11)**@MSNs-CTS, **(12)**@MSNs-CTS, **(11)**@MSNs-Biotin, and **(12)**@MSNs-Biotin gives moderately lower values of 48.0%, 51.1%, 43.6%, and 45.3% at 96 h, respectively. However, under neutral environments (pH~ 7.4), the release profile of nanodrugs is very different, e.g., ZnMBC **11**, and ZnMBC **12** were released from **(11)**@MSNs-CTS, **(12)**@MSNs-CTS, **(11)**@MSNs-Biotin, **(12)**@MSNs-Biotin having a release rate of 37.7%, 39.3%, 28.7%, 31.5%, which are greater than **(11)**@MSNs-CTS-Biotin and **(12)**@MSNs-CTS-Biotin with a release amount of 19.4% and 21.4% in 96 h, respectively. The diverse release behaviours of nanosystems under acidic (pH~ 5.5) and neutral (pH~ 7.4) conditions were triggered by the wrapping of pH responsive CTS outside the MSNs. Indeed, in the neutral medium, the stability of CTS was enough to encapsulate the drugs in MSNs supercages, while in the acidic condition, the amino groups on CTS were protonated, which provided a strong electrostatic repulsion and less effective hydrogen bonding between CTS molecules. In this case, the conformation of CTS was transformed, subsequently the rapid leaking out of ZnMBC occurred. Therefore, the release of ZnMBC from **(11/12)**@MSNs-CTS-Biotin was pH dependent and offered more release content in lower pH values (Figure 5.17a). However, it should be pointed out that **(11/12)**@MSNs-CTS and **(11/12)**@MSNs-Biotin also exhibited a distinct ability of controlled release in acidic and neutral conditions. The faster release of ZnMBC **11/12** from **(11/12)**@MSNs-Biotin under the acidic pH condition probably was attributed to the hydrogen bonds between ZnMBC and the residual amino groups on the surface of MSNs. Under the acidic condition, the amino groups were protonated, and the hydrogen bonds were replaced, finally resulting in the faster release of ZnMBC [30]. All the outcomes established that **(11/12)**@MSNs-CTS-Biotin could regulate the release of ZnMBC in acidic conditions, which demonstrated the feasibility of controlling the release of the drug around the tumor tissues, but not in the normal tissues. Additionally, due to the more pH-dependent character of CTS,

(**11/12**)@MSNs-CTS give a better drug release profile than that of (1/2)@MSNs-Biotin. And it also specified that (**11/12**)@MSNs-CTS-Biotin could attain sustained drug release and result in a longer blood-circulation lifetime. Hence, it was speculated that the pH-responsive drug release behavior entrusted (**11/12**)@MSNs-CTS-Biotin with significant anticancer activity. This distinguishable release behaviours of the nanodrugs can be explained by the pH stability of CTS, as in acidic conditions, protonation of the amino groups on CTS was taking place, which weakened hydrogen bonding between CTS molecules and led to a strong electrostatic repulsion. As a consequence of the conformational changes the MSNs-CTS bonds break, resulting the fast leaking out of ZnMBC **11/12**. Therefore, after being directional through Biotin, nanodrugs enter into the tumour tissues with the interaction of overexpressed integrin followed by the pH-mediated degradation of MSNs-CTS bonds and controlled release of nanodrugs inside cancer cells are observed an acidic environment (Figure 5.18b). All the outcomes established that the nanodrugs can be released in a controlled way in the acidic microenvironment (pH~ 5.5) of tumor, but not in the normal tissues with higher pH (pH~ 7.4).

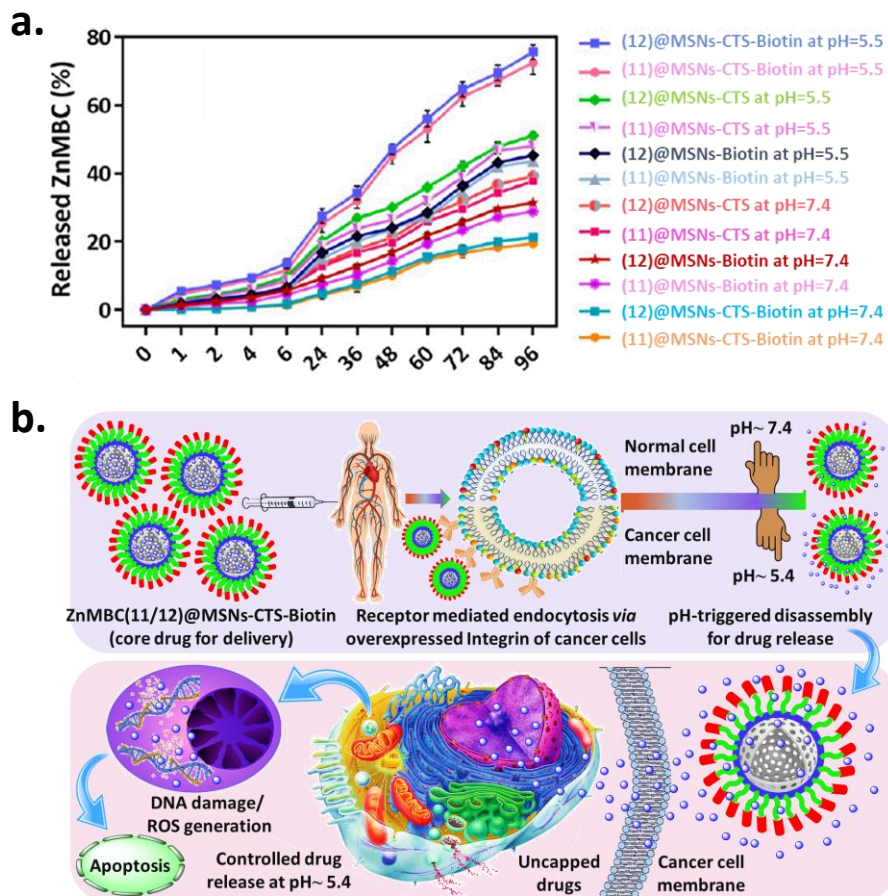


**Figure.5.18:** (a) pH-mediated drug release profile of nanodrugs. *In vitro* release profiles of ZnMBC 11 from (11)@MSNs-CTS-Biotin at pH 7.4 (●) and pH 5.5 (●), and ZnMBC 12 from (12)@MSNs-CTS-Biotin at pH 7.4 (■) and pH 5.5 (■). (b) Representing pH-responsive targeted drug delivery and cellular apoptosis.

### 5.3.3 Stability studies of nanodrugs in biological media

The stability of the compounds (ZnMBC) in physiological conditions is an important factor for almost all biological applications. Thus, an investigation was carried out by dissolving ZnMBC in a 1% DMSO/PBS solution mixture, and their stability was monitored in the time frame of 0 h, 24 h, and 96 h *via* mass spectrometry. No substantial shifting or change in peaks was observed in the mass spectrum of the titled ZnMBC, which obviously indicates the complex stability in the biological medium (Figure 5.19).

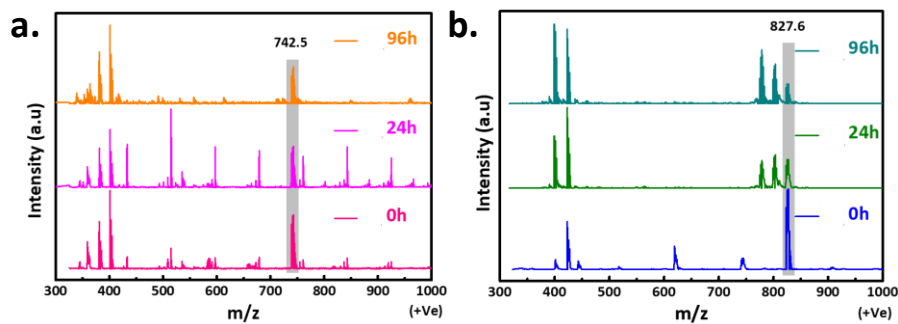


**Figure.5.19:** Mass spectrometry (ESI-MS, +Ve) of ZnMBC 11 (a), and ZnMBC 12 (b) in different time intervals (0 h, 24 h, and 96 h). Condition: 1% DMSO/PBS solution mixture at 25 °C.

### 5.3.4 *In Vitro* cellular uptake of ZnMBC 11/12, (11/12)@MSNs-CTS and (11/12)@MSNs-CTS-Biotin

Cellular uptake efficacy is vital to nanoparticle-mediated drug actions and contributes to anticancer activity. Typically, by active and passive transport, nanoparticles enter cancer cells and can play the role of drug carriers in chemotherapeutics. Nevertheless, the passive process has some limitations due to the random delivery mode. Henceforth, tagging Biotin peptide in the surface of (11/12)@MSNs-CTS can identify and bind to the overexpressed integrin receptor in the cancer cell membrane to upsurge the cellular uptake of the nanomaterials through an active targeting process. Hence, *in vitro* cellular uptakes of ZnMBC 11/12, (11/12)@MSNs-CTS and (11/12)@MSNs-CTS-Biotin were determined quantitatively in normal (HEK-293) and cancer (MCF7) cell lines. Inductively coupled plasma optical emission spectrometry (ICP-OES) was utilized to measure intracellular zinc content.

As indicated in Figure 5.20, the uptakes of core anticancer agents and nanoconjugates were determined by ICP-OES in MCF7 breast cancer cells and HEK-293 normal cells after 4 h of incubation. Results obtained reveal that the uptakes of ZnMBC 11, ZnMBC 12, (11)@MSNs-CTS, (12)@MSNs-CTS, (11)@MSNs-CTS-Biotin, and (12)@MSNs-CTS-Biotin in MCF7 are 0.274, 0.599, 0.166, 0.195, 0.361, and 0.613  $\mu\text{g}/10^6$  cells, respectively. On the other side, for normal cells *viz.* HEK-293 comparatively less cellular uptake is observed for all synthesized complexes and nanosystems. The values obtained

are found to be 0.047, 0.063, 0.025, 0.031, 0.028, and 0.034  $\mu\text{g}/10^6$  cells correspond to ZnMBC **11**, ZnMBC **12**, (**11**)@MSNs-CTS, (**12**)@MSNs-CTS, (**11**)@MSNs-CTS-Biotin, and (**12**)@MSNs-CTS-Biotin system, respectively. The intracellular zinc concentration of (**12**)@MSNs-CTS, and (**11/12**)@MSNs-CTS-Biotin in cancer cells (e.g., MCF7) were found to be higher than that of normal cells (e.g., HEK-293). Also the results revealed that both nanodrugs (**11**)@MSNs-CTS-Biotin, and (**12**)@MSNs-CTS-Biotin exhibited closely higher uptakes in MCF7, while the core agents viz ZnMBC **11**, and ZnMBC **12** have shown relatively minor accumulation in the same cancer cells. Moreover, (**11/12**)@MSNs-CTS shows the lowest uptake among all the titled systems, which may be attributed to the non-targeted behaviour of (**11/12**)@MSNs-CTS. From the above observation it is evident that the nanoconjugate-mediated drugs bring about improvement in the selectivity of ZnMBC uptake between normal cells and cancer cells.

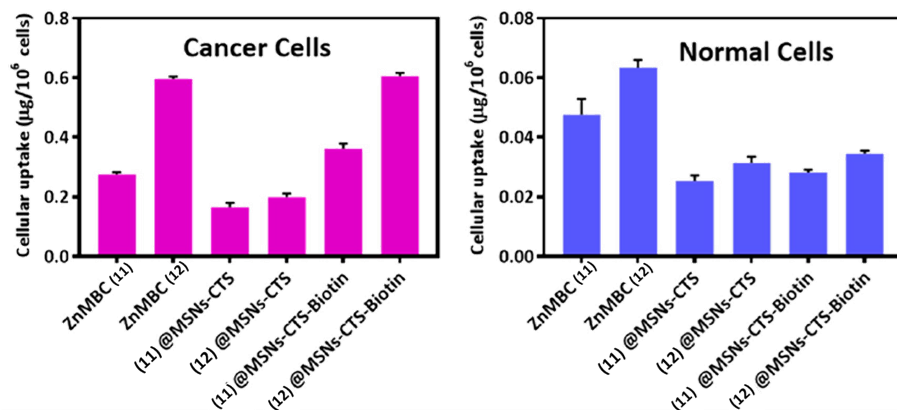


**Figure.5.20:** Cellular uptake/ accumulation study of core anticancer agents ZnMBC **11/12**, (**11/12**)@MSNs-CTS, and (**11/12**)@MSNs-CTS-Biotin in MCF7 cancer and HEK-293 normal cells.

### 5.3.5 Anticancer activity of ZnMBC **11/12** and (**11/12**)@MSNs-CTS-Biotin

In order to overcome the drawbacks of difficulty on aqueous solubility, poor cell membrane penetration efficiency, low selectivity between normal and cancer cells, this study intended to utilize CTS-Biotin-conjugated MSNs as a nanocarrier of ZnMBC to enhance selective cytotoxicity towards cancer cells. Herewith, a series of cancer cells such as MCF7, HeLa, and A431 have been

chosen for performing MTT assay to compare anticancer efficacy with respect to the normal cell *viz.* HEK-293. As summarized in Table 5.5, synthesized compounds (complexes as well as nanoparticles) unveiled significant anticancer activities against cancer cells. Interestingly complexes (ZnMBC **11/12**) and the nanoparticles ((**11/12**)@MSNs-CTS-Biotin) exhibited comparable range of inhibitory concentration ( $IC_{50}$ ) values with respect to the commercially available anticancer drugs (e.g., DOX, 5-FU, *cis*-platin, *etc*) [31]. In some cases, nanodrugs (**11**)/(**12**)@MSNs-CTS-Biotin shows better cytotoxicity than that of 5-FU, particularly against MCF7 ( $10.9 \pm 0.3$  and  $6.5 \pm 0.2$   $\mu$ M for (**11**)@MSNs-CTS-Biotin and (**12**)@MSNs-CTS-Biotin, respectively), though ZnMBC **12** displayed highest anticancer efficacy among all the titled compounds.

In addition,  $IC_{50}$  values were also evaluated for the complexes or nanosystems treated normal cell HEK-293, which revealed very lower cytotoxicity in the range of  $56.4 \pm 0.9$  to  $72.3 \pm 1.7$   $\mu$ M, providing better results (killing rate is less for normal cells and strictly selective towards cancers only) in comparison to the positive controls, thus can further be considered for practical applicability (Figure 5.21).

**Table.5.5.** Comparing  $IC_{50}$  values (in  $\mu$ M, 24 h, 37 °C) of the complexes, nanoparticles, and commercially available chemotherapeutic drugs (FDA approved).

Compound	MCF7	HeLa	A431	HEK-293
ZnMBC <b>11</b>	$12.2 \pm 0.2$	$9.9 \pm 0.3$	$19.7 \pm 0.7$	$58.1 \pm 1.1$
ZnMBC <b>12</b>	$6.7 \pm 0.3$	$6.9 \pm 0.2$	$5.8 \pm 0.6$	$56.4 \pm 0.9$
<b>(11)</b> @MSNs-CTS-Biotin	<b><math>10.9 \pm 0.3</math></b>	$12.5 \pm 0.5$	$28.8 \pm 0.9$	$72.3 \pm 1.7$
<b>(12)</b> @MSNs-CTS-Biotin	<b><math>6.5 \pm 0.2</math></b>	$11.5 \pm 0.5$	$22.9 \pm 1.3$	$66.6 \pm 1.3$
DOX	$4.4 \pm 0.7$	$3.0 \pm 0.1$	$3.1 \pm 0.3$	$11.9 \pm 0.7$
5-FU	$21.7 \pm 0.7$	$5.2 \pm 0.2$	$15.4 \pm 0.6$	$43.9 \pm 1.2$

cis-Platin	$6.5 \pm 0.2$	$11.2 \pm 0.2$	$13.0 \pm 0.4$	$45.4 \pm 1.1$
------------	---------------	----------------	----------------	----------------

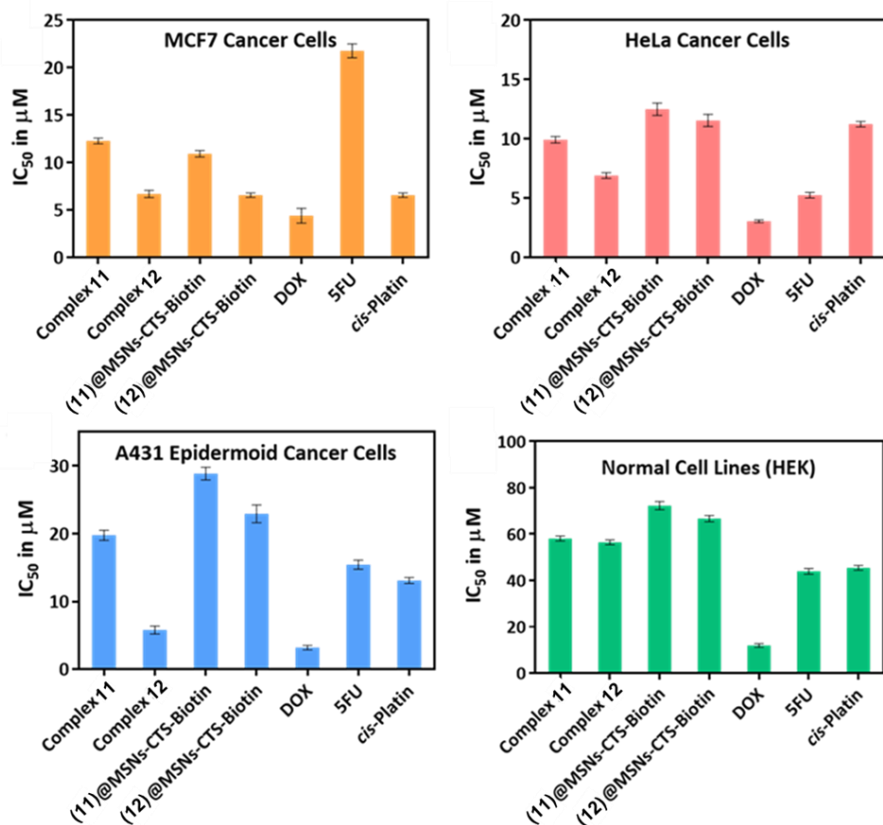


**Figure.5.21:** Induction of apoptosis by measuring  $IC_{50}$  values (after 24 h incubation at 37 °C, 5%  $CO_2$ ) in various cancer cells and normal cell lines after the treatment of ZnMBC 11/12 (complexes), (11/12)@MSNs-CTS-Biotin (nanoparticles), doxorubicin (DOX), 5-fluorouracil (5-FU), and cis-Platin (+ve controls).

### 5.3.6 Metastasis inhibition assay

Compounds that can prohibit cell migration and invasion are in high demand to stop cancer metastasis and the growth process. Metastasis in a later phase of cancer is very dangerous. Non-malignant cells or tissues can easily get affected through long-distance migration of malignant of cancer cells, and therefore cause serious damage to the healthy cells [32]. To reduce the chances of migration of cancerous cells to other organs, inhibiting metastasis phase is a crucial need for the advance chemotherapy. Herein, the untreated cells have

shown the highest wound closure ratio of ~63.6%, whereas wound lower closure ratios are lower when the cells are treated with the metal complexes. At a glance, while treating with IC<sub>50</sub> concentration (PBS buffer of pH~ 7.4) of each complex and nanoparticles against HeLa cells, 11.0%, 10.9%, 23.5%, and 18.0% of wound closure have been observed in case of ZnMBC **11**, ZnMBC **12**, **(11)**@MSNs-CTS-Biotin, and **(12)**@MSNs-CTS-Biotin, respectively. Compound treated cells shows a negligible increase in metastasis toward the scratched wound region, in contrast the PBS treated cells (untreated control) migrated to the scratched wound side, which evidently indicates the potential applicability of the compounds to restrict cancer spreading (Figure 5.22).

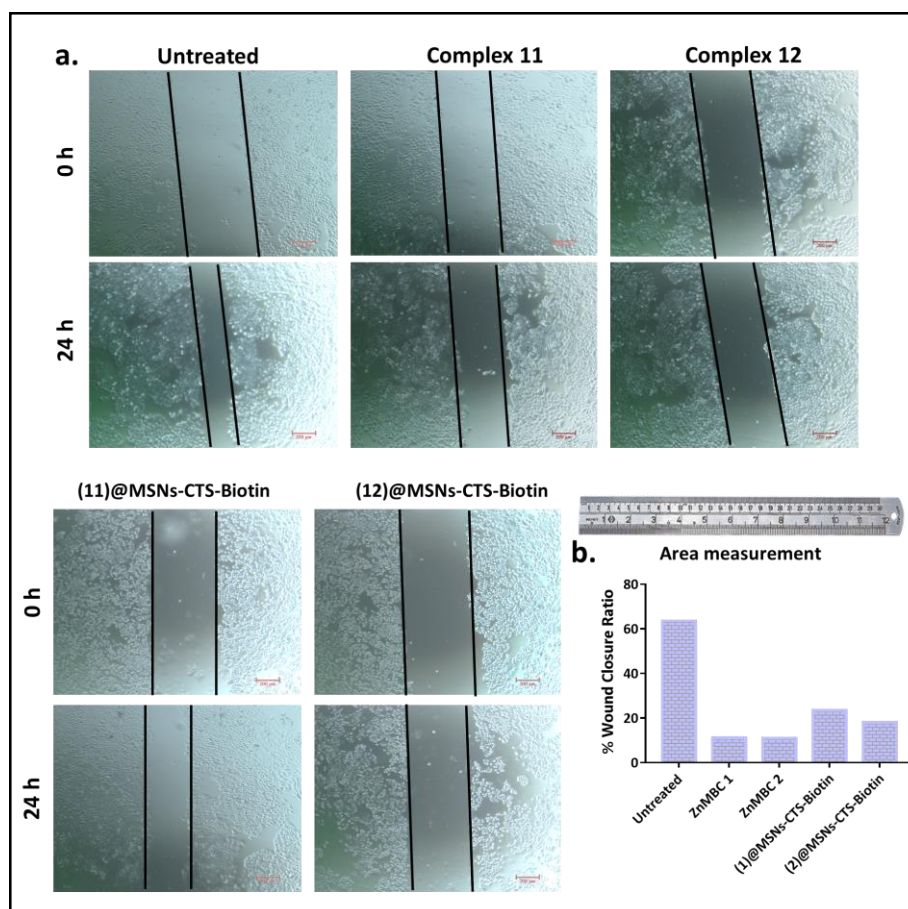


**Figure.5.22:** (a) Wound healing motility assay of HeLa treated with complexes ZnMBC (**11/12**) and nanodrugs **(11)**@MSNs-CTS-Biotin, and **(12)**@MSNs-CTS-Biotin, and untreated as control (Scale bar: 200  $\mu$ m). Bright field images

were captured at 0 h and 24 h. (b) Histogram describing wound closure ratio of heal wound within time lag of 0 h and 24 h.

### 5.3.7 *In Vivo* toxicity measurements in zebrafish embryos

Owing to the anatomical similarity of the zebrafish embryo heart to the human heart, toxicity measurement in zebrafish embryos can be crucial in getting information about the practical usability of nanoparticles (NPs) as anticancer drugs. Therefore, zebrafish embryos were used and exposed to different concentrations (10, 25, 50, 100, 200, 400, 800, 1200 and 1600  $\mu\text{M}$ ) of (11)@MSNs-CTS-Biotin, and (12)@MSNs-CTS-Biotin to observe their mortality, hatching rate, morphology and heart beat rate till 72 h of postfertilization (hpf) following OECD guidelines [33]. (12)@MSNs-CTS-Biotin presented higher cumulative mortality rate than (11)@MSNs-CTS-Biotin at 72 hpf. The NPs (11)@MSNs-CTS-Biotin, and (12)@MSNs-CTS-Biotin showed a lethal dose concentration ( $\text{LD}_{50}$ ) values of 335.5  $\mu\text{M}$ , and 153.6  $\mu\text{M}$ , respectively (Figure 5.23a). The heartbeat of the larvae and the percentage change in a heartbeat upon compound treatment were analysed with respect to control at 48 hpf. Both NPs disclosed reduced heartbeat rates when compared to the control. (11)@MSNs-CTS-Biotin showed 0%, 13.04%, and 44.06% decrease in heart beat rate with respect to control, however (12)@MSNs-CTS-Biotin owing to higher toxicity at 200, 400, 800  $\mu\text{M}$  showed a decrease in heart beat rate of 10.34 %, 23.52 %, and 23.52 %, respectively in comparison to control (Figure 5.23b-c). Hatching rate after 24 h showed 100% for both NPs at 100  $\mu\text{M}$ , whereas no hatchability noticed at  $\geq 400$   $\mu\text{M}$  concentration of NPs and the embryos get killed. 70% and 30% hatchability were observed for (11)@MSNs-CTS-Biotin, and (12)@MSNs-CTS-Biotin, respectively at 200  $\mu\text{M}$ . There were fatal deformities like blood congestion, edema, stunted growth, and tail and head malformation that started to appear in the presence of (12)@MSNs-CTS-Biotin at a concentration  $\leq 200$   $\mu\text{M}$  at 72 hpf, nevertheless (11)@MSNs-CTS-Biotin exhibited deformities like stunted growth [34,35,36]. No notable deformities were observed  $\leq 100$   $\mu\text{M}$  for both NPs (Figure 5.23d). The outcomes on cardiac function indicate that the general

toxicity is low and in favour of further studies of (11/12)@MSNs-CTS-Biotin for their further evaluation as a chemotherapeutic and chemopreventive agent.

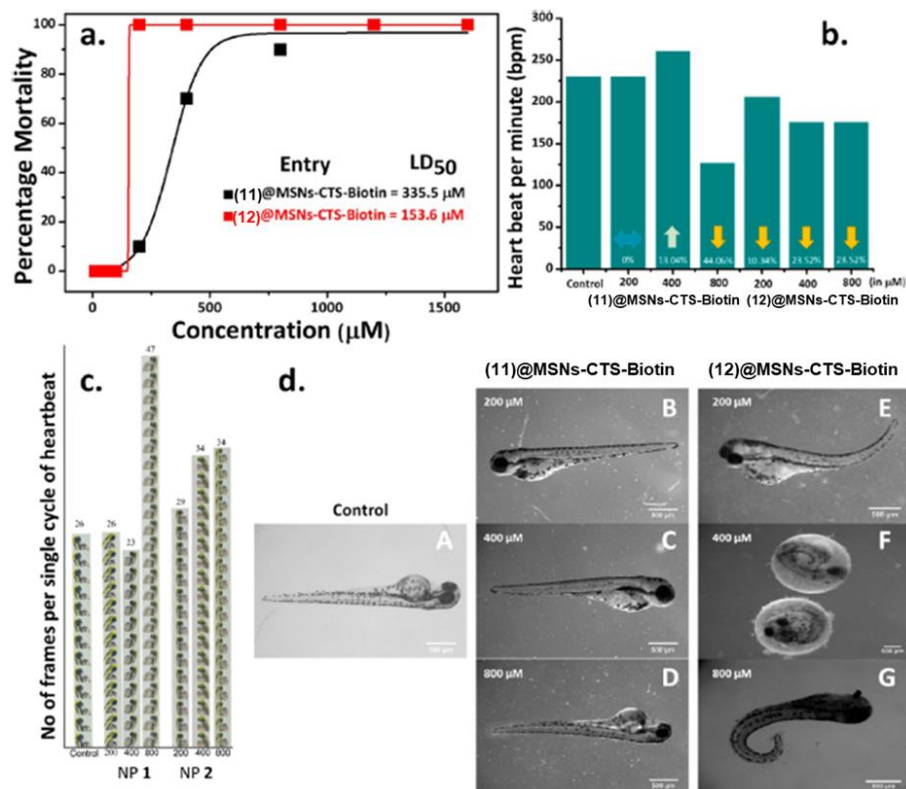


**Figure.5.23:** (a) Toxicity comparison by determining LD<sub>50</sub> of (11)@MSNs-CTS-Biotin (NP 1), and (12)@MSNs-CTS-Biotin (NP 2) in zebrafish embryos at different doses (10, 25, 50, 100, 200, 400, 800, 1200, and 1600  $\mu\text{M}$ ). (b) Bar chart for percentage heartbeat rate (in bpm) of control, NP 1, and NP 2. Arrows denote percentage increase or decrease in heartbeat when compared to control. The first bar represents the control. The next three bars represent the NP 1 (200  $\mu\text{M}$ , 400  $\mu\text{M}$ , and 800  $\mu\text{M}$ ) treated zebrafish embryos with the decrease in heartbeat rate (0%, 13.04%, and 44.06%, respectively). The last three bars attribute the decrease of heartbeat of 10.34 %, 23.52 %, and 23.52 %, respectively, when treated with increasing concentration (200  $\mu\text{M}$ , 400  $\mu\text{M}$ , and 800  $\mu\text{M}$ ) of NP 2. (c) Representing the number of frames for a single systole and diastole for control, NP 1, and NP 2. Higher heartbeat rate has less frames to complete a single systole and diastole whereas lower heart beat rate has higher frames. Each bar signifies the number of frames for single systole

and diastole cycle of larvae incubated with or without nanodrugs. (d) Malformations observed in zebrafish embryos at 48 hpf after treatment with NP 1, and NP 2. Where (A) control zebrafish, (B,C) embryos treated with 200  $\mu\text{M}$  and 400  $\mu\text{M}$  of NP 1 showing no observable deformities, (D) embryos treated with 800  $\mu\text{M}$  of NP 1 displaying stunned growth, (E) embryos treated with 200  $\mu\text{M}$  of NP 2 presents blood congestion, edema, stunted growth, tail and head malformation, (F) embryos treated with 400  $\mu\text{M}$  of NP 2 producing delayed hatching after 48 hpf, and (G) embryos treated with 800  $\mu\text{M}$  of NP 2 screening the dead larvae after 48 hpf.

### 5.3.8 Elucidating binding parameters for compound-biomolecules interaction

In general, nanocarrier based drug delivery requires selective release inside cancer cells to facilitate the interaction between core drug agents and the proteins and/or DNA of that cancer cells. Thus, investigating the extent of such binding interactions *via* spectroscopic assays can have the potential to explain the possible anticancer mechanism or cellular apoptosis. This includes the determination of the intrinsic binding constant ( $K_b$ ) values for CT-DNA, Stern-Volmer quenching constant ( $K_{SV}$ ), binding constant ( $K_a$ ), and bimolecular quenching constant ( $K_q$ ) from the Scatchard equation for BSA, and HSA, respectively. Furthermore,  $K_{SV}$ ,  $K_a$ , and  $K_q$  parameters were also calculated for CT-DNA to determine the specific groove binding ability of the compounds through ethidium bromide (EtBr) displacement assay (Figure 5.24-5.26). At a glance, prominent bimolecular interactions were found between CT-DNA and ZnMBC 11/12, whereas that of ZnMBC 12 showed more interacting affinity with proteins (BSA/HSA) than that of ZnMBC 11. Apart from that, the outcomes of the EtBr displacement assay indicate the strong groove binding ability of the compounds to CT-DNA. It is also well established that the better the binding with biomolecules more will be the biological activity. From the TCSPC data, the fluorescent lifetime quenching is more in the case of ZnMBC 12 (e.g., 5.29 ns to 1.5 ns in the case of BSA, and 3.47 ns to 0.95 ns for HSA, respectively), while treated with both proteins, furnishing better host-guest

interactions (Figure 5.27). Thus, superior binding affinities of ZnMBC **12** towards proteins as revealed by above experiment could be advantageous for higher cytotoxicity of (**12**)@MSNs-CTS-Biotin over (**11**)@MSNs-CTS-Biotin (Table 5.6).

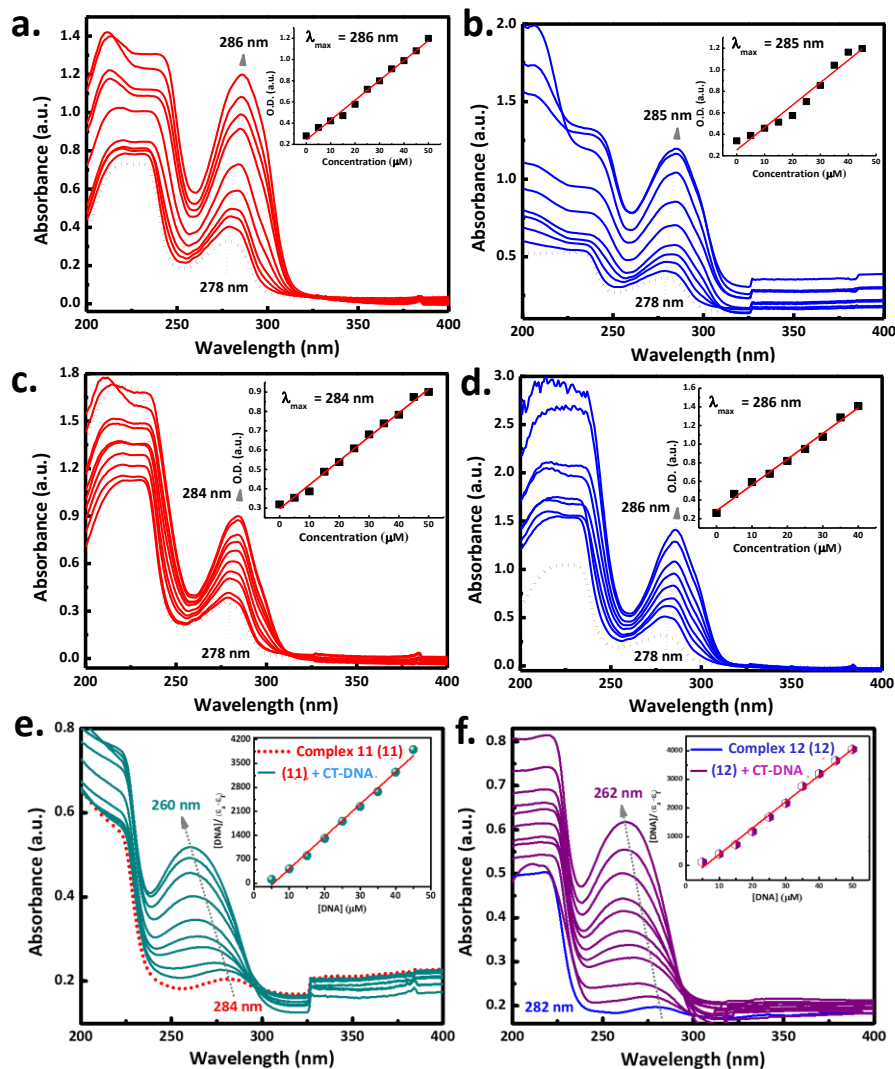


**Figure.5.24:** UV-Visible titration diagram of BSA (10 μM) and HSA (10 μM) by successive addition of ZnMBC **11** [Graph-(a) and (c)], and ZnMBC **12** [Graph-(b) and (d)] (0-50 μM in 0.01 M Tris-HCl buffer). (e-f) Electronic titration of fixed concentration (10 μM) of complex **11** with raising conc. (0-50 μM) of CT-DNA in 0.01 M Tris-HCl buffer of pH~ 7.4. Spectral change happening at 260 nm, and 262 nm for ZnMBC **11**, and ZnMBC **12**, respectively. Arrows indicates the change in absorbance upon increasing DNA

concentration. Inset: Plots of  $[ct\text{-DNA}]$  vs.  $[ct\text{-DNA}]/\varepsilon_a - \varepsilon_f$  for the titration of  $ct\text{-DNA}$  with complexes.

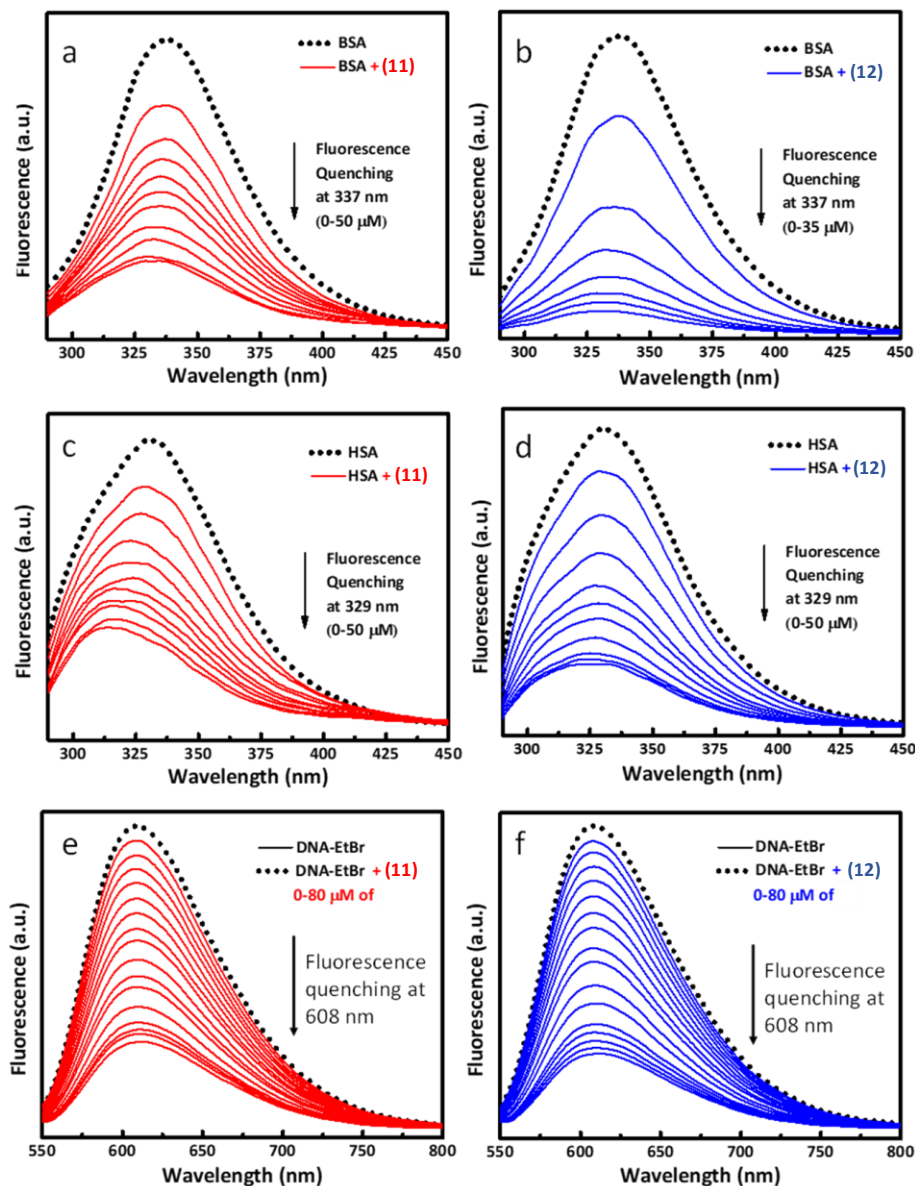


**Figure.5.25:** (a-b) Fluorescence quenching spectra of BSA ( $10 \mu\text{M}$ ) at different concentrations ( $0\text{-}50 \mu\text{M}$ ) of ZnMBC 11, and ZnMBC 12 at 298 K. (c-d) Fluorescence quenching spectra of HSA ( $10 \mu\text{M}$ ) at different concentrations ( $0\text{-}50 \mu\text{M}$ ) of ZnMBC 11, and ZnMBC 12 at 298 K. (e-f) Representing EtBr displacement assay of ZnMBC 11, and ZnMBC 12.  $[CT\text{-DNA}] = 10 \mu\text{M}$  with ethidium bromide (EB  $15 \mu\text{M}$ ) and  $[complex] = 0\text{-}80 \mu\text{M}$  in Tris-HCl/ NaCl

buffer (5 mM/ 50 mM, pH~ 7.4). The arrow shows the fluorescence changes upon increasing the CT-DNA concentration.

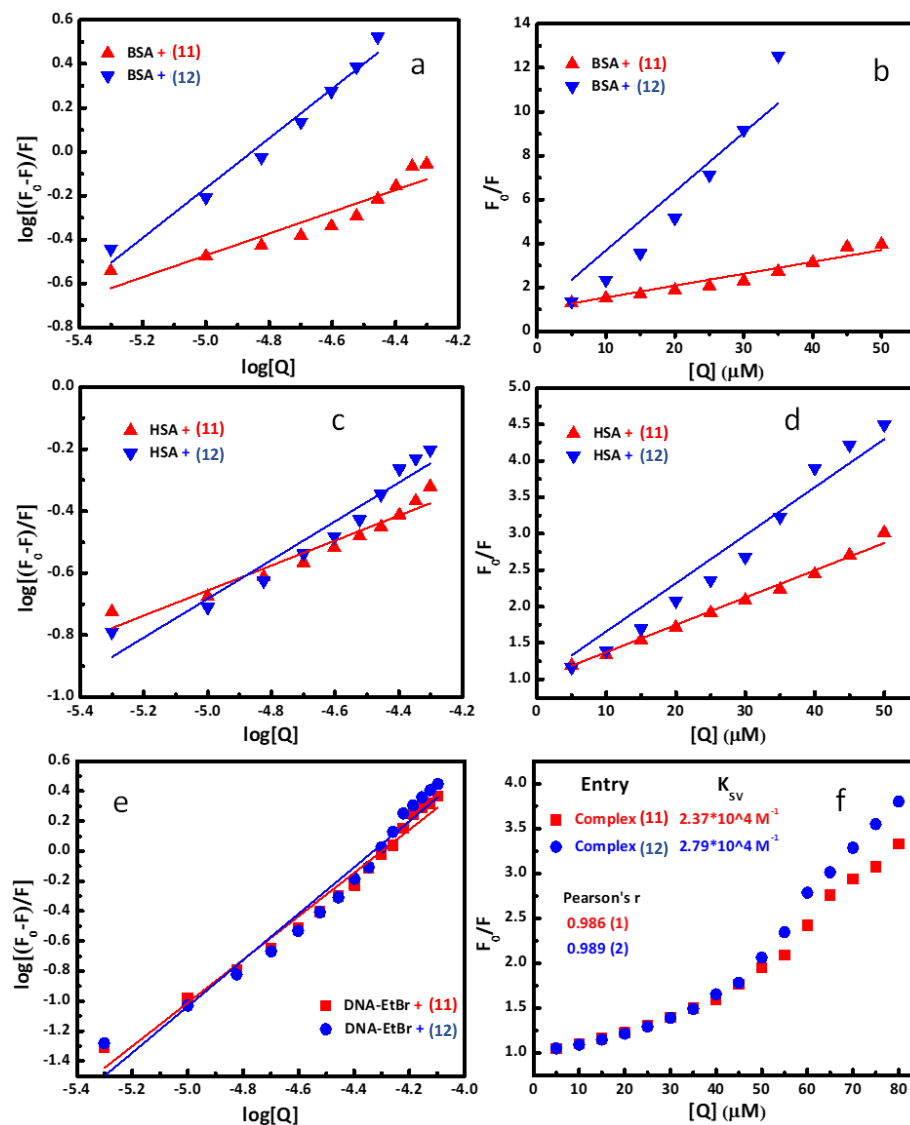


**Figure.5.26:** Fluorescence quenching profile and statistical analysis of ZnMBC 11, and ZnMBC 12: (a, c, and e) Scatchard plots, and (b, d, and f) Stern-Volmer (SV) plots for BSA, HSA, and CT-DNA, respectively.

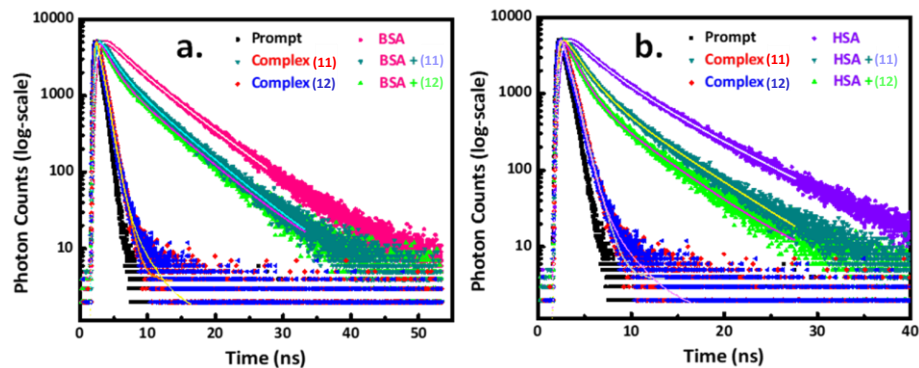


**Figure.5.27:** Measurement of lifetime decay parameters of BSA (left), and HSA (right) before and after the compound treatment (where, **11** = ZnMBC **11**, and **12** = ZnMBC **12**).

**Table.5.6.** Determination of various spectral parameters to check the interaction between the titled compounds with CT-DNA, BSA, and HSA, respectively.

Systems	$K_{SV} (M^{-1})^a$	$K_q (M^{-1}S^{-1})^a$	$K_a (M^{-1})^a$	$K_b (M^{-1})^b$	$n^a$
(1)-DNA	$2.3 \times 10^4$	$3.7 \times 10^{12}$	$4.7 \times 10^6$	$1.8 \times 10^5$	1.5
(2)-DNA	$2.7 \times 10^4$	$4.3 \times 10^{12}$	$4.7 \times 10^6$	$1.7 \times 10^5$	1.5
(1)-BSA	$5.4 \times 10^4$	$8.7 \times 10^{12}$	$1.0 \times 10^2$	-	0.4
(2)-BSA	$2.6 \times 10^5$	$4.2 \times 10^{13}$	$2.5 \times 10^5$	-	1.1
(1)-HSA	$3.7 \times 10^4$	$5.9 \times 10^{12}$	$2.2 \times 10^1$	-	0.4
(2)-HSA	$6.5 \times 10^4$	$1.0 \times 10^{13}$	$2.5 \times 10^2$	-	0.6

Where, a = determined by emission, and b = calculated *via* absorbance spectroscopy.

### 5.3.9 Nucleus tracking *via* two photons confocal microscopy

Cellular apoptosis can happen may be because of various causes, and among them, nucleus damage remains a significant reason. The superior DNA-targeting ability of the compounds may lead to damage inside the nucleus as DNA is the significant component composing this specific organelle. In order to track the anticancer efficacy of the titled nanodrugs, DAPI, a nucleus-staining dye, was chosen to visualize any morphological disruption using two-photon confocal microscopy. As represented in Figure 5.28a, no substantial

cellular stress was observed for HEK-293 normal cells; nevertheless, arrows in Figure 5.28b show considerable cellular apoptosis in HeLa cancer cells when treated with (12)@MSNs-CTS-Biotin. A control experiment was performed in the absence of (12)@MSNs-CTS-Biotin to compare the results, as shown in Figure 5.28c. Similar outcomes were also perceived with (11)@MSNs-CTS-Biotin and summarized in Figure 5.29. Hereafter, this can be concluded that these nanodrugs selectively target cancer cells without affecting normal cells.

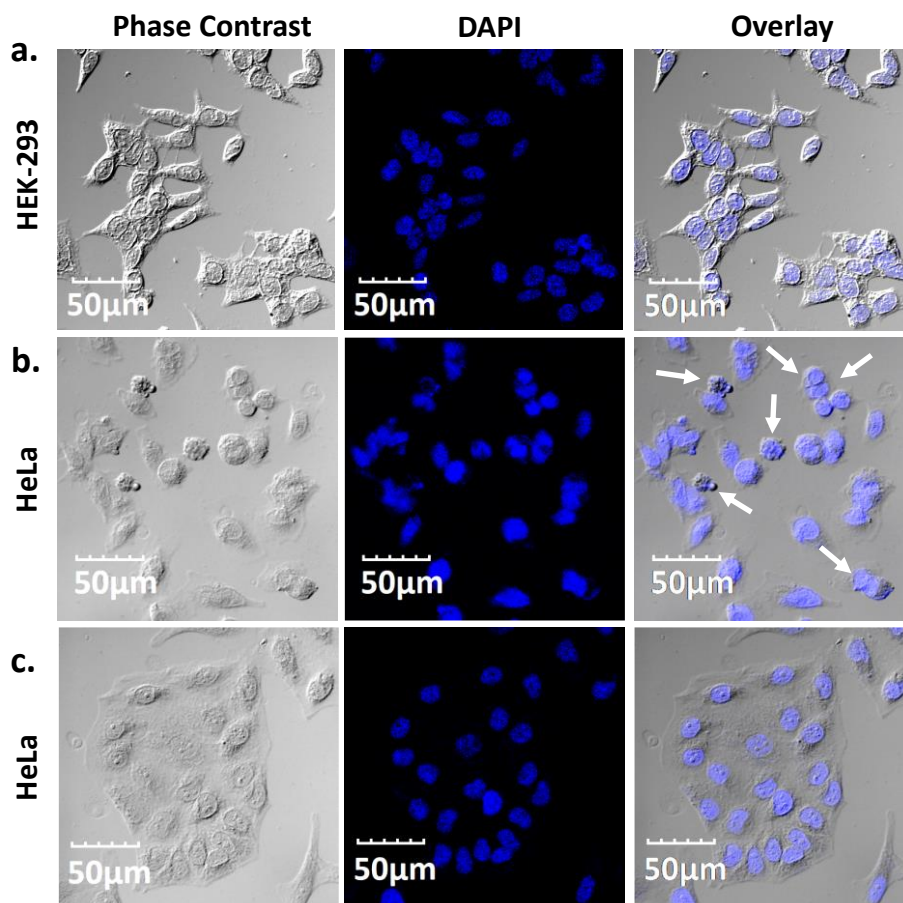


**Figure.5.28:** Two photon confocal laser scanning microscopy (CLSM) profiles after the treatment of (a) (12)@MSNs-CTS-Biotin in HEK-293 normal cells, (b) (12)@MSNs-CTS-Biotin in HeLa cancer cells while arrows denote the significant damage in nucleus, and (c) untreated HeLa cancer cells under physiological condition at 24 h.  $IC_{50}$  concentration of the nanoparticle (12)@MSNs-CTS-Biotin has been used in this experiment.

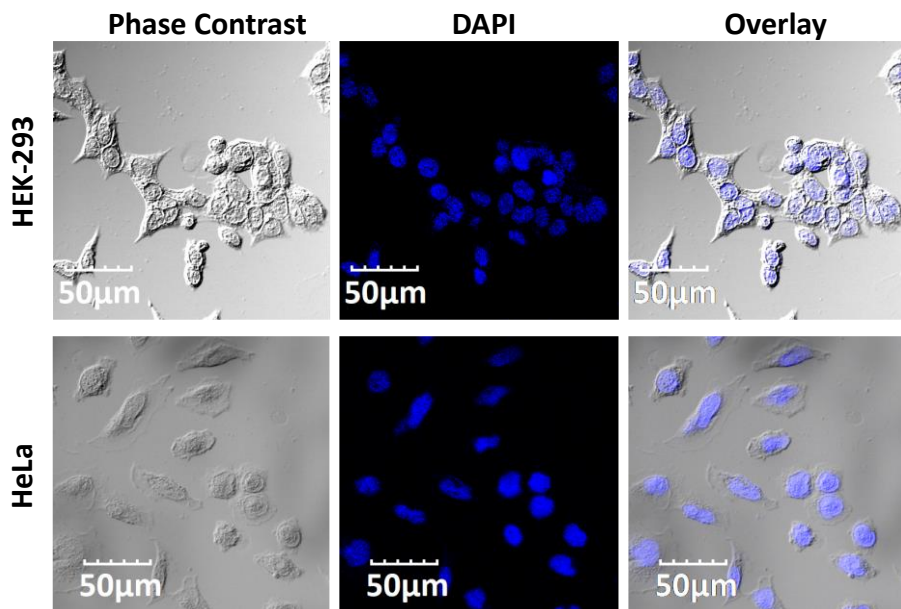


**Figure.5.29:** Two photon confocal laser scanning microscopy (CLSM) profiles after the treatment of (a) (11)@MSNs-CTS-Biotin in HEK-293 normal cells, and (b) (11)@MSNs-CTS-Biotin in HeLa cancer cells while arrows denote the significant damage in nucleus under physiological condition at 24 h.

### 5.3.10 Dual staining assay exploiting various dyes

These nuclear morphological changes during apoptosis were further investigated by exploring double staining assay with DNA binding dyes, e.g., Hoechst and PI. Hoechst dye possesses cell permeable aptitude, which stains both live and dead cells. However, PI is a membrane-impermeable dye that is normally barred from staining live cells [37]. Substantial morphological disruptions were seen with the aid of confocal microscopy when cancer cells were incubated in the presence of synthesized compounds at their  $IC_{50}$  concentrations. As depicted in Figure 5.30, Hoechst stains both viable and apoptotic nuclei with bright blue fluorescence, whereas intense red fluorescence with condensed and fragmented nuclei was observed by staining with PI. In addition, untreated cells show uniformly light blue fluorescence and no red emission, which describes no nuclear disruption. These consequences revealed that nanodrugs have the potential to trigger apoptosis in cancer cells. Besides *in vitro* investigation, *in vivo* approach was also taken to confirm the practical usability of the synthesized nanodrugs. Acridine orange (AO), a dye

having similar properties to Hoechst, was used for dual *in vivo* imaging alongside PI. Minor cellular apoptosis was observed over necrosis using dual stain AO/PI, which stains live and apoptotic cells. The AO/PI apoptosis staining upon treatment with nanoconjugates (11)@MSNs-CTS-Biotin, and (12)@MSNs-CTS-Biotin showed deformations (at 72 hpf) in the yolk sack, heart, and brain region at higher doses (200-400  $\mu\text{M}$ ) only (Figure 5.31), thus extending the support for practical applicability of the compounds in the lower concentration ranges.

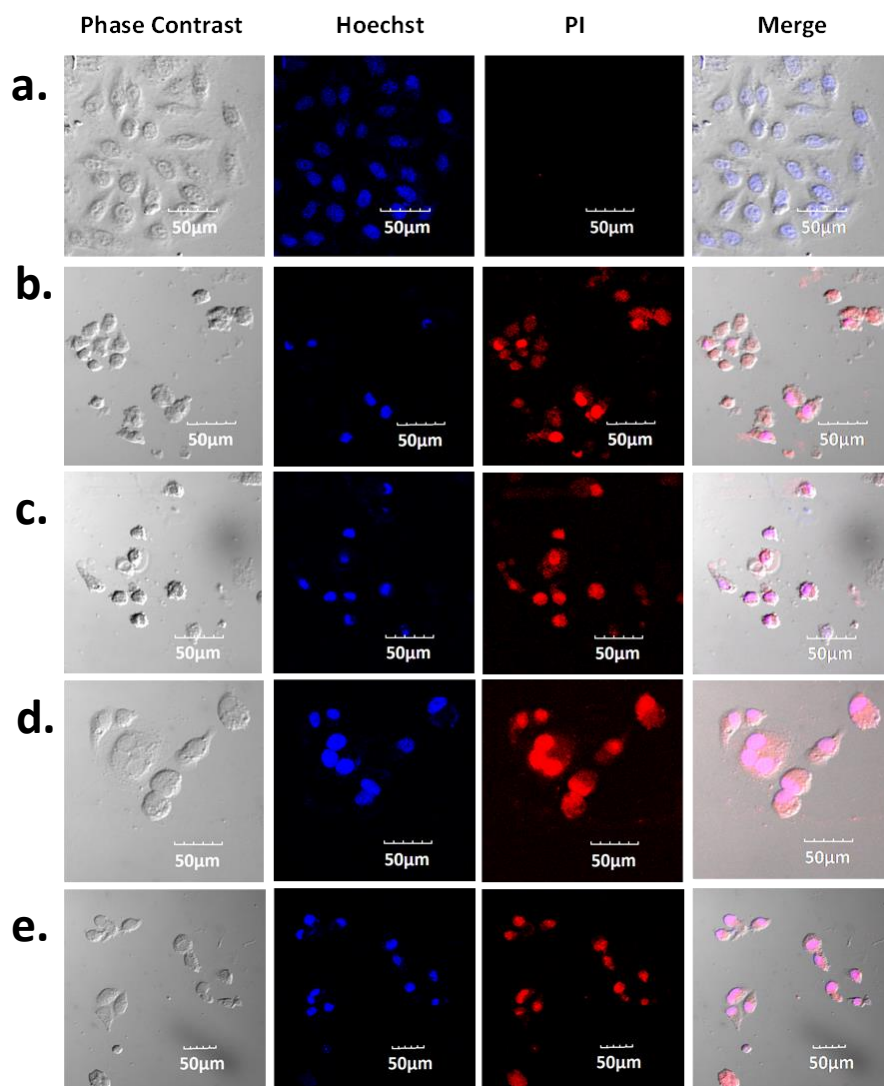


**Figure.5.30:** Hoechst and propidium iodide (PI) dual staining assay profile of HeLa cells after treating with and without core anticancer agents and

nanoparticles after 24 h (a) control (b) ZnMBC 11 (c) ZnMBC 12 (d) (11)@MSNs-CTS-Biotin and, (e) (12)@MSNs-CTS-Biotin.

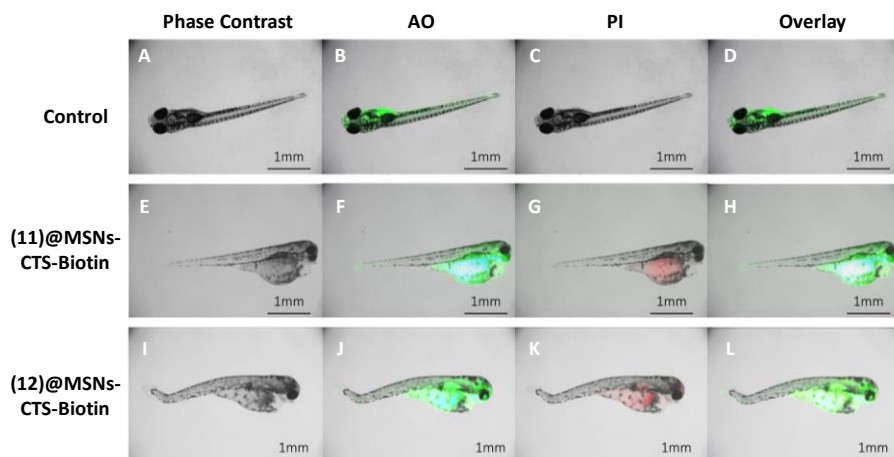


**Figure.5.31:** Nanoparticles (11)@MSNs-CTS-Biotin, and (12)@MSNs-CTS-Biotin induced apoptotic and/or necrotic fluorescence signal. Image of AO/PI double staining in zebrafish after treatment with nanoparticles (72 hpf). (A) Zebrafish control larvae (B) zebrafish control larvae stained with AO emitting green fluorescence. (C) Absence of red fluorescence in control fishes when stained with PI. (D) Merged Image of dual stained zebrafish showing live cells at 72 hpf. (E) 400  $\mu\text{M}$  of (11)@MSNs-CTS-Biotin treated zebrafish showing deformities. (F, G) zebrafish treated with 400  $\mu\text{M}$  of (11)@MSNs-CTS-Biotin and stained with AO, and PI, respectively. (H) merged image of (F) and (G) showing live and dead cells. (I) 200  $\mu\text{M}$  of (12)@MSNs-CTS-Biotin treated zebrafish screening deformities. (J, K) zebrafish treated with 200  $\mu\text{M}$  of (12)@MSNs-CTS-Biotin and stained with AO, and PI, respectively. (L) AO and PI fluorescent-stained merged image displaying live and dead cells. No such deformations were observed at  $\text{LD}_{50}$  concentrations.

### 5.3.11 Monitoring the production of reactive oxygen species (ROS)

ROS plays an important role in regulating cell proliferation, cellular apoptosis, and the mechanistic action of cell death. Excessive and uncontrolled production of ROS cannot be tolerated by cells as they possess inadequate scavenging capacity, which leads to oxidative stress and can accelerate damage inside cellular components. Owing to the abnormal cellular function, cancer

cells are indeed under amplified oxidative stress compared to normal cells. Thus, nanocarrier-based targeted chemotherapy can be the suitable route to enhance anticancer efficacy. Complexes and nanoparticles (at 10  $\mu\text{M}$  concentration) treated HeLa cancer cells were incubated and investigated via DCF-DA assay, which shows extensive ROS overproduction for each compound after 24 h (Figure 5.32a). A significant enhancement in ROS generation was monitored with the gradual increment in time (Figure 5.32b). At a glance, the generated ROS break the two acetate linkages of non-fluorescent DCF-DA to give green fluorescence-based DCF. An intensity profile for all the compounds mediated ROS overproduction has been derived in Figure 5.32c, which suggests the role of the core and nanodrugs in ROS generation, which is followed by cellular apoptosis.

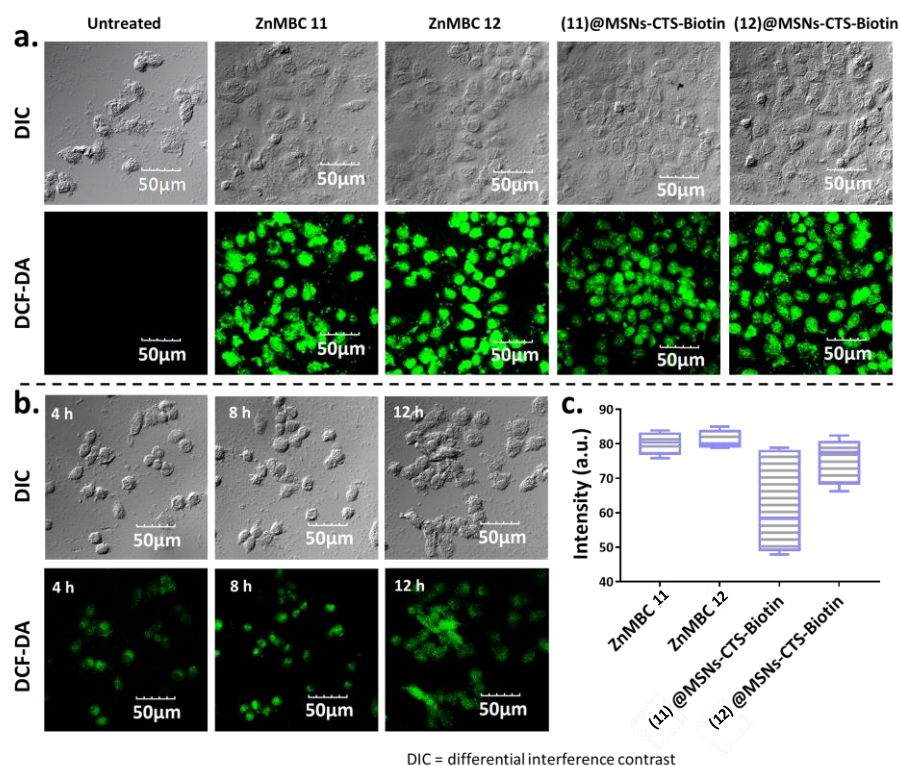


**Figure.5.32:** (a) ROS generation induced by core anticancer agents ZnMBC 1/2, and the corresponding nanodrugs (11/12)@MSNs-CTS-Biotin (at 10  $\mu\text{M}$  concentration) after 24 h confirming the influence of ROS to the cellular apoptosis (in HeLa cell lines). Untreated cells give no green fluorescence. (b) Time dependent ROS production in presence of (12)@MSNs-CTS-Biotin at

*IC<sub>50</sub> concentration. (c) Normalize intensity percentage (including standard deviation) of ROS overproduction calculated using ImageJ programme. DIC denotes differential interference contrast confocal technique.*

#### **5.4 Conclusions**

In a nutshell, MSNs nanocarrier-coated drug delivery systems are successfully fabricated and utilized for targeted anticancer activity. Nevertheless, the zinc complexes showed better cytotoxicity against various cancer cells, but they were found to be less selective towards normal cells than when attached to the nanoconjugates. The pH-triggered release of zinc complexes has been achieved using the CTS tag, whereas modified bioconjugation with Biotin helps in higher accumulation through receptor-mediated endocytosis in cancer cells. The intracellular ZnMBC triggers ROS overproduction that could attack DNA in the nucleus and induce DNA damage-mediated cellular apoptosis. Notably, all the outcomes directed that the nanoparticle-assisted drugs endorsed the enhanced selectivity of ZnMBC between cancer and normal cells, and consequently, it showed an improved anticancer property. The reliability of this approach will offer opportunities to explore more functional and cost-effective drug delivery systems, which could achieve better cellular uptake for enhancing chemotherapy in the future.

#### **5.5 Declaration:**

This chapter is adapted from ACS Applied Bio Materials, 2021, 5(1), 190-204. (DOI: 10.1021/acsabm.1c01041)

#### **5.6 References:**

- [1] Zhong, J., Li, L., Zhu, X., Guan, S., Yang, Q., Zhou, Z., ... & Huang, Y. (2015), A smart polymeric platform for multistage nucleus-targeted anticancer drug delivery. *Biomaterials*, 65, 43-55. (DOI: 10.1016/j.biomaterials.2015.06.042).
- [2] Yang, J., Shimada, Y., Olsthoorn, R. C., Snaar-Jagalska, B. E., Spaink, H. P., & Kros, A. (2016), Application of coiled coil peptides in liposomal anticancer drug delivery using a zebrafish xenograft model. *ACS Nano*, 10(8), 7428-7435. (DOI: 10.1021/acs.nano.6b01410).

- [3] He, L., Huang, Y., Zhu, H., Pang, G., Zheng, W., Wong, Y. S., & Chen, T. (2014), Cancer-targeted monodisperse mesoporous silica nanoparticles as carrier of ruthenium polypyridyl complexes to enhance theranostic effects. *Advanced Functional Materials*, 24(19), 2754-2763. (DOI: 10.1002/adfm.201303533).
- [4] Shi, J., Votruba, A. R., Farokhzad, O. C., & Langer, R. (2010), Nanotechnology in drug delivery and tissue engineering: from discovery to applications. *Nano letters*, 10(9), 3223-3230. (DOI: 10.1021/nl102184c).
- [5] Hudson, S., Cooney, J., & Magner, E. (2008), Proteins in mesoporous silicates. *Angewandte Chemie International Edition*, 47(45), 8582-8594. (DOI: 10.1002/anie.200705238).
- [6] Pan, L., He, Q., Liu, J., Chen, Y., Ma, M., Zhang, L., & Shi, J. (2012), Nuclear-targeted drug delivery of TAT peptide-conjugated monodisperse mesoporous silica nanoparticles. *Journal of the American Chemical Society*, 134(13), 5722-5725. (DOI: 10.1021/ja211035w).
- [7] Rosenholm, J. M., Meinander, A., Peuhu, E., Niemi, R., Eriksson, J. E., Sahlgren, C., & Lindén, M. (2009), Targeting of porous hybrid silica nanoparticles to cancer cells. *ACS nano*, 3(1), 197-206. (DOI: 10.1021/nn800781r).
- [8] Wang, C., Li, Z., Cao, D., Zhao, Y. L., Gaines, J. W., Bozdemir, O. A., ... & Stoddart, J. F. (2012), Stimulated release of size-selected cargos in succession from mesoporous silica nanoparticles. *Angewandte Chemie International Edition*, 51(22), 5460-5465. (DOI: 10.1002/anie.201107960).
- [9] Ferris, D. P., Lu, J., Gothard, C., Yanes, R., Thomas, C. R., Olsen, J. C., ... & Zink, J. I. (2011), Synthesis of biomolecule-modified mesoporous silica nanoparticles for targeted hydrophobic drug delivery to cancer cells. *Small*, 7(13), 1816-1826. (DOI: 10.1002/sml.201002300).
- [10] Tao, Z., Toms, B., Goodisman, J., & Asefa, T. (2010), Mesoporous silica microparticles enhance the cytotoxicity of anticancer platinum drugs. *ACS nano*, 4(2), 789-794. (DOI: 10.1021/nn9015345).

- [11] Maiti, S., Park, N., Han, J. H., Jeon, H. M., Lee, J. H., Bhuniya, S., ... & Kim, J. S. (2013). Gemcitabine–coumarin–biotin conjugates: a target specific theranostic anticancer prodrug. *Journal of the American Chemical Society*, 135(11), 4567-4572. (DOI: 10.1021/ja401350x).
- [12] Yang, W., Cheng, Y., Xu, T., Wang, X., & Wen, L. P. (2009). Targeting cancer cells with biotin–dendrimer conjugates. *European journal of medicinal chemistry*, 44(2), 862-868. (DOI: 10.1016/j.ejmech.2008.04.021).
- [13] Lis, L. G., Smart, M. A., Luchniak, A., Gupta Jr, M. L., & Gurvich, V. J. (2012). Synthesis and biological evaluation of a biotinylated paclitaxel with an extra-long chain spacer arm. *ACS Medicinal chemistry letters*, 3(9), 745-748. (DOI: 10.1021/ml300149z).
- [14] Wei, W., Yuan, L., Hu, G., Wang, L. Y., Wu, J., Hu, X., ... & Ma, G. H. (2008). Monodisperse chitosan microspheres with interesting structures for protein drug delivery. *Advanced Materials*, 20(12), 2292-2296. (DOI: 10.1002/adma.200702663).
- [15] Liu, W. T., Yang, Y., Shen, P. H., Gao, X. J., He, S. Q., Liu, H., & Zhu, C. S. (2015). Facile and simple preparation of pH-sensitive chitosan-mesoporous silica nanoparticles for future breast cancer treatment. *Express Polymer Letters*, 9(12). (DOI: 10.3144/expresspolymlett.2015.96).
- [16] Bruijninx, P. C., & Sadler, P. J. (2008). New trends for metal complexes with anticancer activity. *Current opinion in chemical biology*, 12(2), 197-206. (DOI: 10.1016/j.cbpa.2007.11.013).
- [17] Pellei, M., Del Bello, F., Porchia, M., & Santini, C. (2021). Zinc coordination complexes as anticancer agents. *Coordination Chemistry Reviews*, 445, 214088. (DOI: 10.1016/j.ccr.2021.214088).
- [18] Kundu, B. K., Mobin, S. M., & Mukhopadhyay, S. (2020). Studies on the influence of the nuclearity of zinc (ii) hemi-salen complexes on some pivotal biological applications. *Dalton Transactions*, 49(43), 15481-15503. (DOI: 10.1039/D0DT02941F).

- [19] San José-Enériz, E., Gimenez-Camino, N., Agirre, X., & Prosper, F. (2019). HDAC inhibitors in acute myeloid leukemia. *Cancers*, 11(11), 1794. (DOI: 10.3390/cancers11111794).
- [20] Pape, V. F., May, N. V., Gál, G. T., Szatmári, I., Szeri, F., Fülöp, F., ... & Enyedy, É. A. (2018). Impact of copper and iron binding properties on the anticancer activity of 8-hydroxyquinoline derived Mannich bases. *Dalton Transactions*, 47(47), 17032-17045. (DOI: 10.1039/C8DT03088J).
- [21] Abdel-Rahman, I. M., Mustafa, M., Mohamed, S. A., Yahia, R., Abdel-Aziz, M., Abuo-Rahma, G. E. D. A., & Hayallah, A. M. (2021). Novel Mannich bases of ciprofloxacin with improved physicochemical properties, antibacterial, anticancer activities and caspase-3 mediated apoptosis. *Bioorganic Chemistry*, 107, 104629. (DOI: 10.1016/j.bioorg.2021.104629).
- [22] De Luca, E., Zaccaria, G. M., Hadhoud, M., Rizzo, G., Ponzini, R., Morbiducci, U., & Santoro, M. M. (2014). ZebraBeat: a flexible platform for the analysis of the cardiac rate in zebrafish embryos. *Scientific Reports*, 4(1), 4898. (DOI: 10.1038/srep04898).
- [23] Kundu, B. K., Biswas, S., Mondal, A., Mazumdar, S., Mobin, S. M., & Mukhopadhyay, S. (2021). Unveiling the urease like intrinsic catalytic activities of two dinuclear nickel complexes towards the in situ syntheses of aminocyanopyridines. *Dalton Transactions*, 50(14), 4848-4858.
- [24] Kundu, B. K., Ranjan, R., Mukherjee, A., Mobin, S. M., & Mukhopadhyay, S. (2019). Mannich base Cu (II) complexes as biomimetic oxidative catalyst. *Journal of Inorganic Biochemistry*, 195, 164-173. (DOI: 10.1016/j.jinorgbio.2019.03.023).
- [25] Lv, G., Qiu, L., Liu, G., Wang, W., Li, K., Zhao, X., & Lin, J. (2016). pH sensitive chitosan-mesoporous silica nanoparticles for targeted delivery of a ruthenium complex with enhanced anticancer effects. *Dalton Transactions*, 45(45), 18147-18155. (DOI: 10.1039/C6DT03783F).
- [26] Kundu, B. K., Das, M., Ganguly, R., Bhoje, P. A., & Mukhopadhyay, S. (2020). Role of zeolite encapsulated Cu (II) complexes in electron transfer as

well as peroxy radical intermediates formation during oxidation of thioanisole. *Journal of catalysis*, 389, 305-316. (DOI: 10.1016/j.jcat.2020.06.005).

[27] Kundu, B. K., Chhabra, V., Malviya, N., Ganguly, R., Mishra, G. S., & Mukhopadhyay, S. (2018). Zeolite encapsulated host-guest Cu (II) Schiff base complexes: Superior activity towards oxidation reactions over homogenous catalytic systems. *Microporous and Mesoporous Materials*, 271, 100-117. (DOI: 10.1016/j.micromeso.2018.05.046)

[28] Lee, E. L., & Wachs, I. E. (2008). In situ Raman spectroscopy of SiO<sub>2</sub>-supported transition metal oxide catalysts: an isotopic <sup>18</sup>O–<sup>16</sup>O exchange study. *The Journal of Physical Chemistry C*, 112(16), 6487-6498. (DOI: 10.1021/jp076485w).

[29] Jiang, J., Zhu, P., Li, D., Chen, Y., Li, M., Wang, X., ... & Zhu, H. (2016). High pressure studies of trimethyltin azide by Raman scattering, IR absorption, and synchrotron X-ray diffraction. *RSC advances*, 6(101), 98921-98926. (DOI: 10.1039/C6RA20938F).

[30] Wang, Y., Han, N., Zhao, Q., Bai, L., Li, J., Jiang, T., & Wang, S. (2015). Redox-responsive mesoporous silica as carriers for controlled drug delivery: a comparative study based on silica and PEG gatekeepers. *European journal of pharmaceutical sciences*, 72, 12-20. (DOI: 10.1016/j.ejps.2015.02.008).

[31] Pragti, Kundu, B. K., & Mukhopadhyay, S. (2021). Target based chemotherapeutic advancement of ruthenium complexes. *Coordination Chemistry Reviews*, 448, 214169. (DOI: 10.1016/j.ccr.2021.214169).

[32] Pragti, Kundu, B. K., Sonkar, C., Ganguly, R., & Mukhopadhyay, S. (2021). Modulation of catalytic and biomolecular binding properties of ruthenium (II)-arene complexes with the variation of coligands for selective toxicity against cancerous cells. *Polyhedron*, 207, 115379. (DOI: 10.1016/j.poly.2021.115379).

[33] No, O. T. (1992). 203: Fish, acute toxicity test. *OECD guidelines for the testing of chemicals*, Section, 2, 02-24.

[34] Panzica-Kelly, J. M., Zhang, C. X., & Augustine-Rauch, K. A. (2015). Optimization and performance assessment of the chorion-off [dechorinated]

zebrafish developmental toxicity assay. *Toxicological Sciences*, 146(1), 127-134. (DOI: 10.1093/toxsci/kfv076).

[35] Shaw, B. J., Liddle, C. C., Windeatt, K. M., & Handy, R. D. (2016). A critical evaluation of the fish early-life stage toxicity test for engineered nanomaterials: experimental modifications and recommendations. *Archives of toxicology*, 90, 2077-2107. (DOI: 10.1007/s00204-016-1734-7).

[36] von Hellfeld, R., Brotzmann, K., Baumann, L., Strecker, R., & Braunbeck, T. (2020). Adverse effects in the fish embryo acute toxicity (FET) test: a catalogue of unspecific morphological changes versus more specific effects in zebrafish (*Danio rerio*) embryos. *Environmental Sciences Europe*, 32, 1-18. (DOI: 10.1186/s12302-020-00398-3).

[37] Mukhopadhyay, S., Gupta, R. K., Paitandi, R. P., Rana, N. K., Sharma, G., Koch, B., ... & Pandey, D. S. (2015). Synthesis, structure, DNA/protein binding, and anticancer activity of some half-sandwich cyclometalated Rh (III) and Ir (III) complexes. *Organometallics*, 34(18), 4491-4506. (DOI: 10.1021/acs.organomet.5b00475).

[38] Dai, X., Zhang, B., Zhou, W., & Liu, Y. (2020). High-efficiency synergistic effect of supramolecular nanoparticles based on cyclodextrin prodrug on cancer therapy. *Biomacromolecules*, 21(12), 4998-5007. (DOI: 10.1021/acs.biomac.0c01181).



*Chapter 6*

*General conclusions and future scopes*



## Chapter 6

### General conclusions and future scopes

The thesis presents ruthenium and zinc metal-based complexes with different organic and inorganic ligands of known therapeutic properties and an assessment of their antiproliferative activities. The efficient delivery of the metallodrugs is the other area which is investigated in this work. The mechanistic pathway of the anticancer properties of the complexes is explored through their interactions with various biomolecules, staining techniques and microscopic studies. The Western Blot technique investigates the upregulation and downregulation of the associated proteins in this study.

In Chapter 2, the synthesis and characterization of four ruthenium(II)-arene complexes (**1-4**) are reported. Different analytical techniques have been utilized to characterize, and a DFT study was used to optimize the geometries and calculate the energies of the frontier molecular orbitals. An MTT assay revealed the potency of complexes against MCF-7 (breast cancer) and HeLa (cervical cancer) cell lines. The complexes are found to be specifically cytotoxic against cancerous cell lines, as they were inactive against the normal HEK 293 cell line. An absorption and fluorescence titration study of complexes showed significant interactions with DNA and proteins. Interestingly, all the complexes show potent catalytic activity for the hydrogen transfer of NADH and converted NADH to NAD<sup>+</sup>, which helps to induce the accumulation of intracellular reactive oxygen species (ROS) in MCF-7 cells. The Hoechst staining method was applied to analyze the morphological changes to capture images of apoptotic cells through confocal microscopy.

Four new organometallic Ru(II)-arene complexes (**5-8**) have been synthesized, characterized, and reported in Chapter 3 with anticancer, antimetastatic and two-photon cell imaging abilities. All the complexes are well characterized by spectroscopic techniques (NMR, mass, FTIR, UV-Vis and fluorescence). The stability study of the complexes was performed through UV-visible spectroscopy. The cytotoxicities of all the complexes were screened through an

MTT assay, and the results revealed that the complexes have potential anticancer activity against various cancerous cells (HeLa, MCF7 and A431). Studies with spectroscopic techniques revealed that complexes **5-8** exhibit strong interactions with biological molecules, i.e. proteins (HSA and BSA) and CT-DNA. A plausible mechanism for NADH oxidation has also been explored, and the DFT calculations are found to be in accord with the experimental observation. Furthermore, the complexes are found to be capable of intracellular reactive oxygen species (ROS) generation in the MCF7 breast cancer cell line. The Hoechst/PI dual staining method confirmed the apoptosis mode of cell death. Meanwhile, complexes show capabilities to prevent the metastasis phase of cancer cells by inhibiting cell migration.

Chapter 4 presents a novel drug delivery system (nanogels) that can target cancer cells and release drugs in response to changes in pH levels, minimizing side effects and maximizing effectiveness. These nanogels can be loaded with synthesized glucose ring conjugated ruthenium (II) arene complexes (**9-10**) as anticancer agents. All the spectroscopic and analytical results like NMR, ESI-MS, FTIR, UV-visible, SEM, TEM, XPS, rheology, BET, supports the formation of the proposed compounds and fabricated nanogels. Nanogels (NGs) can display exceptional increased efficacy toward cancerous cells with IC<sub>50</sub> values ranging from 7.50 to 18.86  $\mu\text{M}$  via induced apoptosis in a group of three human cancer cell lines. Apart from its potency, NGs found to be highly selective towards cancer cells. Moreover, based on the results of immunoblot analysis, it can be concluded that the synthesized compounds exhibit a significant increase in the expression of cleaved caspase-3 and a decrease in the expression of the anti-apoptotic protein BCL-XL. Additionally, it was discovered that NG-induced apoptosis is dependent on ROS production and DNA targeting. Furthermore, a narrower range of LD<sub>50</sub> values (1185.93 and 823.03  $\mu\text{M}$ ) was seen after administering NGs to zebrafish embryos *in vivo*.

Chapter 5 opens up a key route toward enhanced chemotherapy with the help of two Zn (II) Mannich base complexes: **ZnMBC (11-12)** synthesized alongside Mannich base ligands to investigate their biological potency.

Further, well-established mesoporous silica nanoparticles (MSNs) have been chosen as carriers of the titled metallodrugs in order to achieve anticancer drug delivery. A pH-sensitive additive, namely, chitosan (CTS) conjugated with biotin, is tagged to MSNs for the targeted release of core agents inside tumours selectively. The CTS blocked **ZnMBC** inside the mesopores of MSNs, and biotin acted as a targeting ligand to improve tumour-specific cellular uptake. It was found that the CTS-biotin surface decoration can significantly enhance the cellular uptake of **ZnMBC** through endocytosis. A panel of four human cancer cell lines has revealed that **ZnMBC** (11/12)@ **MSNs-CTS-biotin** nanoparticles (NPs) can exhibit unprecedented enhanced cytotoxicity toward cancer cells with  $IC_{50}$  values ranging from 6.5 to 28.8  $\mu\text{M}$  through induction of apoptosis. NPs also possessed excellent selectivity between normal and cancer cells, along with their enhanced efficacy. Two-photon-excited *in vitro* imaging of normal (HEK) and cancer (HeLa) cells has confirmed the drug delivery. Also, NP-induced apoptosis was found to be dependent on targeting DNA and ROS generation. Moreover, a lower range of  $LD_{50}$  values (153.6-335.5  $\mu\text{M}$ ) was observed upon treatment of zebrafish embryos with NPs *in vivo*.

In the future, *in vivo* research on mice can be conducted to evaluate the effect of these complexes on the living organism, as this would provide much more in-depth insight into the activities of complexes. Such investigations offer an invaluable opportunity to gain comprehensive insights into the activities and potential therapeutic benefits of these complexes. Additionally, *in vivo* studies on mice can provide valuable preclinical data that can guide the design and optimization of future clinical trials, enabling a more informed and targeted approach towards developing anticancer therapies.